High Power Density Propulsion Motor for Hybrid Electric Aircraft

Nicola Chiodetto

M. Eng

School of Engineering
Newcastle University

A thesis submitted for the degree of
Doctor of Philosophy

August 2021

To Christ and my parents, who freely donated me life and talents.

Acknowledgements

I would like to thank my family for the moral support given, unconditional love, care and blessings they provide me. In terms of technical knowledge and experience I am in debt with Timothy Lisle and Andy Steven for their invaluable advices related to structural analysis, rotordynamics, bearings, fittings, manufacturing and tolerances. I thank John Smith and Merz Court mechanical workshop's team for their work. Likewise I am indebted to Stuart Baker and Jamie Hodgson for their advice and the stator housing manufacturing. Thanks to David Terrington and Bjorn Gudsmussen from Arnold Magnetic Technologies for the technical support, advice and help for the rotor manufacturing. Thanks to Iago, Yerasimos, Giulia, companions in the office and listeners of my endless complains. Thanks to George, Dimitris and Petros for the mathematical, and not only, discussions. This has kept my mind fresh and elastic despite repetitive finite element non stimulating tasks. Thanks to all the other companions of research in the UG Lab. Thanks to all my flat mates in Newcastle during these years who made every house I was a welcoming place. Thanks to my supervisory team: Barrie for his support, help and resources made available; Rafal for patiently listening all the times I popped in the office; Peter for giving me the possibility to undertake this project and have a scholarship.

Abstract

The Civil Aerospace is looking ahead for new solutions that can offer further significant improvement in aircraft efficiencies and emissions. Hybrid Electric Distributed Propulsion (HEDP) aircraft's configurations have been extensively modelled, and these results show it is possible to obtain notable benefits with some authors claiming that overall fuel savings of more than 70% are possible compared with today's designs. However, these models depend critically on electrical power networks and machines being able to operate with significantly improved power densities and efficiencies in the aircraft electric plant. In general these multi-megawatt power systems have been used in applications where volume and weight have been secondary considerations and hence new techniques and approaches are now required. A further issue is designing machines to address other constraints required for aircraft installation, for example motors integrating with propulsive systems.

Hence for these applications new and evermore performing electrical machine designs are now required. The work showcased in this thesis is meant as a beginning to address these new requirements.

Chapter 1 presents the challenges identified and locates the motivation of this work in the more vast application sense of aerospace propulsion. Chapter 2 provides a literature review and initial considerations on the power density increase. Chapter 3 is a collection of methodologies developed for mainly mechanical and initial electromagnetic performance evaluation. Chapter 4 delivers the optimized result for different machines comparison as well as alternative choices of objectives and constraints dictated by the design envelope. Chapter 5 identifies and develops further the chosen candidate: high order effects in the mechanics/rotor-dynamics and rotor losses estimation are thoroughly investigated. Chapter 6 addresses the manufacture choices undertaken and initial tests conducted on the machine. The thesis ends with the conclusions in Chapter 7.

Contents

List of figures

List of tables

Nomenclature

Acronyms

α	Thermal expansion coefficient
β_{PM}	Permanent magnet arc span
$\cos\phi$	Power factor
δT	Temperature difference
δ_{sleeve}	Sleeve interference fit
ε_r	Radial strain
ε_θ	Tangential strain
η	Efficiency
$\hat{B}_{bi}$	Maximum flux density in the back iron
$\hat{B}_{go}$	Maximum air-gap flux density at no-load
$\hat{B}_g$	Maximum air-gap flux density
$\hat{B}_t$	Maximum flux density in the tooth
$\hat{I}$	Peak current value
$\hat{K}_s$	Electrical loading
Λ	Flux linkage
μ_0	Air magnetic permeability
μ_{rec}	Permanent magnet relative recoil permeability
ν	Poisson's ratio

ω	Electrical angular velocity
ω_m	Mechanic angular velocity
Φ	Magnetic Flux
ψ_d	Direct axis magnetic flux
ψ_d	Quadrature axis magnetic flux
ψ_k	Equivalent circuit branch magnetic flux
ψ_{PM}	Permanent magnet flux
ρ	Mass density
σ	Stress
τ	Torque
θ_s	Stator reference frame mechanical angle
A_g	Air-gap area
A_{PM}	Permanent magnet air-gap area
B_r	Permanent magnet remanent flux density
b_s	Slot span
b_t	Tooth span
C_f	Represent the friction coefficient
D	Diameter referred to the stator
D_r	Rotor diameter
D_e	External diameter
E	Young's modulus
f	Frequency
F_d	Linear force density
f_{lkg}	Flux leakage coefficient
g	Air-gap thickness

g'	Equivalent air-gap
g''	Equivalent magnetic air-gap
H	Generic 1D magnetic field
H_g	Magnetic field in the air-gap
h_{bi}	Back Iron height
$H_{g\theta}$	Tangential air-gap magnetic field
H_{gn}	Radial air-gap magnetic field
h_{so}	Slot height of stator at opening
h_s	Slot height
h_{wed}	Wedge height of stator
h_w	Winding radial length
I	Nominal current
J	Current density in the stator winding
k_c	Electromagnetic coupling coefficient
k_h	Hysteresis loss coefficient
k_l	Roughness coefficient
k_w	Winding coefficient
k_{ec}	Eddy current loss coefficient
k_{fill}	Filling factor
l	Lenght of the machine (stack lenght)
L_d	Direct axis inductance
L_k	Equivalent circuit branch inductance
L_q	Quadrature axis inductance
L_r	Equivalent rotor inductance
L_s	Non salient synchronous inductance

l_w	Winding thickness
L_{ew}	End winding length
L_{leak}	Equivalent circuit leakage inductance
L_{md}	Direct axis magnetizing inductance
L_{mq}	Quadrature axis magnetizing inductance
M	Magnetization
m	Number of stator phases
n	Rotational speed [rpm]
N_s	Number of turns
P	Electromagnetic power
p	Pole pairs
P_m	Mechanical power
p_r	Pressure
p_s	Slot pitch of stator
P_{axial}	Axial flow mechanical loss
P_{Cu}	Copper losses
P_{density}	Power density
P_{windage}	Windage flow mechanical loss
P_{AC}	AC power losses
P_{DC}	DC Copper losses
P_{Fe}	Iron core losses
q	Number of slots per phase and per pole
Q_s	Number of stator slots
R_k	Equivalent circuit branch resistance
R_r	Equivalent rotor resistance

R_s	Stator resistance
S	Cross section
S	Safety factor
S_w	Winding cross section
T	Temperature
T_1	First sub-transient time constant
T_2	Second sub-transient time constant
t_{PM}	Permanent magnet thickness
u	Displacement/deformation
U_s	Stator magnetic scalar potential (MMF)
v	Tip speed [m/s]
v_a	Axial velocity
V_n	Nominal voltage
V_w	Winding volume
v_θ	Mean tangential velocity
w_t	Stator tooth width
w_{so}	Slot width of stator at opening

Chapter 1

Introduction

1.1 Background and motivation

The civil aerospace industry is on the cusp of a major historical change. Challenging targets have been set by the civil aviation international authorities, concerning the reduction of green house gases, in NOx emissions and a decrease in noise related to aircraft operation [1]. Fig. 1.1 highlights how a significant share of emissions derives from Transportation.

In 2016 the Airbus Group and Siemens (as per 2019 taken over by Rolls-Royce) signed a collaboration agreement in the field of hybrid electric propulsion. In doing so, they launched a major joint effort towards the electrification of aviation with the goal of demonstrating the technical feasibility of various hybrid/electric propulsion systems by 2020. Both companies are making significant contributions to the project and have sourced a large number of employees in their team to advance European leadership in innovation and the development of electrically powered aircraft.

To give a glimpse of the importance of the topic it is worthy to quote the two companies joint statement of Airbus Group and Siemens in April 2016: *"Hybrid-electric propulsion systems can significantly reduce fuel consumption of aircraft and reduce noise. European emissions targets aim for a 75 percent reduction of CO2 emissions by 2050 compared to the values for the year 2000. These ambitious goals cannot be achieved by conventional technologies. This technology is happening now in Europe and the USA. It is likely to be the biggest change in the Aircraft Industry since the introduction of the jet engine. If so, it will change every major system on the*

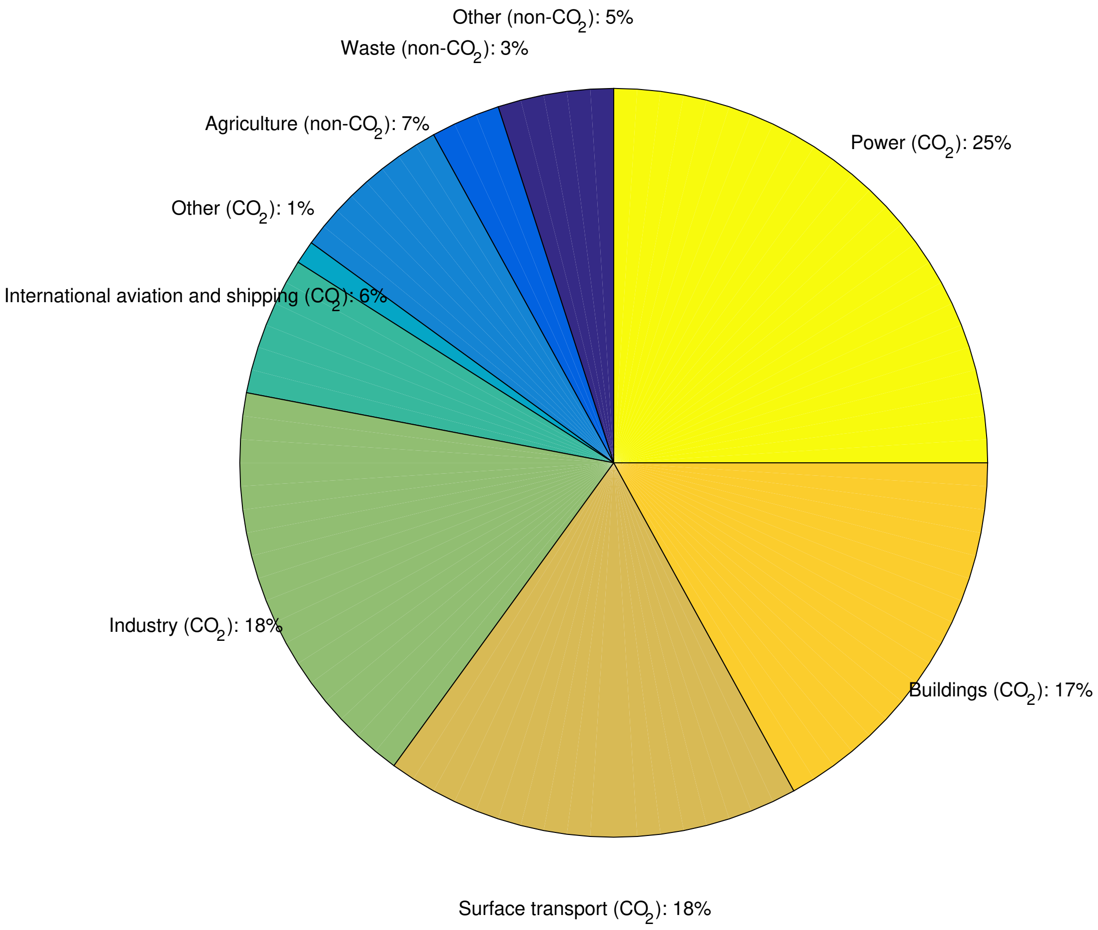

Fig. 1.1. Greenhouse gas emissions in 2010.

aircraft. It is likely to overtake the more standard More Electric Aircraft concept concentrated nowadays mostly in actuation and auxiliary systems. Electrical power technology is the key enabler for this approach."

A key feature is the use of a Hybrid Electric system to separate the generation and propulsion. Despite the name this is not about Hybrid Electric in the manner used for Marine and Automotive applications where the power-train as a whole is integrated in a single unit with mechanical transmission at the end of the line. The objective for aerospace instead is to enable Distributed Propulsion systems via an "electrical gearbox", electric systems are therefore essential to provide this decentralized feature. Such an innovative perspective has posed the most severe technical challenge for Electric Power Systems for many years in order to meet the requirements of Power Density, Efficiency and Safety. This is the critical technology to enable this approach.

Aircraft electrified configurations currently under study are depicted in Fig. 1.2 (courtesy of NASA from [2]):

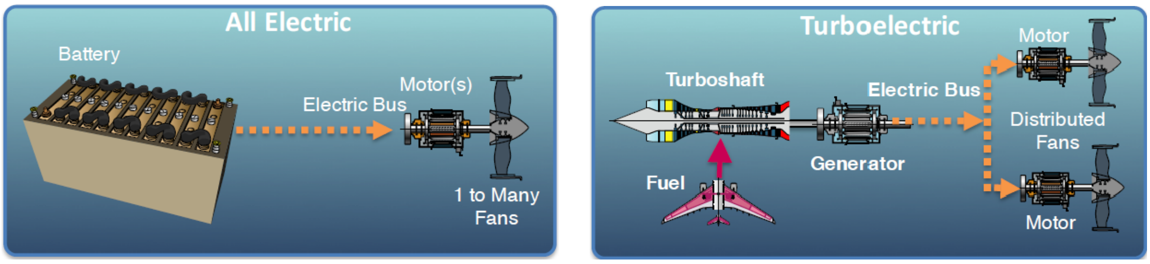

(a) *Fully electric*

(b) *Multiple Fans Turbo-electric*

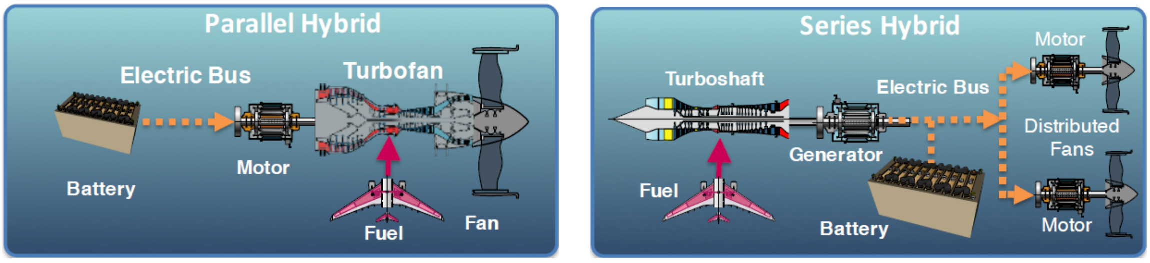

(c) *Parallel hybrid*

(d) *Multiple Fans Series Hybrid*

Fig. 1.2. Sketch of BLI configurations

Multiple propulsion methodologies have been proposed for hybrid electric air-craft, among them the BLI (Boundary Layer Ingestion) aircraft. BLI provides an augmentation of thrust and a reduction of drag force. This ends up increasing the overall aircraft efficiency in terms of fuel consumption. As shown in figure 1.3, air streams along the fuselage are accelerated by additional fans. These should be mounted near the tail, providing maximum drag reduction as the streams are more intense in this zone.

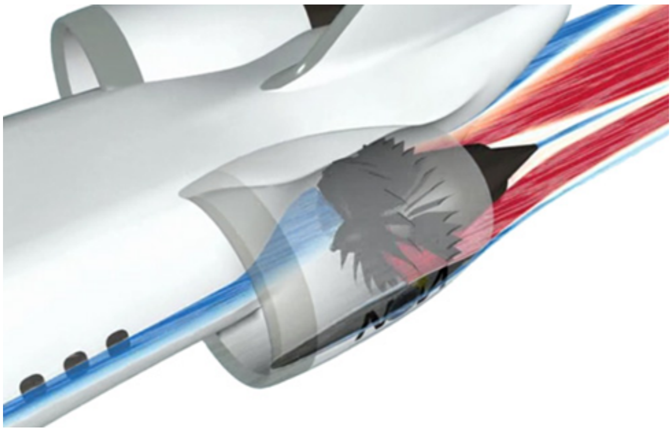

Fig. 1.3. BLI highlight (Courtesy of ONERA)

A further insight on the aerodynamic performance of a BLI structure is provided in Fig. 1.4. The sub-picture on the left shows a theoretical achievement in term of uniform thrust changing the position of the engine from the wing to the aircraft rear/tail. The wing profile is utilized to emphasize the air stream exploitation of BLI against a standard under-wing turbine mounting. The sub-picture on the right defines the benefit of a feasible (keeping the main turbo-engines attached to the wings) BLI system in terms of thrust and drag forces.

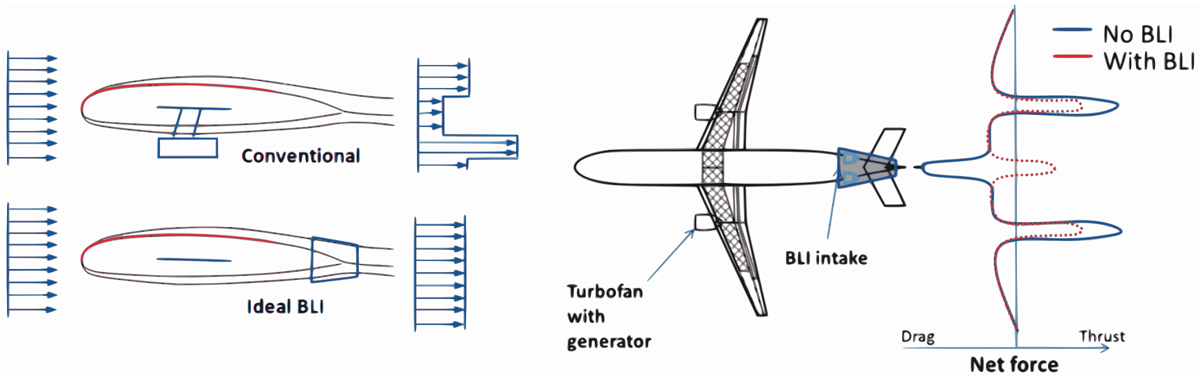

Fig. 1.4. BLI concept from DEAP (Distributed Electrical Aerospace Propulsion) study (Courtesy of Rolls-Royce plc)

Two main-stream concepts can be identified for the BLI configuration as shown in Fig. 1.5. The former employs a single, large tail mounted propeller. This solution is related to the main-stream research conducted by NASA Glenn Research Center [2]. The latter considers the option of distributing the power around the tail by mounting multiple fans around the upper semi-circumference of the fuselage. The benefits of this second solution over the single fan is intrinsic fault tolerant capability and versatility in control. Negative attributes may be related to a more distorted air-stream profile at the aircraft end. The work hereby presented is based on the assumption of a multiple fan configuration. Specifically, this PhD project deals with increasing the power density of an electric motor, which could be installed or provide an initial prototype demonstrator for an aircraft assisted by BLI multiple fans.

No existing electrical machine can accomplish the performance required by the aerospace propulsion sector: in a range of 10-20 [kW/kg]. High speeds/high power solutions, with attention to the cooling side, need to be examined. Based on thermal and magnetic properties electric motors can be grouped into two big families comprising conventional/non-cryogenic and superconducting machines. Conventional motors have been object of intense study reaching excellent levels in terms of power/torque density, as well as compactness, mechanical robustness and thermal management. They are recognized to be a mature and developed technology that has been around for almost two centuries. On the other hand superconducting machines, from the very beginning of their analysis and design, presented several operating and manufacturing issues. This is because extremely high flux density AC fields will create a complicated shielding issue to tackle, without even mentioning the challenges related to cooling. Nonetheless, they have been considered for their theoretical potential to concentrate a high amount of power in relatively small volumes, indeed exploiting extremely high currents and magnetic fields [3]. New impetus has been given quite recently by the adoption of HTS (High Temperature Superconducting) materials which might represent a way forward [4]. These two macro-typologies can be both considered as candidates to cope with the power density issue aforementioned.

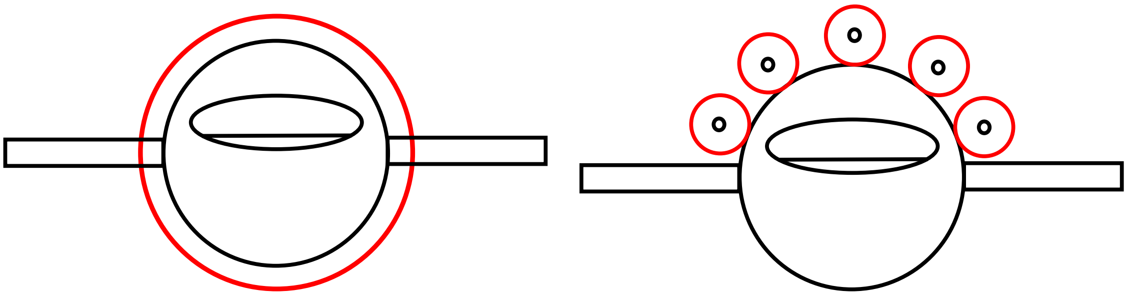
(a) *Single Fan BLI* (b) *Multiple Fans BLI*

Fig. 1.5. Sketch of BLI configuration compared.

NASA defined a road-map as a reference guide for the research in this new field of study [5]. More specifically, the NASA Glenn Research Center set precise targets to be reached at five year intervals. Two main conclusions can be drawn out of this research schedule:

- superconducting machines will be developed alongside the power density improvement of conventional machines.
- the first result to pursue should be increasing the performance of conventionally cooled machines. Emphasis should be given to conventionally cooled machines as it is believed by the electrical community that the boundaries for power density improvement have not been fully explored.

NASA's newly proposed turbo-electric concept aircraft, STARC-ABL (Single-aisle Turbo-electric Aircraft with an Aft Boundary Layer Propulsor), [6] is an example of BLI single fan configuration highlighted in Fig. 1.5

Fig. 1.6. STARC ABL BLI configuration from NASA.

The main objective of this PhD project was to achieve the highest power density possible from a conventional (non-superconducting) electric motor, bearing however in mind the application target. This is true for any motor design as the application will dictate geometrical and operational constraints that will in turn influence the design space envelope.

The targets were summarized at the beginning of the project as follows:

- gaining further insight into high power density solutions among conventional (not superconducting) electrical machine topologies
- designing a high power density electric motor fitted for a BLI multiple fan configuration
- getting more insight into the interaction between diverse physics coming into play in the machine operation: mechanical-electromagnetic-thermal
- prototyping and testing the final defined design

More specifically, the thesis aims to design and test a motor with specifications provided in Tab. 1.1. These specifications were established at the beginning of the design process. The reasons of such numbers are the following:

Power	250 kW
Speed	14000 rpm
Rotor ID	300 mm
Operation	fixed speed, continuous operation (no current/torque overload)

Table 1.1. Initial motor specifications

- the power of one quarter of a Megawatt was defined as a starter for 100 seater aircraft. This was a suggestion of power rating drawn from discussions with aircraft engineers at Cranfield University, who were involved in inter-university research talks in the very beginning of this research. It was identified that half a MegaWatt of power could be delivered by two combined machines of this kind, based on the BLI double motor configuration at the aircraft tail.
- the speed was chosen based on some crude estimation from boundary layer requirements. This is most probably the more debatable specification from an aerospace point of view, because lower speeds, up to 6000 [rpm] were deemed to be sufficient.
- 300mm is the diameter of the BLI fan which is going to be driven by the electric motor. It is shown in details in Chapter 3 and 4 as this choice translates in a Rim Driven Inner diameter specification. A topology chosen in favor of a standard shaft driven. That is the meaning of ID (Inner Diameter).

This investigation is distinct from the more standard concept of the More Electric Aircraft (MEA). As summarized in [7], and previously mentioned in this chapter, actuation is concerned with auxiliary systems mounted on-board to assist flight operation. The work presented in the following is exclusively intended to target the propulsive aspect.

The contribution of this thesis regards an investigation of the power density state of art technologies, an attempt to tackle the most challenging aspects of an increase in power density in all the multiphysical aspects involved. Mechanical and electromagnetic challenges are treated concomitantly as they are intertwined especially for a sound rotor design. The thesis contributes in providing a machine designer with a multiphysic approach encompassing the stress related issues due to retaining forces and material choices as well as rotordynamics issues. The design is driven by state of art optimization algorithms tailored and modified on purpose for specifically defined objective functions and constraints. The connection of the mechanical design with the electromagnetic high order interaction given by the power electronics are given a broader emphasis with respect to previous work, at least at best of the author's knowledge. For the first time a more comprehensive analysis of frequency inductance dependency is incorporated in the optimized design. Partial experimental results on the design soundness are delivered to prove the essential electromagnetic features of the designed device.

Chapter 2

Literature Review

Following the power electronics revolution, increasing power density of electrical machines has been a target. This chapter firstly investigates the state of the art related to electrical machines and drives with a specific focus on aerospace related applications and their power density delivery capabilities. In order to put these in context and render the concept of high power density clearer in terms of physical and engineering quantities the second section of the chapter, with the help of a comprehensive high-speed/high-power graph analysis investigates the issue of power density increase by means of physical utilization factors.

2.1 Literature Review

To cite some of practical achievements, research in this field has been conducted mostly towards the increase of speed, and torque. The ETH spin-off Celereton, Switzerland, is famous for having achieved the maximum speed of 1 million [rpm], [8]. However, in recent years other solutions have been investigated, also taking into account the torque specification. In Newcastle University, Smith designed a High-Speed/High-Power Synchronous machine for a test-rig application [9, 10]. The fundamental operating frequency was fixed to 1 [kHz], against a standard power electronics inverter supply switching of 10 [kHz]. This corresponds to a power rating of 1 [MW] with 30000 [rpm] rated speed. High losses were required to be extracted, therefore the design needed a spiral water jacket wrapped around the stator core, combined with a forced air pumping cooling system for extracting heat from the rotor. The thesis yields a deep insight on several aspects of the high speed machines design process. The machine was successfully prototyped and tested. Although precise estimate for active materials or overall power density, as well as losses mapping, are not provided, the system achieved in testing 1 [MW] power delivery performance in continuous operation, however hitting the temperature limit of the winding electrical insulation coating. In the final conclusions is stated as the machine developed is safe to operate up to 24000 [rpm], around 91% of the rated operation without reaching thermal limits.

In Nottingham University, as part of the EU funded Clean Sky Project a high speed electrical motor has been designed, performing a claimed extremely high 11 [kW/kg], [11]. Peculiarity of the machine was a wet stator submerged in oil pumped at high pressure for handling iron and copper losses. This machine is unique in his field and represents a good reference point.

New ideas and motor configurations have been explored at the Glenn Research Centre (NASA – US) following the concept of cryogenic stator concept, but still with an overall machine configuration which is not superconducting [12, 13]. The main result was achieved building and testing a switched reluctance motor completely submerged in liquid nitrogen for continuous operation. The level of current density reached inside the machine was five times larger than that of a normal convectional (not superconducting) machine. NASA claimed 100 [A/mm^2] for continuous operation. Note that possible superconducting solutions have also been investigated, like the one of [3] achieving a level of current density up to 42 [A/mm^2].

Most of the more recent design improvements are linked with the automotive sector, using the momentum Electric Land Vehicles have acquired on the market as a way to a greener environment. Formula 1 motor-sport showcases a 4.5 [kW/kg] power-train from McLaren technologies [14]. However, other than this number, nothing is known about possible specifications. Yasa Motor and Protean Electric provide relatively high power density between 2 and 6 [kW/kg] (depending predominantly on the overload capability, i.e. short transient operation) even though the main target is rather represented by the torque density (above 24 [Nm/kg] for YASA and above 29 [Nm/kg] for Protean, during overload-peak operation). The former is a yokeless axial flux motor, whereas the latter features an outer rotor targeting in-wheel traction motors. It must be specified as in automotive traction there might be a discrepancy around the aforementioned figures as the motors are designed for both transient and continuous operation.

A closer look at the aerospace sector sees big competitors like Siemens and Honeywell delivering full and hybrid electric propulsive motors. In 2015, Siemens released a breakthrough 5.2 [kW/kg] at a relative low speed of 2.5 [krpm] (Halbach array with direct cooled conductors). Honeywell a 7.9 [kW/kg] high speed motor (19 [krpm]) wound field synchronous rotor. Rolls-Royce and Sheffield University delivered a 4.4 [kW/kg] actuation motor for continuous operation and 6.6 [kW/kg] for peak/overload/transient operation.

All these numbers, regardless of the application tailored, are not capable to overcome a 10 [kW/kg] threshold. Caution must however be applied when citing power density figures as oftentimes it refers to only active mass without accounting for auxiliary and non active components, for example bearings, casing, cooling pumps and oil-water coolant.

2.1.1 Most recent achievements in aerospace

In the more specific aeronautic field of interest, very recent improvements with relatively novel ideas have been put forward by University of Illinois at Urbana-Champaign. The concept is based on a single fan BLI (Boundary Layer Ingestion) arrangement. The motor design employs an outer rotor configuration exploiting a Halbach array and a composite overwrap [15]. The motor is rated for 1MW continuous operation [16] with a relative high pole count and fundamental frequency. Despite being well known that heat extraction might represent a challenge for outer rotors [17], [18] the advantage of the proposed motor is the utilization of a clever heat sink design, fitted within the stator bore, combined with a self pumped air cooling system [19]. The mechanical aspect is extremely challenging and well documented by simulations and tests in [20], [21]. Cantilevered effects and structural retention issues were catered for in order to ensure mechanical integrity. From the stator and winding point of view many challenges are tackled due to very high frequency eddy currents as well as very low inductance due to a slot-less design [22], [23]. Finally, in terms of aircraft level integration the motor is meant to be integrated with the Rolls-Royce LibertyWorks EVE engine concept.

Likewise, intensive research has been conducted at Ohio State University attempting the integration of an Induction motor into a 10 [MW] turbofan. The main breakthrough is the exploitation of a Variable Cross-Section Wet Coil maximizing the heat transfer via fluid cooling.

Both these two last motor technologies claim to achieve something close to 13 [kW/kg] as per power density performance, with an efficiency larger than 96%.

2.2 Physical understanding of power density

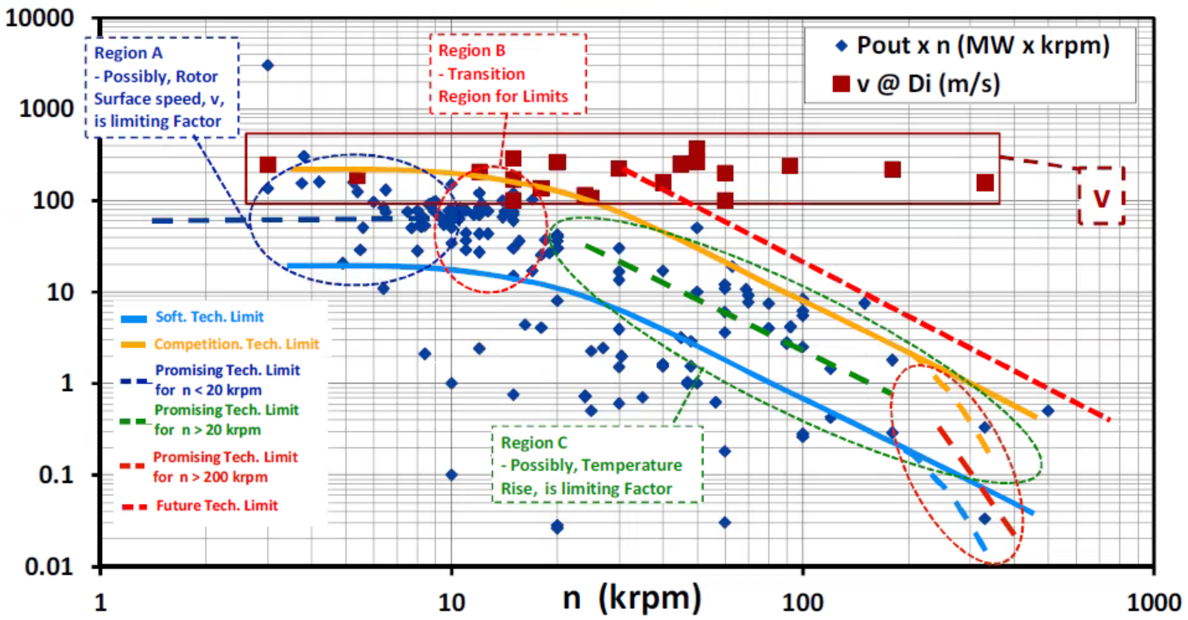

Fig. 2.1. High-Speed/High-Power index and tangential speed as a function of rotational speed [24].

Fig. 2.1, courtesy of [24], and to a certain extent previously addressed also in [14], presents the state of art of electric motors surveyed up to 2014 in terms of power density indexes. Along the vertical coordinates two quantities of interest are addressed. The former is the product of output power and angular speed; the latter the tip speed of the rotor. The red squared dots signify first and foremost the maximum speed physical limitation which is reckoned to be around 200-250 [m/s] given the retaining materials employed and centrifugal forces involved.

Using high performance power switching devices has allowed almost unconstrained frequencies as the machine fundamental frequency has progressively grown higher. Consequently, traditional rotating electrical machines could run faster than ever, by exploiting high frequency rotating magnetic fields. An increase in speed, maintaining the volume, weight, current and magnetic loadings constant, allows, in principle, to increase the power produced per unit mass. If at the same time as boosting the speed, the torque production capability is increased, a high power density machine can be designed [25]. Various review papers, [24, 26, 27], describe the design constraints and challenges of high-speed/high-power electrical machine design. The focus encompasses mechanical retainment constraints that limit magnet exploitation for permanent magnet machines topologies, and equivalently bar shapes/depth and features for induction machines, to effectively deliver sound electromagnetic torque without compromising the rotor mechanical integrity. Attention is also devoted to loss estimation due to high frequency effects (mainly AC losses in copper and iron cores) and their consequent necessary thermal management. Additional losses, such as windage and friction are also of interest due to the high speed of the motor. Recent developments are also treated, focusing on the state of art application given in [28].

In order to highlight the main features of high-speed/high-power machines it is useful to introduce the problem in terms of different physical utilization factors for an electrical machine. Namely: mechanical, electromagnetic and thermal. In the following $\hat{K}_s$ and $\hat{B}$ will refer to the peak Electric and Magnetic loading, respectively. When utilized with subscript g the latter will refer to the more specific magnetic loading (peak value of the first harmonic component) in the air-gap.

- high speed operation introduces considerable mechanical stress in the rotor due to centrifugal forces. Centrifugal forces are quadratically proportional to the tip speed (v [m/s]) and linearly proportional to the density ρ:

  $$\sigma \propto \rho v^2 \tag{2.1}$$

  More than that, the dependency is not actually on the n[rpm], but rather on the maximum peripheral speed v. High speed (rpm n) machines do not necessarily possess a high torque and vice-versa. The torque τ is quadratically proportional to the stator bore diameter D. Considering this, (2.2) allows the definition of a high speed index as a product of rpm velocity n and power P_m, as it is employed for the comparison conducted in Fig. 2.1.

  $$\sigma \propto v^2 \propto n^2 D^2 \propto n(n\,\tau) \propto n P_m \tag{2.2}$$

  Eq. (2.2) starts from a maximum admissible material stress via the density (2.1), which is proportional to the square of the tip velocity. This is in turn split into the product of square rpm velocity and bore diameter. Remembering that the torque is proportional to the square of the diameter then the product speed by power follows as the speed index.

- high speed operation coupled with high power requirements leads to efficiency related issues: AC winding losses in the stator armature as well as iron losses in the stator and rotor cores rises due to high frequency flux density variation. Electromagnetic losses are thus responsible for frequency design constraints and sizing limitations.

  AC winding losses, are more difficult to compute than standard DC losses. A variety of methods have attempted successfully their estimation. From analytically based ones like [29] and [30], to different degrees of computational efficiency exploiting numerical analysis as the ones presented in [31], [32], [33], [34], [35], to experimentally verified ones [36], [37] [38].

  The electric loading of (2.3) is derived for slotted (upper) and slotless (lower) configurations, where k_w and k_{fill} are the winding and fill factor coefficients, J h_s b_s and b_t the current density, the slot height, slot and tooth span. Assuming a constant slot to tooth width ratio both h_s and h_w are proportional to the rotor radius, yielding the last proportionality expression between current density and rotor radius.

$$\hat{K}_s \approx \begin{cases} k_w k_{\text{fill}} J h_s \dfrac{b_s}{b_s + b_t} \\ k_w k_{\text{fill}} J h_w \end{cases} \propto J\, r_r \tag{2.3}$$

  This allows a derivation for DC and AC winding, as well as for iron losses: (2.4) (where ρ_w and l stand for the winding resistivity and axial length, V_w for the winding volume) and (2.5).

$$\begin{gathered} P_{DC} = J^2 S_w \rho_w l \propto J^2 r_r^2\, l \propto J^2 r_r^3; \\ P_{AC} \propto J^2 f^2 V_w \propto J^2 f^2 r_r^3 \end{gathered} \tag{2.4}$$

  Core (Iron) losses as [39],[40],[41] are proportional to the mass via a coefficient C to account for hysteresis and additional losses and to the square of both frequency and flux density; being the mass proportional to the volume a relation with the rotor radius is derived:

$$P_{\text{Fe}} = C m_{Fe} f^2 \hat{B}_g^2 \propto r_r^3 f^2 \hat{B}_g^2 \tag{2.5}$$

- thermal utilization is strictly related to electromagnetic losses which are controlled, either by reducing the electromagnetic loading of the machine, or by enhancing the heat extraction capability of the cooling system .

The electrical loading, defined as the linear current density along the stator bore, neglecting the air-gap length, is proportional to both slot current density and rotor radius: (2.3). Therefore the power can be derived from the shear stress. The Maxwell's Stress Tensor theory, [42], [43], provides a force per unit-area equal to:

$$\sigma_{\mathrm{F}} = \frac{1}{2}\mu_0 H^2 \tag{2.6}$$

where H is the magnetic field intensity.

The stress occurs in the direction of lines of force and creates an equal pressure perpendicular to the lines. For an electrical machine considering the stress decomposition in radial and tangential components it can be observed that the latter is providing the torque causing the rotation, whereas the former is only the cause of radially pulling forces. The tangential force is proportional to the product of radial H_{gr} and tangential $H_{g\theta}$ component of the magnetic field by:

$$\sigma_{\mathrm{shear}-\theta} = \mu_0 H_{gr} H_{g\theta} = \hat{B}_g \hat{K}_s \tag{2.7}$$

which equivalently can be written as the product of flux density normal to the lines of force and the electrical loading.

Finally, introducing the speed and relating the shear stress to the power, proportionality of speed and power is established.

$$P \propto \hat{B}_g \hat{K}_s \lambda_{\mathrm{rot}} \left(\frac{D_r}{2}\right)^3 f \tag{2.8}$$

Where the rotor aspect ratio can be defined as a constant $\lambda_{\mathrm{rot}} = l/D$. Given a constant thermal management/losses dissipation along a range of different radius (volume) and speed, (2.9), where

S is the heat transfer surface available:

$$\frac{P_{\mathrm{diss}}}{S} = \frac{P_{\mathrm{DC}} + P_{\mathrm{AC}} + P_{\mathrm{Fe}}}{S} = \text{const.}^{1} \tag{2.9}$$

the variation of flux density and current density, according to (2.4) and (2.5), must follow the following trends:

$$J \propto \frac{1}{\sqrt{D_r/2}}; \quad B_n \propto \frac{1}{\sqrt{D_r/2f}}. \tag{2.10}$$

This yields a rough power proportionality to the radius, which can be expanded further accounting for the peripheral speed expression dependence upon radius and frequency as follows:

$$P \propto \left(\frac{D_r}{2}\right)^3 \propto \frac{v^3}{f^3}. \tag{2.11}$$

The key point provided by a theoretical revision can be summarized as follows: a power density increment cannot be simply reached by increasing the speed, as long as the thermal management/cooling system maintains a fixed heat removal capacity. The increase of power density can be achieved if and only if the speed increase is accompanied by a better cooling performance.

On the basis of this, it is possible to comment and gain further insight on the different parts of Fig. 2.1, as discussed in [24]. That does not come to a great surprise as thermal management is one of the key factors, when developing high-performance electrical machines. This said it will be observed throughout this thesis that application oriented designs, like the one under analysis are also constrained geometrically (fans diameter and speed requirement), limiting the design envelope and the performance achievable.

- region A exhibits relatively low n ($<$ 10000 [rpm]). This region consists of very high power machines, generally limited in number of poles. This implies a relatively low n, thus not giving rise to considerable iron and winding losses; relieving the thermal stress. Hence,

---

[1] From here it can be clearly seen that, if the losses to be dissipated increase due to higher speed, the S heat transfer surface must increase as well to keep the same thermal management level performance, or equivalently the heat transfer coefficient must be improved.In other words the power loss per unit surface is area is constant.

the sole peripheral mechanical speed constraint is seen as the major constraint, i.e. at these speeds the mechanical stresses reach the possible limit that materials can withstand.

- region C ($>$ 20000 [rpm]) highlights an index (2.2) drop, signifying the relationship established in (2.2) is no longer general. In other words the dependence on rotor tip speed is not enforced any more. In this range the frequencies start to increase and the thermal limit becomes of paramount importance. In this region equation (2.11) is fully enforced. Another way of seeing it is considering that $f \propto n$, so that:

$$n\,P \propto \frac{v^3}{n^2}. \tag{2.12}$$

- region B is a transition between the two aforementioned.
- it is clear an improvement can be reached by increasing the thermal machine capability, allowing the high speed/high frequency trend in region C to be lifted to higher power levels.

2.3 Further considerations

In relation to the literature review conducted thus far, for this specific academic research the possible electrical machines candidates can be categorized as follows:

- Fairly conventional machines, i.e. high aspect ratio (longer axial length with respect to machine diameter) radial flux machines
- Rim Driven Designs
- Other designs such as axial flux electrical machines

Regardless the type of machine, all intrinsically present a degree of difficulty: from the operation of the machine itself, to the manufacture of it. Design issues can be summarized as follows:

- Mechanical constraints

  - thermal stress of materials which in turns affect their performance because of expansion and/or interference fits variability
  - air-gap length, retaining materials, stresses in possible brittle PMs (very prone to tensile shear stresses)
  - structural integrity of the "Fan/Motor" solution in case of Rim-Driven designs
  - rotor-dynamics: rotational modes, vibrations, resonances

- Electro-magnetic/Thermal constraints: for keeping dimensions small, reduce weight, i.e. high-power-density:
  - increasing the number of poles allows a proportional reduction of magnetizing core volume, though the fundamental frequency increases accordingly. The core losses will increase in general with the square of this frequency [39], [40].
  - AC winding losses increase, at least as far as the eddy currents are concerned, following a squared proportional trend. In addition the winding will experience proximity AC losses, depending on the conductors arrangement in the slot, circulating current losses in any parallel path due to leakage inductance unbalance among conductors, and finally AC fringing flux dependent losses from the rotor time varying flux coming from permanent magnets in the rotor.
  - rotor eddy current losses is an issue if asynchronous armature space harmonics are present, due to the winding arrangement, as well as permeance harmonics due to slotting features, and time harmonics coming from the power electronics
  - a difficulty to get core back weight decrease is relative to the cross section of the machine, e.g. as long as the outer diameter of the machine is high, for instance due to geometrical constraints, it is difficult to bring down the weight as the core weight depends on the square of the diameter
  - thermal stress in the slots and end-winding affects the insulation and poses serious limits on the continuous operation of the machine, and reducing reliability

A BLI targeted design is constrained, as mentioned briefly previously, by geometrical and speed limitations. The geometry is dictated by the maximum or minimum volume the propeller occupies for optimal exploitation of boundary layer air streams as well as the speed is dependent on the maximum efficiency obtainable in drag reduction by boundary layer acceleration. Fitting this design within previous analysis the machine under investigation will most likely be located in the transition region of graph 2.1. It will possess a relative high torque and most likely high speed at the same time. In other words neither an extremely high speed (in terms of [rpm]), nor a very low speed with excessively high torque are considered. That implies the thermal challenge may be the main issue to cope with at the considerably high frequency is thought to operate. Although the rotational speed might not be too high, the actual tip speed will be of concern as the constraint modeling will throughly address.

Chapter 3

Design Constraint Modelling

3.1 Physical Limits and machine topology choice

It is worthy to analyze the maximum power density that theoretically, i.e. up to the minimal physical constraints list, a standard (non superconducting) permanent magnet electrical machines can provide. This chapter provides this analysis in the very beginning, giving an analytical explanation of the electromagnetic performance before providing a very first optimization results for an idealized linear machine model. The second part of the chapter introduces the choice of the radial machine topology and it addresses the modeling aspects of a high speed permanent magnet machine, both mechanically and electromagnetically. Thirdly, a first power density optimization with some crude values of current density is provided, drawing initial conclusions regarding modeling multi-physical challenges that pave the way for the fuller analysis of the subsequent chapters.

3.1.1 Idealized linear machine

The initial approach investigated the limits of a permanent magnet electrical machine in terms of the highest power density achievable. The electrical machine has been idealized as a linear (rolled over along the air-gap) geometry. In this way we can decouple the number of poles from the theoretical considerations over mechanical and electromagnetic limits. The machine has an idealized cross section with a translational rotor motion. Symmetry allows an infinitely wide and deep air-gap so no end effects need to be considered. Two configurations have been compared: a slotless (so called air-gap winding machine) and a slotted machine. Moreover, the slotted electrical machine has been considered with a semi-closed slot design. Figure 3.1 shows the geometrical features of the two solutions. From top to bottom the different layers of material in the slotless configuration consist of Cobalt-Steel (CoFe), copper winding, air-gap, carbon fibre sleeve, Samarium Cobalt PMs, solid-magnetic steel. The carbon fibre sleeve is in this case not designed for sustaining any stress. A dummy thickness value of 1 mm is used for roughly investigating the physical limits. As for the slotted machine, it is the same, apart from the winding positioned within the Cobalt-Steel stator slots. A single slot per pole per phase combination is used. The space envelope constraints are very loose, on purpose, to estimate the maximum state of art performance, without physical limitations, other than the electromagnetic material characteristics, and reasonable drive/electronics electrical parameters. The following are assumed:

- the CoFe is employed for maximum flux density knee point (2.1[T])
- no limits in voltage or current level
- no thermal limits
- current density set at 30 [A/mm^2]
- non-conductive sleeve, as specified before only representative
- solid steel has an equal permeability to a standard laminated SiFe
- current imposed is purely sinusoidal
- The fundamental frequency is set to 3 [kHz] [1]

Analytical explanation of power density limit

Since we are investigating a geometrically linear machine we are interested in the figure of merit provided by the force per unit length. In simple electromagnetic terms the Lorentz's force $J \times B$ explains the force process generation as the interaction of the B flux density field delivered by

---

[1] This is considering a switching frequency which is at least 10 times higher than the fundamental as amply discussed in [44], [45] bringing the inverter spec close to the limits of actual Silicon Carbide switching devices.

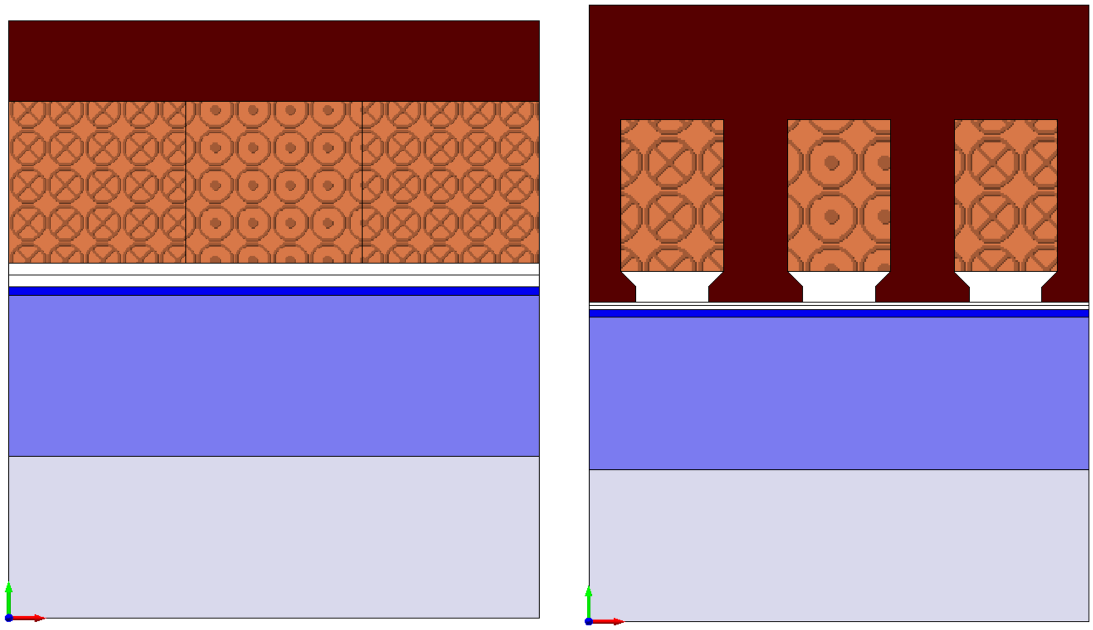

(a) Slotless geometry.

(b) Slotted geometry.

Fig. 3.1. Idealized geometry of the PM electrical machine

the energized magnets on one hand, and the J current density provided on the other side of the air-gap by the armature winding on the other hand. In a similar way for the definition of shear stress for a rotating geometry in (2.7) we have the force density expressed as:

$$F_d = \frac{\hat{B}_g \hat{K}_s}{2} \tag{3.1}$$

where the two fields are assumed to be perfectly sinusoidal, therefore the net force produced is computed by the product of their rms values. The electric loading $\hat{K}_s$ is proportional to winding factor k_w and fill factor k_{fill}, as well as the air-gap winding thickness.

$$\hat{K}_s = k_w k_{\text{fill}} \sqrt{2} J_{\text{rms}} h_w \tag{3.2}$$

Being a linear geometry the power is then proportional to the product of tip speed and force. Therefore for a constant velocity we can assume the following power proportionality:

$$P \propto J h_w \hat{B}_g \tag{3.3}$$

From this last equation, it seems that either increasing the electrical loading directly via J or the magnetic loading $\hat{B_g}$, or the winding length h_w, will deliver a higher power. The magnetic loading is far from uniform in terms of dependence from mainly air-gap and permanent magnet thickness: this is represented in Fig. 3.2, along the lines of [46]. P_L and P_{M0} stand for leakage and internal magnet permeances, respectively. While the former does not have a defined closed form expression, the latter is conveyed by (3.4). In this equation β_{PM} stands for the magnet arc span, over a single pole, in electric radians, A_{PM} stands for magnet pole area, t_{PM} stands for magnet thickness (magnetization direction radial), L_{stk} is the stack active length and p the pole pairs count.

$$P_{\mathrm{M0}} = \mu_{\mathrm{rec}}\,\mu_0\,\frac{A_{\mathrm{PM}}}{t_{\mathrm{PM}}} = \mu_{\mathrm{rec}}\,\mu_0\,\frac{\beta_{\mathrm{PM}}}{p}\frac{r_M L_{\mathrm{stk}}}{t_{\mathrm{PM}}} \tag{3.4}$$

In terms for flux sources F_a illustrates the armature magneto-motive-force, whereas Φ_r is the permanent flux generated by the magnet. R_g is the reluctance of the magnetic air-gap as per (3.5).

$$R_g = \frac{g'}{\mu_0 A_g} = \frac{1}{\mu_0 L_{\mathrm{stk}}}\frac{p}{\beta_{\mathrm{PM}}}\frac{g'}{r_g} \tag{3.5}$$

where r_g is the middle gap radius (average radius between stator inner bore and rotor outer bore).

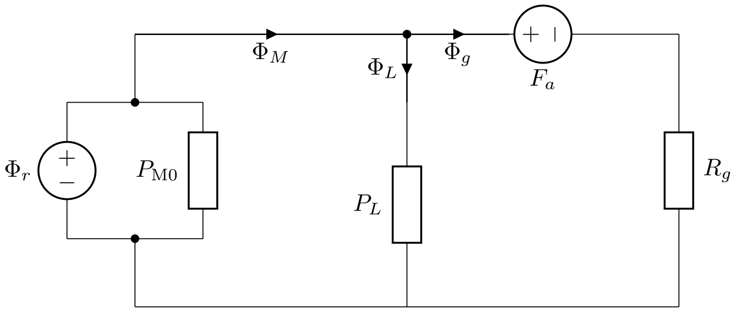

Fig. 3.2. Simplified linear magnetic circuit.

Considering the mechanical clearance g as a constant and the same for the magnet length, we can define a convenient parameter called flux leakage coefficient with the purpose to identify the amount of magnet flux unable to link the armature winding. The proportionality is inverse with respect to the winding height (radially outward for a radial flux machine) by Ampere's law, (3.6).

$$f_{\mathrm{lkg}} = \frac{\Phi_g}{\Phi_M + \Phi_L} \propto \frac{1}{h_w}. \tag{3.6}$$

From the circuit of Fig. 3.2 the remanent flux results to be transferred to the air-gap according to (3.7), where f_{lkg} takes into account, as previously mentioned, all the non linkage flux.

$$\Phi_g = \frac{f_{\mathrm{lkg}}}{1 + f_{\mathrm{lkg}} P_{\mathrm{M0}} R_g} \Phi_r \tag{3.7}$$

The correspondent flux density turns out to be then as (3.8):

$$\hat{B}_g = \frac{f_{\mathrm{lkg}} \dfrac{A_{\mathrm{PM}}}{A_g}}{1 + \mu_{\mathrm{rec}} \dfrac{A_{\mathrm{PM}}}{A_g} \dfrac{g'}{t_{\mathrm{PM}}}} B_r \tag{3.8}$$

where A_g stands for the area of the air-gap respectively, t_{PM} the effective air-gap and magnet thickness, respectively, with B_r being the remnant flux density of the magnets. Note that, the bigger air-gap, the lower the flux leakage (value between 0 and unity) factor. Also, considering the total pole span for the permanent magnets $A_{\mathrm{PM}} \approx A_g$ the final flux density can be delivered in a simpler form as per (3.9), where the effective air-gap has been expanded accounting for his proportionality as sum of mechanical gap, magnet length and winding height, giving rise to the three addendum within parenthesis at the denominator.

$$\hat{B}_g \propto \frac{1}{h_w + \mu_{\mathrm{rec}} \left(\dfrac{g}{t_{\mathrm{PM}}} + \dfrac{h_w}{t_{\mathrm{PM}}} + 1 \right)} \tag{3.9}$$

Thus (3.10) expresses the power proportionality following from (3.3):

$$P \propto \frac{h_w}{h_w + \mu_{\mathrm{rec}} \left(\dfrac{g}{t_{\mathrm{PM}}} + \dfrac{h_w}{t_{\mathrm{PM}}} + 1 \right)} \tag{3.10}$$

However, our main interest in aerospace applications is the power density, that is power per unit mass. We know that the total mass (moving and non moving parts of the machine) will increase proportionally to both h_w and t_{PM}. Hence:

$$P_{\mathrm{density}} \propto \frac{h_w}{h_w + \mu_{\mathrm{rec}}\left(\dfrac{g}{t_{\mathrm{PM}}} + \dfrac{h_w}{t_{\mathrm{PM}}} + 1\right)} \frac{1}{h_w + t_{\mathrm{PM}}} \tag{3.11}$$

Nonetheless, this does not yield the entire picture yet. For instance, if we have thick magnets we will need more core back, both on stator and rotor sides to carry a bigger flux. Therefore the mass dependence is not linear with t_{PM}. Conversely, if the winding thickness increases, less core back is needed as there is going to be more leakage flux. The last equation can be therefore presented as follows:

$$P_{\mathrm{density}} \propto \frac{h_w}{h_w + \mu_{\mathrm{rec}}\left(\dfrac{g}{t_{\mathrm{PM}}} + \dfrac{h_w}{t_{\mathrm{PM}}} + 1\right)} \frac{1}{h_w^{\alpha} + t_{\mathrm{PM}}^{\beta}} \tag{3.12}$$

where $\alpha < 1$ and $\beta > 1$.

We can see that there is going to be a plateau where the power density reaches its limit. With a dummy example the trend of magnetic loading, power and power density are shown in Fig. 3.3. The power density maximum is highlighted by the red dot, showing the compromise between permanent magnet increase and winding length increase.

The aforementioned analytical presentation describes the interaction and trade-off between different design quantities for a slotless machine. For more complicated geometries, like the slotted ones the proportionality trends and equations are harder to derive and prone to many more considerations and hypotheses regarding the magnetic circuit of the machine.

Numerical optimization results and comparison

An optimization procedure has been carried out targeting the power density maximization. Results are provided in Fig. 3.4. The higher or lower tolerance signifies a more or less narrow

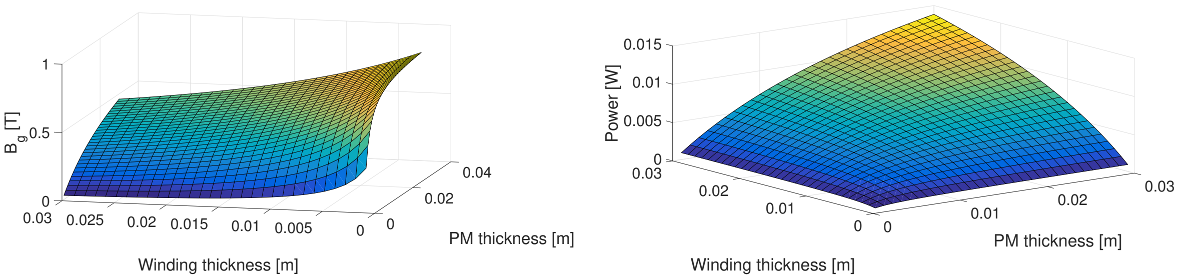

(a) Magnetic loading trend.

(b) Power trend.

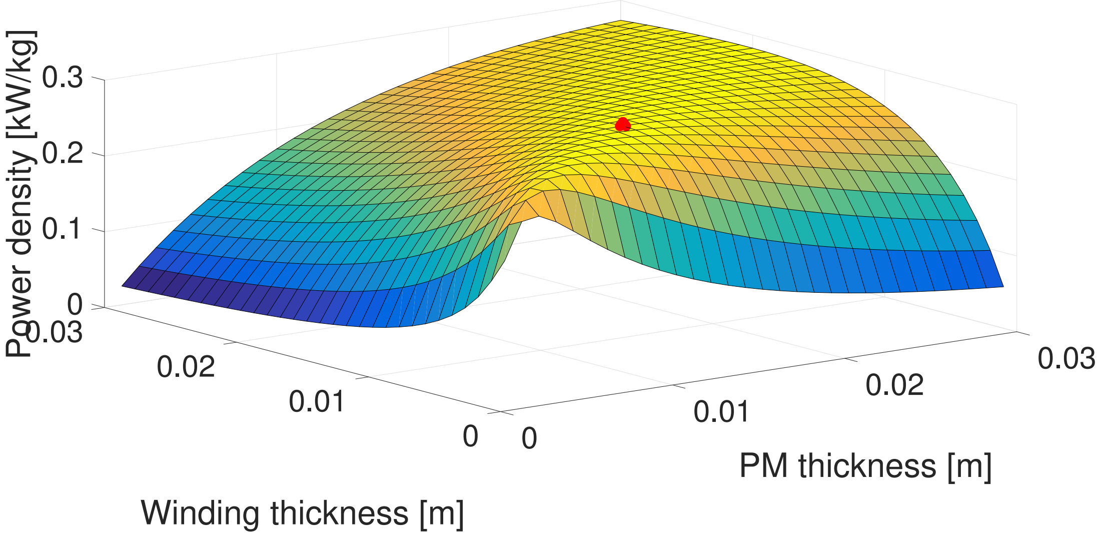

(c) Power density trend.

Fig. 3.3. Trends for the different quantities of interest in a dummy geometry.

variation performance from different generations within the optimization scheme used in this case (OptiNet-MagNet finite element optimizer-software) [47].

It is clearly visible as the slotted configuration outperforms the slotless one. This is mainly due to the very large effective air-gap of this last one, significantly increasing the leakage flux. As there is neither proper mechanical design for the sleeve and the air-gap thickness, nor an overall thermal analysis limitation, the power density levels obtained $\approx 47[\mathrm{kW/kg}]$ can be considered as a physical, however only theoretical limit. In other words, it indicates what can result from the product of electric and magnetic loadings without including any limiting factors.

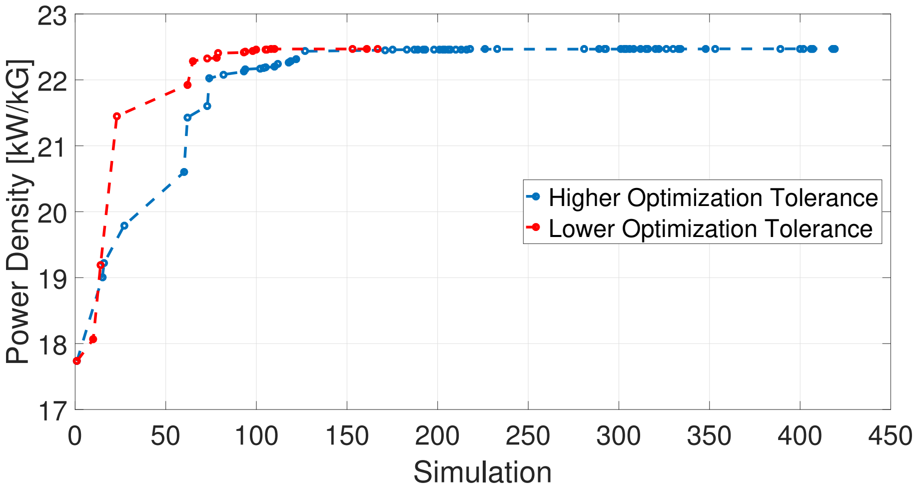

(a) Slotless geometry power density.

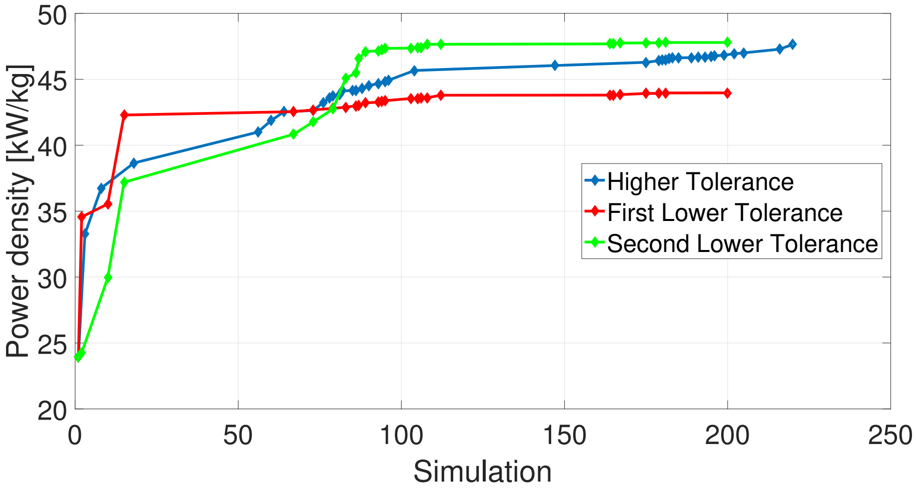

(b) Slotted geometry power density.

Fig. 3.4. Idealized geometry of the PM electrical machine optimization with different convergence tolerances.

3.1.2 On the radial machine choice

This research concerns a hypothetical fan which is integrated into the rotor , having the blades are closed along a shroud at their tips. Different solution types could be employed, Fig 3.5:

- Induction Machines
- Permanent Magnet Machines
- Axial flux Machines

Early on within the design process, it has been decided that the PM solution (radial flux), will be investigated. PM electrical machines possess high torque density [Nm/kg]. The power factor is, usually, significantly better than induction machines, [48]. As the application is thought to this design stage, a fixed speed, no specific requirement of a broad speed range like a flux weakening region is taken into account. In this case, the Surface Mounted Permanent Magnet Machine (SMPM) performs better than an Interior Permanent Magnet (IPM) machine, which is preferred instead for wide flux weakening operations. Furthermore the IPM does not guarantee enough mechanical robustness due to the small iron rotor bridges, essential for ensuring a proper electromagnetic torque generation. In more details a Surface Permanent Magnet (SPM) configuration offers several benefits, among which:

- high speed capabilities
- higher power density, high efficiency η, high power factor $\cos\phi$
- Halbach arrays could diminish considerably the rotor core back [49], [50]

On the other hand, some drawbacks also have to be recognized:

- a very big retaining sleeve giving reduced torque density [51], [52], [53],
- a demagnetization problem at high temperature/torque requirements, when rotor losses are also high, [54], [55], [56], [57], [58]
- no starting torque, so a drive and power electronics are essential

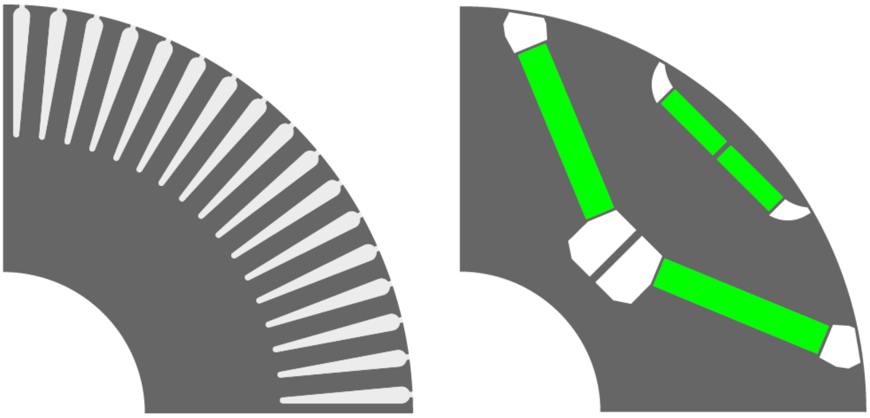

(a) Induction Motor (b) Interior permanent magnet rotor.

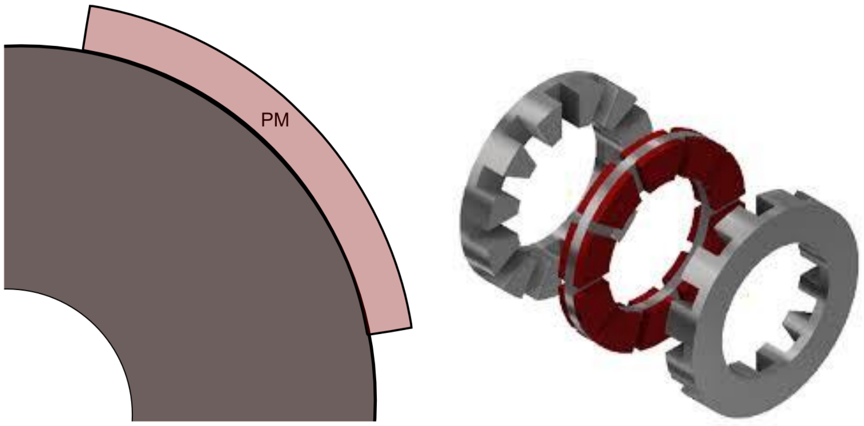

(c) Surface permanent magnet rotor. (d) Axial Flux Topology.

Fig. 3.5. Different types of rotor topologies

3.1.3 Halbach-Array

As previously mentioned, from this point on, regardless the machine being direct or rim driven, the optimization will be based on the assumption to employ a Halbach array of permanent magnets. The Halbach topology optimizes the exploitation of the magnetic field. This magnetic arrangement inherited his name from the studies of Klaus Halbach, a physicist at Lawrence Berkeley National Laboratory [59]. The concept of a Halbach array is based on the principle of an alternating pattern of magnetization. This allows the magnetic field to be bounded to only a single side of the array. To obtain this, the field is concentrated on one side of the array, whereas it is in principle nullified on the other. Such an architecture enhances considerably the magnitude and the shape of the magnetic field with theoretically, the same magnet mass. The simplest Halbach array arrangement is based on the earlier work of Mallinson, dated almost a decade before [59] Halbach. Mathematically, Mallinson proved that such a field can be generated by any Hilbert transform pair. The most straightforward system makes use of $\pi/2$ magnetically displaced adjacent segments (the alternating pattern), as visible in Fig. 3.6 (a). Conversely the most complicated, and idealized [60], is represented by a continuously varying direction of magnetization around the circumferential periphery. This is of course an ideal case, which clashes against manufacturing difficulties, ending up usually in choices of a high number of discrete pieces in a flux focused field arrangement; Fig. 3.6 (b). The arrow in the figure provides the direction of the segments' magnetization. The magnet array is encapsulated in the standard SPM structure of magnetic rotor-back iron and a retaining (non magnetic in this case) sleeve. The Halbach array is a configuration which became popular already in the early 90s, [49], [50], and it is applied in state of art performing machines in more recent years: [61], [62], [63]. Sub-figure (b) yields an appreciation of what the magnetic flux field lines look like. The discretized direction of magnetization can be represented as per (3.13):

$$M = M_r \left[\cos\left((k-1)\left(\phi - \frac{\pi}{2}\right)\hat{\rho} + \sin\left((k-1)\left(\phi - \frac{\pi}{2}\right)\hat{\phi}\right] \tag{3.13}$$

In (3.13) M_r stands for the radial magnetization vector in [A/m]. $\hat{\rho}$ and $\hat{\phi}$ stand for radial and polar principal coordinate vectors. k belongs to the integer field, and according to its sign it determines whether the magnetic field is to be confined inward or outward with respect to the magnetized ring itself.

Despite the considerable magnet thickness required by Halbach arrays to operate effectively, they represent a good electromagnetic solution. The Halbach arrays optimize the machine magnetic circuit exploitation, i.e. the thickness of flux paths shrinks. Targeting a quasi-ideal sinusoidal flux density, the Halbach arrangement creates a lower harmonic content, yielding a quantitatively reduction of electromagnetic-power losses. The study performed will start considering a theoretical high number of segments per pole (7 differently magnetized segments). This will be shown in the proceeding to be too complex, and a trade-off in terms of segment count and economically well shaped flux density is selected.

Rim drives benefits have been presented in Chapter 3. In this analysis the rim-driven rotor

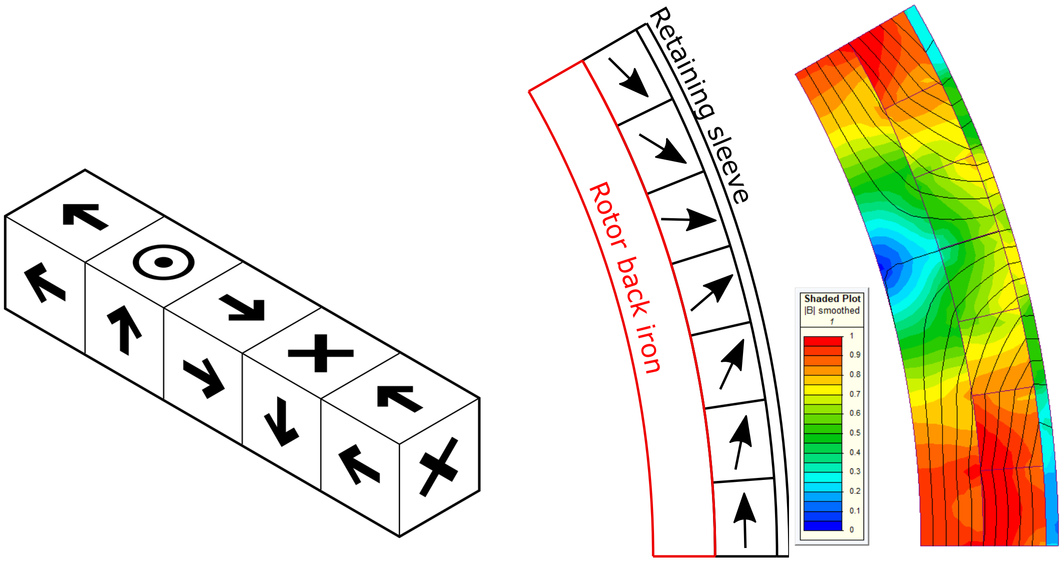

(a) (b)

Fig. 3.6. Halbach Configurations

(Fig. 4.9 (a)) topology consists of a high strength solid steel shroud, on top of which PMs are positioned. To retain the magnet segments, a sleeve wraps the entire rotor assembly.

3.2 Mechanical constraints modeling

Provided that an aerodynamic design is feasible and sound at the fan/propeller side, the mechanical design of the electrical machine is twofold:

- The retaining sleeve has to be designed carefully to maintain the rotor assembly intact, i.e. the magnets at any moment should not deform enough the sleeve to reach stator rubbing or even break apart and provoke a catastrophic rotor failure.
- The permanent magnet bodies do not have to lose contact with the solid rotor: loss of torque transmission (lift-off condition). Some of the retaining materials can in fact possess a higher elasticity than the shaf/rotor yoke, thus allowing a retention, yet a loss of contact from magnet base and rotor.

To analyze the implications of a retaining medium for mechanical integrity onto the electromagnetic performance, the sleeve sizing has been incorporated in the mechanical analysis by means of a general mathematical formulation, taking into account all the possible mechanical interactions between the rotor components.

3.2.1 Model Theory

A two dimensional analytical model is first employed, based upon the Hooke's law. Along with this assumption other simplifications have been introduced: the thick walled thin cylinder plane stress model has been chosen, as the machine is expected to exhibit a very high ratio between radius and axial length. This is why there is no stress assumed along the z axial coordinate. Moreover, all the materials are considered isotropic, i.e. the material mechanical properties are homogeneous and do not vary along a particular direction. This is not strictly true for the carbon fibre (which for example exhibits an orthotropic behavior) or any other composite material. Nonetheless, such an assumption is needed to ease the heavy computational burden. In terms of stress, and also temperature gradient, dependence of the strain, the Hooke's law takes the following form in (3.14):

$$\begin{cases} \varepsilon_r = 1/E^* \, \sigma_r - \nu/E^* \, \sigma_\theta + \alpha^* \, \Delta T; \\ \varepsilon_\theta = -\nu/E^* \, \sigma_r + 1/E^* \, \sigma_\theta + \alpha^* \, \Delta T. \end{cases} \tag{3.14}$$

To achieve a closed form mathematical definition of the stress distribution within the different material layers considered, the stress/strain relation (3.15) is employed alongside the force-equilibrium equation. The former one follows the definitions given by (3.15), whereas the latter by (3.16).

$$\begin{cases} \varepsilon_r = \dfrac{du}{dr}; \\ \varepsilon_\theta = \dfrac{u}{r}. \end{cases} \tag{3.15}$$

$$\frac{d\sigma_r}{dr} + \frac{\sigma_r - \sigma_\theta}{r} + \rho \, \omega_m^2 \, r = 0. \tag{3.16}$$

By expressing (3.14) as a function of strain dependency on displacement, and by combining this with (3.15) and (3.16), the displacement can be written in differential form as:

$$\frac{d^2u}{dr^2}+\frac{1}{r}\frac{du}{dr}-\frac{u}{r^2}+\frac{1-\nu^2}{E}\rho\,\omega_m^2\,r=0. \tag{3.17}$$

The solution of (3.17) yields a general expression for the displacement:

$$u=A\,r+\frac{B}{r}-\frac{(1-\nu^2)\rho\,\omega_m^2\,r}{8E} \tag{3.18}$$

where A and B are constants to be determined.

Combining (3.18) with the definition given in (3.15) and the inversion of (3.14), the radial and hoop stresses at any radius r can be obtained. There are double the number of constants than the number of material layers present in the concentric 2D model. Therefore as many equations have to be established, in terms of boundary conditions, to obtain these unknown coefficients. For a rim driven machine, such as for instance in [64], the concentric geometry is actually hollow. Rim drives are common in the marine thrusters. Related benefits are the absence of mechanical couplings and a fan flow free from obstruction A more detailed view of the Rim Driven Rotor topology chosen is provided Fig. 3.7. In practice the fan blades exert a radially inward retaining force on the rotor core back, rather than following the classical approach of [27]. If this is ignored than a worst case scenario is obtained as a result for the hoop stress on the rotor core. Gathering boundary conditions in compact form, by addressing i as the layer/material index, we can express the stresses conditions as in (3.19):

$$\begin{cases}\sigma_r(r_{\text{inner}})=0;\\ \sigma_r^i(r_i)=\sigma_r^{i+1}(r_i);\\ u_r^{i+1}(r_i)-u_r^i(r_i)=\delta_i;\\ \sigma_r(r_{\text{outer}})=0;\end{cases} \tag{3.19}$$

The relationships established by (3.19) describe the radial stress continuity at different material interfaces. Furthermore, the presence of a shrink interference fit is accounted for by means of

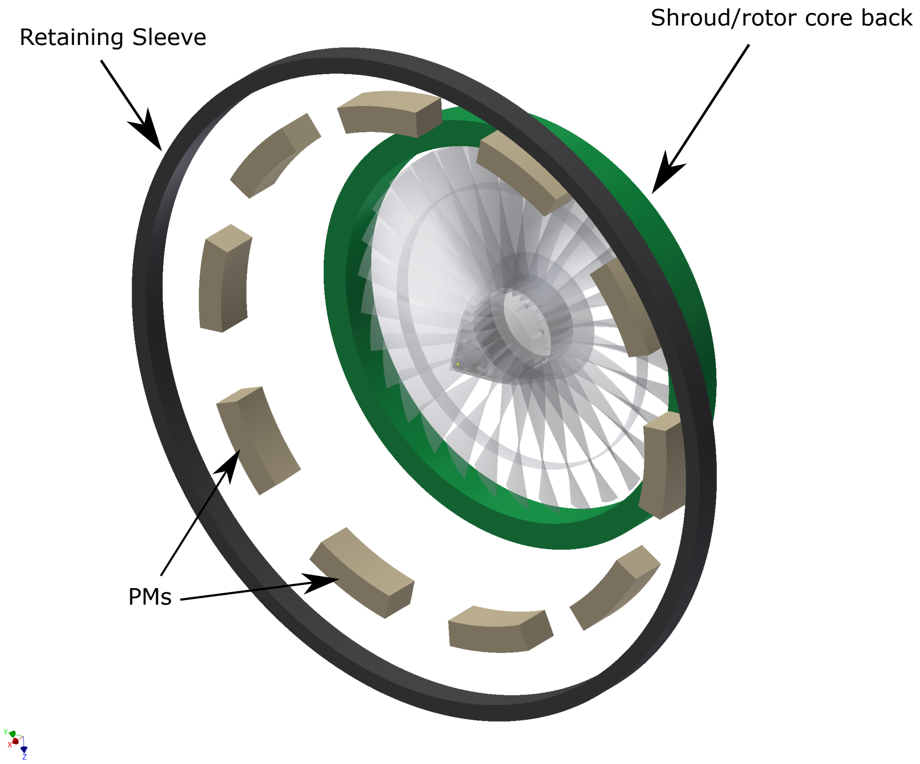

Fig. 3.7. Rotor Assembly view.

the δ_i term inclusion in the displacement equalization equation.

The most simple model chosen to describe the physical interaction is sketched in Fig. 3.8:

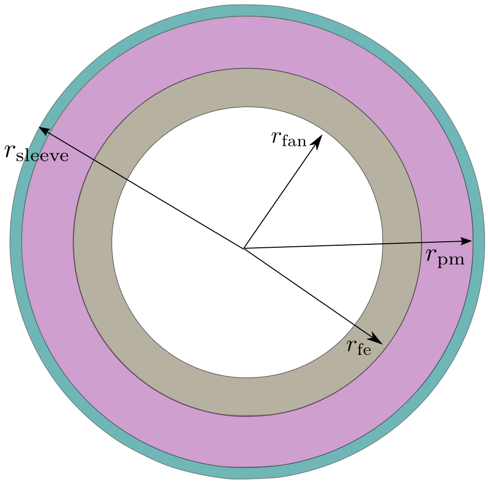

Fig. 3.8. Mechanical model.

In this way the equations presented in (3.19) become specific:

$$\begin{cases}\sigma_r^{\text{Shroud}}(r_{\text{fan}}) = 0;\\ \sigma_r^{\text{Shroud}}(r_{\text{fe}}) = \sigma_r^{\text{PM}}(r_{\text{fe}});\\ u_r^{\text{Shroud}}(r_{\text{fe}}) - u_r^{\text{PM}}(r_{\text{fe}}) = 0;\\ \sigma_r^{\text{PM}}(r_{\text{pm}}) = \sigma_r^{\text{Sleeve}}(r_{\text{pm}});\\ u_r^{\text{PM}}(r_{\text{pm}}) - u_r^{\text{Sleeve}}(r_{\text{pm}}) = \delta_{\text{sleeve}};\\ \sigma_r^{\text{Sleeve}}(r_{\text{sleeve}}) = 0;\end{cases} \tag{3.20}$$

where δ_{sleeve} stands for the interference between sleeve and magnets, due to either wrapping or shrink fit technique. A deeper and broader explanation of the mechanical theory for high-speed machines is available at both [65], [27].

3.2.2 Actual theory and trace of implementation

There are two objectives for the calculation:

- determine the required sleeve thickness, for given magnet and rotor yoke dimensions
- determine the level of interference fit required between sleeve and magnet to prevent magnet from lift off

This recasts the mechanical problem to a double unknown optimal search. Criteria to identify this problem is presented in [65]. The concept is to reach the lift-off condition approximately when the sleeve yield strength is reached. This ends up in solving two algebraic equations. This is possible in the application (spindle) described in the cited reference, where the shaft/rotor back did not withstand any significant deformation. Nevertheless, this is not always true: the tensile strength in the rotor-back of a Rim Driven machine does count. This is essentially due to the hollow ring shape typical of this configuration. Moreover, the radial geometrical dimensions are considerable, developing stresses not negligible in the structure, in this case the solid rotor core back, supporting the permanent magnet.

3.2.3 Mechanical Analysis Example: Analytical

The example provided in Fig. 3.9, gives an explanation about why the aforementioned approach does not suffice in case of hollow shaft/rotor core back, in this specific case a rim-driven assembly. While the radial stresses are not compromising the rotor structure, the tangential stresses are out of admissible range for both rotor core (stainless steel) and PMs (SmCo) [2]. It is evident as the radial stress is a continuous function across the radial cross section, with the absolute value peak located at the interface between permanent magnet outer surface and sleeve inner surface, in compression. On the other hand the hoop stress is far from being a continuous function with respect to the radius, and the wider discontinuity is visible again at the interface between magnet and sleeve. The highest tension is along the inner sleeve interface.

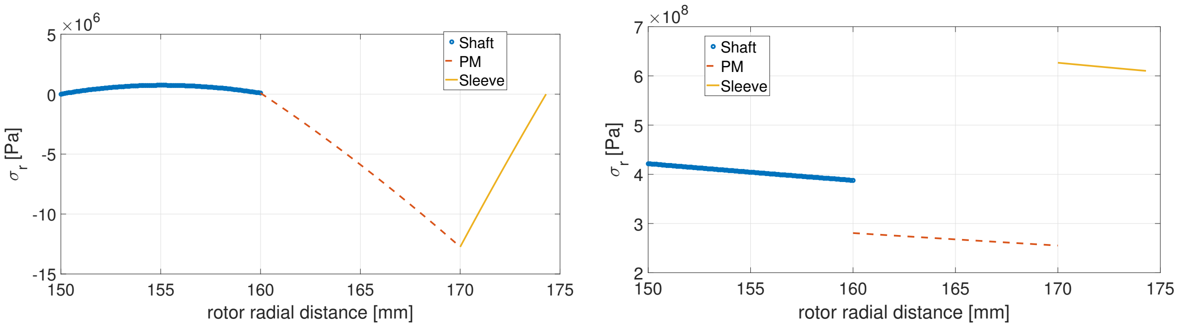

(a) Radial dependence of radial stress.

(b) Radial dependence of tangential stress.

Fig. 3.9. Stresses in Rotor Components/Layers

3.2.4 Mechanical FEA Analysis

In order to prove that the analytical model is reflecting the real physics, a mechanical Finite elements analysis (FEA) is needed as partial validation. Tables 3.1 and 3.2 provide the initial design dimensions for the rotor, and the analytical computed stresses in the critical points of the assembly, respectively. The dimensions of sleeve and interference are computed following the basic model presented in section 3.2.2.

The FEA results, assuming the same hypothesis of isotropic material, provide very close results as reported in Fig 3.10.

---

[2] The initial dimensions considered are: $r_{\mathrm{fan}} = 0.150[\mathrm{m}]$, $r_{\mathrm{fe}} = 0.160[\mathrm{m}]$, $r_{\mathrm{pm}} = 0.170[\mathrm{m}]$, $v_{\mathrm{overspeed}} = 16800[\mathrm{rpm}]$ (20% more than rated speed). In this case the Stainless steel was an S430 with a tensile strength of around 500 MPa, whereas the PMs cannot withstand a tensile stress of more than 140 MPa

Table 3.1. Initial dimensions/parameters

r_{fan}	0.150	[m]
r_{fe}	0.160	[m]
r_{pm}	0.170	[m]
r_{sleeve}	0.1727	[m]
δ_{sleeve}	0.338	[mm]
v_{speed}	14000	[rpm]
ΔT	100	[°C]

Table 3.2. Critical stresses (analytical)

Critical stress	Analytical	FEA	Unit
$\sigma_\theta^{\text{Shroud}}(r_{\text{fan}})$	417	417.76	[MPa]
$\sigma_\theta^{\text{PM}}(r_{\text{fe}})$	278	278.44	[MPa]
$\sigma_r^{\text{PM}}(r_{\text{fe}})$	-13	-13.93	[MPa]
$\sigma_\theta^{\text{Sleeve}}(r_{\text{pm}})$	931	932	[MPa]

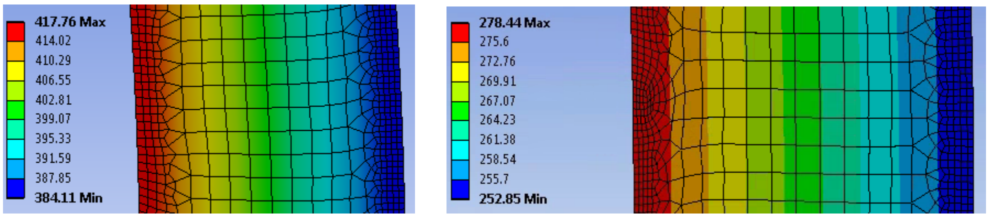

(a) $\sigma_\theta^{\text{Shroud}}$ (b) $\sigma_\theta^{\text{PM}}$

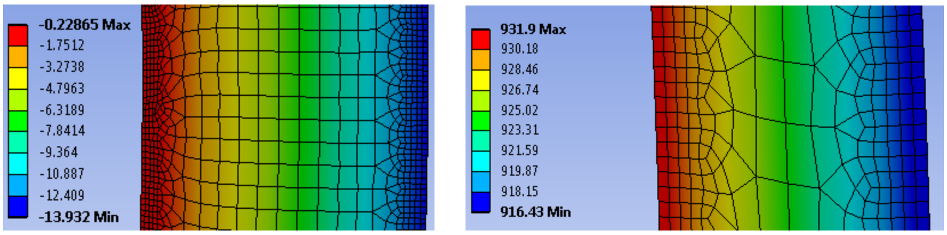

(c) σ_r^{PM} (d) $\sigma_\theta^{\text{Sleeve}}$

Fig. 3.10. FEA Stresses in Rotor Components/Layers

3.2.5 Final model

The sleeve design is not as easy a task as it might have seemed in the beginning. The rotor design must be robust enough to prevent any failure occurrence. This means the following:

- the maximum stress (here assumed the tensile stress), in every rotor component must be under the yield strength of the material.
- the lift-off condition must not occur for the PMs. Equivalently, the radial stress at the interface Rotor-back-PMs must be negative.
- the PMs should sustain the compression at zero speed due to the retaining sleeve interference
- the sleeve should hold the maximum pre-stress applicable from the manufacturer

Consequently, this more complete approach employed to design the sleeve tries to tackle all the issues from a broader perspective. The main idea is the following: since the designer desires to keep the sleeve thickness as small as possible (for minimizing the leakage and maximizing linkage flux, and torque), and at the same time the interference fit as small as possible (for manufacturing reasons), the problem can be cast into a numerical optimization search. Along with variables and objectives the optimization is driven by the constraints listed before. Employing a mathematical description the problem can be cast in the form expressed by (3.21):

$$\begin{cases} \min\left[l_{\text{sleeve}}\right] \\ \min\left[\delta_{\text{sleeve}}\right] \\ \dots \\ \sigma_{\theta}^{\text{Shroud}}(r_{\text{fan}}) < \sigma_{y}^{\text{Shroud}} \\ \sigma_{\theta}^{\text{PM}}(r_{\text{fe}}) < \sigma_{y}^{\text{PM}} \\ \sigma_{\theta}^{\text{Sleeve}}(r_{\text{pm}}) < \sigma_{y}^{\text{Sleeve}} \\ \dots \\ \sigma_{r}^{\text{PM}}(r_{\text{fe}}) < 0 \\ \dots \\ \sigma_{r}^{\text{PM}}(r_{\text{fe}}, dT = 0, \Omega = 0) < \sigma_{c}^{\text{PM}} \\ \dots \\ \sigma_{r}^{\text{Sleeve}}(r_{\text{fe}}, dT = 0, \Omega = 0) < \sigma_{\text{pre-stress}}^{\text{Sleeve}} \end{cases} \tag{3.21}$$

where $\sigma_{y}^{\text{material}}$ is the yield strength of for any material, σ_c is the compressive strength, $\sigma_{\text{pre-stress}}$ is the maximum tensile stress reachable from the manufacturing technique used to create the interference fit.

In the end the problem will find the Pareto's front of a multi-objective optimization. The Pareto's front is obtained by means of a genetic algorithm whose implementation is highlighted in Fig. 3.11. From an initial population of unfitted individuals to a final one where the objectives are minimized/maximized with constraint handling respected. It is obvious that the first population is scattered all over the design space, as the combinations sleeve-interference are totally random and do not respect, neither constraint nor any minimization criteria. As the evolution process proceeds the population inherits a higher fitness, progressively adapting, fulfilling constraints and following minimization objectives. Eventually it reaches the uniform non dominated border in the final generation.

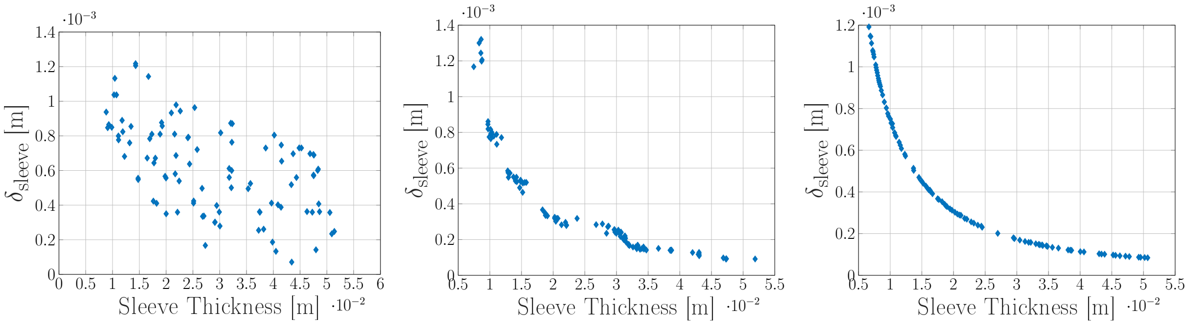

(a) First generation.

(b) Halfway evolution.

(c) Final generation.

Fig. 3.11. Genetic Optimization Evolution Procedure

For a non-trivial multi-objective optimization problem, no single solution exists that simultaneously optimizes each objective. It is almost always the case, that the objective functions are conflicting, and there exists a number of so called Pareto optimal solutions. A solution is called non-dominated or Pareto optimal, if none of the objective functions can be improved in value without degrading some of the other objective values.

All the non-dominated solutions for both interference δ_{Sleeve} and sleeve thickness are represented in Fig. 3.12. Without additional subjective preferential information, all Pareto optimal solutions are considered equally good. Nonetheless, since the electromagnetic performance, i.e. torque density, is inversely proportional to the sleeve thickness, the choice undertaken during the further study is highlighted by the arrow and encirclement. Obviously, the methodology presented fits the needs of the designer according to what type of manufacture the construction of the machine relies on. In other words, every point of the front is theoretically optimum, so the designer could opt, for instance, for a thicker sleeve and a lower interference, when for example the manufacture is not able to reach such levels of shrink fitting and/or there is less interest to preserve a highest torque density. For completeness it must be underlined that the material mechanical modeling carried out thus far is linear. This means that the material is assumed not to experience plastic deformations, but rather remain within elastic behavior range. Plasticity is in any case not desirable, as it will compromise the material permanently.

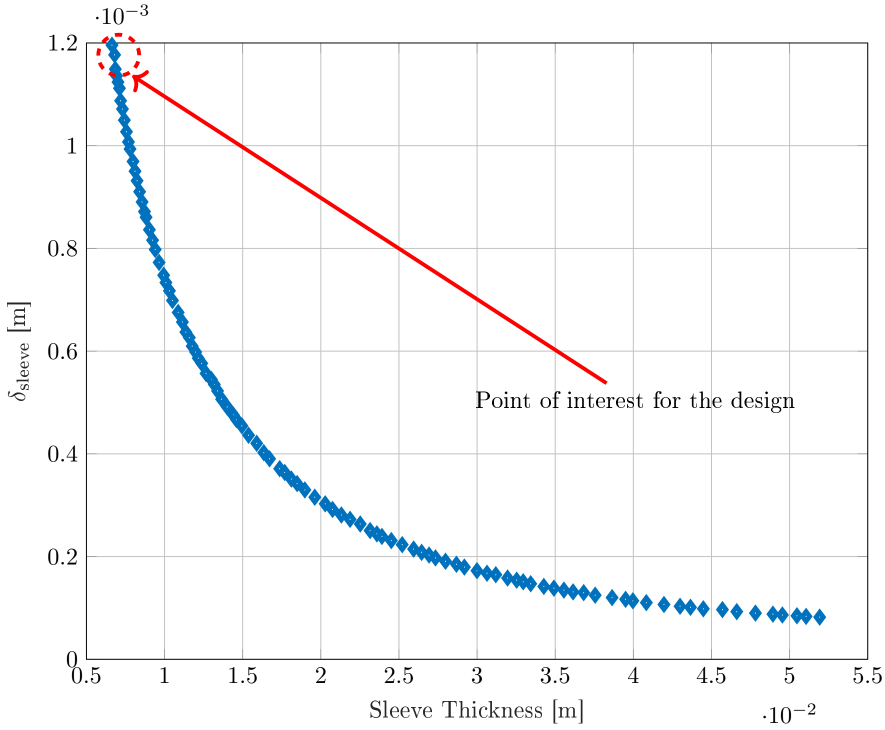

Fig. 3.12. Final Pareto front for Interference and sleeve thickness combination choice.

3.2.6 Rotor-dynamics

For any rotating equipment critical rotational speeds stem from an unbalance in the centre of mass. It is always the case that a residual unbalance is present. Critical speeds see the growth of a system resonance due to vibrations induced in the overall system (rotor and supporting components like bearings, gearboxes and static surrounding parts of the same assembly). There can be different modes of vibration depending on the shape and freedom of movement the rotating machinery exhibits. Vibrations categories can be distinguished as flexural (also called lateral) and torsional [66],[67],[68]. Other vibrations can be bouncing [3] or rocking, [69] Simpler methods like [70] provide a simplistic approach for the determination of the n-th bending-flexural speed.

$$\omega_c = \frac{\pi^2}{k\,l}\sqrt{\frac{E\,I}{\rho\,S}} \tag{3.22}$$

where S is the cross section of the cylinder. E is the Young's modulus of the rotor, I the second moment of inertia for a cylinder around its principal axis (axis of rotation), n the order of the flexural mode, k a safety factor with respect to the rated machine angular frequency and ρ the

---

[3] This is the so called 0 order mode. It is a flexural mode, a parallel displacement of the axis of rotation.

density of the material. This model assumes a very simplified assumption of a single unit rotating cylindrical part (shaft), with no additional interaction, e.g. bearing stiffness and support. As will be shown in detail in Chapter 5 this approach is too approximate for rotors with unusual shapes or composite structures.

Rayleigh's method is based on an energy balance between kinetic and potential components, approach given for example in detail in [71]. Critical speeds can be computed according to the following, in the same form adopted in [10]:

$$\omega_c^2 = \frac{\int_0^L E(z)I(z)\left(\frac{d^2y(z)}{dz^2}\right)dz}{\int_0^L y^2(z)m(z)\,dz} \tag{3.23}$$

where L is the length of the shaft, z is the axial coordinates along which the integrals are computed, y is a test function representing the deflection, chosen (usually sinusoidal-cosinusoidal). E and I retain the same meaning as in (3.22) Nonetheless, the formulation of (3.23) suffers from the drawback of possessing limited information about the real geometry of the machine as the integration is effectively taking place only axially. As will be investigated in details in Chapter 5, Finite Element methods will need to be employed for rotor-dynamic modal analysis, due to their capability to account for any geometrical variation, differing from a simple cylinder (for instance catering for all the moment of inertia terms, i.e. the inertia is mathematically represented by a full tensor with nine different components in a 3D space) and interaction with bearing supports.

3.3 Initial Electromagnetic modelling

3.3.1 Integral slot vs Fractional slot combination

Historically, integral slot combination for winding of electrical machines have been preferred, for their poor spatial harmonic content due to the discretization of the winding along the air-gap. This was a major driver in a scenario dictated by induction machines, where it is essential having an integral combination of slots and poles, although the windings mass is always considerable, especially with respect to the non active end winding. Integral slot wound machines result with chunkier and heavier end winding than a similarly magnetically and electrically loaded fractional slot wound machine. With the advent of variable speed drives and the use of permanent magnet materials in the design of synchronous motors using fractional, in other words non integer ratio combinations of slots and poles, winding arrangements have brought some benefits. In the preliminary research stages this solution has been therefore considered.

The Fractional slot solution is appealing, mainly because of the following reasons [72]:

- a fault tolerant prone configuration [73], in some circumstances is even possible to have no mutual magnetic coupling between phases.
- the end-winding length is reduced, hence decreasing copper loss and mass, increasing power density.
- it also unlocks winding configurations such as the irregularly distributed teeth, which has the following key advantages:
    1. increasing the tooth width enhances magnetic flux linkage. Equivalently, the winding pitch factor is increased.
    2. subdivision of the magnetic path: different teeth withstand different level of flux, depending upon the winding arrangement, i.e. whether a tooth is wound or not.
- modularity and broader choice of slot/pole combination.
- cogging torque reduction [74]
- short circuit current reduction [75], [76]

Conversely, preferring a fractional slot arrangement rather than an integral one is not free from issues. The price to pay is defined in terms of efficiency. In fact the following limitations have to be considered for an adequately efficient design:

- Rotor losses could be very high, as the fractional slot solution allows sub-harmonics, i.e low order harmonics, to arise. These could be very harmful in terms of total efficiency, but also dangerous when related to PMs demagnetization, which is a temperature dependent parameter. To cope with this issue, generally high efficiency fractional slot electrical machines utilize a Q/p ratio equal to 3 [77], [78]. This winding arrangement guarantees no sub-harmonics in the MMF spectrum. Moreover, the first higher harmonic possesses already half the pole count of the synchronous main harmonic. Generally this is the solution with the lowest rotor losses level.
- Unbalanced forces can occur for some particular slots/poles combinations, [79].

For an initial comparison between integral and fractional slot for the preliminary choices we can analytically define an initial design by simply exploiting the scaling 1D laws.
The torque τ, power P, PM thickness t_{PM} can be expressed as follows in (3.25):

$$\tau = \frac{\pi}{4} D^2 \, l \, \hat{K}_s \hat{B}_g \cos\phi \, \eta . \qquad P = \omega_m \tau \tag{3.24}$$

$$t_{\mathrm{PM}} = \mu_{\mathrm{rec}} \, g'' \, \frac{B_{go}}{B_r - B_{go}} \tag{3.25}$$

where $\cos\phi$, η, ω_m stand for power factor, efficiency and angular speed respectively. g'' is the actual magnetic air-gap considering the Carter [80] and saturation factor [81], [82], [83]. Constraints are set:

- Internal diameter of the rotor (Shaft is substituted by the fan)
- Power and speed are given

Therefore, assuming electrical loading $\hat{K}_s$ and flux density in the air-gap $\hat{B}$ we can derive a rough value for the active length l. Having said that, the electromagnetic losses could be quite considerable given the high frequency operation. This is true for the stator winding losses as well as for the PMs and solid rotor core back, if present. The geometrical parameter l_{sleeve} cannot be treated as independent of other rotor dimensions. Namely it is primarily affected by both rotor back thickness r_{bi} and the PM height t_{PM}. Thus, the mechanical model for the retaining sleeve dimensioning is embedded in the optimization. That is, for every simulation/individual of the population (supposing a Genetic Algorithm is utilized) the sleeve thickness is adjusted to sustain the stresses in the rotor. The optimized geometrical cross section of the machine is provided as an example in Fig. 3.13, and a closer look at the optimization procedure is highlighted in Fig. 3.14.

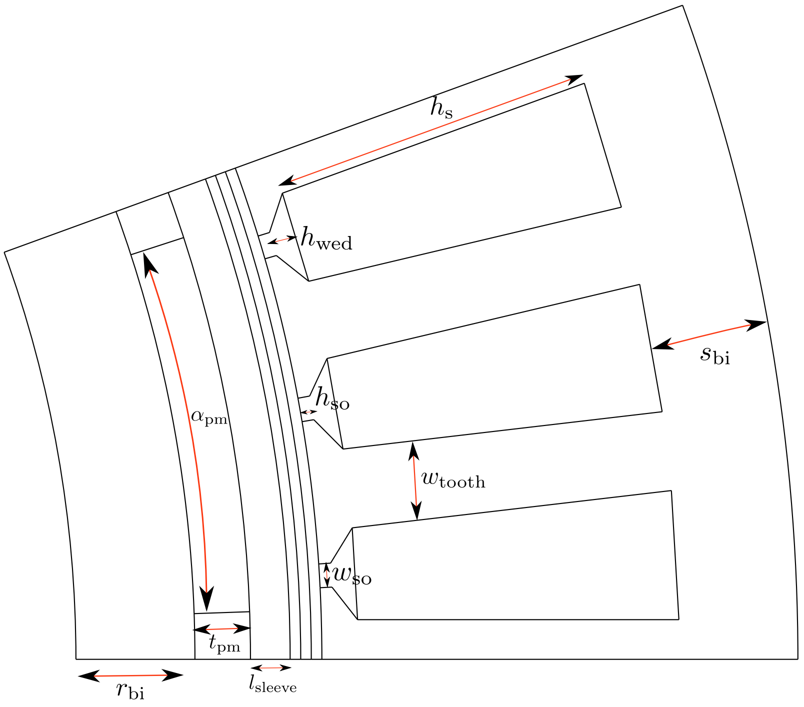

Fig. 3.13. Single pole cross section optimized, with parameters varied.

3.4 Results for power density optimisation

Given the roughly known geometrical constraints, the investigation has started with the unique optimization objective represented by the highest power density achievable, i.e. in this first stage the losses were not considered. Both integral slot and fractional slot solutions have been examined, defining a set of pole pairs (frequency related to speed) and excitation current density (associated with the electrical loading). All the different current densities have been used with all the poles combinations.

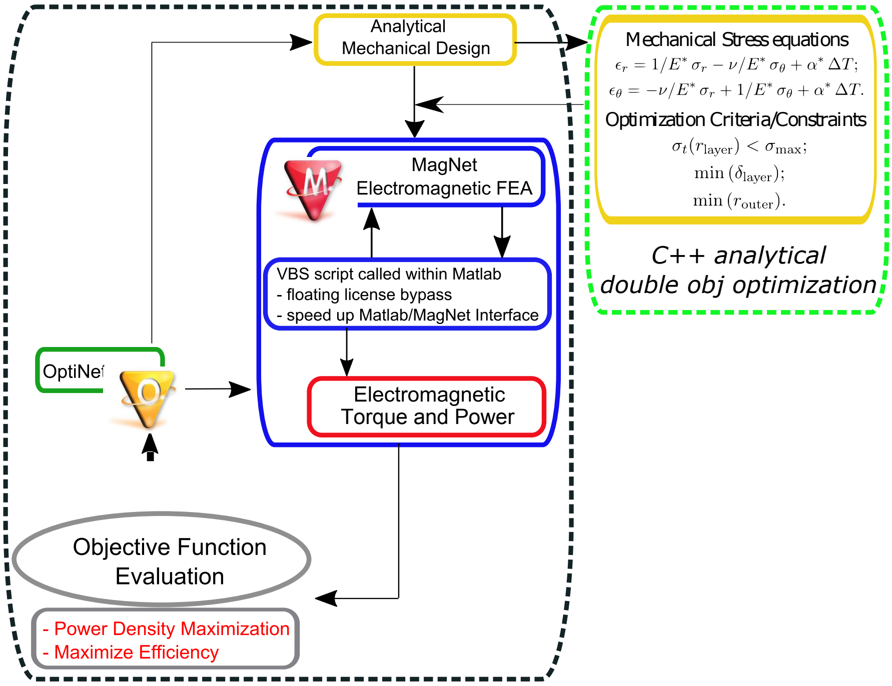

Fig. 3.14. Embedded .exe created from C++ called in the optimization scheme.

Frequency[Hz]/Poles	J [A/mm^2]
1400 / 12	5
2100 / 18	10
2800 / 24	15

Table 3.3. Combination of poles and current density.

In this initial approach both the integral and fractional slot solutions have used a fill factor of 0.5. Moreover, the end-winding dimensions have been included in the weight estimation. For Fractional Slot, in this case single tooth non-overlapped winding, the end-winding length L_{ew} can be roughly estimated as per (3.26) and (3.27), [84]:

$$L_{\text{ew}} = \frac{3}{2}\frac{\pi}{4}\frac{\pi D}{Q} \approx 1.2\frac{\pi D}{Q}. \tag{3.26}$$

whereas for integral slot, overlapped winding:

$$L_{\text{ew}} \approx \left(\frac{3}{2}\frac{\pi}{4m} + \frac{m-1}{m}\right)\frac{\pi D}{2p} \approx 2.5\frac{D}{p}. \tag{3.27}$$

where Q, p, D, m stand for stator slots number, pole pairs, stator bore diameter, number of phases, respectively. Only three-phase machines have been simulated. The optimization relies on a genetic algorithm, aiming at the maximization of power density/minimization of weight. The following assumptions were made in terms of electromagnetic FEA simulation:

- the excitation current on the stator side is defined as a perfect sinusoid, assuming the current control is ideally not prone to any total harmonic distortion, THD.
- the simulation is 2D with rotation. Since we are not interested in the losses we can decouple the time-stepping backward Euler scheme for solving the partial differential equations PDEs implemented in FEA, and ignore the eddy currents. As a consequence the simulation time is improved.
- Adaptive time-stepping is used to further speed up the computation.
- The machine geometrical periodicity is exploited:
    1. As it is an integral slot only one pole is needed, with means of odd periodicity conditions
    2. The fractional slot needs two poles, because of the combination chosen (3 slots/2 poles), with even boundary conditions
- the machine is simulated for only one-sixth of the electrical period. This is justified by the torque ripple periodicity, which lays within this time span.
- the stator core is considered to be made of very high-performing JNEX-900 electrical steel.
- the rotor core back of both the integral and fractional slot configuration consists of solid stainless steel S430 Ferrite Steel. Theoretically, this should represent the highest strength magnetic steel available.
- the stator winding is made of copper.
- the PMs are SmCo Recoma 33. This is the second best grade (in terms of magnetic energy product) of permanent magnet available from Arnold Magnetic Technologies. The PMs

are assumed in all cases to operate at a higher temperature than ambient: 100 °C. SmCo was chosen because of the harsh environment in which the machine is supposed to operate at altitude. NdFeB was not recognized to be the best choice.

- Carbon Fibre is needed for the retaining sleeve. It is the only material capable of sustaining elevated tangential stress without significantly increasing the effective machine air-gap.

Finally, the combination of slots and poles in this first investigation has been chosen according to Tab. 3.4.

INTEGRAL SLOT Slots / Poles	FRACTIONAL SLOT Slots / Poles
36 / 12	18 / 12
54 / 18	27 / 18
72 / 24	36 / 24

Table 3.4. Combination of slots and poles for different configurations.

Two flux density plots pictures of optimized machines for the two different configurations and number of poles analyzed are represented in Fig. 3.15:

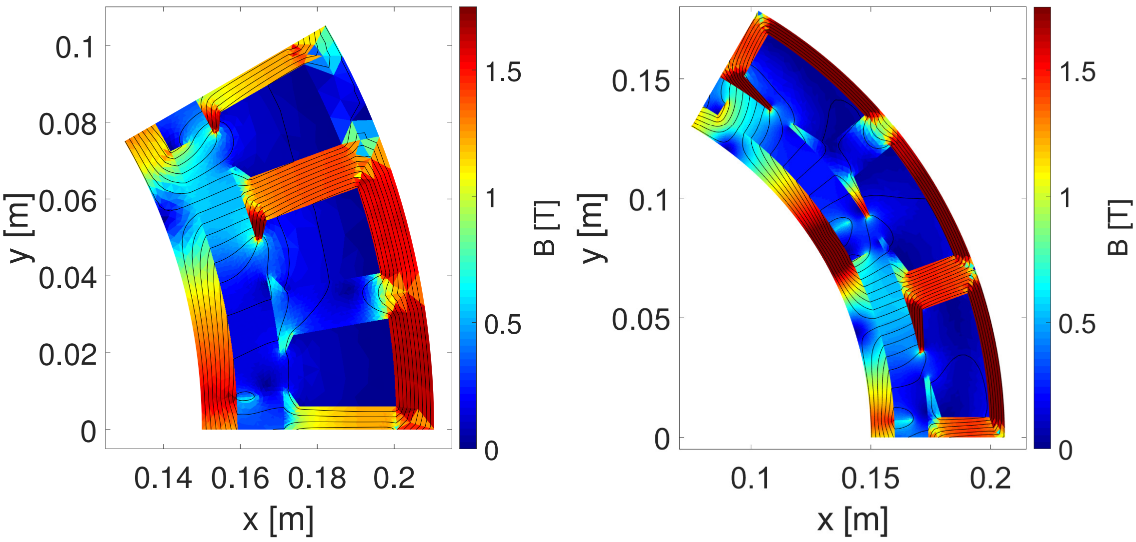

(a) Integral slot 36 Slots / 12 poles

(b) Fractional slot 18 Slots / 12 poles

Fig. 3.15. Comparison of integral and fractional slot configurations for the lowest frequency.

Comparison of results for the two different optimization are shown in figures 3.16 and 3.17.

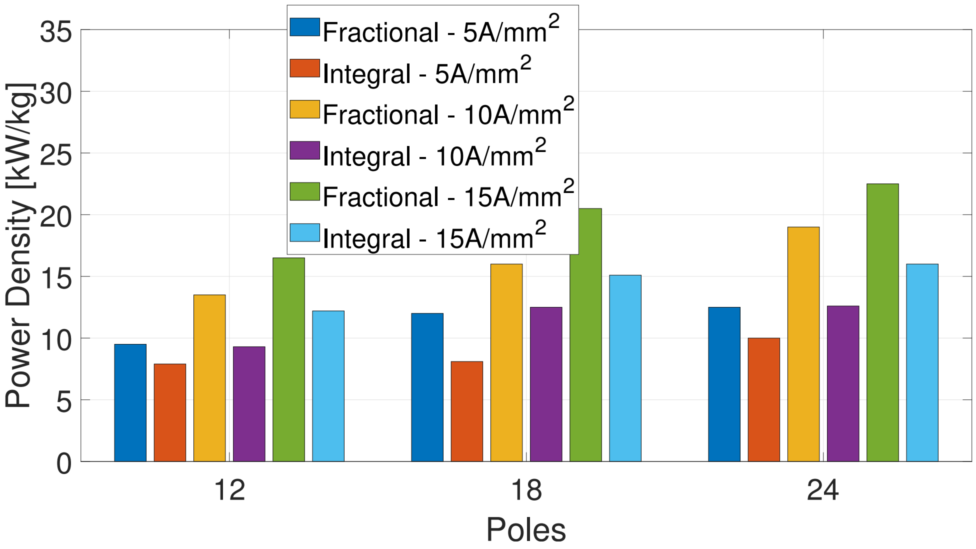

Fig. 3.16. Power density vs pole number for different J.

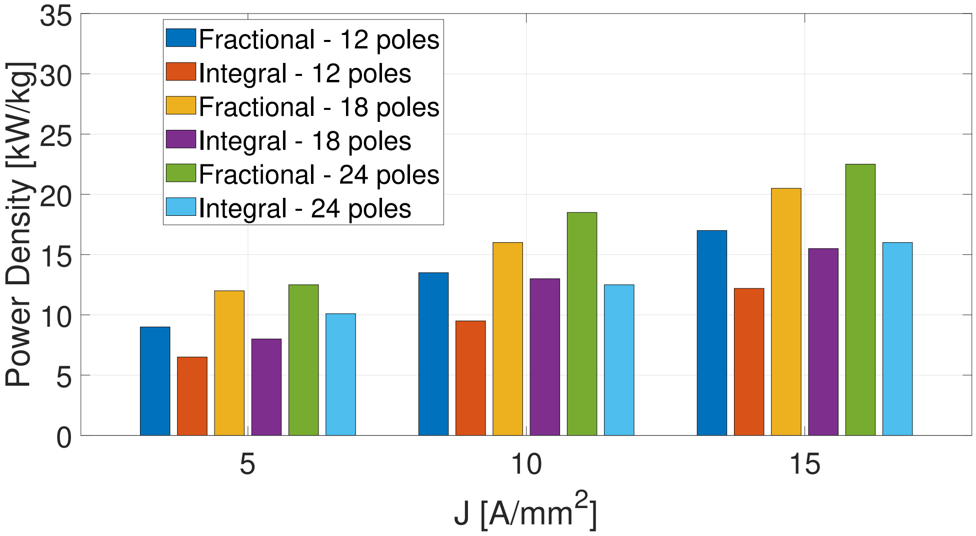

Fig. 3.17. Power density vs J for different pole number.

It is clear from Fig. 3.16 and 3.17 that the power density for both fractional slot and integral slot machines increases following an approximately linear trend along with the current density increase and the frequency increment. Particularly, in almost all cases, the fractional slot solution power density exceeds the integral slot by at least 30%. This seems to be an attractive margin, considering that weight minimisation is a major requirement.

3.5 Results for power density and loss optimization

A more precise optimization relies on the evaluation of machine losses along with the weight estimation. This is because it could be meaningless achieving the maximum power density along with a very low efficiency. As the BLI aerodynamic concept is all about minimizing fuel consumption, the electrical equipment must have a certain efficiency level, which should be theoretically as high as possible. Losses in a Surface Mounted Permanent Magnet Synchronous electrical machine are represented by:

- Stator winding losses: these could be split into DC resistive losses and AC resistive losses.
- Iron Losses: the laminated core has eddy current, hysteresis and additional/anomalous losses.
- Rotor losses: all the conductive components rotating in the machine maybe subject to eddy current losses.
- Windage loss and mechanical loss are associated with the air friction within the air-gap, bearing losses and any other loss in additional mechanical components integrated in the machine.

3.5.1 Rotor Losses

An issue of paramount importance is represented by the rotor loss. Rotor losses are due to eddy currents. Eddy currents are generated by asynchronous harmonics components of the magnetic field rotating at a different speed from the synchronous one. Asynchronous harmonics are due to space harmonics (discrete winding distribution pattern) and/or time-harmonics (static converter fed machines with a certain THD in both voltage and current source).

Rotor losses are usually small for electrical machines running at low frequencies and equipped with integral slot distributed winding. However, at higher speed (higher frequency) losses increase considerably following a parabolic relationship with regards to the magnetic field time-harmonics. Moreover, if the winding presents a fractional slot-pole combination the space harmonics could become quite considerable, creating a serious problem in terms of rotor heat generation and consequently a higher probability of demagnetization.

In order to address this issue both the integral slot and fractional slot solution have been investigated for the lowest frequency value: the 12 poles combination (1400 [Hz] fundamental frequency) has been chosen as a benchmark.

In order to better understand the difference between Asynchronous harmonic content for Integral against fractional slot solutions we must recall the electrical loading (3.28) and magneto-motive-force MMF/Magnetic scalar potential definition (3.29) for a three phase rotating electrical machine [81]:

$$K_s = \sum_{\nu}^{\infty} \frac{3k_{w\nu}N_s\hat{I}}{\pi D}\cos(\nu(p\theta_s+\pi/2)-\omega t).^{4}. \tag{3.28}$$

From the electric loading, the magnetic potential can be computed as the integral along the air-gap, which is:

$$U_s(\theta_s) = \int K_s(\theta_s)\frac{D}{2}d\theta_s = \sum_{\nu}^{\infty} \frac{3}{\pi}\frac{k_{w\nu}N_s\hat{I}}{\nu 2p}\sin(\nu(p\theta_s+\pi/2)-\omega t). \tag{3.29}$$

By using the star of slot theory [81] it is easy to derive the harmonic spectrum for the different combinations of slots and poles, as shown in Fig. 3.18. The Q stands for number of slot, D and S for double and single layer, respectively. It is very clear that the higher the number of slots, the lower the harmonic content is, for the integral combinations. Moreover, the chording in double layer winding provides a massive reduction of the 5th and 7th harmonics. The 3rd harmonic is inserted for completeness, although in a three phase balanced machine it does not occur in the

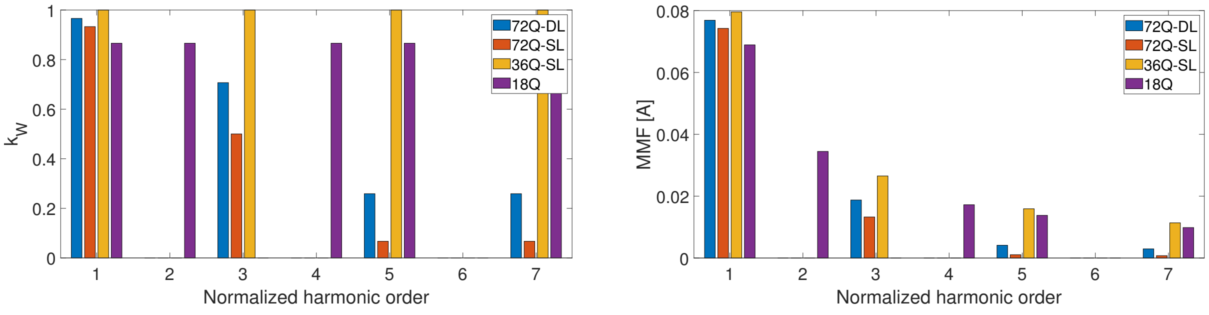

(a) Winding coefficients comparison

(b) MMF harmonic coefficient comparison

Fig. 3.18. Space harmonics content comparison between integral and fractional configurations.

---

[4] ν stands for the harmonic order, $k_{w\nu}$ the harmonic winding coefficient, N_s the number of series turn per phase, $\hat{I}$ the peak phase current, D the stator bore diameter, θ_s the stator mechanical angle, ω the electrical anguler frequency

MMF content, as it is a zero-sequence one and it is intrinsically canceled out by the interaction among phases.
On the other hand, the fractional slot counterpart exhibits more harmonics. Mainly all the 2^{nd} multiple family. Nonetheless, as previously mentioned, this is the less harmful combination due as there are no sub-synchronous components.

Integral slot solution: rotor losses

The integral slot combinations considered in the optimization all possess $q = 1$ (slots per pole per phase). This configuration is the easiest, and quickest to simulate as the pole span is reduced to its minimum. Nonetheless such a combination has considerable space harmonics, harmful for all the rotor conductive parts. To ameliorate this q has been doubled. Increasing the number of slots provides a more sinusoidally shaped armature reaction distribution/MMF. Therefore, a further specific geometrical optimization has been carried out for the 72 slots - 12 poles combination.
An additional improvement in terms of rotor losses is given by chording. As it is well known from the old theory of induction motors [83], the short-pitching 5/6 yields the best compromise for decreasing 5^{th} and 7^{th} space harmonics. Thus, the increased slot number combination and a single slot double layer chording further reduces rotor eddy current losses. Fig. 3.19 highlights the subdivision of losses between rotor conductive parts. In all cases there is no PM segmentation, i.e. only a single PM per pole is employed. It is clear that both increasing the number of slot and the chording contribute to a substantial decrease in losses.

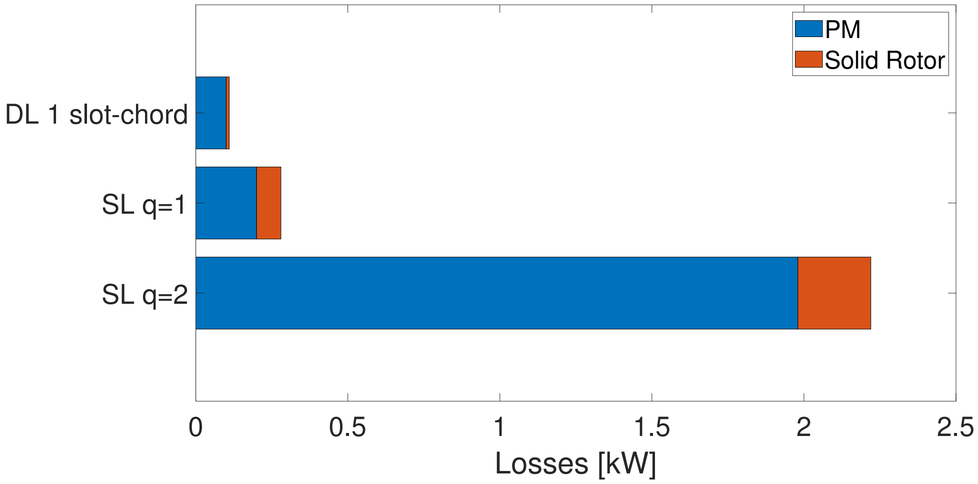

Fig. 3.19. Initial comparison Integral solution rotor losses for 72 slots-12 poles.

Fractional slot solution: rotor losses

The fractional slot solution intrinsically possesses a much richer space harmonic content. Moreover, it is broadly recognized that high efficiency motors respect the aforementioned 3 slots - 2 poles rule, cited several times in the previous sections, in order to minimize eddy current losses. Consequently, there is no freedom of choice in increasing the stator slots number, unless a higher frequency/number of poles is selected. Fig. 3.20 shows how the rotor eddy current loss is excessive, even when adopting a high degree of segmentation [5].

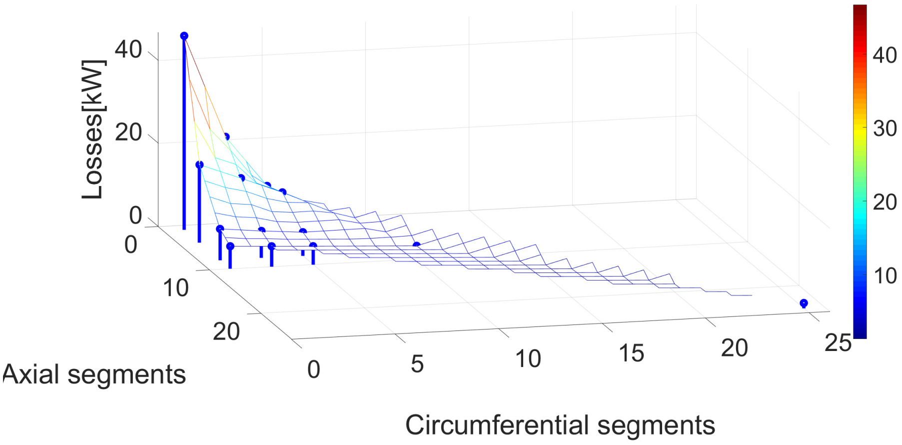

Fig. 3.20. New rotor assembly.

Loss in the solid rotor back under the magnets increased as more segments were used. This is due to the decrease of PM shielding effect as a result of the segmentation level increase. Such losses are unacceptable. In order to overcome this issue we could assume, in the first place, a lamination material employed for the rotor back assembly such as JNEX 900 steel laminations. The rotor losses will concentrate prevalently within the magnets. The rest are due to eddy current and hysteresis losses in the lamination. This solution provides circa 30% less electromagnetic losses in the rotor assembly. However, even if this solution looks attractive, the lamination is not able to withstand the same mechanical stresses as a solid stainless-steel component. Moreover, the laminations cannot be directly attached to the fan blades. This creates the necessity to consider an extra layer within the rotor assembly. An overview of the updated rotor structure is given in Fig. 3.21. The optimization scheme has been carried out for an 18 slot, 12 poles combination

---

[5] The segmentation is intrinsically affecting a 3D phenomena, as the eddy currents develops in the 3D space coordinates. An approximation have been used to rescale the resistivity of the permanent magnets, thus taking into account the end effects according to the circumferential and axial span of every single segment. [85]

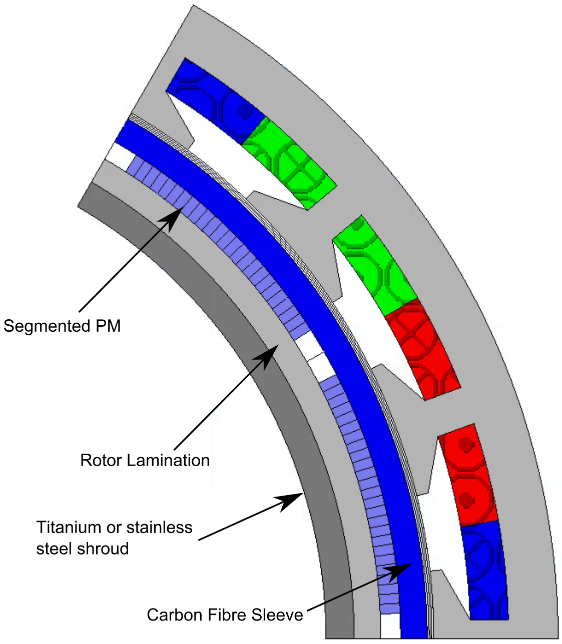

Fig. 3.21. New rotor assembly.

using the aforementioned mechanical structure in the following way:

- the objective function is the weight to be minimized
- the constraints are imposed to be the minimum torque to reach the machine rated power, along with a maximum amount of rotor losses set to an initial value equal to the 0.5% of the total electromagnetic power
- the solid rotor part has been investigated for both Titanium based alloy material, and stainless steel.
- the analytical mechanical model provided in the beginning of this chapter has been modified to incorporate the additional concentric layer. Moreover the interference between rotor shroud and lamination is considered to be 0.1 [mm]. Quick hand calculations demonstrate no pre-stress issues are encountered in the range of diameters investigated for the lamination layer tensile strength.

The results of the optimization are described by the histogram in Fig. 3.22. They demonstrate how a sensible fractional slot design in terms of losses has an inevitable reduction in power density. Furthermore, the stainless steel solution is better in terms of both losses and power

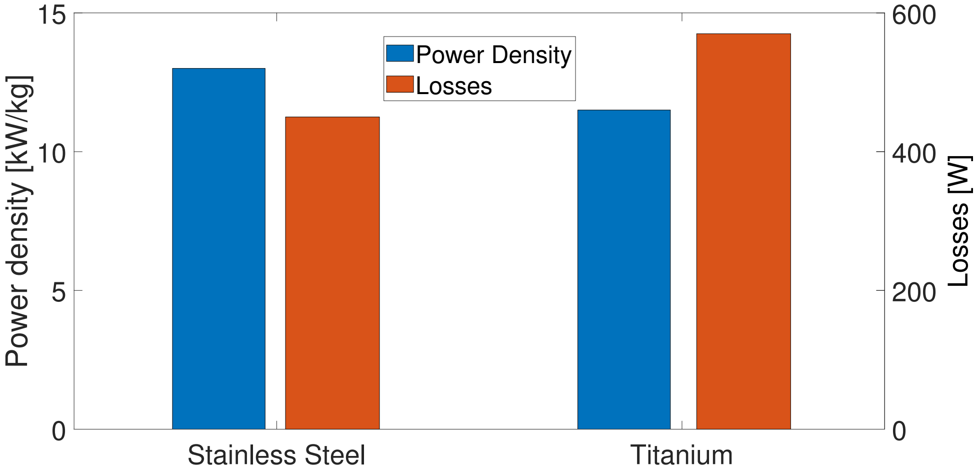

Fig. 3.22. Titanium vs Stainless steel shroud optimized geometries.

density. The disadvantage of titanium is that it is more conductive than solid stainless steel. Moreover, it is a non-magnetic permeable material. This entails that magnetic flux lines tend to avoid traversing it. As a consequence, no additional torque is developed in this component, only losses. On the other hand, the highest strength magnetic steel can represent a flux path, providing a small additional torque, together with lower eddy current loss generation.

3.5.2 Losses in Stator Windings

The winding losses in stator windings include:

- Intrinsic winding losses due to a perfect sinusoidal waveform, in case of inverter fed electrical machines, or very well performing current control from the power electronics/inverter side.
- Higher Order Harmonic losses due to current harmonics. Additional current harmonics, higher than the fundamental, are, for instance, due to Voltage Source Inverter configurations. In this case the machine inherits from the power electronics a certain degree of THD (Total Harmonic Distortion).

The losses in the stator winding can be divided into two different categories, namely DC and AC losses. DC losses are due to the resistance and RMS current flow in the conductors cross section. On the other hand, AC losses are usually associated with the skin and proximity effects over the conductors. Skin and proximity effect both entail an uneven distribution of current over the conductor cross section, which in turn increases the ratio between the AC equivalent resistance and DC resistance [86], The skin effect regards the non-uniform current distribution due to the self generated flux of the conductor. Proximity effect, as the name suggests, implies an uneven current flow because of flux interaction caused by adjacent conductors which influence each others' electromagnetic field. However, more causes for AC losses can be identified, especially in electrical machines with stator cores [87]:

- Fringing/leakage flux in the slot opening: the flux lines are distorted, due to the slot opening at the air-gap. Consequently strands positioned close to the slot experience a higher magnetic field variation over time, increasing their losses. Leakage flux generated eddy currents are the dominating component of the AC losses for most types of slotted machines.
- External flux: PMs can be the cause of external flux crossing the air-gap and entering the slot from the slot opening. Thus, further flux lines will impinge the winding, increasing once again the eddy current losses.
- The use of parallel strands potentially creates an unbalanced current distribution across the conductor arrangement within slots. This phenomena is known as circulating current losses. It is due to self and mutual inductance difference among strands belonging to the same coil, and positioned at different slot levels: a strand located in the slot bottom will show a higher inductance than a strand positioned at the top.

Saying that, a fast and reliable method of modelling the AC losses in the stator winding is needed for addressing this crucial loss component. A fast semi-numerical model has been developed and it is embedded in the multi-objective optimization process. The model makes the following hypothesis:

- strands are uniformly and evenly distributed within the slot cross section
- transposition of the wires along the machine axial length is employed, i.e. circulating current losses withins the same coil are neglected, as the inductance difference of every single strand is averaged out along the machine length.

Exploiting these assumptions, we recall as the winding losses can be derived for the DC component (for a cylindrical conductor) as:

$$P_{\mathrm{DC}}(t) = \frac{4\rho_c l}{\pi d_c^2} i^2(t). \tag{3.30}$$

where ρ_c, d_c, l are conductor resistivity, cross section diameter and length.

Whereas the definition of Square Derivative Field approach yields the AC Losses [30]:

$$P_{\mathrm{AC}}(t) = \frac{\pi l d_c^4}{64\rho_c}\left(\frac{d\vec{B}}{dt}\right)^2 .^6 \tag{3.31}$$

Since all the waveforms are assumed associated to the synchronous reference frequency (first harmonic feeding the machine circuit) it is convenient to define the mean losses as an integral quantity:

$$P_{\mathrm{Cu}} = \frac{1}{T}\int_0^T \Big(P_{\mathrm{DC}}(t) + P_{\mathrm{AC}}(t)\Big)\, dt \tag{3.32}$$

Analytical models employed for example in [10] are not to be trusted since the 1D model just accounts for skin and/or proximity effect, but no leakage or external flux is properly taken into account. Instead the different approach presented in [30] will be employed and implemented.

3.5.3 Additional losses

Losses the have not been included in the analysis thus far conducted that are in addition to electromagnetic phenomena are the mechanical losses. Windage and friction losses due to aerodynamic interaction as well as bearing friction are a fraction of power loss which is not negligible, especially for high speed motors. These losses are very difficult to determine, however some crude estimates for some of them can be given as follows.

Windage losses are computed with well established analytical/empirical formulations [26], expressed in (3.33):

$$P_{\mathrm{windage}} = \mathrm{k}_1 \mathrm{C}_{\mathrm{f}} \rho \pi \omega^3 r_r^4 l_r^4 \tag{3.33}$$

---

[6] Important to stress the vector feature of this derivative. The losses are directly dependent on the square power of the vector time derivative.

where k_1 is a roughness coefficient for the air-gap (usually for a slotted stator this is considered 2.5). C_f represents a friction coefficient dependent on density, air-gap length as well as fluid turbulence via Reynolds' number. This is a considerable quantity due to the high rotor tip velocity.

When an axial flow is allowed within the air-gap, for cooling reasons, it encounters a tangentially rotating fluid. Due to conservation of angular momentum, the rotor will create losses, accelerating the fluid coming into the air-gap, deflecting it's velocity vector tangentially. It is possible to quantify the power needed in this process computing the axial flow angular momentum. By then rescaling with mean velocities this additional power loss can be quantified as follows in (3.34). The loss represents a situation with two concentric cylinders. A further assumption made, as in [88], [89], [90] is that the cooling fluid exhibits solely axial velocity component at the gap entrance.

$$P_{\mathrm{axial}} = 2/3\pi\rho\, v_a v_\theta\, (r_s^3 - r_r^3)\omega \tag{3.34}$$

where v_a is the mean axial velocity and v_θ is the mean tangential speed. This last is usually assumed to be a half of the rotor tip speed.

The losses lately mentioned will be included in the more comprehensive optimisation presented in the next chapter.

Chapter 4

Detailed Optimisation

In this chapter more detailed optimization results are given. Figure 4.1 schematically depicts the optimization procedure implemented. The optimization procedure is carried out by means of a modified version of the popular (Non-dominated Sorting Genetic Algorithm) NSGA-II [91], [92], [93]. Some modifications to this popular algorithm have been implemented based on [94] in order to accommodate the inclusion of hard constraints; namely the elimination of geometrically unfeasible structural cross sectional dimensions, as well as possible voltage constraints. Every optimization run explores a design space consisting of 40 generations with each population of 100 individuals. The optimization is performed twice, forming a double run. As a consequence 4000 simulations and objective function evaluations are performed twice for each machine investigated. The optimization seeks a double-objective minimization to reduce both mass and losses. It aims to optimize the machine structure via a parametric change of the geometrical dimensions of cross section and axial length. The whole optimization is conducted exploiting parallel computation techniques, in order to evaluate more individuals of the same generation at the same time. All the values of interest computed throughout the optimization, based on 2D time-domain simulations: mass (including the end winding mass), rotor eddy current losses, iron losses, winding losses divided into DC and AC components, shear stress and electric loading values. The flow-chart presented in Fig. 4.2 is accordingly adjusted to fit the analysis of every section of the chapter. The input values are the same as those exemplified in Fig. 3.13. The output value is the final fittest generation. All the results have to be presented as a family of solutions. This is due to the multidimensional nature of the optimization. Having more than one objective to minimize/maximize for, and with often opposing targets, the solution is represented by a so called Pareto front. Therefore an optimal solution per se, cannot be identified unequivocally. A choice needs to be made at the final stage, narrowing down the choice of design to a trade-off between the contrasting performances related to the different objectives.

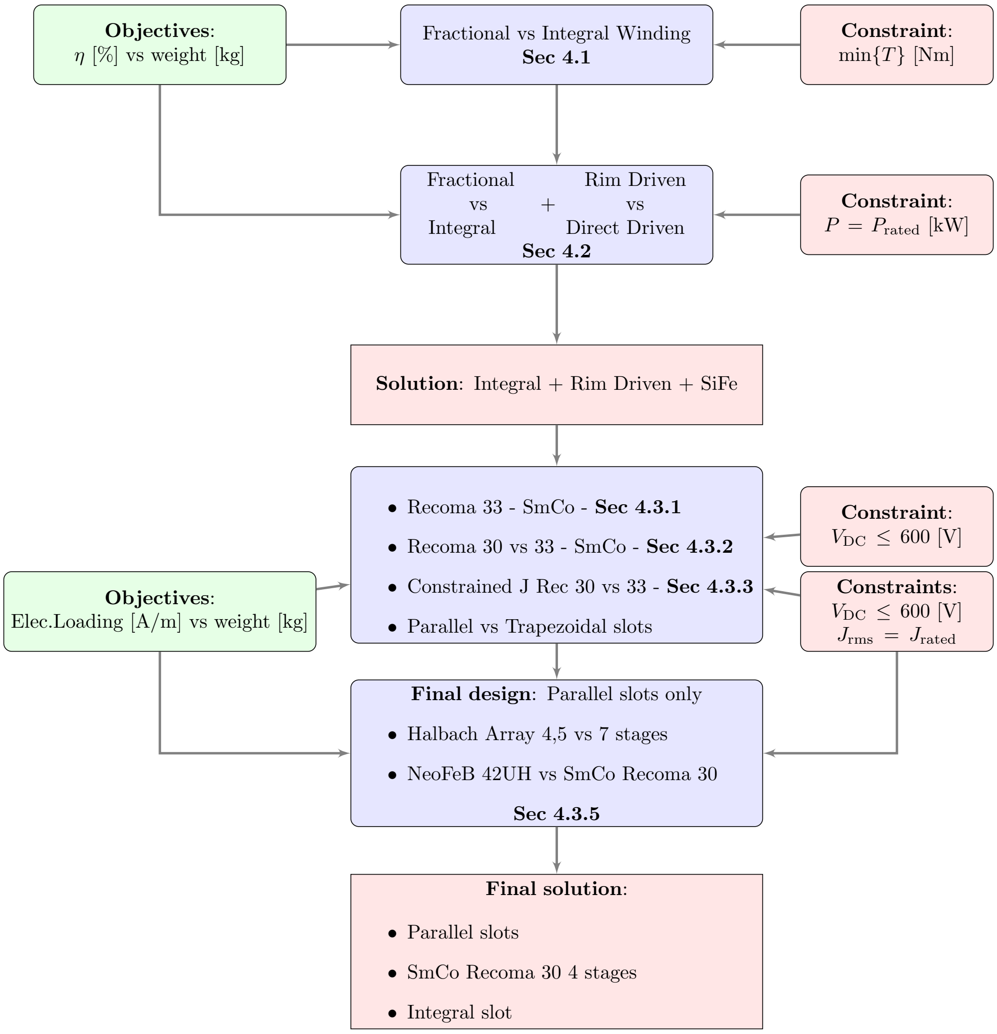

Fig. 4.1. Optimization procedure.

To highlight a clear differentiation between consecutive stages of the design process and deal with the large volume of results, it is necessary to summarize the steps taken in the analysis. As the investigation progresses the analysed level of detail increases and a graphical visualization is given in Fig. 4.1. The chapter, after presenting the optimization flow, starts with some initial comparison of winding arrangements for Rim-Driven machines (Section 4.1). This is then followed by a trade-off study between rim and direct driven arrangements considering the two winding solutions (Section 4.2). From this point on the only design choice is narrowed down to a Rim-Drive integral slot topology. Further details are progressively added to the optimisation procedure in the subsequent sections. First the voltage constraint, then the comparison between 2 different grades of magnet material, and finally to the identification of the best slot shape as well as the compromised number of Halbach segments.

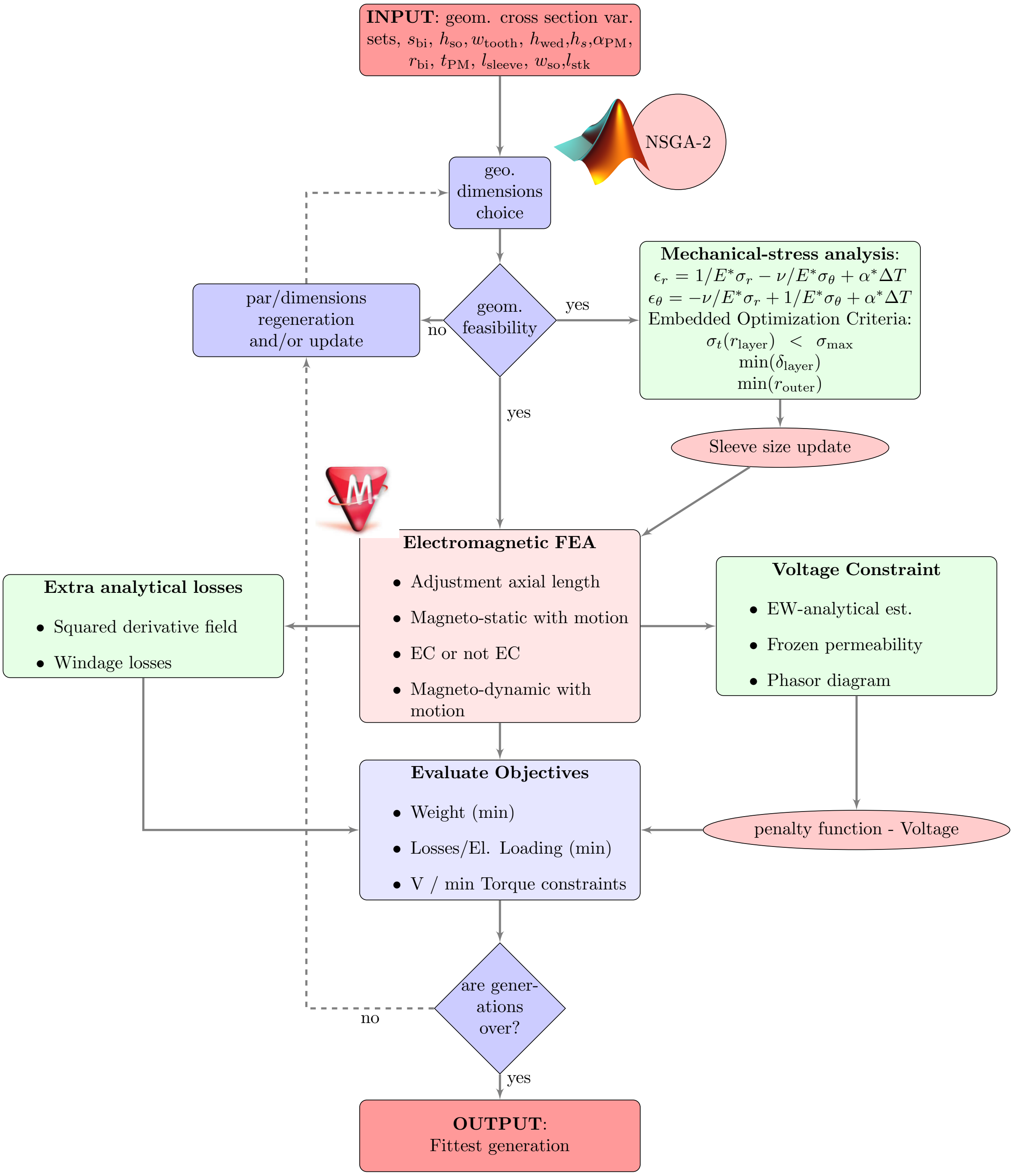

Fig. 4.2. Optimization flow chart

The flowchart in Fig. 4.2 starts with the definition of the sets within which the geometrical parameters are free to vary. A pseudo-random number generator is employed by the NSGA for generating the parameter in the sample space. The first hard constraint encountered during the optimization cycle is the geometrical feasibility evaluation. This avoids the consideration of geometries with features that might overlap, therefore having no meaning for the Finite Element solver. The mechanical dimensioning of the sleeve is first performed using the theory presented in Chapter 3. The electromagnetic analysis is then performed by the solver (this case Infolytica MagNet [95]). Depending on the type of optimization approach the various types of solver setting available are selected (these are listed in the flow chart Electromagnetic block). Once again, according to the analysis performed the electromagnetic FEA can be accompanied by softer constraints handling like the voltage limit, which is refined by the usage of the frozen permeability method to extract the actual voltage at the terminal of the motor. Extra analytical estimations can be carried out as well. Once all the information required has been gathered, the fitness function evaluation and constraint violation checks for every individual in the population are performed. Such a scheme keeps running until all the generations have been evaluated.

The materials assumed, along with their properties, are given in Tab. 4.1. For the carbon fibre the property depends on the fibre direction, namely being orthotropic parallel and transversal/orthogonal direction. Modification to the material assumptions are made separately within each section and are specified, if and when employed. Different sections' results are based on distinct assumptions related to both objectives and constraints implementation. Details are provided for each one of the sections, explaining conditions imposed.

Table 4.1. General Initial Material Properties

	Material	Density [kg/m^3]	Other properties
Shaft	S455 Stainless	7800	$\rho = 0.6\mu\Omega$m
Magnets	Recoma 33E	8300	$\rho = 0.9\mu\Omega$m
Sleeve	Carbon Fiber	1600	$\rho \approx 20\mu\Omega$m $\parallel$ direction $\rho \approx 1$mΩm $\perp$ direction
Winding	Cu	8960	Fill factor = 40%/60%
Cores	SiFe/CoFe	7490/8120	0.1/0.14mm

4.1 Initial comparison: fractional vs distributed winding

A comparison between solely Rim-Driven topology with fractional and distributed winding arrangement is performed, employing a non-linear constrained minimisation algorithm. The torque is constrained to be higher than the targeted design value. Conversely the current density, thus the armature current, is left free to vary in the design space accordingly; in order to achieve the power goal. Weight and losses are concurrent objectives to be minimized. Mathematically this is expressed in (4.1).

$$\begin{cases} \min\left(\text{Weight[kg]}\right) \\ \min\left(\text{Losses[kW]}\right) \\ \forall \quad J_{\text{rms}}[\text{A}/\text{mm}^2] \\ \forall \quad \tau \geq \tau_{\text{rated}}[\text{Nm}] \\ s_{\text{bi}}, h_{\text{so}}, w_{\text{tooth}}, h_{\text{wed}}, h_s, \alpha_{\text{PM}}, r_{\text{bi}}, t_{\text{PM}}, l_{\text{sleeve}}, w_{\text{so}}, l_{\text{stk}} \end{cases} \tag{4.1}$$

As previously extensively explained in Chapter 3 the sleeve thickness is assessed for every single individual tested throughout the population's evolution. Results for this first optimisation approach are summarized in Fig. 4.4, 4.5, 4.6 and 4.7. They represent the objective functions of Efficiency η and power density [kW/kg]; the DC and AC winding losses; the rotor eddy currents in and iron core losses; the mechanical losses due to the two windage components and the shear stress; respectively. All of them are presented against the weights of the final optimized generation. The comparison has been performed between an integral slot solution with 36 slots and fractional slot solution with 18 stator slots. In order to prove that the optimization was reliable, Fig. 4.3 delineates the evolution of the population fitness over the generations. This specific optimization is a single run for the fractional slot 18-12 combination. Sub-figure (a) portrays the whole Pareto's front motion throughout the process, whereas sub-figure (b) zooms over the last generations rendering a better view of a smooth convergence to the usual final shape of a Pareto's boundary for contrasting objectives. From blue to red the colormap presents the generation number, showing how the population progressively evolves according to the scheme characterized by Fig. 4.2.

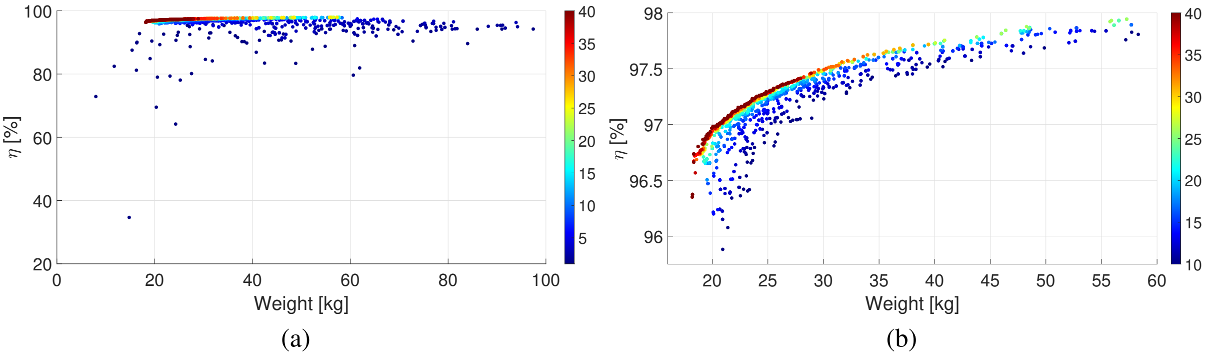

Fig. 4.3. Pareto fronts evolution over generations: Efficiency vs Weight (a), Zoom in (b)

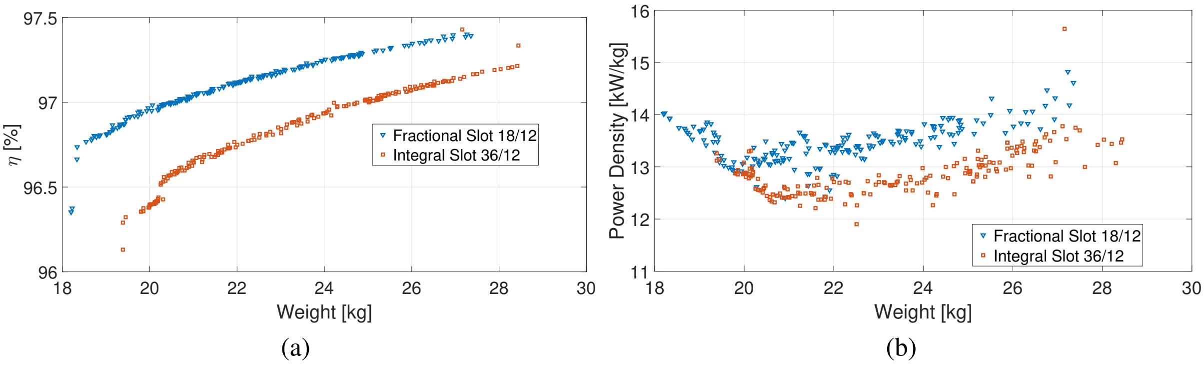

Fig. 4.4. Main Pareto Fronts: Efficiency vs Weight (a), Power Density (b)

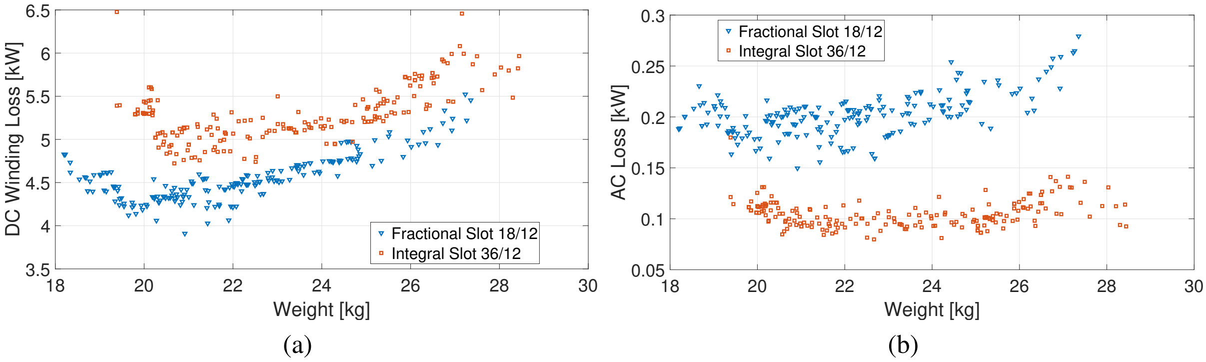

Fig. 4.5. DC (a) and AC (b) losses in the winding

Rather than giving an already refined answer for a final design we can clearly see that some expected behaviors occur. The optimization algorithm is working effectively representing similar patterns for different runs, converging to a neat Pareto front like in Fig. 4.3. The efficiency drops when the weight is reduced, as expected due to the antagonist role of the two fitness objectives. The fractional slot solution apparently provides a slightly higher efficiency (about 1% in surplus).

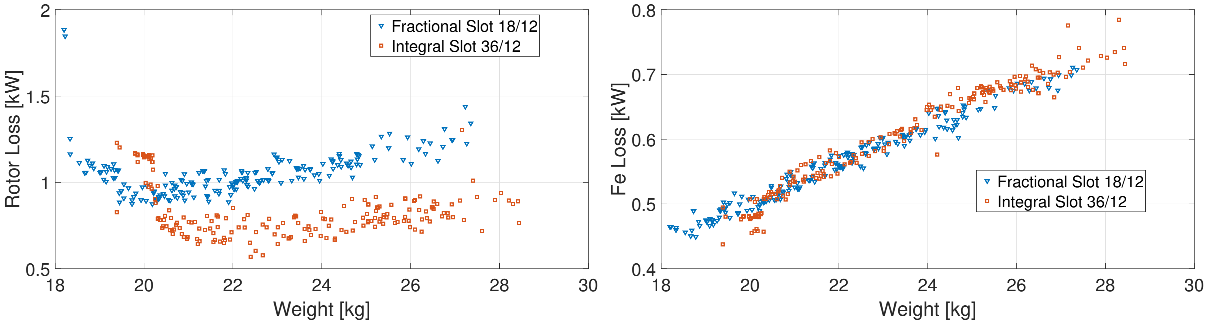

(a) (b)

Fig. 4.6. Rotor (a) and Overall Iron (b) losses

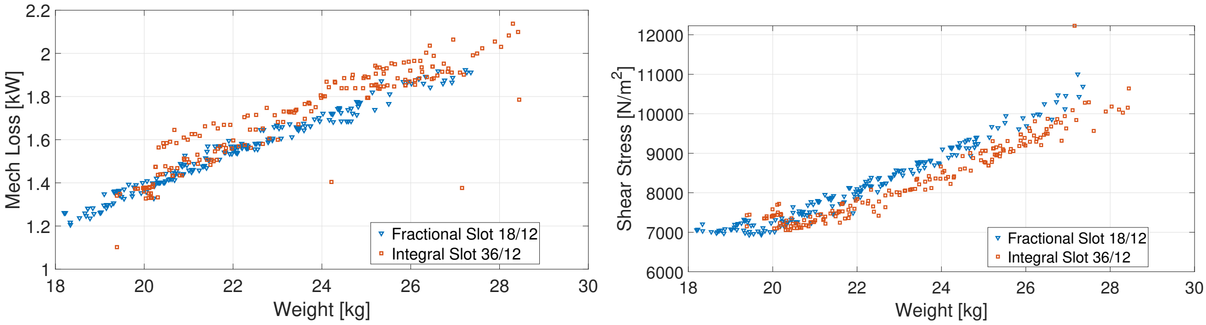

(a) (b)

Fig. 4.7. Mechanical Losses (a) and magnetic shear stress (b)

AC losses are higher for fractional slots since the slot opening is generally wider allowing more rotational and fringing flux to penetrate the slot. On the contrary, DC losses are higher for integral slot solutions, because for the same performance, the slots are smaller and therefore the DC resistance (which is inversely proportional to the winding cross section surface) is higher. Rotor losses are higher in fractional configurations due to higher asynchronous harmonic content. Iron losses do not vary much among winding patterns, and are significantly lower than with the winding losses. From this beginning the winding loss is predominant throughout the rest of the design. The DC loss variation is larger than the AC loss variation counterpart, determining no compensation in efficiency, given and observed the quasi-equivalent for the remaining loss split. This closes the circular reasoning on the slightly higher efficiency for fractional slots: given the limited amount of slots for a favourable electromagnetic fractional slot design, the winding and the end windings in particular are chunkier as they need to fit the same inner geometrical minimum diameter constraint. This was derived following the consideration given in Chapter 3, (3.26), and will be explicitly seen in further more refined optimisation in section 4.2.1.

Although this initial analysis yields a flavour for a rough design/performance, with the current density free to vary there is no consideration of thermal and insulation stresses on the machine. In the next sections the analysis and optimization are progressively refined, taking into account more detailed and precise features.

4.2 Comparison ensuring a constant power

In order to keep the comparison of the optimized machines consistent, current density is defined as a variable to minimize, rather than a fixed quantity. This section compares a broader spectrum of results considering a direct driven alternative. Halbach arrays are introduced as a means to increase the power density and reduce the machine cross section. Features of Direct Drive and Rim Drive are recalled before introducing in detail the peculiarities of Halbach arrays alongside the features of Fractional and Integral slot winding arrangements. The mathematical formulation of this minimization problem yields (4.2).

$$\begin{cases} \min\left(\text{Weight[kg]}\right) \\ \min\left(\text{Losses[kW]}\right) \\ \forall \quad J_{\text{rms}}[\text{A/mm}^2] \\ \text{such that} \quad \tau = \tau_{\text{rated}}[\text{Nm}] \end{cases} \tag{4.2}$$

As both angular rotational speed and power are known, the current to deliver the equivalent average torque is found. The mean torque, at MTPA (Maximum Torque per Amp) condition, for a surface permanent magnet motor is well known (4.3), which does not involve any reluctance torque component:

$$\tau = \frac{3}{2} p \lambda_m i_q \tag{4.3}$$

The current needed is computed, by means of a quick iterative procedure, from the flux linked with the PMs. This is determined in a few seconds, as the flux information at steady state condition only requires modelling one sixth of the electrical cycle. This assumes that the dq synchronous reference frame relies on a theoretically ideal sinusoidal time distribution of the voltages and current inputs. The remaining flux waveform can be reconstructed assuming a balanced three-phase system. Due to saturation the actual current angle for Maximum Torque Per Amp can be achieved for current angles slightly larger than $\pi/2$ (a small demagnetizing component of i). The electromagnetic losses consist of eddy current losses in the rotor conductive parts, DC and AC current losses in the stator winding, and iron losses in the lamination parts. Rotor eddy currents and iron losses are directly computed from the time-stepping simulation process, averaging them out over a period. Winding losses are computed by means of the already detailed post-processing technique mentioned in section 3.5.2. To minimize the AC losses, a Litz-Wire strand is assumed. According to the strand diameter, alongside with the slot fill factor assumption, a wire positioning in slot is assumed by means of the procedure presented in [35]. This employs a hexagonal tessellation which in general provides the optimal filling of a set of round conductors. Fig. 4.8 helps to convey graphically this concept for a single slot filled with circular strands. A very fine mesh in the slot is then utilized for employing the spatial average of the time-averaged-squared-field-derivative modelling presented in [30], where the magnetic field is interpolated at the strand centre.

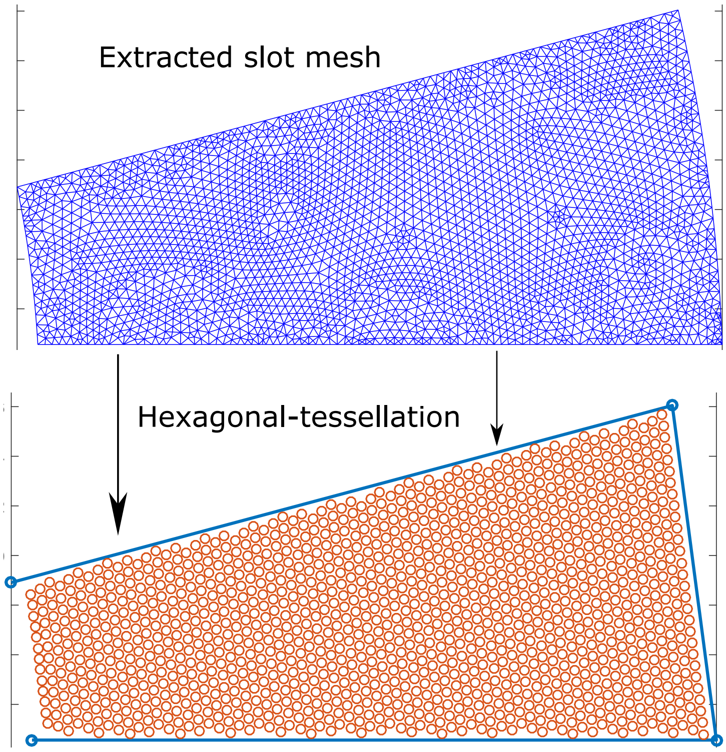

Fig. 4.8. Post-Processing (mesh extraction and slot tessellation) example for a slot.

At this stage, no time-harmonic due to power electronic switching is considered, i.e. the electromagnetic modeling has a perfectly sinusoidal current-source. A further, significant, and possibly undermining hypothesis, is the worst case scenario assumption of 200°C stator winding temperature operation (continuous duty). This has a strong effect on the DC losses. Finally, to achieve a trade-off between the intrinsic three dimensional feature of the rotor eddy currents and the 2D high computation speed, a rescaling of permanent magnets conductivity is applied to give a representable value of magnet loss. This is done following the model proposed in [85] and employed throughout [96], [97], [98], [99], [100], according to the geometrical dimensions dictated by the magnet segmentation assumptions.

4.2.1 Shaft Driven vs Rim Driven

The conventional topology that can be employed is a shaft drive (Fig. 4.9 (b)): the electrical machine drives the fan-shaft from the rear. This must comply with the aerodynamic requirements of the fan and duct overall system. Generally, the vast majority of work performed by the fan blades occurs in a cross sectional span within 50 to 85% of the fan diameter. For this reason the optimization process have been constrained to respect this feature, i.e. machine external diameter (at the stator bore) must not exceed half the fan diameter, as specified in Table 4.2.

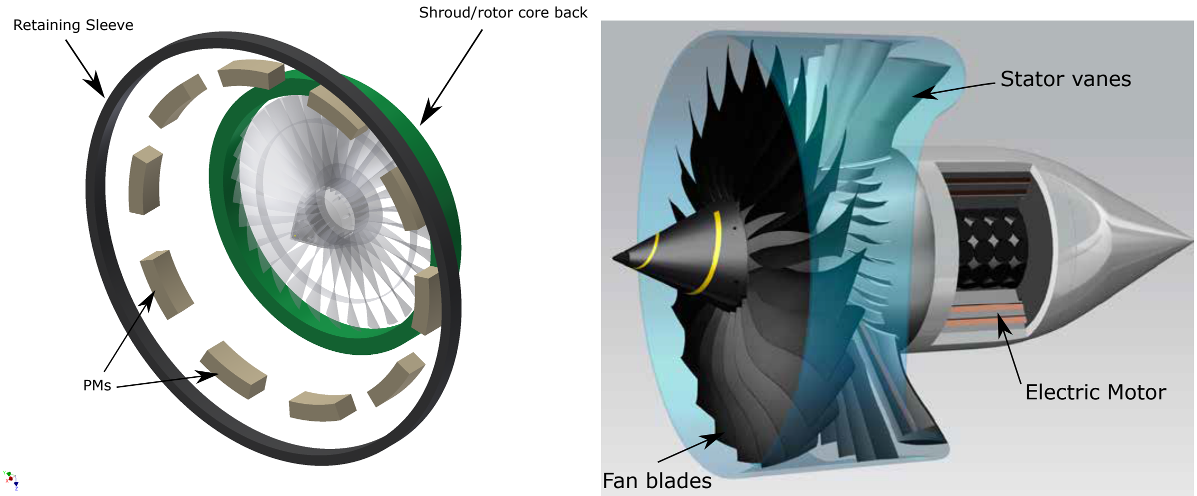

(a) (b)

Fig. 4.9. Rim Driven (a) vs Shaft Driven (b)

Table 4.2. Specifications for comparison

Ext./Int. diameter	150 (interior rotor)/300 mm (Rim Driven)
Rated speed	14000 rpm
Power	250 kW
Cooling	Preferably forced air
Operation	Constant speed at cruise

Rim-Driven Fractional Slot Winding

Fractional-slot windings usually provide a better exploitation of copper filling the slots. This is due to compressing the coils and wrapping them around teeth. In this analysis, the fill factor for this circuit scheme is considered to be: $k_{\text{fill}} = 0.6$. Another major role is played by the end-windings: wrapped teeth/concentrated winding configurations allow a considerable reduction of end-winding length, equivalently diminishing weight and volume of the non-active electric circuit part. The only combination considered for this topology consists of 3 slots per pole pair, as this is the well recognized most efficient solution in terms of rotor losses. This is the only case in which there is no sub-harmonic, and first higher order harmonic is double the pole count of the synchronous fundamental one. Yet, with this arrangement, the rotor losses are still large. It is noticed that, although utilizing a costly and spread segmentation of PMs, the losses are not sufficiently reduced, due to eddy currents in the solid rotor-back/fan-shroud. The only way to reduce such losses is to employ a lamination bulk around the solid steel ring which closes the blade tips. Due to segmentation, PMs do not play a significant role in shielding the rotor flux, if this were not the case it would increase the losses in the magnet segments themselves. Therefore, the penetrating asynchronous flux harmonics are channelled along the highly permeable laminated core, to prevent excessive eddy currents from being induced in the solid steel.

Rim-Driven Integral Slot-Distributed Winding

Integral-slot/distributed winding solutions offer a much lower space harmonic content. Additionally, higher order harmonic impact can be reduced by short pitching. The 5^{th} and 7^{th} space MMF harmonics will be dramatically reduced, causing the rotor losses to be almost negligible. Recognized disadvantages are the considerably longer end-windings and reduced fill factor (compared to the fractional slot winding): the copper is assumed to be $k_{\text{fill}} = 0.4$.

Fig. 4.10 shows the electrical machine topologies considered. The external sketch compares side by side the cross section layouts of a Rim-Driven design, whereas the innermost one incorporates the direct driven counterpart. This has been centered at an intuitive position to resemble the actual geometrical limit, dictated by the Outer Boundary which is defined to be 50% of the turbine

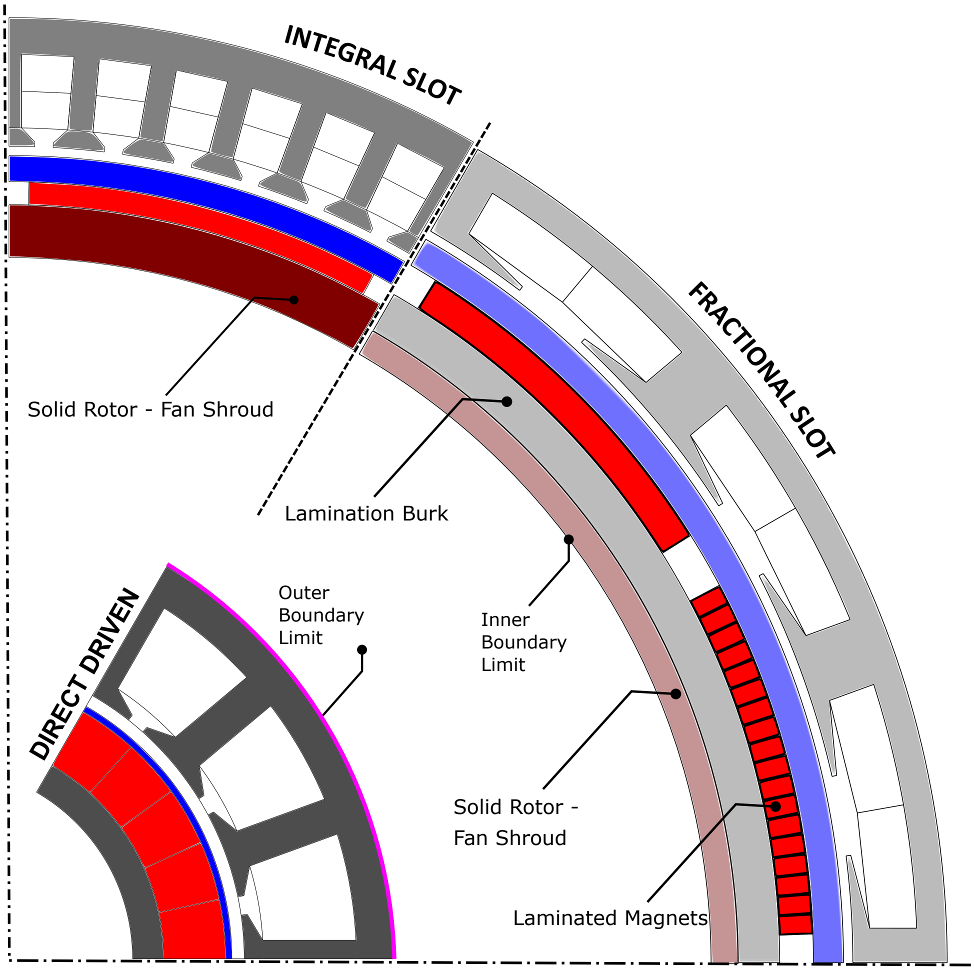

Fig. 4.10. Cross section comparison fractional-vs-integral.

blade radius [1]. Further modeling assumptions are hereby briefly summarized: no retaining force from the interior fan/blades structure is considered, posing the design in a worst case scenario and increasing the safety margins. Tab. 4.3 succinctly lists properties assumptions.

Table 4.3. Rotor Parts Mechanical Properties

Material	Yield Stress	Young Modulus	Therm. Coeff.
Shaft	600 MPa	200 GPa	12e-6 1/K
Magnets	140 MPa	120 GPa	8e-6 1/K
Sleeve	1600 MPa	186 GPa	-1e-6 1/K

---

[1] The figure is representative of a general SPM machine, therefore, when considering Halbach arrays in the Rim-Driven topology there is no void pocket between a pole and another, but all magnet segments/stages are adjacent circumferentially

Further assumptions are the rotor operating temperatures, fixed at 100° C. The safety factor for all the components is 1.2. For the rotor assembly employed in the fractional slot rim-driven configuration, an interference of 0.1 [mm] is assumed between lamination and solid steel shroud. Finally, the sleeve is sized to permit 20% over-speed operation.

In order to keep the comparison of optimized machines consistent, no current density is imposed at the beginning of any structural-geometrical variation. Instead, since both angular rotational speed and power are known, the winding current to deliver the equivalent average torque is found. The mean torque, at MTPA condition is the target to be achieved.

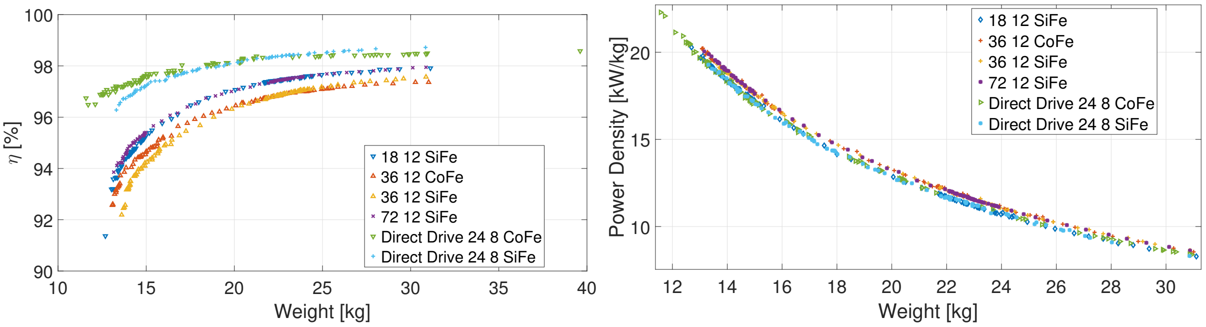

(a) (b)

Fig. 4.11. Main Pareto Fronts: Efficiency vs Weight (a), Power Density (b)

Results for this optimisation approach are summarized in Fig. 4.11, 4.12, 4.13, 4.14 for the main objective functions of efficiency and power density; the loss split between winding, rotor and core; the mechanical losses alongside the current density necessary for keeping the rated torque; and further details concerning electric loading, magnetic shear stress in the airgap, the mass of the rotor along with the axial length variation. Legends differentiate in all plots the combination of slots and poles, addressing fractional and integral configurations as well as the core material. When the graph refers to the direct drive, this is specified. It is otherwise assumed that all the other graphs refer to the rim-drive. The power density refers to only active parts of the motor. The stresses in the different components of an optimized solution can be appreciated in Fig. 4.15. It is noticeable as the stress concentration accumulates at the edges of the PMs touching the inner sleeve surface; sub-figure 4.15 (a). Overall the sleeve inner diameter is subject to tangential stress. Given the fact that the magnet segments form a continuum medium circumferentially, the concentrated compression on the sleeve at the magnet outer corners is almost negligible from simulation and are not expected to be harmful in the real assembly. Sub-figure 4.15

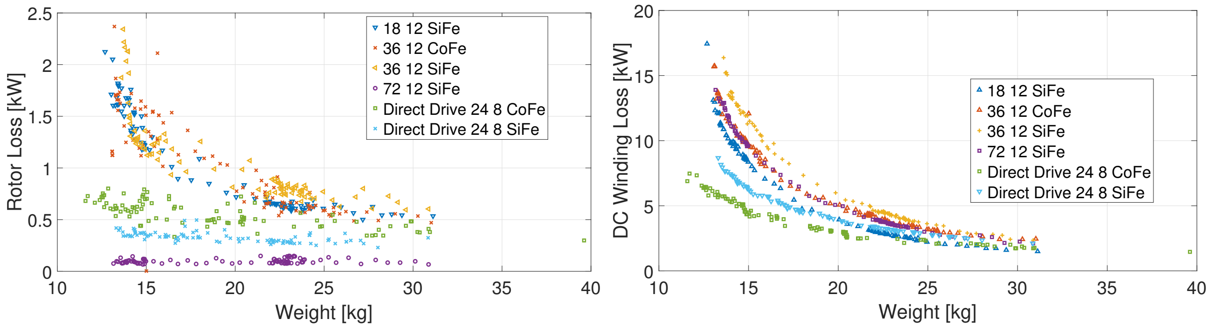

(a) *Rotor Loss*

(b) *DC winding loss*

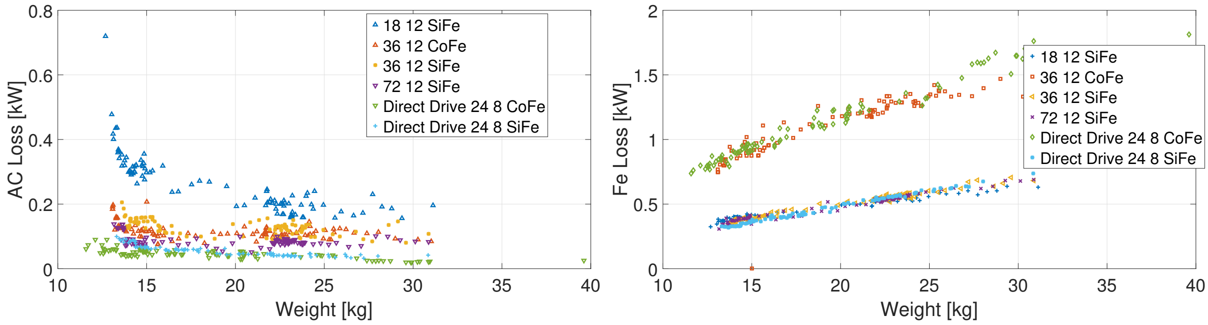

(c) *AC winding loss*

(d) *Iron Loss*

Fig. 4.12. Losses Split Share

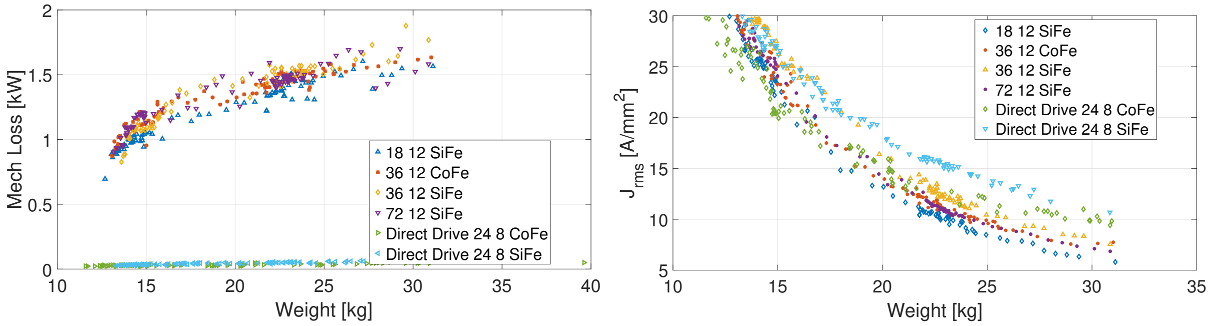

(a)

(b)

Fig. 4.13. Mechanical losses (a) and current density (b)

(b) emphasizes the most important aspect for torque transmission assurance, which is the compression at the inner and outer magnet boundaries. This ensures that both shaft and sleeve are effectively trapping the magnets, ensuring no lift-off. Finally, sub-figure 4.15 (c) highlights the fact that the outer shaft is in tension, and also how the inner radius is subject to compression. This signifies that the pre-stress given by the sleeve at zero speed is not expected to be entirely released during operation.

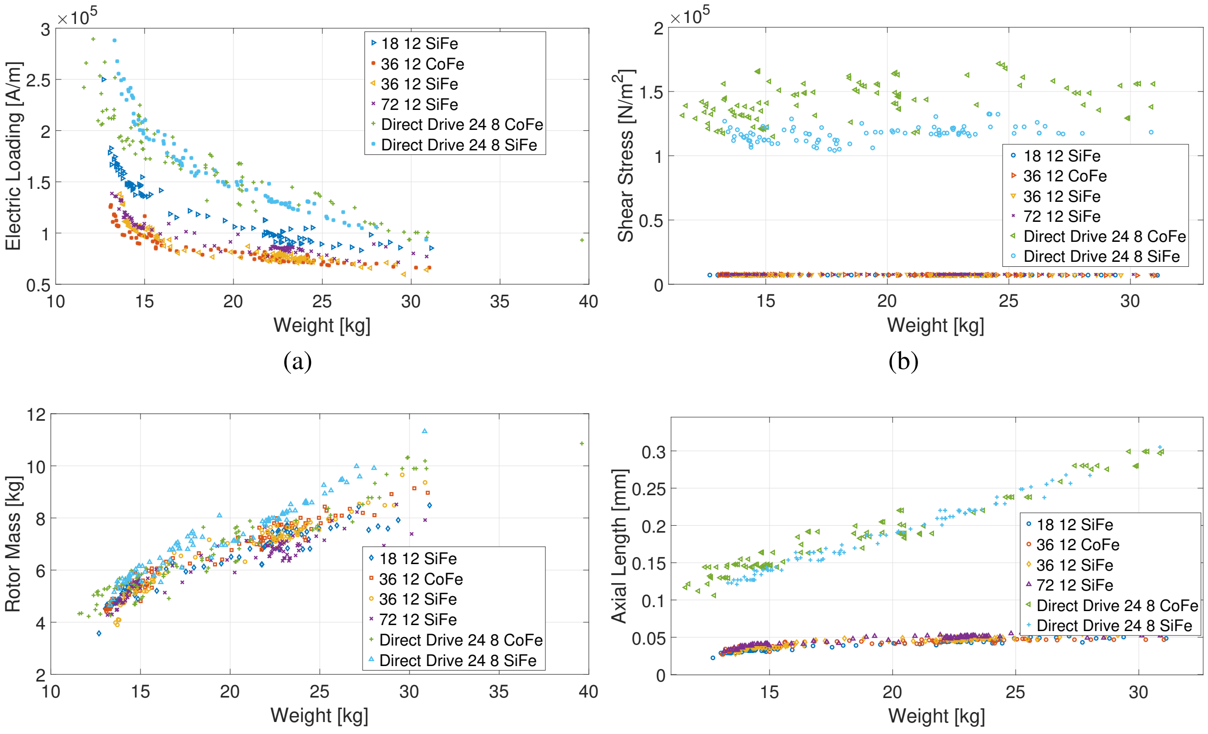

(a)

(b)

(c)

(d)

Fig. 4.14. Electrical Loading (a), Shear Stress (b), Rot. Mass (c), Axial Length (d)

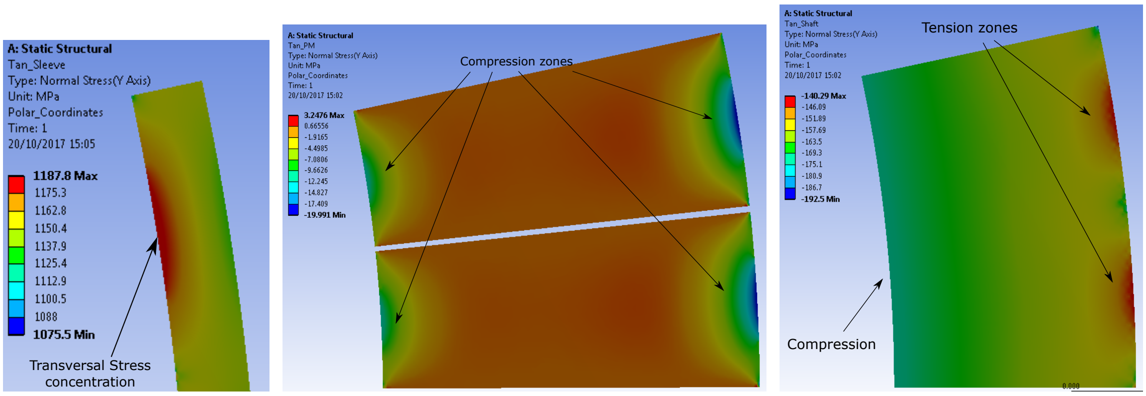

(a) *Tension on sleeve*

(b) *Tension on Halbach segments*

(c) *Tension on Shaft*

Fig. 4.15. Tension on rotor components

An interesting observation is drawn in Fig. 4.16. The filled area 2D plot shows the mass split for the machine active part components for all the individuals of the last generation derived at the end of the Multi Objective Optimization (all the individuals of the last Pareto Front). Subfigures (a), (b) and (c) feature the Rim-Drive solution (12-poles) for different combinations of slots and poles. What is remarkable is that, the Fractional slot solution (a) does not over-perform in

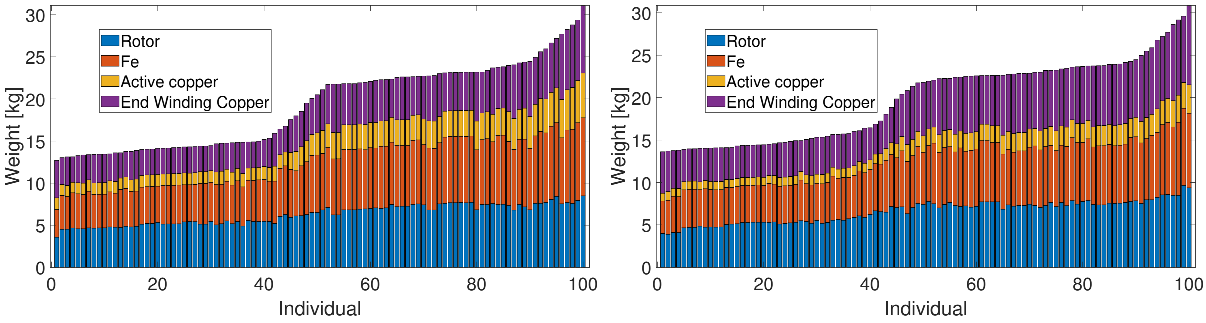

(a) *18-12 SiFe mass split* (b) *36-12 SiFe mass split*

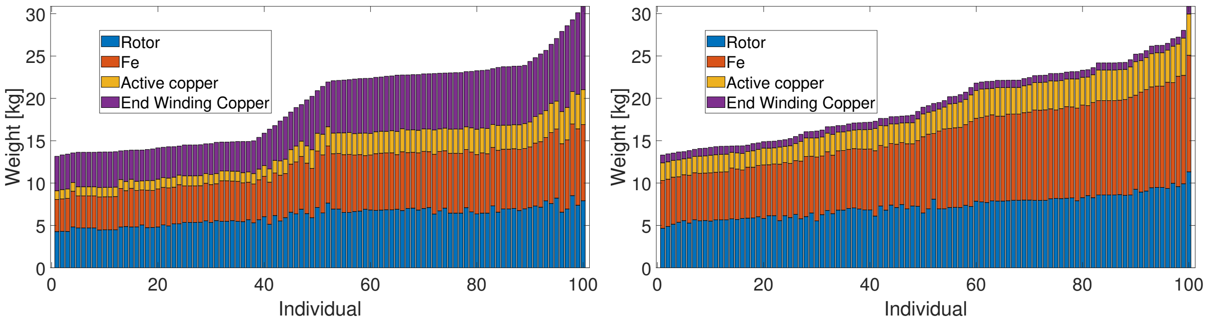

(c) *72-12 SiFe mass split* (d) *24-8 SiFe mass split*

Fig. 4.16. Mass Split

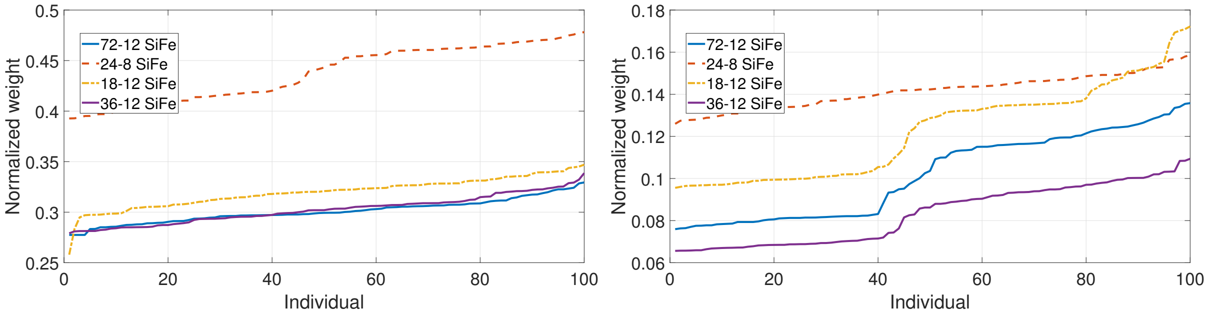

(a) *Core mass split* (b) *Active Cu mass split*

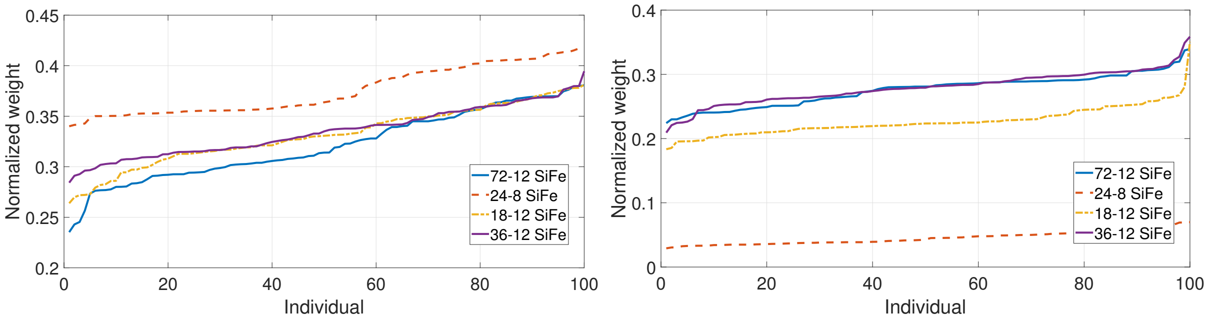

(c) *Rotor mass split* (d) *End Winding mass split*

Fig. 4.17. Normalized mass split

terms of winding mass as well as overall mass. In general the fractional arrangement allows for a smaller end-winding length, therefore most generally lower end-winding associated mass. Unfortunately, given the limited amount of slot combinations, and the intrinsic small number of slots given the number of poles for the most efficient ones, confines the slots in a domain that possess an elevated conductor mass. Fig. 4.17 investigates the normalized weight, i.e. the ratio between the different sub-assembly parts with respect to the total weight.

4.2.2 Discussion and partial conclusions

In summary, this last section has compared an optimized structural design between a direct drive machine coupled with the load through a shaft, and a rim driven aerospace propeller. The latter is a configuration which unlocks the boundary of integration among components, as it effectively combines the motor and load together. The conclusions drawn here build up on the ones delineated by the initial comparison solely focused on fractional vs integral for rim-driven only. Under certain assumptions, as expressed in (4.2)), different designs have been compared broadening the investigation span to different core lamination material as well as different poles and slot combinations. Overall this has shown how a rim-drive configuration could represent an alternative to a usual direct-drive in term of power density levels. Based on Fig. 4.11, 4.12, 4.13, 4.14, the following observations can be made.

Fig. 4.12 (d) clearly highlights how iron loss increase linearly with weight, but more importantly how the losses for cobalt iron are twice as much those for silicon iron, irrespectively of the configuration chosen, either direct or rim driven. Therefore, using CoFe (Hyperco 50A 0.006) [101], instead of very low loss SiFe [102] laminations does not yield any significant advantage. It can be concluded that the benefit of increased saturation point for cobalt iron does not allow to outperform the higher steel alloy density and losses (without considering the additionally considerably higher cost).

Comparing all sub-figures in Fig. 4.12 the loss share is for all designs dominated by DC ohmic losses. For any level of weight, i.e. any cross sectional area, the DC loss value is always greater than all other single loss components. Sub figure Fig. 4.12 (b) exemplifies this. A direct drive configuration in this case provides a slightly bigger advantage especially for lighter machines.

As far as the rim driven configuration is concerned, the fractional slot arrangement provides an almost not noticeable advantage being the hyperbolic decaying trend with the weight increase slightly lower in value than the integral slot arrangement. On the other hand Fig. 4.12 (c) clearly witnesses the much higher presence of unwanted AC losses in fractional slot windings: these are up to four times as much those for a direct drive or short pitched wound rim drive arrangements. Fig. 4.12 (a) depicts the rotor losses behavior, witnessing how substantially different is the loss distribution dependency based on both machine topology and winding arrangement. This is represented by the lowest purple values for a 72-12 combination, which reduces at maximum the asynchronous harmonic due to a single slot shortening pitch. Conversely, fractional windings produce large rotor losses which makes them not viable for this application, this is visible especially for high values of the 18-12 SiFe combination. Relatively high are also the integral slot winding that are not short pitched, i.e. the 36-12 combination. Direct drive rotor losses are more than twice as much those of the best performing 72-12 SiFe rim driven design. Overall we can on this point conclude that, although distributed arrangements, especially for rim driven topologies, have longer end-windings and therefore greater DC winding loss, they exhibit fewer spatial harmonics and low rotor eddy current losses.

Windage losses, Fig. 4.13, in the rim drive are at least, one order of magnitude greater with respect to those in direct drives. This is simply related to a much higher tip velocity. As expected there is not any substantial variance with respect to different winding arrangements.

The rim driven designs operate with much lower electric loadings as observed in Fig. 4.14 (a) and are consequently more likely to operate at lower temperature. Direct drives are the worst performing in this case, reaching peaks of almost 300 [kA/m] for the lightest designs in the final Pareto front. This is because the cross sectional area is considerably smaller than the rim driven counterpart, significantly limiting the surface area along which the electric armature operates, hence increasing the load the machine needs to sustain electrically. The 18-12 fractional slot comes as second worst performing. This is due to the limited number of slots, that although chunkier will still need to allow a higher current flow, for a similar stator inner bore radius, thus yielding electrical load. The lowest value is given by all rim driven integral slot arrangements, which for all weights values on average is limited to 100 [kA/m]. This is due to the intrinsic well distributed load along the stator bore due to the higher number of slots per pole, and the large stator bore radius value due to the rim drive topology. In light of these considerations it is anticipated to be a measure for discerning the best among possible optimized designs.

To explain Fig. 4.14 (b) very high radial stresses in the rim driven motor force the utilisation of a thicker retaining sleeve. In turns this reduces the magnetic loading, and so the machine produces a much lower electromagnetic shear stress: the effective magnetic air-gap is significantly increased dropping the value of the flux density, decreasing in turn the shear stress as per definitions given in Chapter 2.

Fig 4.14 (c) and (d) highlight the aspect ratio for different machine topologies. Because of the much larger cross sectional area constraints imposed onto the rim drive, axial stack lengths are very much reduced, whereas direct drives are limited in external diameter, thus forcing the motor stack to lengthen axially.

Fig. 4.11 (a) at first glance presents a more efficient choice dictated by the direct drives, followed by the less efficient fractional slot 18-12 and the integral slot 72-12 solutions, these in turn leaving slightly behind the integral slot rim drive that are not short pitched. At the same time Fig. 4.11 (b) yields almost equivalent values in terms of power density, not advocating for an evident best topology/arrangement. Nonetheless, especially as far as the electric loading considerations previously addressed, the result of the investigation thus far conducted is that the Rim-Driven topology selection as preferred, combined with an integral slot winding arrangement. This is because of limited rotor loss, AC winding loss, but most importantly the electric loading estimate, which relates to the cooling effectiveness of a machine: direct drive designs may require forced cooling, whilst the rim driven designs may not.

Based on the previous points of discussion it is concluded that:

- the choice worthy to be taken forward is the optimisation solely of a Rim-Driven configuration
- the integral slot winding arrangement is preferred to a fractional slot counterpart and it will be the only one considered and implemented

4.3 Rim-Driven Comparison with Voltage Constraint

Thus far, no assumption or constraint has been made on number of turns or rated machine voltage. Progressively the analysis has focused to increase efficiency whilst reducing mass taking into account first an unconstrained torque, voltage, power, and current density level. In the last section the sole freedom was left for current density and voltage. As stressed in the last bullet point of the previous section, the direct drive option is inferior and so it was decided to continue the analysis for Rim-Drive solutions only. In this section a voltage constraint has been included to the drive requirement: the DC-link voltage is bounded at 600 Volts. For all previous designs it has been observed that employing a single turn per coil for integral slot and two turns per coil for fractional slot designs was already yielding voltages in the constraint range. Therefore a single turn is the bounded integer value given for the number of turns when defining coils in the circuit. Due to the fact that from now on there is a single topology, reducing the number of runs and candidates, the optimization can take more computational burden to account more precisely for the circuital features. This last aspect is better taken into account by phasor quantities. Fig. **??** depicts the standard phasor diagram for a Permanent Magnet Machine. In the analyses conducted the diagram is made simpler as the only current injected flows along the q axis, as an isotropic magnetic circuit is assumed, as is usually the case for Surface Permanent Magnet Motors. The DC-link limitation has been dealt with using a frozen-permeability study for every individual simulation. These are based on [103] and [104]. Such an approach, although more computationally intense as a surplus for every function evaluation, gives a more accurate estimate of the different voltage components (see Fig. 4.18) due to armature and magnet flux. The frozen permeability takes into account the iron non linearity in this estimation, allowing a superposition effect which is otherwise not possible by simply adding up the voltage due to no load operation along with a completely demagnetized motor fed with solely armature current. Some succinct points are noteworthy:

- as stated in introducing this section from all the previous optimization runs it has been recognized that the number of conductor per phase per slot is either 1 or 2. This is mainly due to the very high rotational speed.
- Varying the voltage level is one of the criteria utilized in a preliminary optimization.

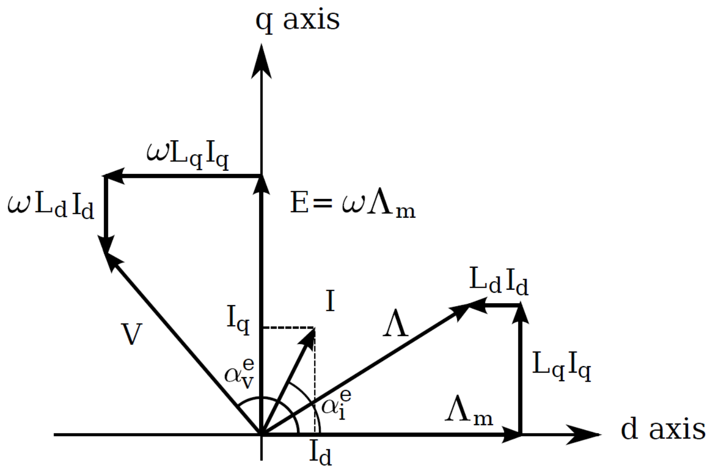

Fig. 4.18. Phasor Diagram of a Permanent Magnet AC synchronous motor.

- Recoma 30 Samarium Cobalt material for the PM has been investigated against the initial Recoma 33. This has been suggested by the manufactures, as a trade-off between remanence field, performance and cost.
- different configurations have been looked at in terms of slot shape and magnet arrangement. Namely, parallel slots against parallel teeth, as well as Halbach array versus usual unidirectional magnetized magnets, have been investigated.
- a current density constraint has been imposed: a dedicated subsection is present for results and consideration of this choice.

Some additional remarks:

1. The time-stepping FEA does not include rotor eddy currents as the integral slot choice creating low frequency space asynchronous harmonics. Rotor losses are assumed to be small, creating no damping effects on the torque. This makes the optimisation almost twice as fast as the one with eddy currents included. Full losses will be included in the final design.
2. AC losses in windings are neglected. This is deemed to be justifiable from previous optimization observations concerning the comparison fractional-vs-integral slot solutions. Integral slot designs have lower eddy currents loss. This intrinsically benefits the optimisation, reducing the convergence time.

3. Legends for all the results presented in the following refer to the core material: either to CoFe (Cobalt Iron) or SiFe (Silicon Iron), number of slots and poles. Voltage constrained solutions are specified as # $\mathrm{V_{DC}}$; whenever Par is mentioned this relates to a parallel slot solution, unless otherwise stated all the slot shapes are trapezoidal. This is the case already for Fig. 4.19. If an optimisation is unconstrained this is specified. This means that the Voltage constraint is not enforced. If the number 1 and 2 appear after a material specification this is to present a multiple optimization run that is reported in order to robustly assess whether the algorithm converges properly. This happens in Fig. 4.20 and 4.21.

4. In subsections 4.3.1 and 4.3.2 the optimization formally is

$$\begin{cases} \min\big(\mathrm{Weight[kg]}\big) \\ \min\big(\mathrm{Losses[kW]}\big) \\ \forall \quad J[\mathrm{A/mm^2}] \\ \text{such that} \quad \tau = \tau_{\text{rated}}[\mathrm{Nm}] \\ \forall \quad V_{\mathrm{DC}} \leq 600[\mathrm{V}] \end{cases} \tag{4.4}$$

4.3.1 Recoma33 SmCo, free J variation

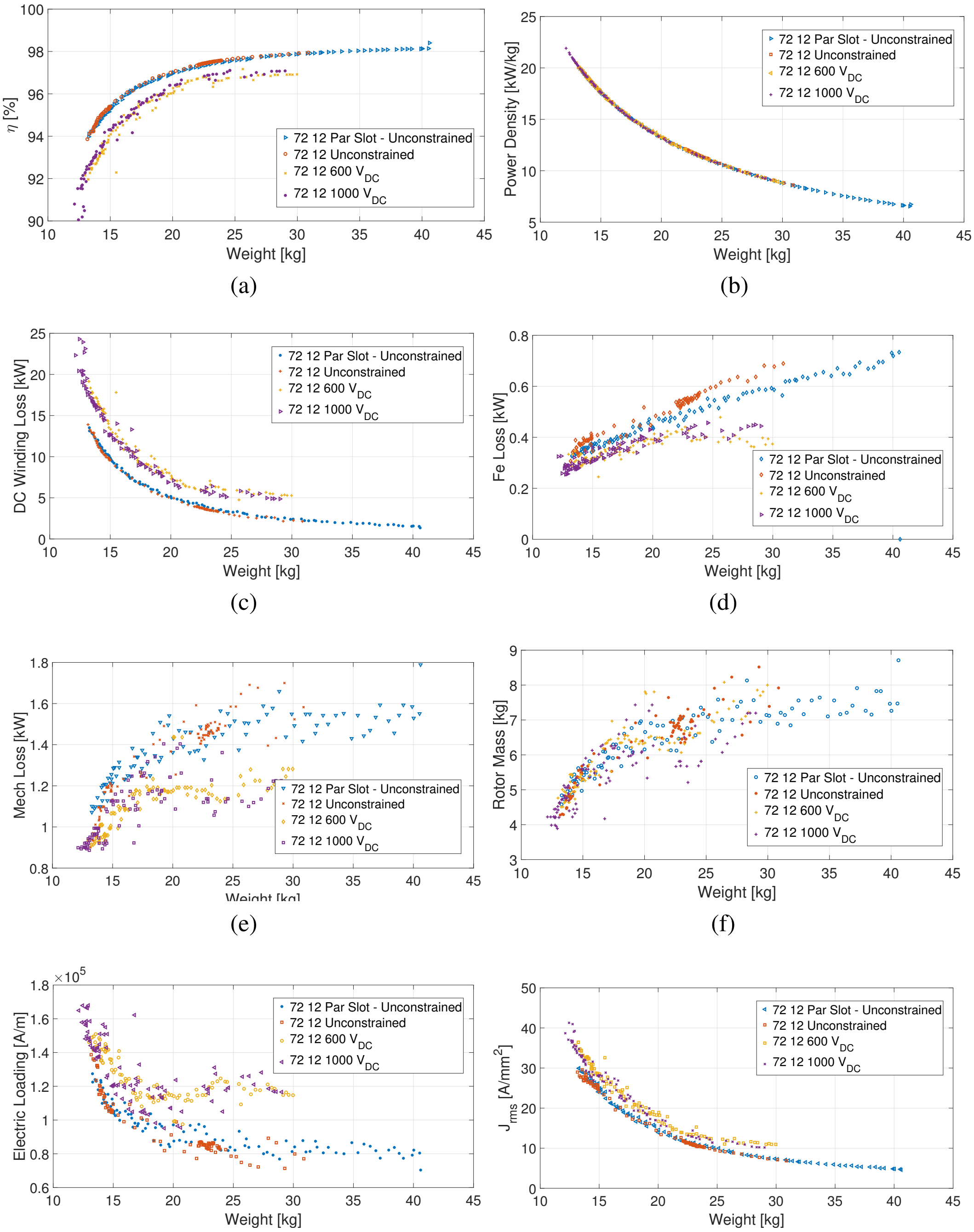

(a) (b) (c) (d) (e) (f) (g) (h)

Fig. 4.19. Efficiency vs Weight (a), Power Density (b), DC loss (c), Fe loss (d), Mech. loss (e), Rotor mass (f), El.Loading (g), J (h)

4.3.2 Recoma33 vs Recoma30 SmCo, free J variation

In this section different grades of SmCo PM material are compared. Moreover, the carbon fibre assumption in this case is advised by the manufacture. Thus far, every mechanical calculation was performed assuming values taken from pre-existing academic literature [27]. In this deeper detailed optimisation the carbon fibre composite chosen comes from the manufacturers' values, named as IM10 [2].

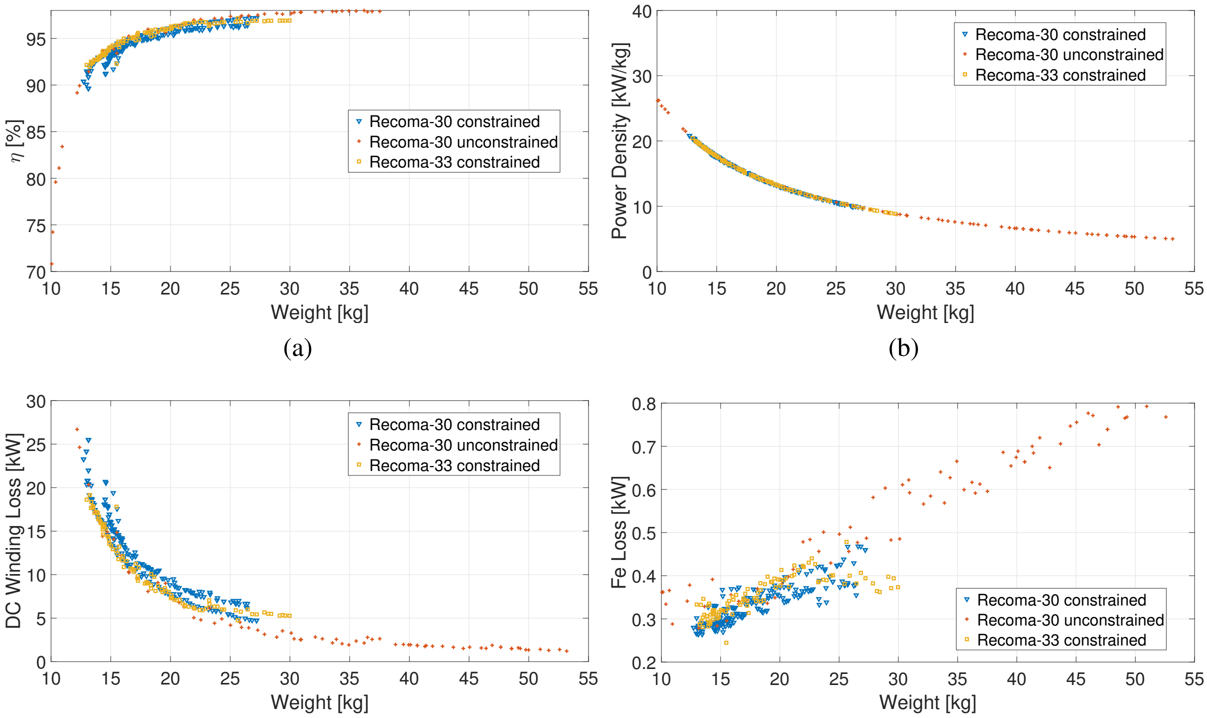

(a) (b) (c) (d)

Fig. 4.20. Efficiency vs Weight (a), Power Density (b), DC loss (c), Fe loss (d)

---

[2] Composite features consist in: UTS (ultimate tensile strength) of 2500 MPa; Young modulus of 190 GPa. It can be used only under 180 degrees celsius.

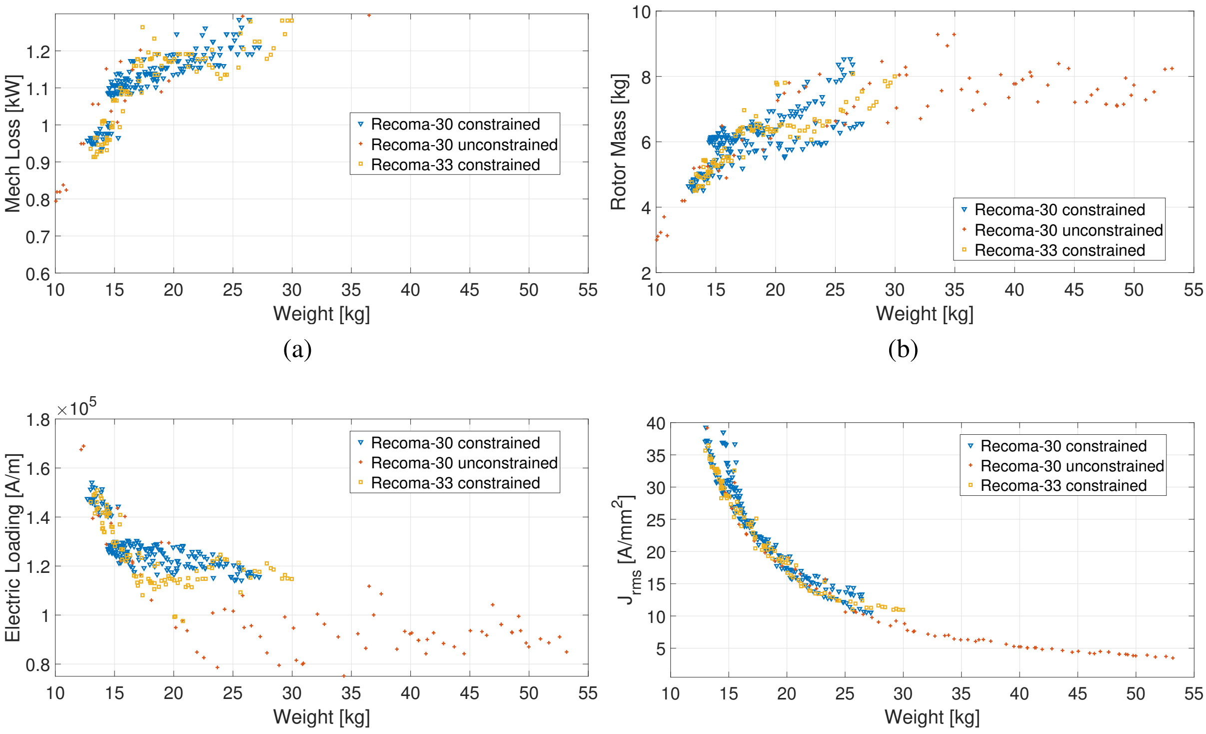

(a) (b)

(c) (d)

Fig. 4.21. Mechanical loss (a), Rotor mass (b), El.Loading (c), J (d)

4.3.3 Constrained current density comparison

Thus far, the current density has been left free to vary in the envelope space. This does not really set any boundary in terms of thermal utilization. There is a necessity to take into account this aspect. Thermal modelling is only approximate because there is little conditions. The current density is then fixed. Torque is adjusted to the target value in a pre-static simulation, for each simulated individual, deriving the stack length a posteriori in the evaluation stage of Fig. 4.2. All the antecedent explored designs considered a standard trapezoidal slot. Nonetheless, considering parallel slot walls in the stator lamination can offer the benefit of fitting a higher fill factor formed winding. A counterpart design with a parallel slot will then feature a fill factor $k_{\text{fill}} = 0.45$. Voltage and material constraints have been kept the same as the previous section analysis. Nonetheless, a new approach for defining the objective function has been implied: the fitness function tries to minimize the electric loading and mass. It has been decided that greater importance is given to the rotor weight in terms of mass. The mass objective disguises under the following notation:

$$M = \frac{\alpha_S m_S + \alpha_R m_R}{\alpha_S + \alpha_R} \tag{4.5}$$

Weights for the two masses are chosen to be: $\alpha_S = 1$ and $\alpha_R = 2$. Hence, implying a penalty on the rotor mass, with respect to the stator. Justifications and reasons leading to choosing (4.5), are as follows:

- as the greatest component of losses is the DC winding loss, minimizing the electric loading (as defined in Chapt. 3 in (3.1)) with a fixed current density is equivalent to minimize the volumetric copper losses. This can be seen by considering $K_s J \propto I_{\mathrm{rms}}^2/m^3$. It is the main aim of the optimization, as thermal stress is understood to be key for power density
- providing a higher penalty for the rotor mass minimization will result in a lighter rotor structure. This will relieve both shaft design constraints and bearing load issues
- a shorter rotor will entail a more robust rotor-dynamic behaviour
- a lighter rotor design is also preferable in terms of fan design, for integrity preservation and inertial purposes

$$\begin{cases} \min\big(\text{Weight}[\text{kg}]\big) \\ \min\big(\text{Losses}[\text{kW}]\big) \\ \text{such that} \quad J = 12[\text{A}/\text{mm}^2] \\ \text{such that} \quad \tau = \tau_{\text{rated}}[\text{Nm}] \\ \forall \quad V_{\text{DC}} \leq 600[\text{V}] \end{cases} \tag{4.6}$$

Since the current density has been fixed in order to freeze the design, along with the electric loading, it sets some guidance on the thermal behaviour of the motor. Gaining insight from other academic publications as [64], looking at similar machine specifications, provides a range close to 13 $[\text{A}/\text{mm}^2]$. This is a value usually achieved with water cooling. However, air cooling might be sustained as a thermal management solution, given the extremely low temperature and high velocity of the air, at altitude. Although, the better cooling is expected at lower temperatures, being the coolant a gas, the positive benefits may partially be offset by a considerable drop in temperature. This aspect is worthy to consider in light of the impossibility to test at this stage of research the equipment at those conditions, and it is outside the scope of this work. Therefore, a more cautious choice of 12 [A/mm^2] has been made as per (4.6). Considering that usual industrial induction motors are designed for 6 [A/mm^2] in natural air cooling (not forced) conditions, doubling this number sets an even and neat value as a target.

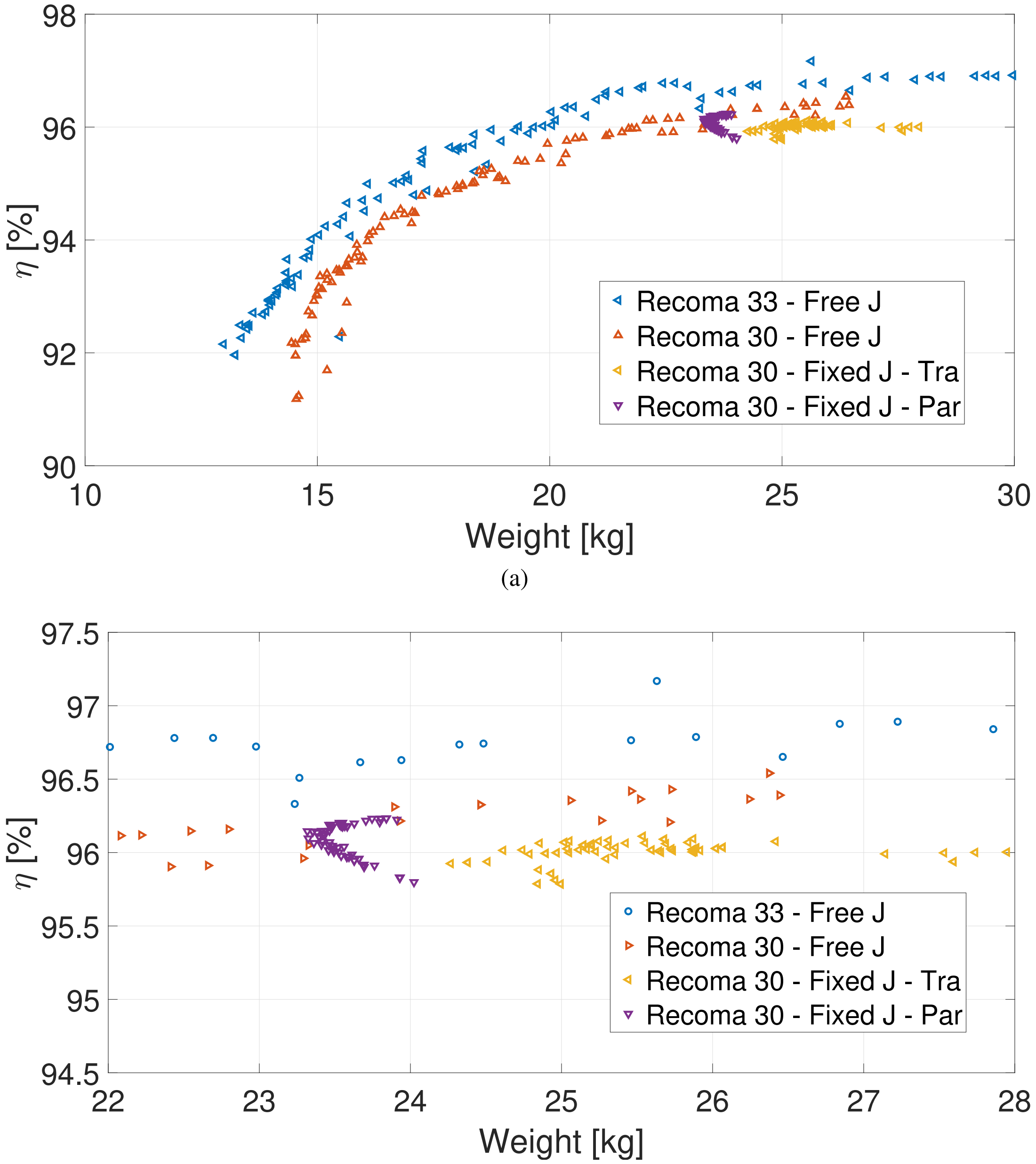

(a)

(b)

Fig. 4.22. Efficiency vs Weight (a), Efficiency Zoom (b)

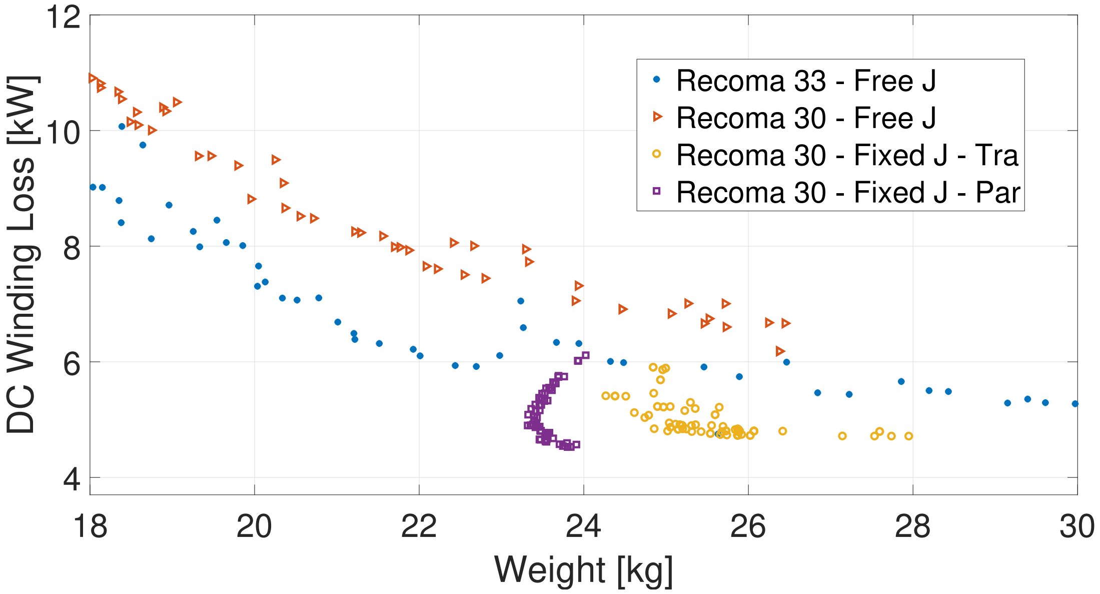

(a)

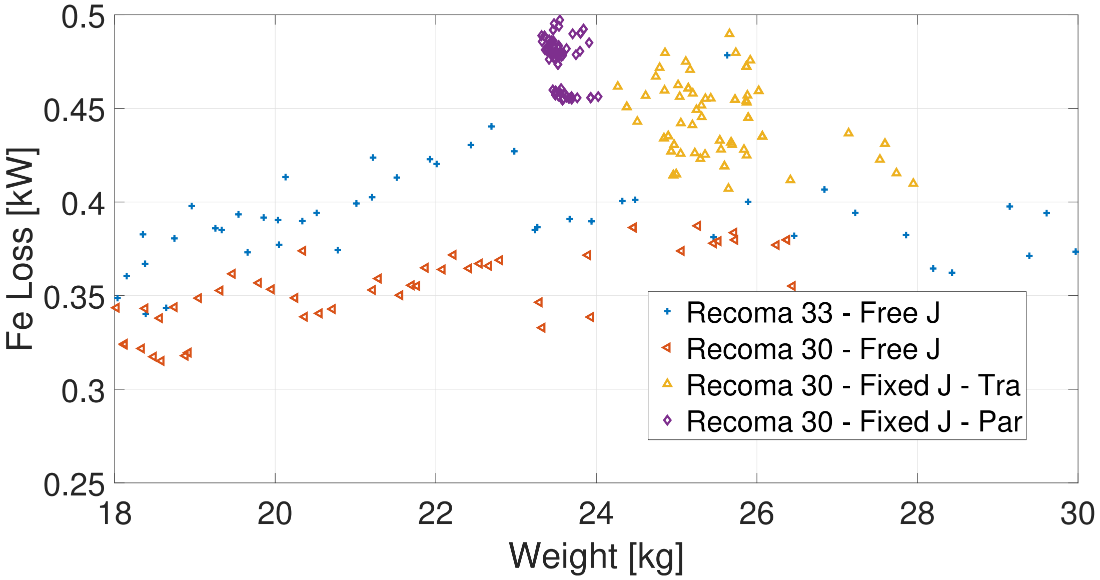

(b)

Fig. 4.23. DC loss (a), Fe loss (b) as a function of mass

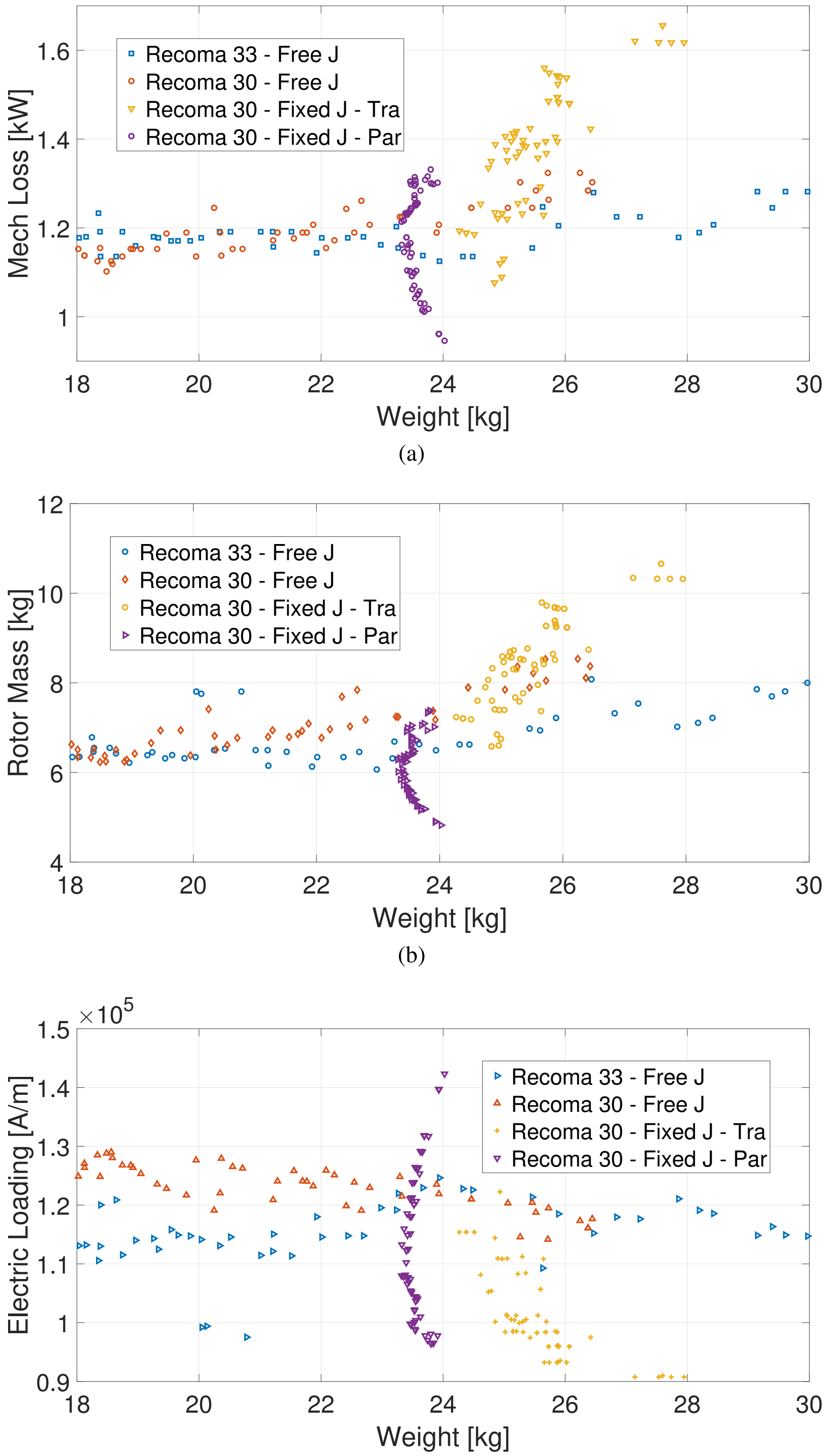

(a)

(b)

(c)

Fig. 4.24. Mechanical loss (a), Rotor mass (b), El.Loading (c)

4.3.4 Considerations and partial conclusions

First of all, fixing the current density unsurprisingly limits the mass reduction. This behaviour can be appreciated in both Fig. 4.20 (a) and 4.22 (a). Pareto's fronts, in case of constrained current density also assume a more peculiar half-moon shape peaking at a weight boundary in between 23 and 25 [kg]: this is due to the weighted fitness function definition. This is captured in Fig. 4.22 (b), where a zoom in for the constrained J solutions only is provided.

Secondly, there is no significant difference between employing a Recoma 30 or Recoma 33 PM grade. This can also be seen earlier in subsection 4.3.2 in Fig. 4.20 and 4.21. It was decided to choose the former, allowing a saving in the rotor material cost at the manufacturing stage.

Thirdly, it is worth noticing the Halbach array solution with parallel slot design seems to slightly outperform the trapezoidal shape; Fig. 4.22, 4.23, 4.24. This is noticeable immediately from the efficiency graphs of Fig. 4.22 (a) and (b). The trapezoidal slot has higher DC losses as shown in Fig. 4.23 (a). The fact that the trapezoidal slot must accept a lower fill factor impacts on the copper utilization, conversely demanding an increase in magnet usage, hence requiring a larger magnet outer diameter and therefore a larger sleeve. This brings to a final increase of rotor mass as it can be seen by Fig. 4.24 (b). The second objective function, (Electric Loading without looking at the mass discrepancy) is slightly in favor of the trapezoidal lamination, because for a constant current density the diameter along which the current is spread is bigger, given the larger rotor.

It was already judged at the beginning of this chapter that the Halbach array is the most power dense magnetic circuit construction. This solution also seems to be the most attractive in terms of mechanical retainment challenges: since the Halbach array covers the entire pole span, there is no danger of isolated concentration of hoop stresses along the sleeve inner boundary due to magnet edges.

In addition, from a mechanical perspective, a trapezoidal slot choice might cause manufacturing issues when dealing with such narrow teeth along a large stator bore peripheral diameter. This can be appreciated by a comparison of the two geometries in Fig. 4.25. These represent two best candidates along the Pareto's fronts, chosen in order to not exceed 100000 [A/m].

Finally, Fig. 4.26 yields further details concerning the magnetic circuit utilization at an ideal, Maximum Torque Per Ampere (MTPA) point (only i_q fed motor). First, the average flux density in the main stator flux channels (teeth and core back) is slightly lower for the parallel slot solution. Second, the non rectangular tooth shape for this last configuration allows to lower flux density at the slot bottom, as well as the optimum stator yoke is slightly larger than the trapezoidal one resulting in an additional reduction in flux density. As commented before the trapezoidal optimum form has a wider magnet thickness.

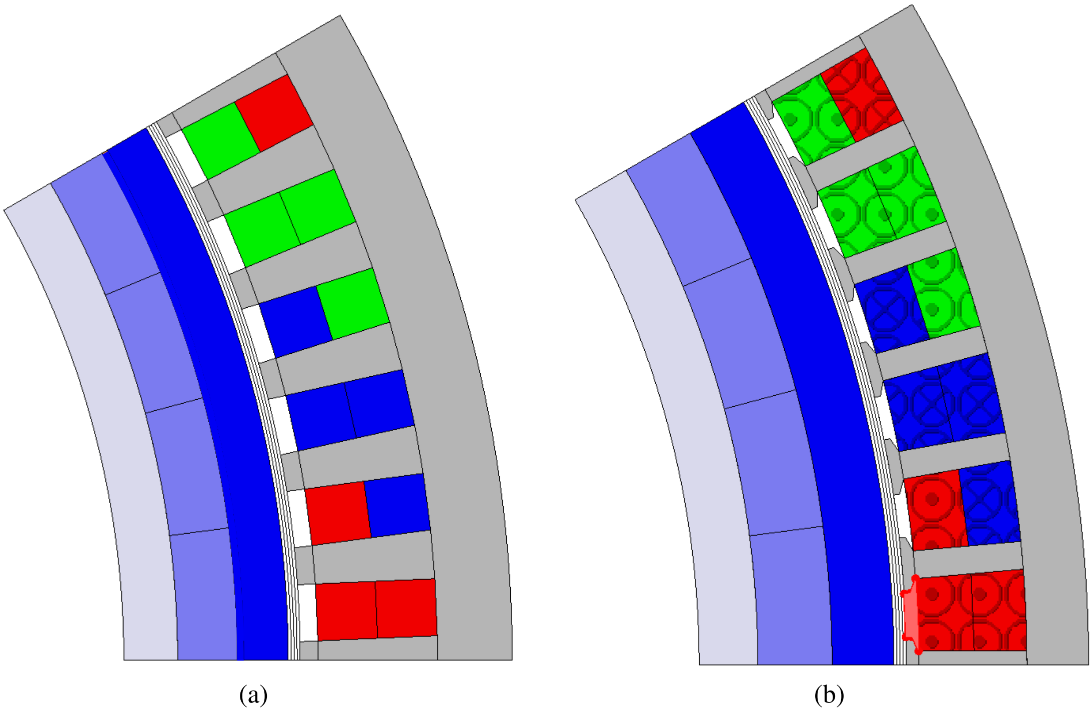
(a) (b)

Fig. 4.25. Parallel slot (a), vs Trapezoidal slot (b), solid view comparison.

A parallel slot geometry has been determined to be preferable. Not only it will provide a stiffer stator stack solution, but will free up the practicability of a rectangular Litz wire. Compact solutions employing this winding type can achieve very high fill factors.

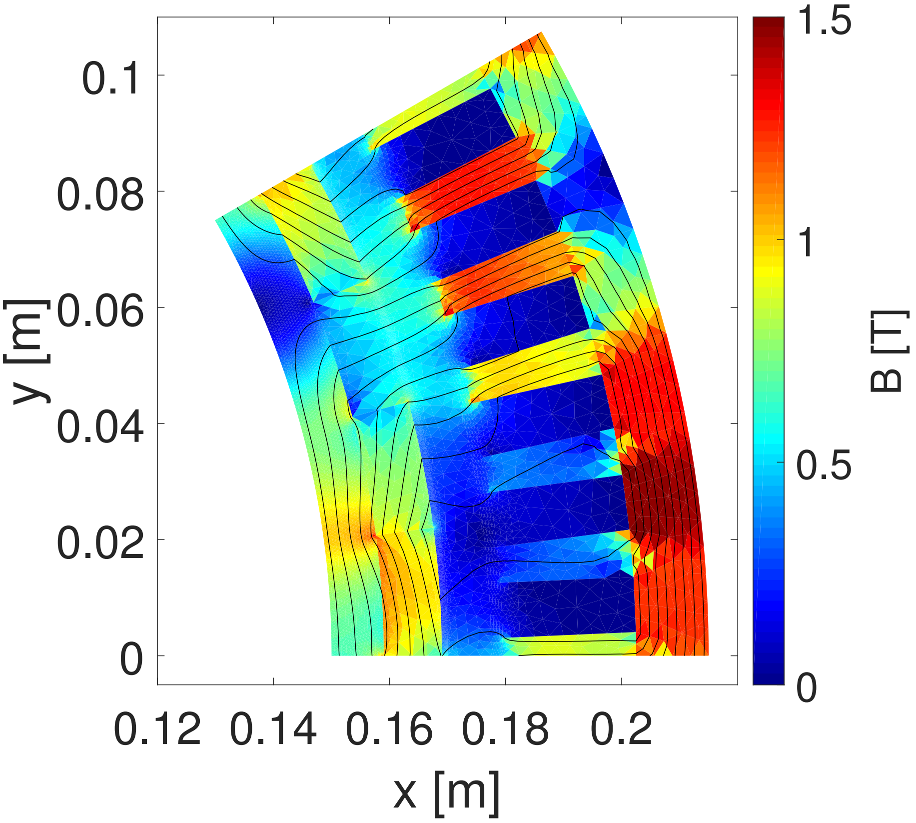

(a)

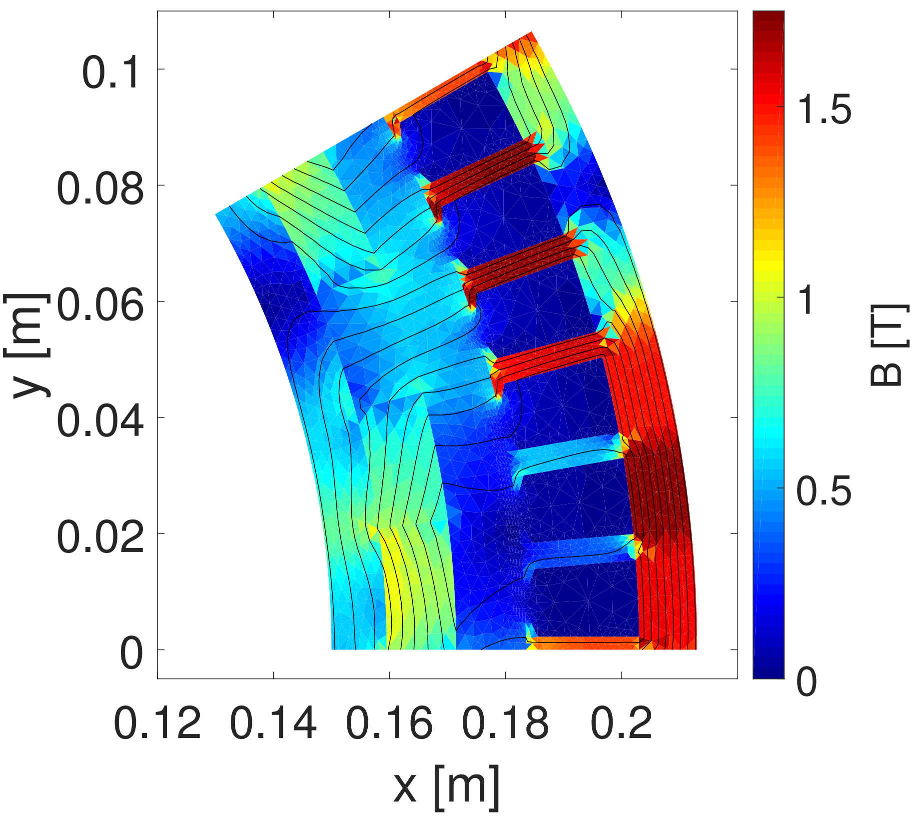

(b)

Fig. 4.26. Parallel slot (a), vs Trapezoidal slot (b), Flux Density Map Comparison.

4.3.5 Final optimization and main design choices

In the final stages of this preliminary design, the only mention of alternative permanent magnet grades thus far relates to two different Samarium Cobalt alloys (30 vs 33). It was observed that employing Recoma 33 is not much better than a less magnetically energy dense Recoma 30. At this point of the design stage a Neodimium Iron Borum was suggested during early discussion of the manufacture process. Therefore, in order to assert the final design this magnetic alloy is considered. In addition employing an even higher strength retaining bandage composite is suggested. Related to these last points the rotor magnetic manufacturing (Arnold Magnetics) partner advised slightly different magnetic and mechanical choice changes.

- magnetically, it is worth considering NdFeB against SmCo. At this optimization stage there is no real deep knowledge of the losses. It is worth an evaluation of this solution as NdFeB provides a higher power density: its lower density allows thinner sleeves; its higher energy product delivers smaller design solutions. Being fully encapsulated by a retaining sleeve and end-plates at the rotor axial ends, NdFeB permanent magnet blocks are not affected by the corrosion usually encountered in aerospace applications.

- mechanically, the solutions employed in Sections. 4.1 and 4.2 are based on standard literature properties given in Tab. 4.1, whereas in a more detailed optimization of sub-sections 4.3.1,4.3.2 and 4.3.3 are based on manufacturing properties of IM10 compound. Good candidates in the last generation Pareto's front possess a considerably large sleeve thickness value. To alleviate this material over-utilization and simultaneously hope for a magnetic loading gain a recently developed [105] fibre composite material could be employed: Zylon fiber could be the substitute of Carbon fibre. There are some major benefits of using Zylon, but also some major drawbacks.

  Benefits Zylon can be wrapped with higher pre-load than Carbon fibre: sleeve stress after cure can exceed 1200 [MPa] (Carbon fibre can usually reach 1000 [MPa]). Zylon has a negative Coefficient of Thermal Expansion (CTE), making it easy to work with because the fibre can't be loaded too much during the room temperature wind, as the fibre will then break during cure or service, when the hub expands and the sleeve shrinks. Zylon is light (specific weight 1.56 [kg/m^3]), hence the self stress due to the weight of the sleeve is reduced compared to a Carbon sleeve.

Drawbacks The fibre starts to degrade if used at high temperature, so it can only be used for applications up to about 180°C. There's no suitable resin at the moment to work at higher temperatures. The tests performed by the Zylon manufacturer, Toyobo, indicate $\approx 5\%$ reduction in strength after 100 hours at 200°C. Zylon shows some creep and it is uncertain how poor its high temperature creep performance is. The material is fairly poor at holding epoxy resin. To combat this a hybrid sleeve with a thin layer of carbon fibre on the inside and another on the outside to ensure that the resultant is a composite should be used. Having negative CTE, leads to very different load cases at minimum and maximum temperature, however it may be possible to use this fact and limit the rotor speed somewhat at cold start. The material is sensitive to light, so should be protected as much as possible from both visible and UV light. Zylon is also sensitive to high humidity particularly at elevated temperatures. Finally, it is significantly more expensive than Carbon Fibre in terms of both raw material and processing cost.

Evaluating what has been so far mentioned suggested to investigate a final comparison between NdFeB and SmCo solutions. Further tuned assumptions are as follows:

- a stator featuring parallel slots
- a rotor sleeve made of filament wound Zylon, protected by a top layer of Carbon Fibre
- a reduction to a focused four stages Halbach array for cost reduction and manufacture handling simplicity
- NdFeB 42UH grade is compared to SmCo Recoma 30

The implication of a reduction from seven to four stages of focused PM segments was investigated progressively reducing from 7 to 5 to finally 4 stages. This is dealt with in Fig. 4.27. The SmCo solution features in this case the two final Pareto's front for both runs, showing the good agreement and reliability of this last stage of optimisation.

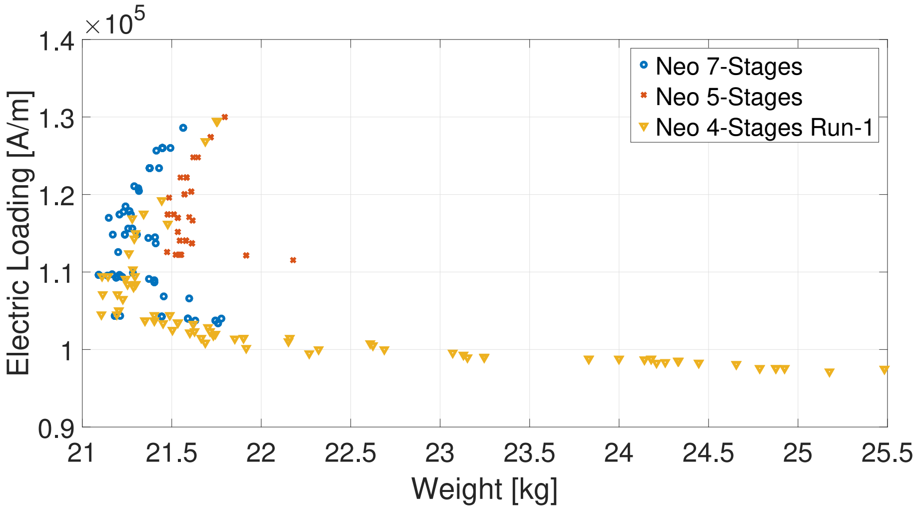

(a) *NdFeB 42UH*

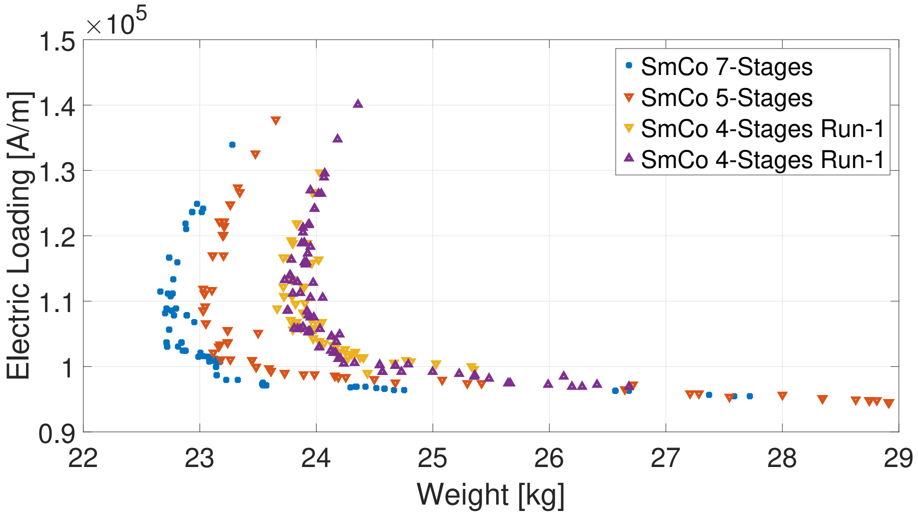

(b) *SmCo Recoma 30*

Fig. 4.27. NdFeB vs SmCo optimizations over different Halbach array stages per pole.

Ultimately, the design-candidate from the Pareto's fronts is chosen assuming a maximum electric loading of 100000 [A/m]. This is deemed to be a suitable equivalent thermal level for the motor. Hence, a dominant solution in this respect is picked as soon as the Pareto front crosses this threshold highlighted by the horizontal dashed line both Fig 4.28 (a) and (b).

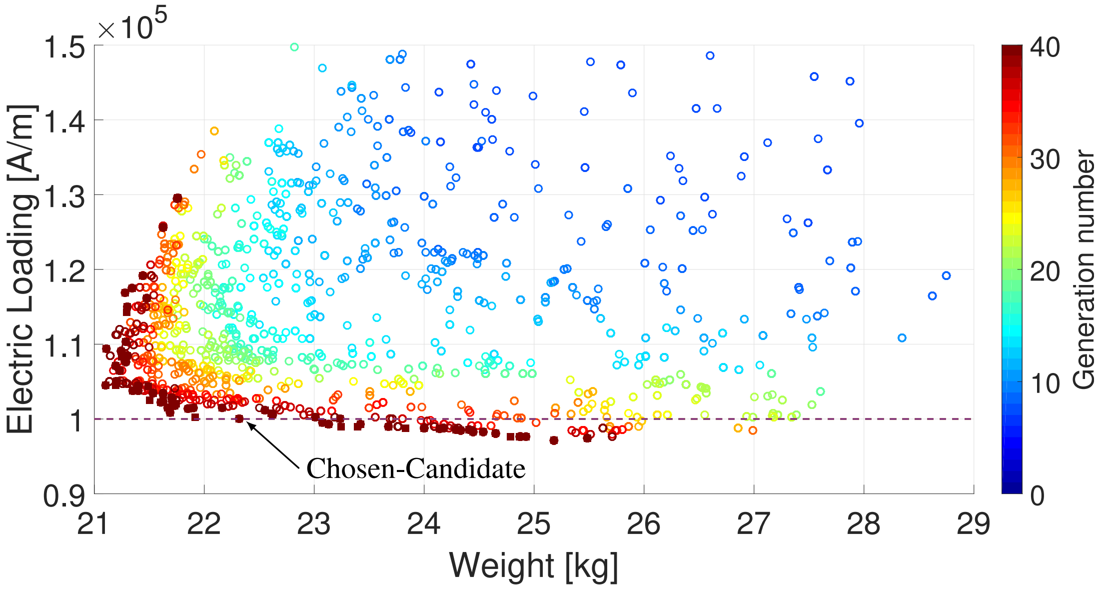

(a) *NdFeB 42UH Optimization*

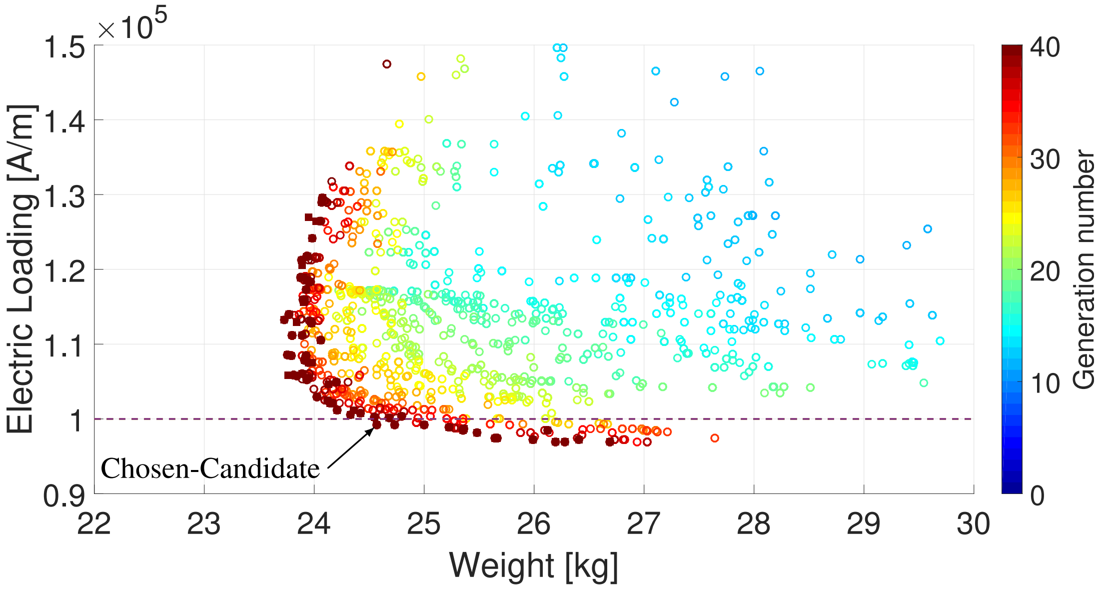

(b) *SmCo Recoma 30 Optimization*

Fig. 4.28. NdFeB vs SmCo optimizations over different generations.

Chapter 5

Finalizing the Design

The final machine design consists in taking the choice of optimal design identified from the last Pareto's front and ameliorate the machine characteristics to allow the machine to be built within the mechanical tolerances and fully optimized electromagnetic performances. Therefore the scope of this chapter is twofold: gaining a deeper insight on second-order effects affecting both the mechanics and the electromagnetic behavior of the electrical machine. Specifically the electromagnetic involves the final choice of the iron alloy, but more importantly and extensively treated is the electromagnetic shielding. The shielded rotor construction consists of a metallic conductive layer, also called canned rotor, surrounding the magnets, usually bing placed under the retaining sleeve, which has the benefit to reject high frequency harmonics responsible of otherwise excessive losses in the magnets, which could be prone then to demagnetization due to loss-driven temperature increase. The shielding effect was investigated in the past for instance in [106] and [107] where emphasis was given to the modified characteristic of the electromagnetic circuit. In [108] the interaction with the drive was first taken into account. More recent studies have also given emphasis to the shielding effect analysis: [109]. The chapter has a section regarding the electromagnetic design tuning for rotor loss reduction as well a subsequent section including a more comprehensive study of the drive current distortion and electromagnetic shield interaction with an ad-hoc state space dynamic model representing the equivalent circuit alteration due to the newly inserted rotor conducting component.

The ultimate mechanical design tuning is also addresses considering the final considerations on the retaining sleeve, the nature of the spoked shaft/hub assembly, bearings and rotor-dynamics behavior, the end-plates and their electromagnetic interaction in the assembly.

The final section addresses the stator thermal aspects.

5.1 Extended electromagnetic modeling

5.1.1 Iron losses

Iron losses are a substantial component of the loss split. All the design optimization carried out thus far assumed JNEX900 and CoFe alloys as core pack material. As it was pointed out in Chap. 4, the usage of CoFe was discarded for the following reasons: although the saturation limits would allow a higher magnetic loading, the losses were still considerably high (around double the silicon iron); the mass density of this alloy is higher and therefore the overall power density was not greater, although with lower volume; the cost of CoFe was prohibitive. As for JNEX900, being a peculiar and very costly Silicon Iron it could not be afforded. The choice has shifted to cheaper and more available NO20 Cogent steel. A comparison of the losses is given by Fig. 5.1. NO12 has been added for comparison completeness. An remarkable increase is seen especially directly proportional in terms of eddy currents, moving from JNEX to NO12 and end up to NO20. The overall losses are more than three times higher. Yet they should not represent the main component of the loss which is taken by the copper.

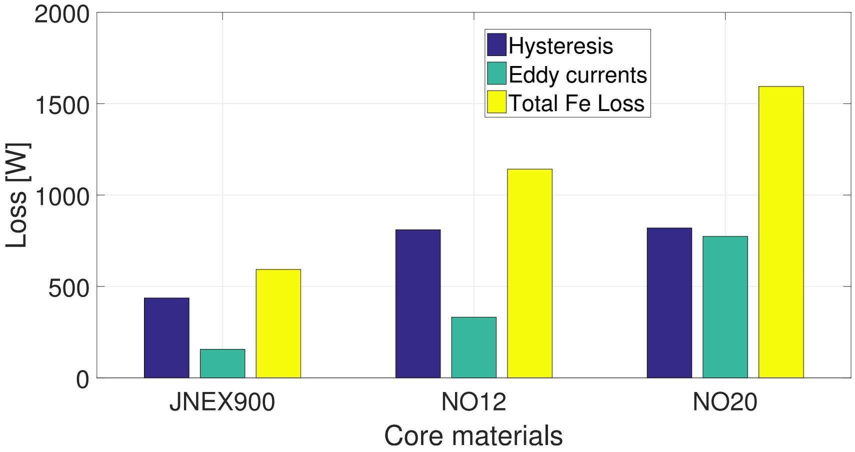

Fig. 5.1. Iron losses comparison.

It is almost universally recognized as the iron losses for laminated cores can be subdivided in three subcategories. Namely: hysteresis, eddy currents and excess losses. These three terms appear in the model of Bertotti at [39] and [40]. The hysteresis loss represents a form of static energy loss. Faraday's law is at the base of the eddy current formation accounted for in the second term of (5.1). Excess losses are finally included with the last term.

$$P = k_h f B_p^{\alpha_h} + k_{ec} f^2 B_p^2 + k_e f^{1.5} B_p^{1.5} \tag{5.1}$$

The software package used in this work yields a blended value excess losses within hysteresis and eddy current ones, utilizing the following (5.2), based on Steinmetz's equation rather than Bertotti's, [41]. α and β are derived from material loss data interpolation, whereas s is the harmonic order.

$$P = k_h f^{\alpha} B_p^{\beta} + k_e (s f B_p)^2 \tag{5.2}$$

Fig. 5.3 (a) presents the approximate 3D finite element geometry used to estimate the overall inductance, which includes 3D effects as the machine is very short axially.

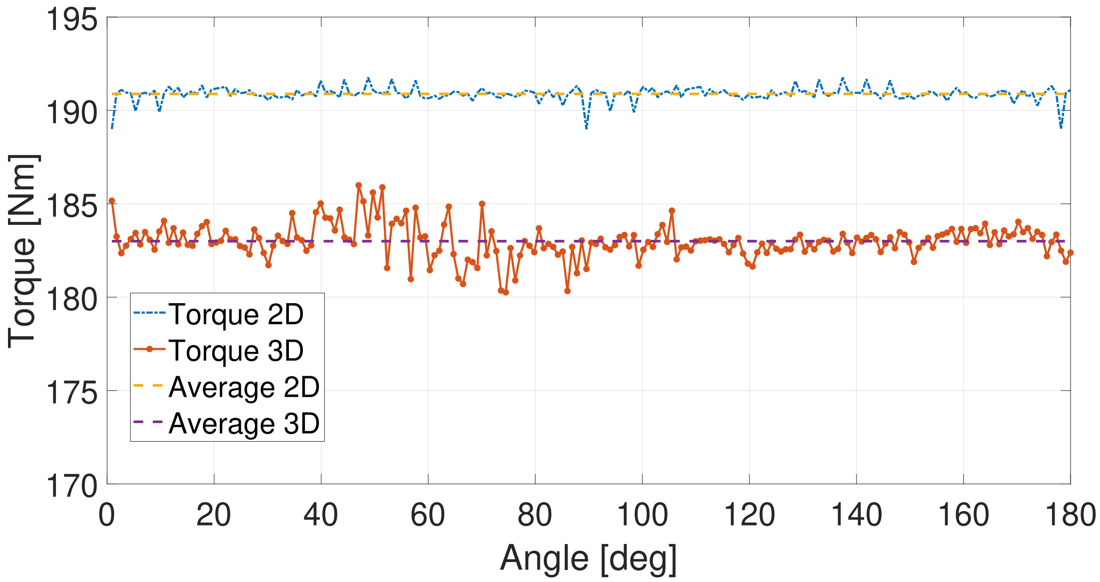

Fig. 5.2. 2D vs 3D torque, simulation, sinusoidal excitation.

Fig. 5.2 (a) compares the simulation of 2D and 3D torque estimation (over one electric semi-period). Some leakage flux is expected due to fringing and end effects. It is indeed the case: the 3D torque exhibits a drop of around 4% with respect to the 2D estimation. Fig. 5.3 portrays the flux density in 3D space. Fig. (5.4) proves the suitability of the Halbach array showing the three dimensional No-Load flux linkage across the three phases of the machine (a), together with the harmonics magnitude (b) in logarithmic scale. It is clearly noticeable as the first harmonic completely dominates the waveform, being essentially sinusoidal.

Slot-poles combination and short pitching choice constitute the "cleanest" solution in terms of spatial harmonics. Nonetheless, the rotor losses are considerably high when the ripple is included in the armature current spectrum. Even though employing a higher number of segments, especially axially [110] decreases the overall losses because of an increase in the eddy current path, it conversely increases the amount of rotor loss caused by time harmonics whose pole pitch is wider than space harmonics. This results in a higher depth of penetration into the rotor. Consequently, eddy currents tend to circulate within a skin layer at the permanent magnet radial edges rather than on the outer radial surface as occurs with space harmonics, effect observable in Fig. 5.5. No permanent magnet rotor can withstand such losses, without causing an ever-lasting detriment of magnetization properties due to the increased temperature. To tackle this issue either an extremely fine segmentation (employing segments thinner than the skin depth related to the time-harmonic frequency) or permanent magnet screening against harmful asynchronous harmonics could be utilized. The former solution is too challenging, both in terms of manufacturing and cost, consequently the latter approach has been chosen.

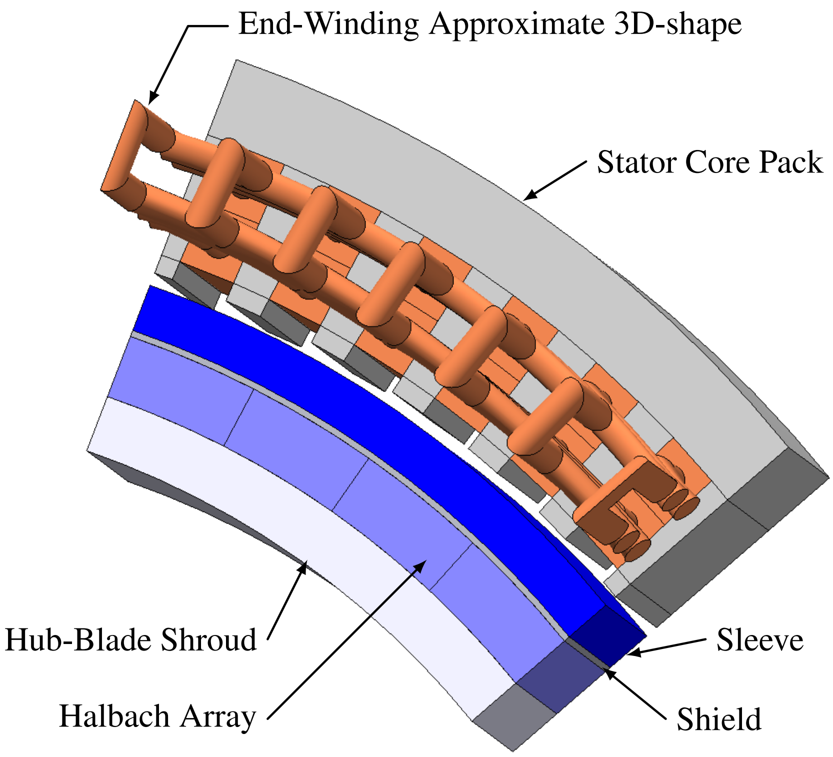

(a) *3D geometry used for FEA analysis*

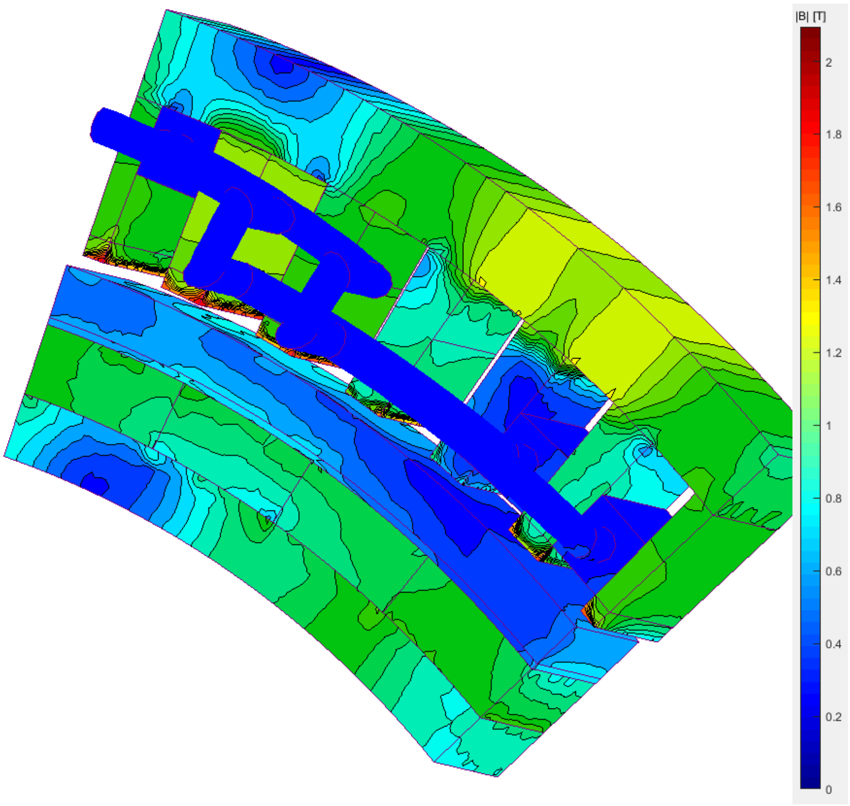

(b) *3D Flux density plot*

Fig. 5.3. FEA 3D analysis (sinusoidal excitation).

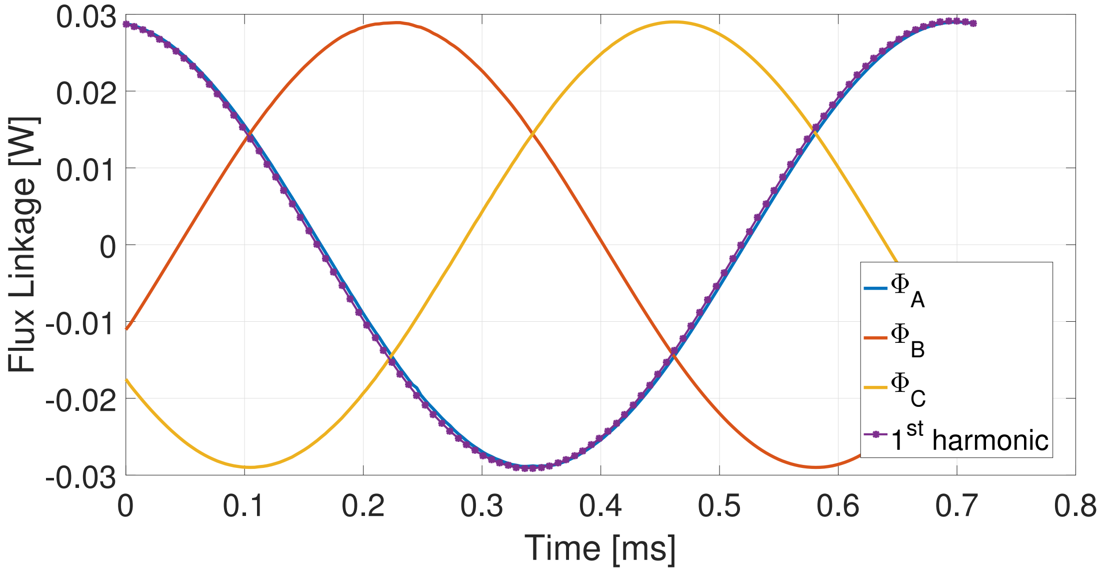

(a) *No Load flux linkage over time*

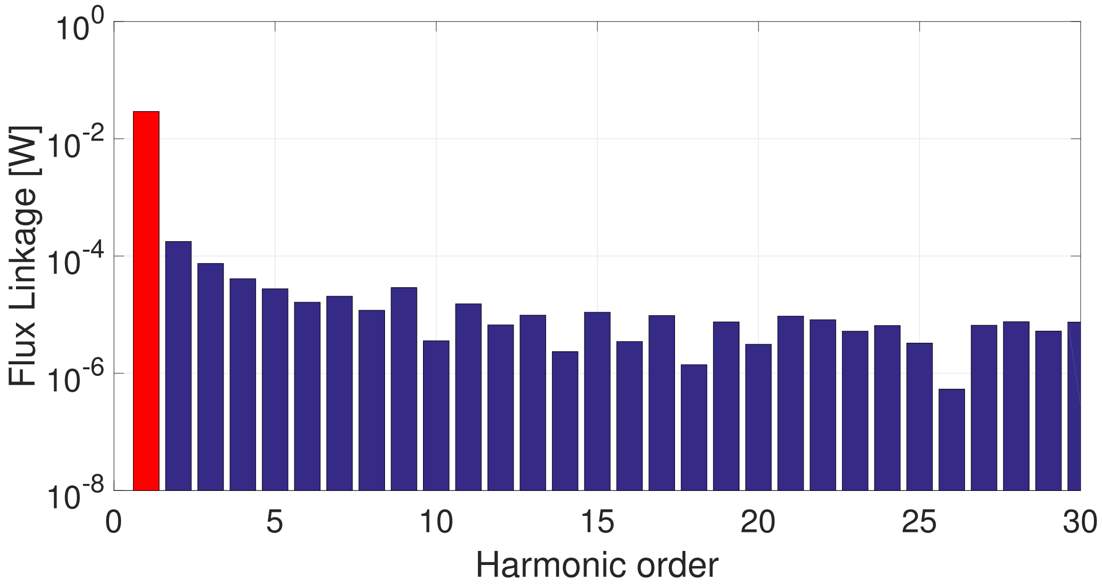

(b) *Log scale of flux linkage harmonic order*

Fig. 5.4. No load flux linkage from Halbach array.

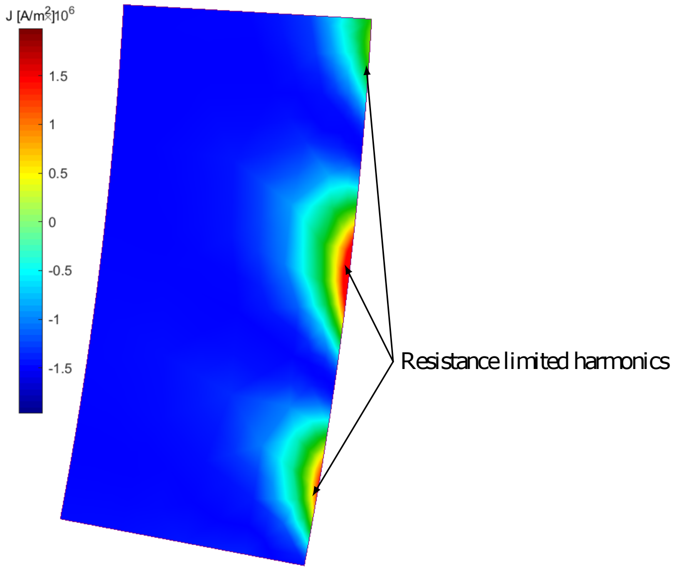

(a) *Space-harmonics ECs behaviour in a PM*

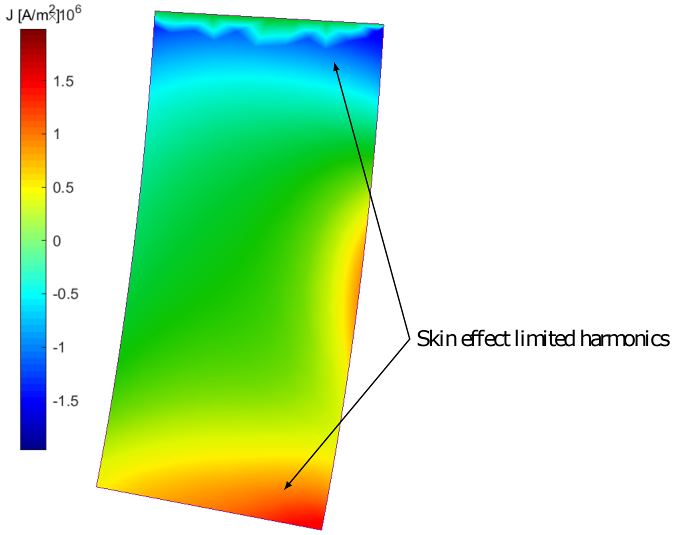

(b) *Time-harmonics ECs behaviour in a PM*

Fig. 5.5. Space harmonics (sinusoidal current) vs time harmonics (current ripple inclusion)

5.1.2 Inclusion of Drive Total Harmonic Distortion

A dynamic model of the SPM motor, along with the inverter behavior and current control loop has been implemented. Overall this can be considered an extension and more in depth analysis of what presented in [108]. The scheme adopted is sketched in Fig. 5.6. The control methodology is the simplest possible: PI controllers are embedded in the current loop for the 2 axes of the machine. Only the current loop is simulated, assuming a constant current reference and no transient in speed operation. Hypotheses under which the estimation is conducted are:

- a SPM dynamic model with a single value inductance $L_d = L_q$
- an ideal inverter: lossless and with no switching dead times
- 600V DC Link
- discrete time behaviour: modulation indexes are discrete functions of time as they are applied once per sampling period
- Space Vector Pulse Width Modulation (SVM-PWM) is utilized as the switching method
- only cascaded PI controllers are employed: there is no speed loop into the control, assuming a constant speed
- the current reference on the d-axis is zero: MTPA operation condition is employed by controlling the q axis current (standard orthogonal angle with no demagnetizing current)
- the two switching frequencies have been modelled, 14kHz and 28kHz: 10 times and 20 times the fundamental frequency, respectively.

In order to simulate closed loop current control, resistance, inductance and PM flux values must be estimated, Tab. 5.1. The resistance has been computed analytically without considering increments due to AC effects: the wire resistance employed here has less impact than the inductance. The PM flux is assumed for 100 °C operation. This has been portrayed before in Fig. 5.4. The air-gap exhibits a constant reluctance along the d and q axis due to the SPM Halbach array.

Current ripple is presented in Fig. 5.7 (a). The related frequency spectrum is highlighted in Fig. 5.7 (b). The close-up helps to show the high order harmonics due to the Voltage Source

Table 5.1. Electro-magnetic parameters

R_s	6.3 mΩ
$L_d = L_q$	32.5 μH
ψ_{PM}	0.29 Wb

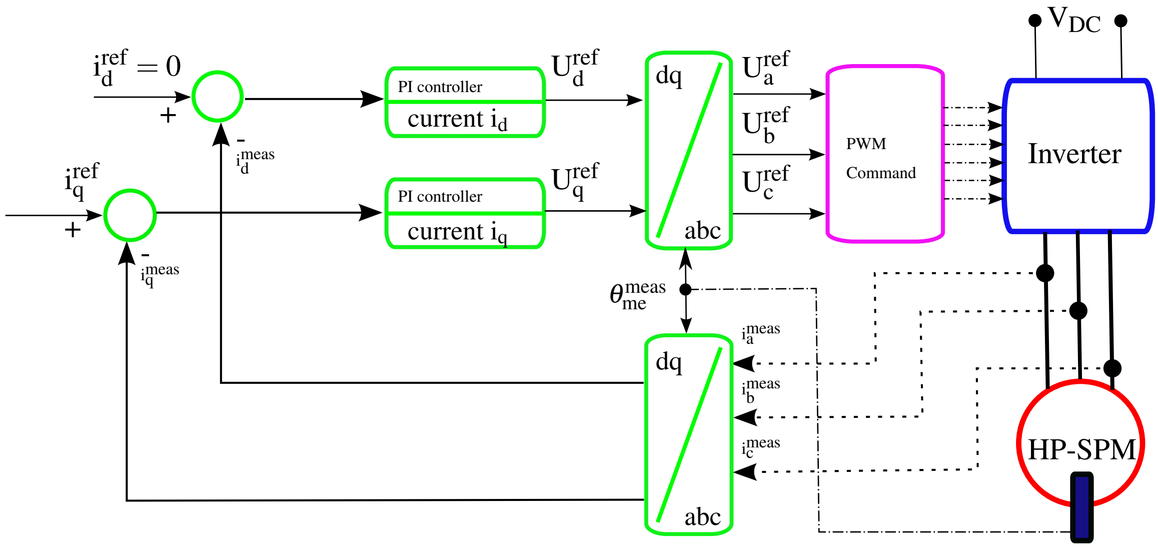

Fig. 5.6. Current control loop for determining current ripple

Inverter clearly creating the side-bands of the converter switching frequency. A Total Harmonic Distortion (THD) in the current waveform has been estimated 8.4 % for the lower switching frequency, whereas less than 4% for a higher switching frequency.

Inclusion of current ripple brings in torque ripple. Fig. 5.8 underlines the significant ripple induced in the torque waveform: the torque values are derived from a 2D finite element simulations, comparing an ideal sinusoidal current feeding the stator windings, with a current possessing the ripple previously evaluated circulating in a machine employing copper and aluminium rotor shields. Average electromagnetic torque and the torque ripple, computed as in (5.3) and (5.4):

$$\langle \tau_{em} \rangle = \frac{1}{2\pi} \int_0^{2\pi} \tau_{em}(\theta)\, d\theta \tag{5.3}$$

and

$$\Delta\tau_{em} = \frac{\max[\tau_{em}(\theta)] - \min[\tau_{em}(\theta)]}{\langle \tau_{em} \rangle} \tag{5.4}$$

A clearer comparison is underlined from the close-up with the ideal sinusoidal current condition: indeed from an ideal situation in which the ripple is almost non-existent (distributed winding

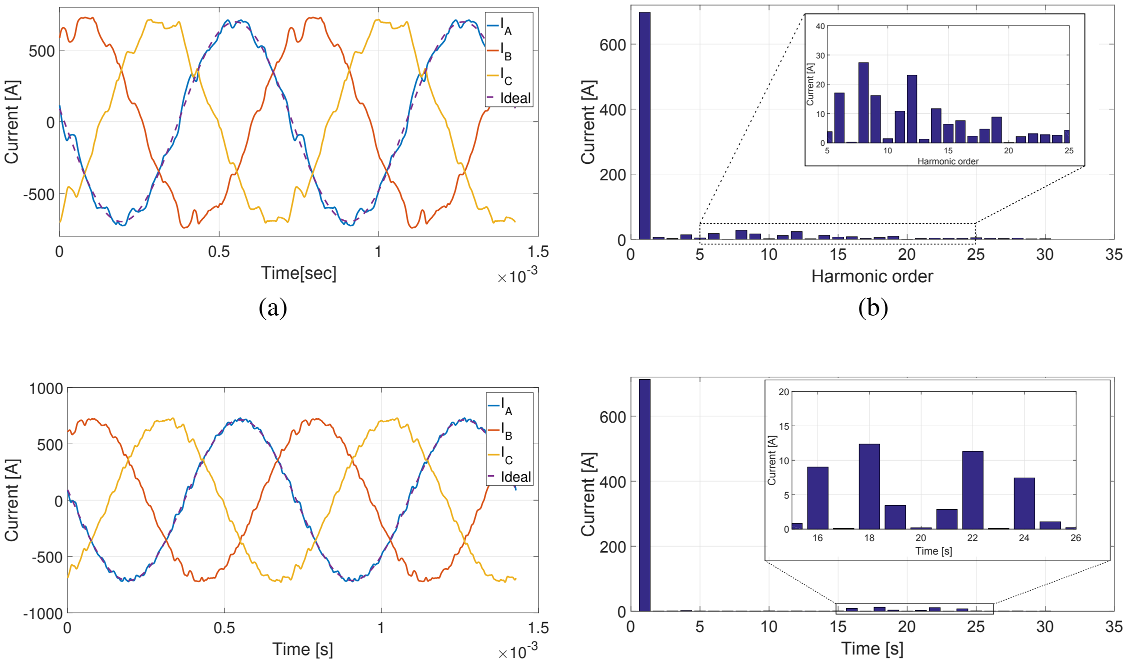

(a) (b)

(c) (d)

Fig. 5.7. Current Ripple and harmonic spectrum for different switching frequencies.

with very low content of spatial harmonics) to the values under ripple operation. The average value drops from around 191 [Nm] to 182 [Nm]: a decrease of just less than 5%. The ripple, from a completely negligible 0.15 % increases as far as 29%. A higher switching frequency slightly relaxes these complications, delivering an average torque of 184 [Nm] (4% less than sinusoidal reference) and a lower ripple of 12%. A reduction is given by the lower first harmonic content in the more distorted current spectrum of the voltage fed inverter simulation.

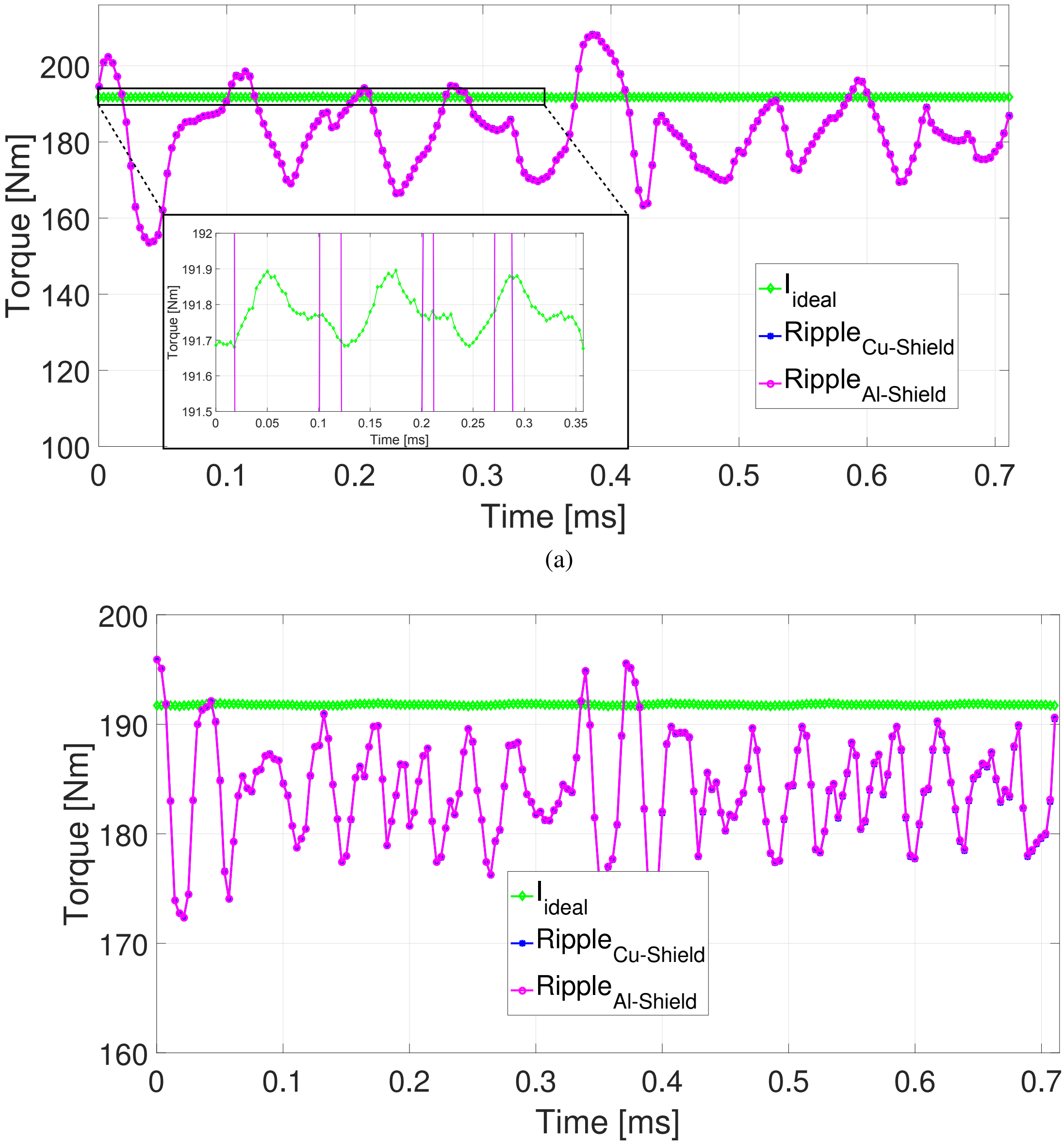

(b)

Fig. 5.8. Torque ripple at 14 kHz (a) and 28 kHz (b) switching.

5.1.3 Shielding sizing and implications

The electromagnetic shield is an additional electrically conducting sleeve surrounding the magnets. It is located circumferentially between the retaining sleeve and the magnet array. A sizing for the shield has been attempted, comparing copper and aluminium as screening material. The loss trend for different shield thickness is plotted in Fig. 5.9. The simulation have been conducted aiming to preserve the torque for the rated power (250 [kW]) and rated speed (14000

[rpm]). A high operational temperature (200°C) for the shield has been assumed, as a worst case scenario in terms of increased resistance due to temperature rise. Copper seems to give a slight advantage on overall loss reduction. Moreover, there is no gain to be had from increasing the shield thickness beyond 1.00 [mm]: this will be detrimental for the torque density and sleeve stresses.

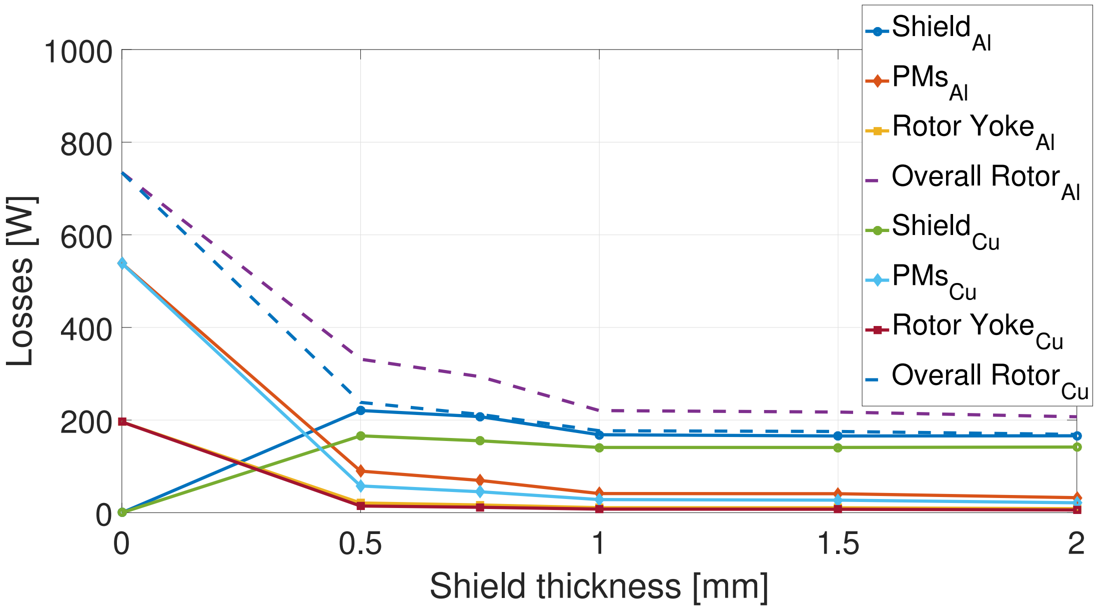

Fig. 5.9. Shield sizing

The principle behind the shield functioning is that it forms a highly electrically conducting barrier above the magnets. Alternating fluxes are reduced by eddy currents in the shield and prevented from inducing larges losses in the less conducting magnets. The above principle works if the fluxes are skin limited within the shield. Under these conditions the shield produces an MMF which is equal and opposite to the alternating flux source. However, if the alternating fluxes are large, and of lower frequency content, they pass through the shield, whose presence actually increases the overall loss.

High frequency fluxes are generally created by time harmonics of current created by the PWM switching harmonics. Losses from this source are reduced by the shield. Low frequency fluxes are instead space harmonics generated by the winding and are particularly large when fractional slot windings are used. There pass through the shield and the shield has a negative effect, increasing the losses. For the machine designed, being an integer slot winding the choice, the space harmonics are low, as throughly discussed in the previous two chapters. Consequently, the overall impact of the shield is positive, reducing losses by a factor of about 4, for a shield thickness of 1.0 [mm].

The shield will have a non negligible impact on No-load, exhibiting losses. The shield eddy currents screen against tooth ripple harmonics. It is possible to appreciate their entity by Fig. 5.10: almost all loss in this case is in the shield. Spatially it in noticeable as the main loss component is represented by the shield. The eddy current is almost exclusively confined in case of No-Load, to the shield, witnessing the effectiveness of this additional employed component. The loss is due essentially by permeance variation. This is expected as the radial magnetic field dips, due to stator slotting, are exacerbated by the open slot choice adopted. This observation is even clearer when considering the periodicity of the loss itself indeed at No load as the variation over time is presented by Fig. 5.11. It is noticeable a 24 repetition (after simulation-start-up transient) pattern over an electrical period. The magnetic field alongside a pole pair (on the rotor reference frame) sees 12 flux pulses (72 slots over 6 pole pairs). Therefore the magnetic flux density field can be thought as proportional to a single value (assuming the first harmonic of field only) synchronous with the rotor rescaled by a sinusoidal function, (5.5):

$$B(t) \propto B_1 \sin\left(Q_s/p\theta_r\right) \tag{5.5}$$

Eddy current losses are most generally proportional to the squared derivative field of the flux density [30], therefore the derivative square in time (as $\theta_r = \omega_s t$) will be cosinusoidally square. This implies that the losses will be proportional to a co-sinusoidal function with double the initial frequency, (5.6).

$$P(t) \propto B_1^2 \cos\left(2Q_s/p\omega_s t\right) \tag{5.6}$$

Hence confirming a loss pulsation 24 times faster than the fundamental frequency.

Employing a screening component such as a shield, within an electromagnetic assembly, affects the device as parasitic eddy currents come into play in the overall power balance. In particular, a SPM motor equipped with a shield will experience a behaviour similar to the one wound field synchronous generator equipped with damper cages exhibit [107]. A frequency response analysis has been carried out in order to obtain the inductance variation over the frequency spectrum. The frequency response is shown in Fig. 5.12.

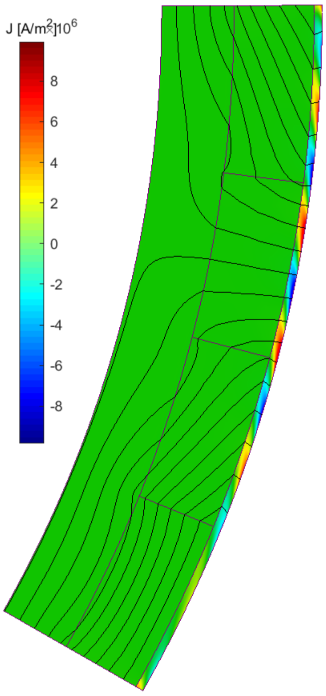

Fig. 5.10. Eddy current particular in rotor components.

Physically, this is due to the rejection effect of the eddy currents against the inducing flux. This is very well represented in the Fig. 5.13. Subfigure (a) highlights the low frequency fundamental harmonic emphasizing the linkage property of the flux behaviour. Conversely in subfigure (b) the flux lines are clearly rejected from entering the rotor magnetic path at high frequency, causing all the flux to leak. This happens at the first significant time harmonic, six times higher in frequency than the fundamental (8400 [Hz]), being it the fifth harmonic from the PWM. As a consequence, the lower the number of linking lines of force, the smaller the inductance. Asymptotically, at infinite frequency, all the flux will be leaking, therefore representing the only leakage inductance, both for the active part and end winding.

The inductance which is usually considered a function of current and rotor position $L = f(\theta, i)$ becomes dependent on three variables: $L = f(\theta, i, \omega)$. The assumption adopted so far considered a single value inductance: neither affected by the rotor position, nor current level (this is very often the case for standard industrial drive control purposes). The former is ensured by an isotropically magnetic rotor, whereas the latter by a low magnetic stress in both air-gap and lamination stack: the machine is almost operating in linear iron conditions. From this point onwards the frequency variation has been taken into account in the design refinement.

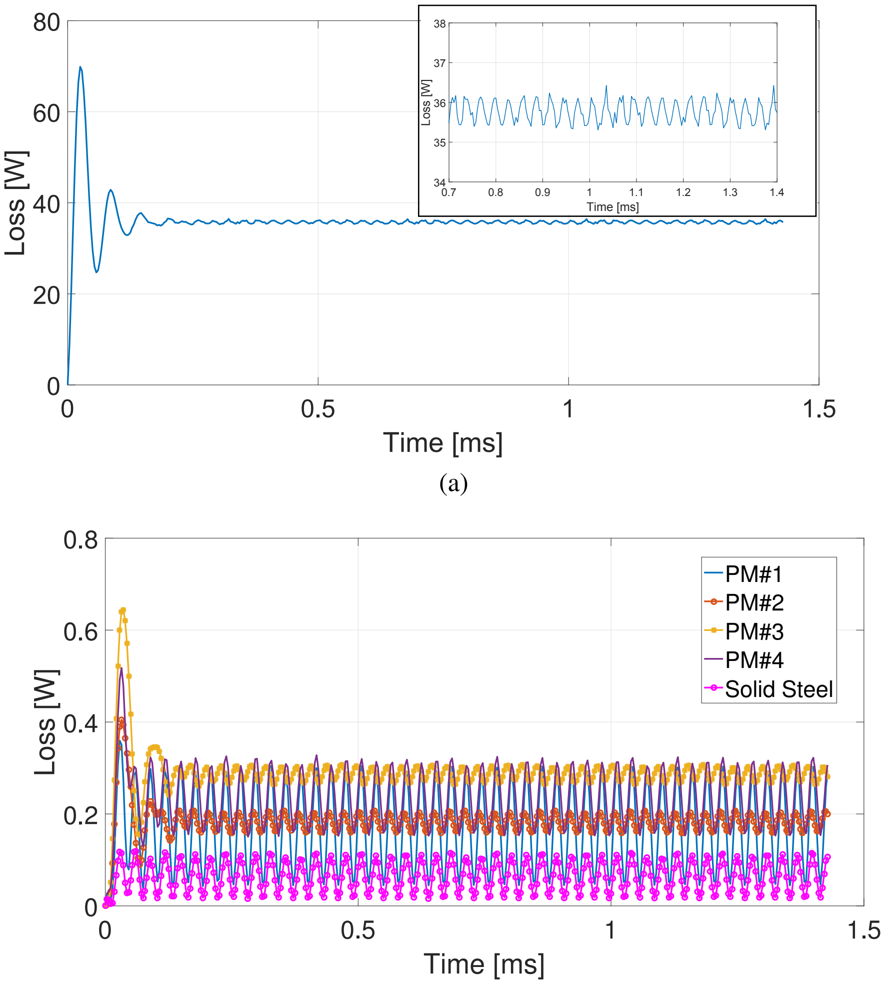

(a)

(b)

Fig. 5.11. Losses in rotor components (2D FEA simulated) at No-Load.

The easiest step is exploiting the superposition principle for different voltage harmonics. In other words the current harmonics due to the power electronic converter can be considered by decoupling all the harmonics separately. The voltage generated by the PWM switching scheme (in our case a Space Vector Modulation) is the sum of fundamental and high-order (ripple) components. For a single phase this is succinctly expressed by (5.7):

$$v_{line}(t) = v_{line,1}(t) + \sum_{n=1}^{\infty} v_{line,n}(t) \tag{5.7}$$

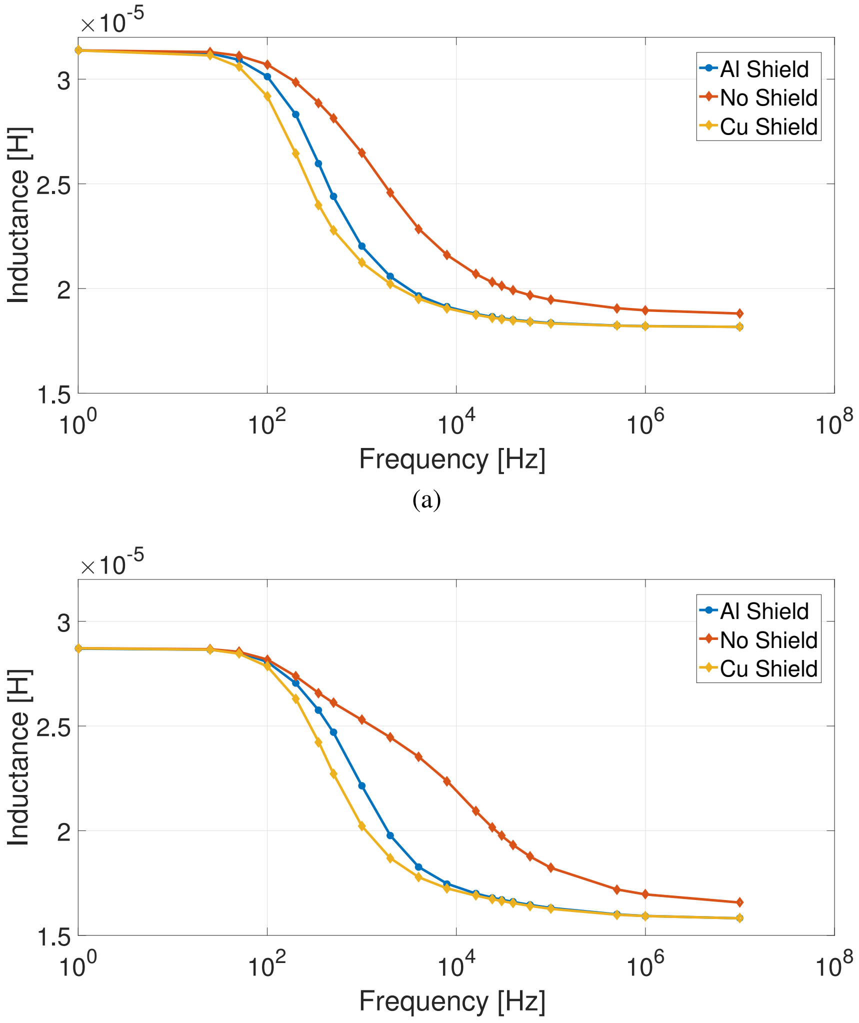

Fig. 5.12. Harmonic response for different shields, SmCo (a) vs NdFeB (b).

To simplify the analysis the resistance term is neglected. Hence the current ripple can be derived from simply (5.8):

$$i_{ripple}(t) = \frac{1}{L}\int_0^t \sum_{n=1}^{\infty} v_{line,n}(\xi)\,d\xi \tag{5.8}$$

which needs to be updated to (5.9):

$$i_{ripple}(t) = \int_0^t \sum_{n=1}^{\infty} \frac{1}{L_n(n)} v_{line,n}(\xi)\,d\xi \tag{5.9}$$

This is a very crude method, that theoretically considers an ideal operational case in which all the harmonics are uncorrelated, with no closed loop behaviour. The next section provides a

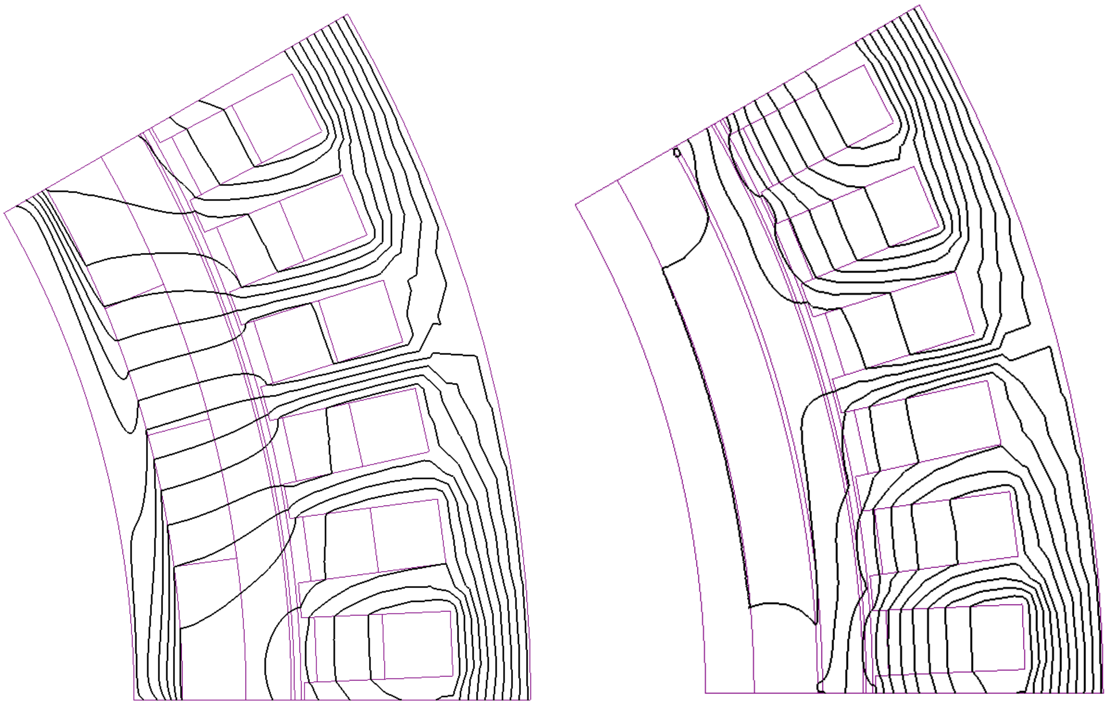

(a) *Fundamental frequency operation* (b) *1st significant higher harmonic*

Fig. 5.13. 2D time harmonic at different frequencies.

more appropriate approach to improve the accuracy this type of modelling, which is presented extensively in [111], [112] , [113] .

5.1.4 Dynamic modeling of the shielded rotor

A more accurate and mathematically sound modeling of the real dynamics of the machine consists of employing a modification to the two-axis rotating frame equivalent circuit as reported in [107]. Effectively, the dynamic model will see an extra branch added for taking into account eddy current effects. The parameters can be derived considering the electro-magnetic coupling effect between the armature circuit and the eddy current circuit, created by the conductive rotor components, prominently affected by the shield. Rotor eddy currents involve both resistive and inductive effects, so resistance and inductance lumped parameters are employed for the rotor branch modeling. Following the mathematical model of a transformer, the stator is the primary whilst the rotor is the secondary circuit: the coupling is expressed by two voltage equations in the frequency domain, (5.11):

$$V_s = \mathrm{j}\omega L_s I_s + \mathrm{j}\omega M I_r \tag{5.10}$$

$$\mathrm{j}\omega M I_s + (R_r + \mathrm{j}\omega L_r) I_r = 0 \tag{5.11}$$

Deriving I_r and substituting in the first equation, the primary circuit voltage is as in (5.12):

$$V_s = \mathrm{j}\omega L_s \left(1 - \frac{\mathrm{j}\omega M^2 / L_s}{R_r + \mathrm{j}\omega L_r} \right) I_s \tag{5.12}$$

As a consequence the inductance seen by the stator armature assumes complex values. If again we consider the hypothesis of an equivalent inductance along the two rotating d-q axes. Being our machine a surface permanent magnet, and with a Halbach array covering the entirety of the rotor circumference both direct and quadrature inductances can be regarded as equal and referred as L_s. This parameter can be written as a frequency dependent function in the complex plane, (5.13):

$$L_s(s) = L_s s \left(\frac{1 + sT_1}{1 + sT_2} \right) \tag{5.13}$$

Hence, this notation stands for a singular value synchronous inductance, which can be easily estimated at zero frequency condition. From the theory of wound field synchronous generators constants T_1 and T_2 are pertinent the to open-circuit sub-transient state and the short circuit sub-transient state, respectively.

Both the time constants can be expressed as (5.15):

$$T_1 = T_2(1 - k^2) \tag{5.14}$$

$$T_2 = \frac{L_r}{R_r} \tag{5.15}$$

It is common convention to define k_c as the coupling coefficient between the two inductive circuits, (5.16):

$$k_c = \frac{M}{\sqrt{(L_s L_r)}} \tag{5.16}$$

The general value of L_s for a zero frequency comprises magnetizing inductance and pure leakage, (5.17).

$$L_s(0) = L_m + L_{leak} \tag{5.17}$$

It can be seen from (5.13) that if the frequency is large enough the stator inductance will approximate to (5.18):

$$L_s(\mathrm{j}\omega) \approx L_s \frac{T_1}{T_2} = L_s(1-k^2) = L_{leak} \tag{5.18}$$

and it is effectively equal to the pure leakage component, usually referred to as the sub-transient inductance. As we possess the frequency response in presence and absence of eddy currents the value of coupling coefficient can be determined extrapolating the highest frequency value of inductance, which is asymptotically a constant. Simultaneously, knowledge of inductance phase variation can be beneficial to obtain T_2. In fact, the phase variation can be expressed via an arctan difference, (5.19):

$$\phi = \arctan\left(\omega T_1\right) - \arctan\left(\omega T_2\right) \tag{5.19}$$

The point at which the phase is such that ωT_2 represents a point of interest for the filter-wise (5.13) (equal to unity) the numerator phase angle will reduce to $\arctan\left(1-k^2\right)$ in the numerator and $\pi/4$ in the denominator. By knowing k it is straightforward to numerically identify the correspondent frequency at which this point stands. Extrapolating k is done employing the aforementioned (5.18) for high frequencies. In this specific case the reciprocal of ω provides T_2, finally yielding T_1 via the coupling relationship (5.15). Hence, the obtained time constants T_1 and T_2 allow to define the fitting function over the frequency spectrum.

Eventually, the extra branch parameters appearing in circuit Fig. 5.17 can be captured by equating the equivalent inductance complex expression (5.20) with the fitted function (5.13).

$$L_{eq} = L_{leak} + L_m \left(\frac{R_k + \mathrm{j}\omega L_k}{\mathrm{j}\omega L_a + R_k + \mathrm{j}\omega L_k} \right) = L_d(0) \left(\frac{1+\mathrm{j}\omega T_1}{1+\mathrm{j}\omega T_2} \right) \tag{5.20}$$

The inductance variation and related interpolation developed thus far as in [107], is represented by the fitting of Fig. 5.14. The inductance is expressed in both real and imaginary components and exploiting the phase identification method previously described both complex components fittings are identified. This is carried out for both absence of shield, a 1.00 [mm] Aluminium shield and a 1.00 [mm] Copper shield. The fitting curves are identified by the smoothed lines. The imaginary component is even less than one order of magnitude with respect to the real component. It is worth to notice as both complex inductance components do not properly interpolate the frequency dependent function throughout the whole spectrum. This is an indication that a higher order dynamics is probably involved. To assess this point other two interpolation methods have been used for comparison. The Levenberg–Marquardt algorithm is performed instead of the method by [107] over the first order approximation given in (5.13). These are presented in Fig. 5.15. There is still some discrepancy left between the actual function and the fitting.

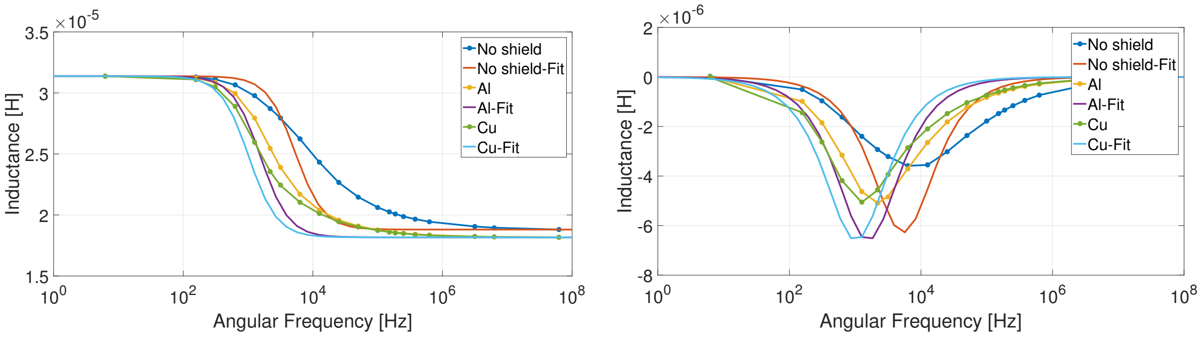

(a) $\mathrm{Re}(L_d(\omega))$ (b) $\mathrm{Im}(L_d(\omega))$

Fig. 5.14. Complex Inductance components with Miller's et all, approach.

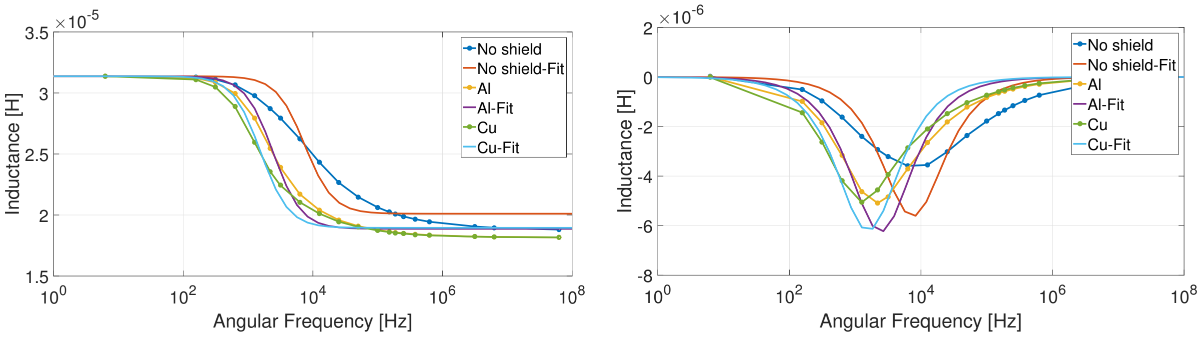

(a) $\mathrm{Re}(L_d(\omega))$ (b) $\mathrm{Im}(L_d(\omega))$

Fig. 5.15. Complex Inductance components with First Order fitting

An even more accurate attempt is given by considering a second order dynamics, of the form expressed by (5.21). A much more satisfying fitting is yielded as highlighted in Fig. 5.16. This makes the representation of any circuit extension even more elaborate of the one that is presented in the following section. However, for the sake of simplicity and still reasonable parameters identification the first order fitting has been employed in the circuit extension.

$$L_s(s) = L_s s\left(\frac{1+sT_1+s^2T_3}{1+sT_2+s^2T_4}\right) \tag{5.21}$$

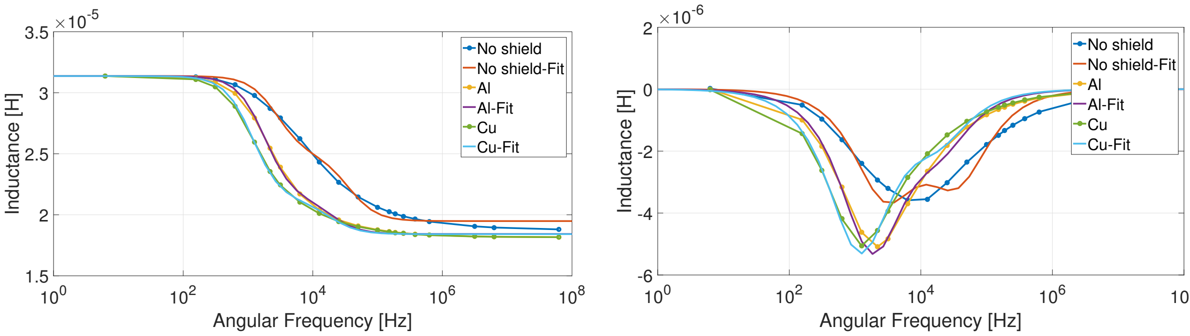

(a) $\mathrm{Re}(L_d(\omega))$ (b) $\mathrm{Im}(L_d(\omega))$

Fig. 5.16. Complex Inductance components with Second Order fitting

5.2 Extended circuit

The second order effects due to the electromagnetic shielding analyzed in the previous section demand a more in depth and accurate representation of the machine dynamic model. The dynamic behaviour can be cast into state space analysis form augmenting the states from the standard 2x2 system describing the SPM motor. This yields a model accounting for eddy currents in the rotor, in a similar way to how the induction motor is treated. Topologically speaking a wound rotor synchronous machine equipped with damper windings [114], or an online starting synchronous permanent magnet machine [115] could be treated dynamically in the same way. Two extra branches are added to the two different circuit sides, direct and quadrature, accounting for eddy current damping effects.

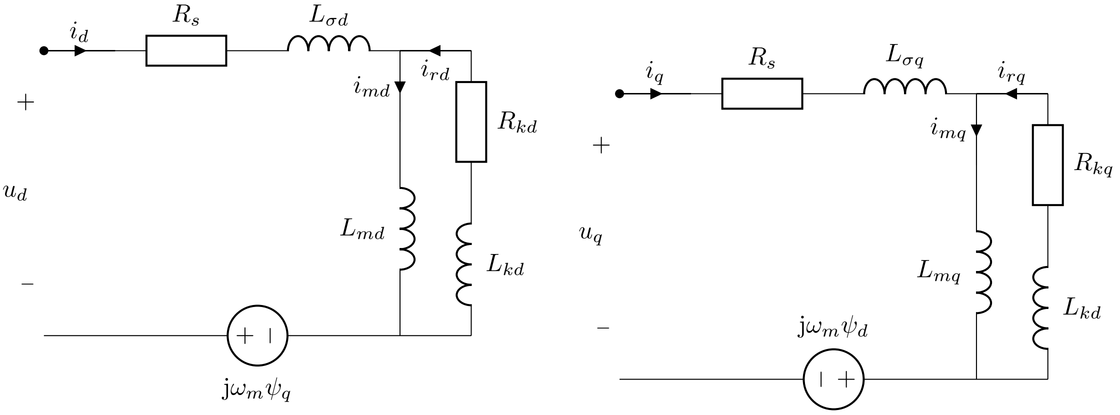

(a) *D-axis circuit* (b) *Q-axis circuit*

Fig. 5.17. Extended equivalent circuit in rotating coordinates.

Assuming an extra branch for both *d* and *q* axis yields equations (5.22):

$$\begin{cases} v_d = R_s i_d + \dfrac{d\psi_d}{dt} - \psi_q \omega_m \\ v_q = R_s i_q + \dfrac{d\psi_q}{dt} + \psi_d \omega_m \\ 0 = R_{kd} i_{kd} + \dfrac{d\psi_{kd}}{dt} \\ 0 = R_{kq} i_{kq} + \dfrac{d\psi_{kq}}{dt} \end{cases} \tag{5.22}$$

The subscripts *kd* and *kq* represent all the lumped parameters quantities along the extra branches, which are short-circuited and connected in parallel to the magnetization branch. A state space representation in terms of fluxes [106], is given by (5.23):

$$\begin{cases} \dfrac{d\psi_d}{dt} = v_d + \omega_m \psi_q - R_s i_d \\ \dfrac{d\psi_q}{dt} = v_q - \omega_m \psi_d - R_s i_q \\ \dfrac{d\psi_{kd}}{dt} = -R_{kd} i_{kd} \\ \dfrac{d\psi_{kd}}{dt} = -R_{kq} i_{kq} \end{cases} \tag{5.23}$$

where the flux expressions for both axes can be expressed as (5.24):

$$\begin{cases} \psi_d = L_d i_d + L_{md} i_{kd} + \psi_{\mathrm{PM}} \\ \psi_q = L_q i_q + L_{mq} i_{kq} \\ \psi_{kd} = L_{md} i_d + L_{kd} i_{kd} + \psi_{\mathrm{PM}} \\ \psi_{kd} = L_{mq} i_q + L_{kq} i_{kq} \end{cases} \tag{5.24}$$

The parameters having an extra *m* in the subscript highlight the mutual inductance only (whereas we remember that L_d or L_q alone stand for the cumulative inductance, i.e. both mutual and leakage). The computation of a closed form state space model for current and fluxes dynamics is succinctly synthesized by (5.25):

$$\begin{cases} \dfrac{d\boldsymbol{\psi_s}(t)}{dt} = \boldsymbol{A}\boldsymbol{\psi_s}(t) + \boldsymbol{B}\boldsymbol{u_s}(t) + \boldsymbol{b}\psi_{\mathrm{PM}} \\ \boldsymbol{i_s}(t) = \boldsymbol{C}\boldsymbol{\psi_s}(t) + \boldsymbol{d}\psi_{\mathrm{PM}} \end{cases} \tag{5.25}$$

In this case the vector $\boldsymbol{\psi_s}$ has components: d and q for the standard branch and k_d, k_q in the extra branch. The matrices involved in the full state formulation take the form highlighted in (5.27), (5.28), (5.29), (5.30). Fictitious parameters are introduced to make notation more concise. L_{ls} and L_{MD}, L_{MQ}, stand for leakage inductance and two additional mutual inductances along the two axes, respectively. The definition of L_{MD} is given in (5.26). Equivalently the definition of L_{MQ} is the same, just employing L_{kd} and L_{md} instead.

$$L_{\mathrm{MD}} = (1/L_{ls} + 1/L_{kd} + 1/L_{md})^{-1} \tag{5.26}$$

$$\boldsymbol{A} = \begin{bmatrix} \frac{R_s L_{MD}}{L_{ls}^2} - \frac{R_s}{L_{ls}} & \omega_m & \frac{R_s L_{MD}}{L_{ls} L_{kd}} & 0 \\ -\omega_m & \frac{R_s L_{MQ}}{L_{ls}^2} - \frac{R_s}{L_{ls}} & 0 & \frac{R_s L_{MQ}}{L_{ls} L_{kq}} \\ \frac{R_{kd} L_{MD}}{L_{ls} L_{kd}} & 0 & \frac{R_{kd} L_{MD}}{L_{kd}^2} - \frac{R_{kd}}{L_{kd}} & 0 \\ 0 & \frac{R_{kq} L_{MQ}}{L_{ls} L_{kq}} & 0 & \frac{R_{kq} L_{MQ}}{L_{kq}^2} - \frac{R_{kq}}{L_{kq}} \end{bmatrix} \tag{5.27}$$

$$\boldsymbol{b} = \begin{bmatrix} \frac{R_s L_{MD}}{L_{ls} L_{md}} \\ 0 \\ \frac{R_{kd} L_{MD}}{L_{kd} L_{md}} \\ 0 \end{bmatrix} \tag{5.28}$$

$$\boldsymbol{C} = \begin{bmatrix} -\frac{L_{kd}}{(L_{md}^2 - L_d L_{kd})} & 0 & \frac{L_{md}}{(L_{md}^2 - L_d L_{kd})} & 0 \\ 0 & \frac{L_{mq}}{(L_{mq}^2 - L_q L_{kq})} & 0 & -\frac{L_{kq}}{(L_{mq}^2 - L_q L_{kq})} \\ \frac{L_{md}}{(L_{md}^2 - L_d L_{kd})} & 0 & -\frac{L_d}{(L_{md}^2 - L_d L_{kd})} & 0 \\ 0 & \frac{L_{mq}}{(L_{mq}^2 - L_q L_{kq})} & 0 & -\frac{L_q}{(L_{mq}^2 - L_q L_{kq})} \end{bmatrix} \tag{5.29}$$

$$\boldsymbol{d} = \begin{bmatrix} \frac{L_{kd} - L_{md}}{L_{md}^2 - L_d L_{kd}} \\ 0 \\ \frac{L_d - L_{md}}{L_{md}^2 - L_d L_{kd}} \\ 0 \end{bmatrix} \tag{5.30}$$

The comparison shown in Fig. 5.18 and Fig. 5.19 is the result of a steady state current control strategy. A two degrees of freedom PI controller, based on the robust pole placement technique proposed in [116] is employed. The control is performed at constant rated 14000 [rpm] speed,

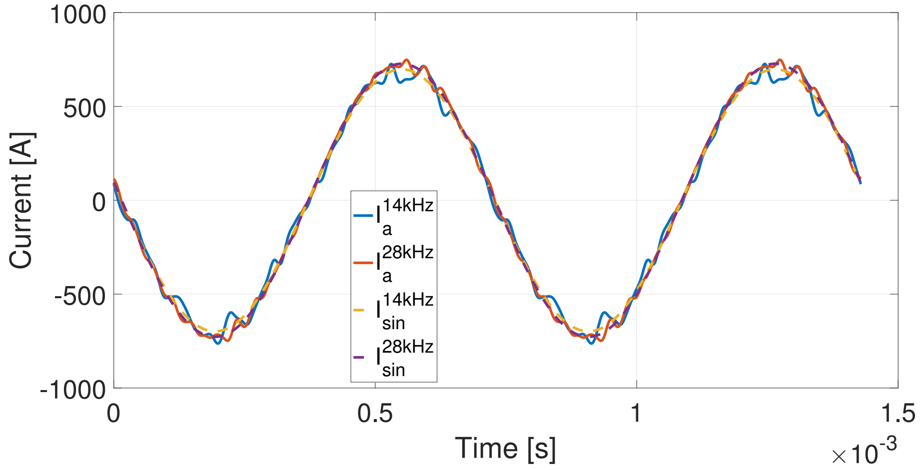

(a) *Standard circuit current waveforms*

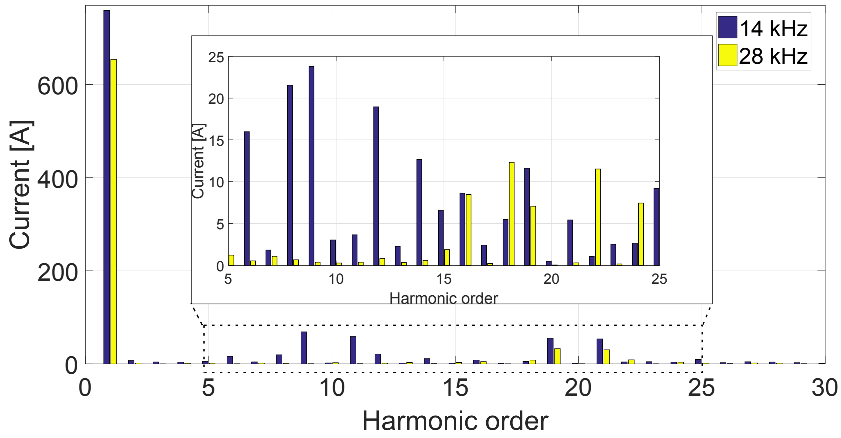

(b) *Standard circuit harmonic content*

Fig. 5.18. Standard circuit resulting waveforms at different switching frequencies.

tracking a full rated load current, all required for the q axis. In both figures the complete waveform is compared with the dashed line representing the first harmonic component (this one referred with the "sin" sub-script). The higher switching preserves a higher fundamental harmonic content, which is ultimately the one responsible for torque generation. This justifies for the 14 [kHz] switching the small, yet detectable, drop of torque for the same current, reported in subsection 5.1.2. The VSI switching logic is based on Continuous Space Vector Modulation with an equal sampling and switching frequency. Considering a Voltage Source Inverter fed motor, the current ripple is anticipated to have a significant impact on the motor performance. [117]. It is interesting to notice as even the extended circuit dynamic model can follow a current reference simply controlling the only two available states, d and q axis currents. This seems to be an indication of the current control method robustness, even in the presence of rotor eddy current

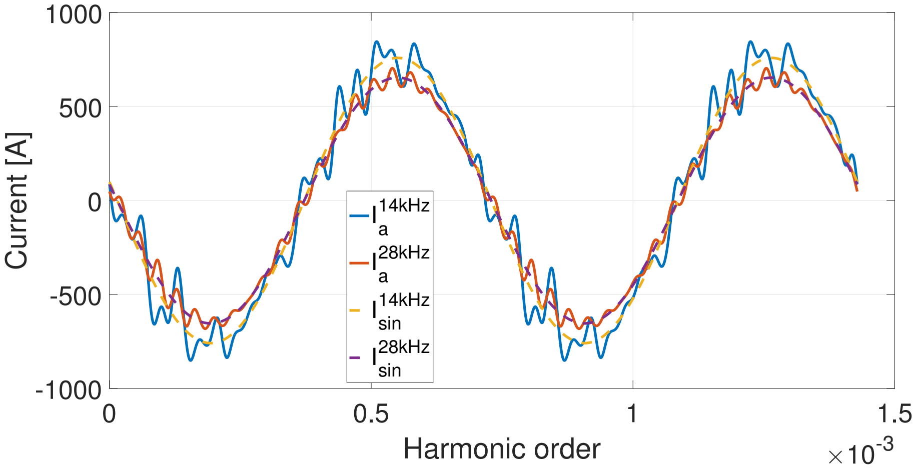

(a) *Extended circuit current waveforms*

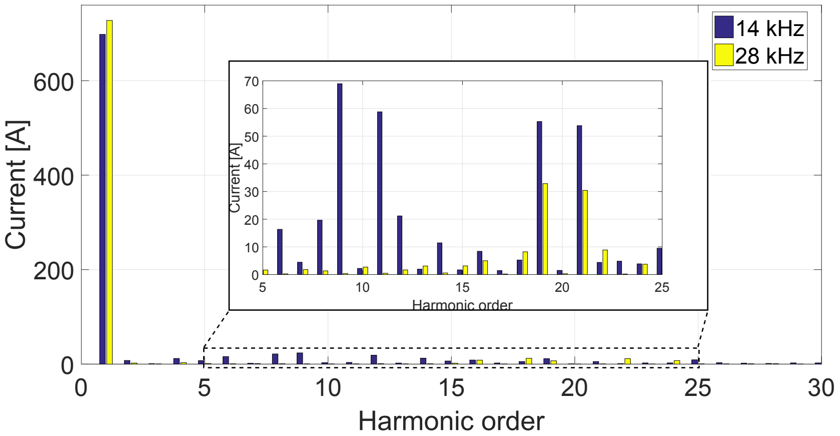

(b) *Extended circuit harmonic content*

Fig. 5.19. Extended circuit resulting waveforms at different switching frequencies.

damping. It is in fact worthy to observe as the two extra branches of Fig. 5.17 are described by two unaccessible states, unless a proper observer is designed for them.

5.3 Mechanical Structural Integrity

The sleeve size dimensioning is performed according to an extended analytical model embedded in the optimization process, as presented in Chapter 3. The final materials employed for the rotor components are shown in Tab 5.2. The rotor has been simulated by means of 3D mechanical FEA, to check component stresses both at zero and over-speed (+20% than nominal) conditions, as per Fig. 5.20. The figure shows the simulated domain [1], restricted to a single axially-half cut spoke, exploiting the geometrical symmetry. At zero-speed the radial stress concentration occurs at the spoke smallest cross section, while the tensile stress peak value belongs to the inner diameter of the retaining sleeve. For the over-speed condition, the arrows point to the real peak value of stresses (numerical errors affected sharp corners that for the sake of simulation time were left in the modelled geometry, but are not present in reality).

Table 5.2. Rotor Parts Mechanical Properties

Material	Material	Yield Stress	Young Modulus	Therm. Expansion Coeff.
Shaft/hub	Stainless Steel 17-4PH	900 MPa	200 GPa	12e-6 1/K
Magnets	SmCo-Recoma 30	140 MPa	120 GPa	8e-6 1/K
Sleeve	Zylon/Carbon Fibre	>3000 MPa	186 GPa	-1e-6 1/K

The tensile stress is again maximum around the inner bore of the sleeve. Radial stress concentration affects the smallest spoked cross section, but now in expansion (positive pressure). The outer shaft diameter does not experience positive pressure values, witnessing no lift-off. Care must be taken because there is inaccurate modelling of the retaining sleeve: Zylon is an anisotropic composite fibre, but it has been modelled as a solid medium. This is due to difficulties in accurate modelling of composite fibres in FEA codes, as well as no availability of anisotropic behaviour data for this specific fibre [2]. Results must then be taken cautiously in terms of accuracy. Nonetheless, no particular stress concentration was observed in the other components, apart from the fibre, encouraging the assumption of a safe operation within the machine speed range. Fig. 5.20 highlights the worst case conditions with a maximum tensile stress for over speed above 1700 [MPa] and for zero speed 1400 [MPa]. Being a composite fibre, Zylon yield stress is equivalent to the ultimate tensile stress. Zylon stress goes as high as 5.8

---

[1] For a complete view of the rotor structure refer either to Fig. 5.26 in the proceedings of to Appendix A.

[2] Even if these were employed the simulation time for the domain analyzed would be prohibitive.

[GPa], [105], but as defined in Tab. 5.2 for safety reasons a 3000 [MPa] has been deemed as safety margin. This compares to about double the simulated maximum tensile strength value. Equivalently the maximum radial stress for the steel made spoke is below the yield strength of the 17-4PH alloy employed. These results give enough confidence the structural design is sound.

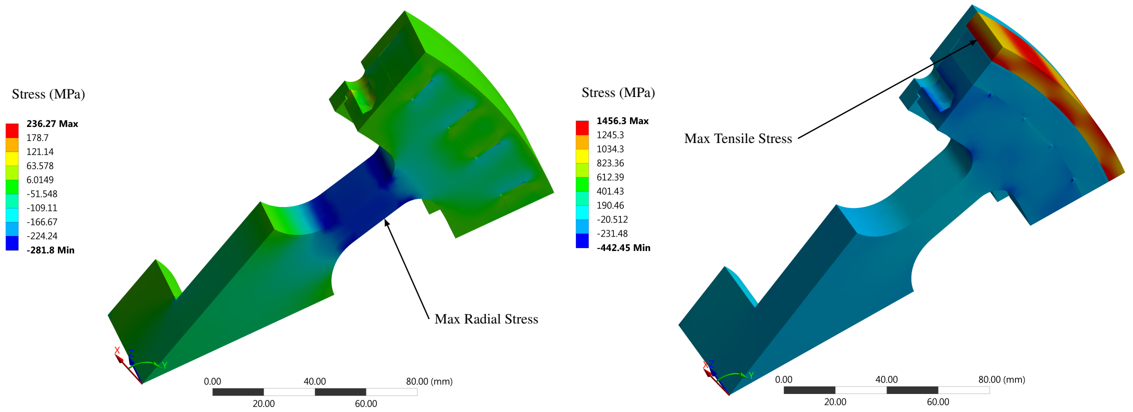

(a) *Zero-speed radial stress* (b) *Zero-speed tensile stress*

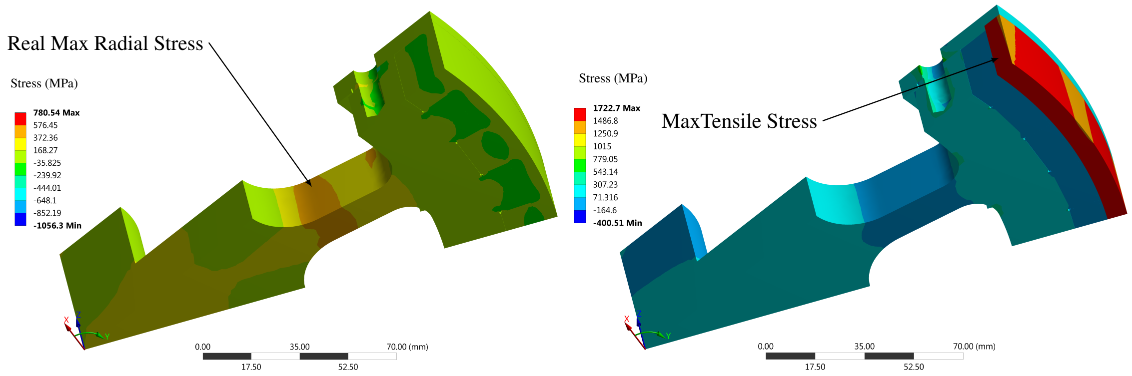

(c) *Over-speed radial stress* (d) *Over-speed tensile stress*

Fig. 5.20. Structural analysis

5.3.1 End-Plates

The presence of end-plates/cheeks/collars on the rotor is fundamental. The plates do not just constrain the PMs segments axially, they also provide a counteracting force against the axial expansion experienced by the sleeve. The wrapping process itself involves considerable pre-tension build up onto the bandage layers: the wound filament tries to relax, escaping at the axial ends. From previous manufactured rotors it has been observed that forces are substantial: end rotor plates deflected enough to allow the fibre to penetrate between collar and magnets. Once this happens the first fibre going into the gap will open it up allowing more filaments to enter, thus pushing the collar out further. If this is allowed, the PMs axial edge could be damaged, quite catastrophically. Thus it is very important to ensure there aren't any axial gaps in the rotor which could open up and deflect the end-cheeks. If the collars are solid enough then they will not move even if a few strands enter into a tiny gap. When winding over an existing cured sleeve, then the existing sleeve is already stretched and will not shrink in the radial direction, instead it will expand axially for two reasons:

- The radial pressure of the new wind will compress the sleeve radially and thus force it out axially.
- Tension in the new layer will reduce radial stress in the layer it is being wound on to, causing it to escape axially

Utilizing end-plates poses challenges; not only mechanically, but also electromagnetically.
Mechanically, the end plates must be able to sustain axially induced and centrifugal forces throughout the speed and temperature range of the machine. Electromagnetically, the plate should not modify the electromagnetic behavior of the assembly as a whole. It is indeed very tempting to have a single shaft/hub radially supporting the magnet assembly and simultaneously providing an axial and circumferentially castellated feature to sustain axial forces. If the material is even slightly magnetic, a risk of magnetic short-circuiting could arise. This effect is clearly noticeable in Fig. 5.21. Fig. 5.22 depicts the short circuiting effect on the Halbach array flux. The magnetic plate reduces the flux-linkage by 30%.
Electromagnetically, the conductivity should be preferably small enough to reduce the formation of eddy currents to a point where they do not create significant extra rotor losses. The most

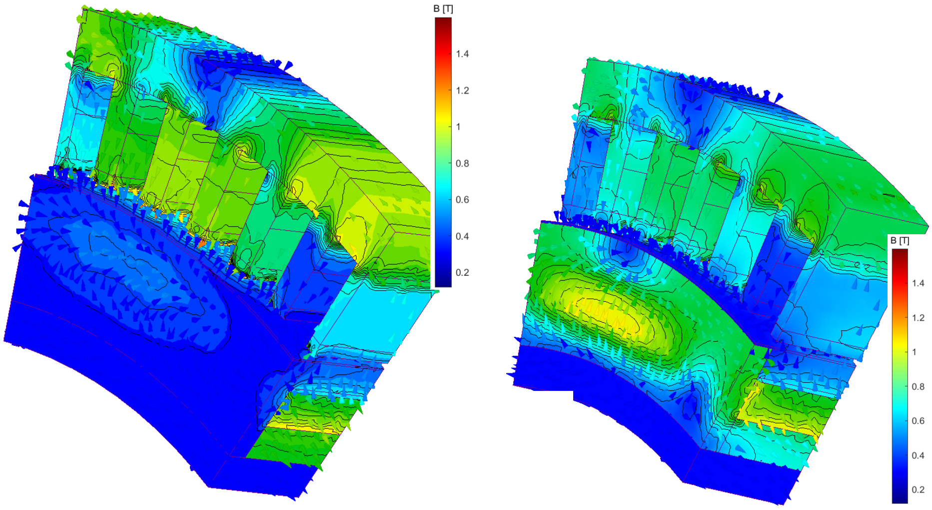

(a) *Non Magnetic Collar* (b) *Magnetic Collar*

Fig. 5.21. Flux map comparison between magnetic and non magnetic collar.

Material	Yield Strength [MPa]	Density $[\mathrm{kg/m^3}]$	El. Cond. [Scm]	Therm. Cond. [W/mK]
Ti-6Al-4V	880	4430	562000	6.7
Stainless Steel 316	300	8000	1350000	16.2
Inconel 718	1100	8190	800000	11.4

Table 5.3. End-plates material properties.

pertinent properties of possible rotor materials provided by the manufactures are listed in Table 5.3.

As in many cases the options are conflicting. Diamagnetic stainless steel (316 alloy) constitutes by far the cheapest option, and the most appealing thermally. Unfortunately, it must be discarded for the lowest yield strength capability, without considering the detrimental highest electrical conductivity among the possible choices. The final selection, between Titanium and Inconel, is substantially dictated by cost and weight factors. Inconel is very expensive and its machining process is a tough challenge to undertake, due to the material's tendency to harden when worked. In addition, the density is twice as much as the Titanium, contributing to a significant drop of rotor power density. On the other hand Titanium, despite having the lowest thermal conductivity, offers a sensible compromise between robustness and weight. Moreover, it has a lower electrical conductivity, limiting the loss increase. Finally, the specific alloy Ti-6Al-4V (grade 5) is widely available, so it has been picked as the preferred material.

The axial arrangement of the rotor parts can be seen in detail in Fig. 5.23(a). Note that there

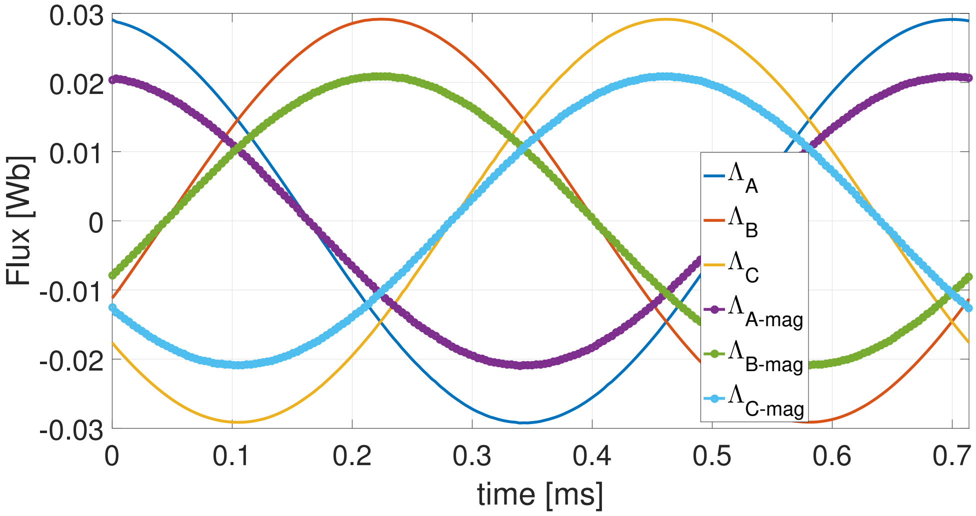

Fig. 5.22. Flux linkage comparison between magnetic and non magnetic collar.

must be a contact point between end plate and the PM at the PM outer diameter only. In this way the end-plates are not flexed outwardly by a lever point at, or below, the bottom of the PM. The lever point arises because the plates will be bolted at the outer shaft-assembly axial ends. With a clamping force due to the bolts at the lower edge of the end-plate a reactive force works to close the gap at the PM outside diameter. Without a gap the reactive force is still located at the lower PM edge, so that there is a lever effect trying to create a gap at the PM outside diameter.

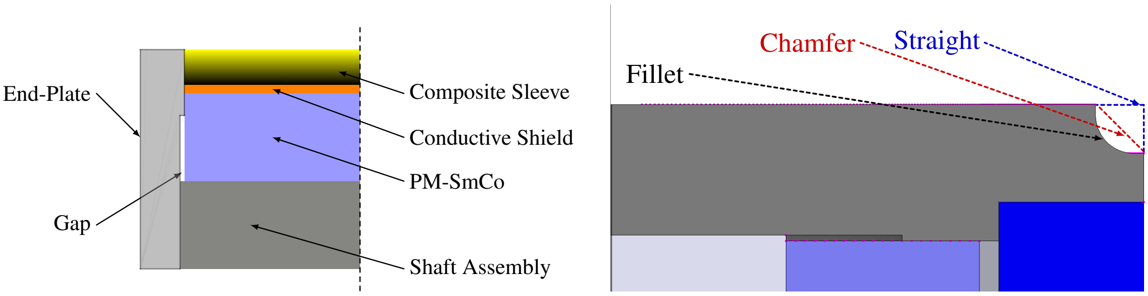

(a) *End Plate arrangement* (b) *End plate feature*

Fig. 5.23. Axial rotor containment with end-plate feature.

Eddy current losses are intrinsically a three dimensional effect. Employing titanium rings effectively adds a conductive component which is subject to asynchronous flux density harmonics. This will generate additional losses. An estimation of these has been attempted using FEA. Losses have been computed for a 14 [kHz] switching frequency with a single inductance (over frequency) dynamic model (standard dynamics for SPM motor) control scheme. The shield is effectively screening the PMs and the conductive shaft. Considerable losses are detected in the end plate. Means to reduce these high losses in the end-plates are needed. Due to space restrictions, and modifications limitations, a fillet feature has been investigated along the rotor outer periphery. This reduces the end-plate loss, Fig. 5.24 (b). The related loss distribution is visualized in Fig. 5.24 which shows the induced current density pattern. For simulation timing reasons the cut-out of the machine was simulated at half axial length and single pole. For machinability purposes the easier choice of material removal adopted is a 45° chamfer, Fig. 5.23 (b). This feature is imperative for the drive to operate at high switching frequencies without exceeding excessive losses in the rotor.

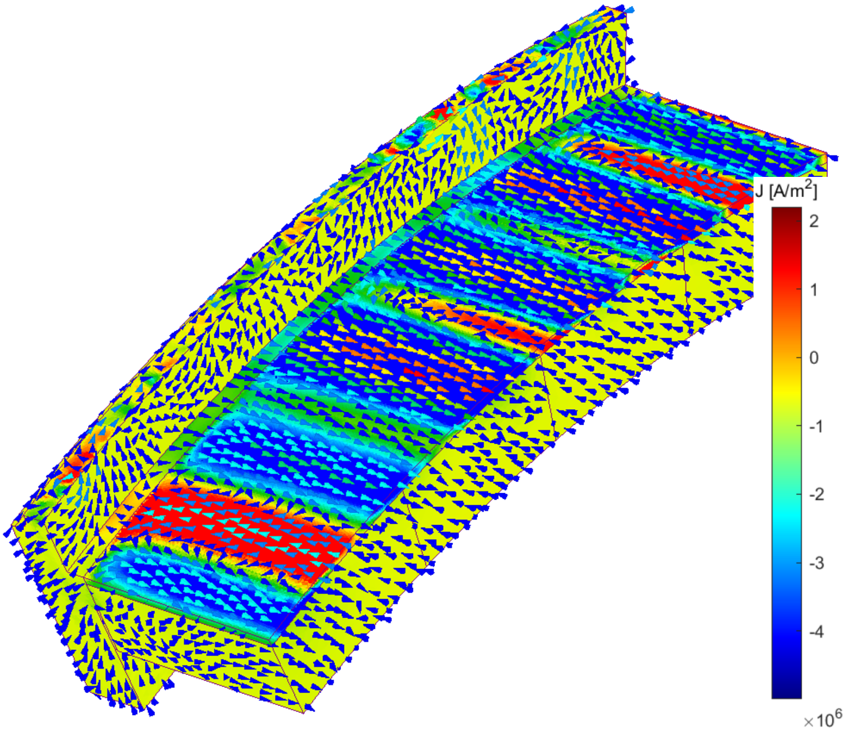

(a) *Current density pattern*

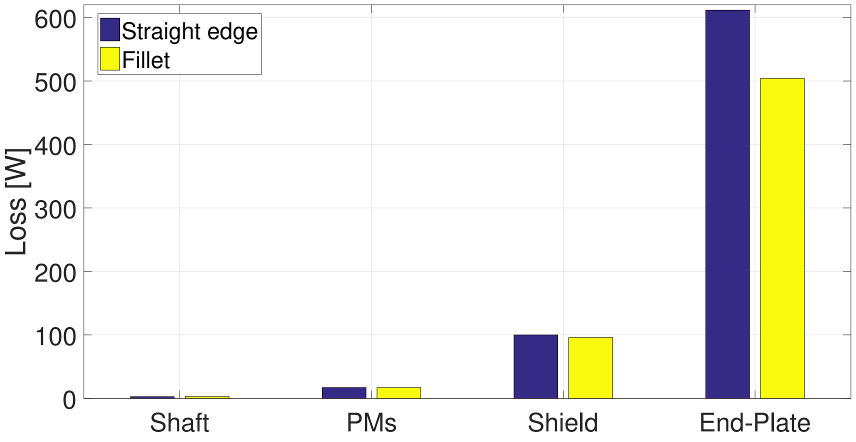

(b) *Rotor loss split*

Fig. 5.24. EC density pattern in rotor conductors with losses comparison.

5.4 Bearings

High speed operation of this machine requires high precision bearings: standard ball bearings cannot withstand high velocities. Bearing material and lubrication play a notable role in determining the speed range and limits. It is well known that ceramic bearings can be extremely expensive: this option had already been ruled out from the very beginning. Due to equipment availability the lubrication advised was grease, rather than the more complicated oil jet lubrication. This ensures no extra equipment is needed for bearing cooling. Nonetheless, angular contact bearings do not come with seals. Attention must be paid to carefully prevent inevitable grease leaks towards other parts of the motor. Furthermore, grease will degrade and reduce with time, so bearings must be frequently lubricated with extra grease when needed.

Apart from bearing type, ball material and lubrication options, the arrangement choice is equivalently crucial: this determines not only speed capability, but also directly affects the stiffness of the entire spinning assembly as well as bearing life. As the machine under study is a prototype, bearing life has been given secondary importance. The major driver for defining a suitable choice has been dictated by the stiffness and correct operation of the rotor. The choices available were:

- a pair of pre-loaded angular contact bearings back to back at the Non Drive End (NDE) coupled with a cylindrical roller at the Drive End (DE). This arrangement has been employed in high speed existing solutions [11] as it guarantees a good stiffness due to mainly the angular contact pair, as well as a good radial load compliance at the shaft DE, feature which is peculiar of the cylindrical roller configuration.
- a pair of pre-loaded angular contact bearings back to back at the DE, coupled with a single row of angular contact bearings at the NDE, softly constrained by a spring-washer solution.

The first arrangement has been considered to be unsuitable due to the under-loaded cylindrical roller. An under-load condition is estimated at the DE. The load the bearings are subjected to is primarily due to the rotor weight. In this case the bearing does not exhibit a radial load, since the torque ripple is expected to be very low, rather an electric motor delivers a pure torque averaged over one sixth of an electric cycle, whereas in other applications such as internal or reciprocating combustion engines very unbalanced and non symmetric torque profiles cause significant radial loads to the bearings. The self-weight of the rotor is almost insignificant in the load balance. Provided there are no considerable unbalances during operation (these can be due to either intrinsic rotor unbalance due to manufacture, or eccentricity, or both), combined with the absence of gearboxes or other radial load components at the shaft, the bearings do not experience much radial load.

The second arrangement ensures a minimum load condition for all bearings in the assembly. The single bearing at the NDE provides an axially floating slack mechanical constraint. This ensures expansion release due to heat, and is compensated for by the washer that still keeps the outer race loaded. In both arrangements the spindle bearing pair has a reducing speed factor related to the type of reciprocal single bearings in the pair positioning (back-to-back, face-to-face or tandem). This factor applies in this case due to the low intrinsic pre-load expected. If on one hand employing a paired arrangements of angular contact bearings helps to increase the equivalent stiffness of the arrangement, on the other it brings the pair speed limit down.

The final choice is presented in Fig. 5.25: (a) depicts a cut-out of the shaft whereas (b) shows the diagram representation of the arrangement along the axial profile with the red arrows signifying the loads. HCB71909-C-T-P4S-DUL for the back to back DE pair, whereas HCB71908-C-T-P4S-UL for the NDE washer preloaded [118] [3].

---

[3] HCB stands for Hybrid Standard ceramic bearings, the subsequent numerical values represent the dimension series (light, medium or heavy) along with the the bore size code, C is an alphanumeric specifying the contact angle, T stands for the presence of a cage as guiding medium, P4S is an internal code for standard tolerance levels from manufacturer, U is for single whereas DU for double set (pair), L for light pre-load.

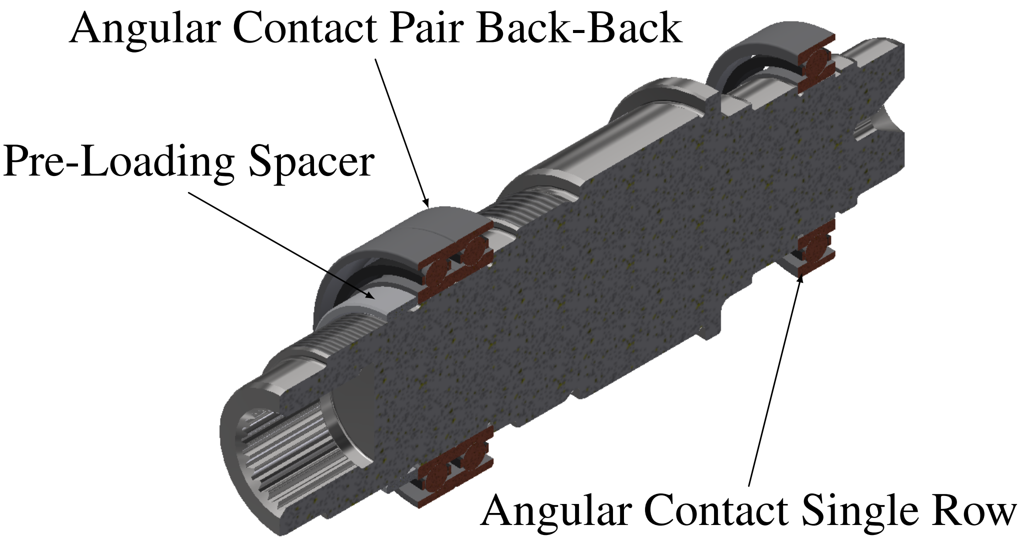

(a) *Shaft cut-out*

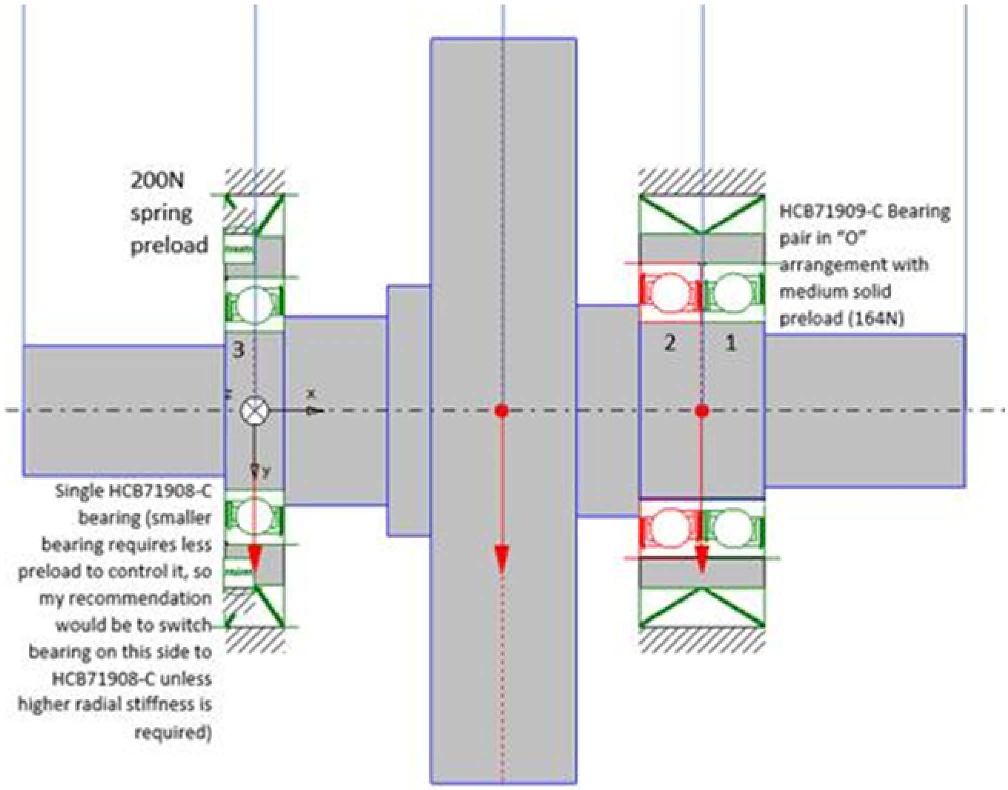

200N spring preload

HCB71909-C Bearing pair in "O" arrangement with medium solid preload (164N)

Single HCB71908-C bearing (smaller bearing requires less preload to control it, so my recommendation would be to switch bearing on this side to HCB71908-C unless higher radial stiffness is required)

(b) *Bearings sketch/loading/choice*

Fig. 5.25. Bearings arrangement.

5.5 Rotor-dynamics

Any rotating system is prone to instability, mostly due to resonant modes occurring around specific frequencies at which the rotor component is self-ecxited. Intrinsically speaking the rotor geometry exhibits a very low torsional stiffness. This is due to the unusually low aspect ratio (rotor-length over rotor outer diameter), and is further exacerbated by the presence of spokes. As a proof of concept, spokes could be omitted. However, they are necessary in terms of manufacturing process, in order to allow clamping tools to be put in place when the retaining sleeve is wrapped around the rotor.

5.5.1 Parametric analysis

As will be shown later in this section, the torsional and bending vibrations seem to occur outside of the operating speed range (0-14000 [rpm]). No coupling assumptions have been considered in the modelling between the different rotor assembly components. This is equivalent to assume a worst case scenario, as the stiffness is reduced with respect to reality: a lower stiffness for the same moment of inertia delivers lower resonance frequencies. Positioning of critical speeds in the frequency spectrum is mainly dictated by:

- bearing distance from the rotor center of mass
- bearing stiffness
- structural properties of the rotor itself

Concerning the first point, the bearing distance variation has an implication on the bending mode frequency, as shown in [119]. The Rim-Driven rotor is thought of as a disk body attached to a flexible uniform shaft, sustained by rigid bearings, the stiffness matrix on the rotation plane is inversely proportional to the bearing distance from the center of mass. This occurs because the disk which intrinsically possesses almost the totality of mass and moment of inertia contribution of the rotor.

As regards the torsional modes, increasing the inter-bearing distance is detrimental (if the shaft stretches axially), since for a larger shaft length the twist angle of the structure for a constant torque, modulus of rigidity of the material and torsional constant (peculiar of the beam geometry), is higher.

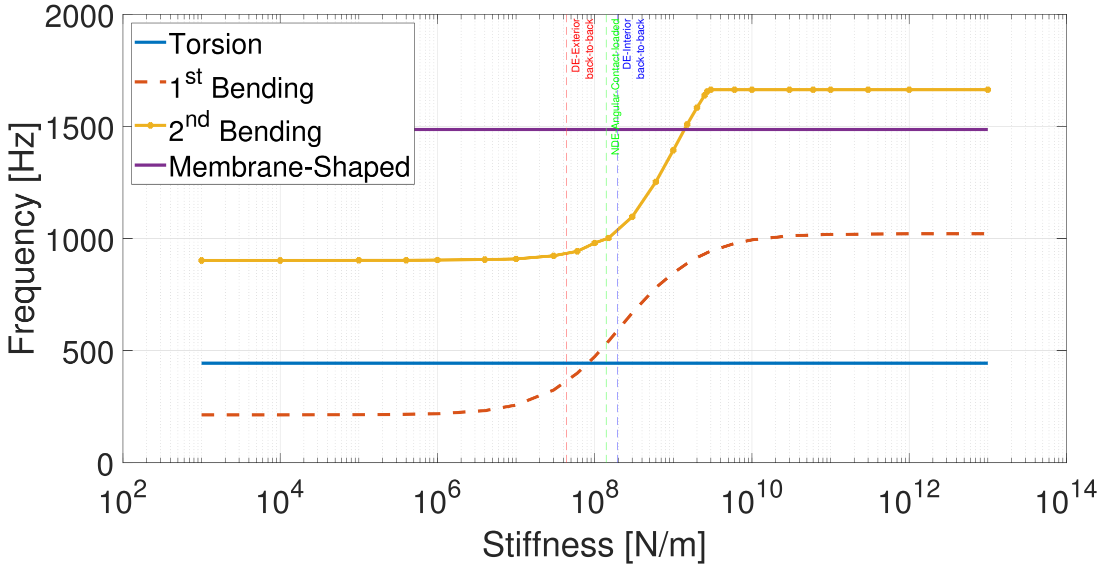

Fig. 5.26. Geometrical features varied for sensitivity and optimization against critical speeds.

Fig. 5.26 illustrates the variation of resonant frequencies for the shaft/hub assembly. Clearly noticeable is the invariance of torsional and membrane-shaped modes with the stiffness. This is because the former depends on the torsional stiffness of the assembly as well as the inter-bearings distance. The latter is a sole property of the geometrical structure. The dependency of bending frequency on bearing stiffness is both evident and expected. The second bending frequency presents a much sharper saturation knee, but it is high in magnitude and is not expected to create an issue. Bearing stiffness values were provided by the manufacturer, based on overall rotor mass and bearing location with respect to the centre of mass. These are unfortunately located in the fairly low range ($10^7 - 10^8$[N/m]), yet still position the resonances outside the machine speed range. All the resonant frequencies have been computed without considering damping, at null speed, without therefore accounting for the gyroscopic effect.

Fig. 5.27 sketches the geometrical variations investigated for increasing the critical speed with different vibration modes. The investigation has been conducted on the shaft only, as this is the only non-active part over which there was a design freedom.

Fig. 5.28 assumes a constant distance between bearings. Furthermore, in first approximation, the bearing stiffness does not change when the geometrical features of outer and inner fillets are varied. This is not strictly true, as the load due to the mass and small variations of moment of inertia of the disk will affect the bearing stiffness. However, these possible variations have been hypothesized to be minimal compared to the difference in critical speeds that the geometrical changes bring forth. Results in Fig 5.28 are presented in terms of contour plots, highlighting the level surfaces related to simultaneous variation of inner and outer fillets for the spoked rotor disk geometry. The optimal choice is dictated by the lowest critical speed, which happens to be a torsional mode. In the plots a round blue dot identifies the optimal combination. Nevertheless this has not been the final design choice, as employing such a small outer fillet would have compromised the stress resilience of the outer rim. Therefore, coloured in red, the diamond shaped dot locates the design decision as a sub-optimal choice.

Fig. 5.29 shows the first 4 resonant mode shapes for the final design. The bearing supports have been modelled as localized springs with isotropic stiffness along the radial cross sectional axis. Magnifying representation coefficients have been specified in captions for all the different modes. Finally the numerical values are summarized in Tab. 5.4. It is very clear that all the frequencies are reduced with respect to the shaft only. This is obvious and expected due to additional consistent weight and moment of inertia, due to magnets, retaining axial plates, bolts, shield and composite wrapping. As anticipated before, these were not assumed to contribute in any way to the structure stiffness, even if up to a certain degree they probably participate. It is difficult to understand how much this impacts the real stiffness due to the uncertainty related to the nature of the material contact and manufacturing of the assembly.

For the sake of observational completeness, extra geometrical features recognizable in the vibration plot are represented by the end plates and their retaining bolts.

Table 5.4. Natural frequencies

Mode	Vibration type	Frequency [Hz]	speed [rpm]
1	Torsional	338	20280
2	Bending	409	24540
3	Second Bending	781	46860
4	Membrane-shaped	1150	69000

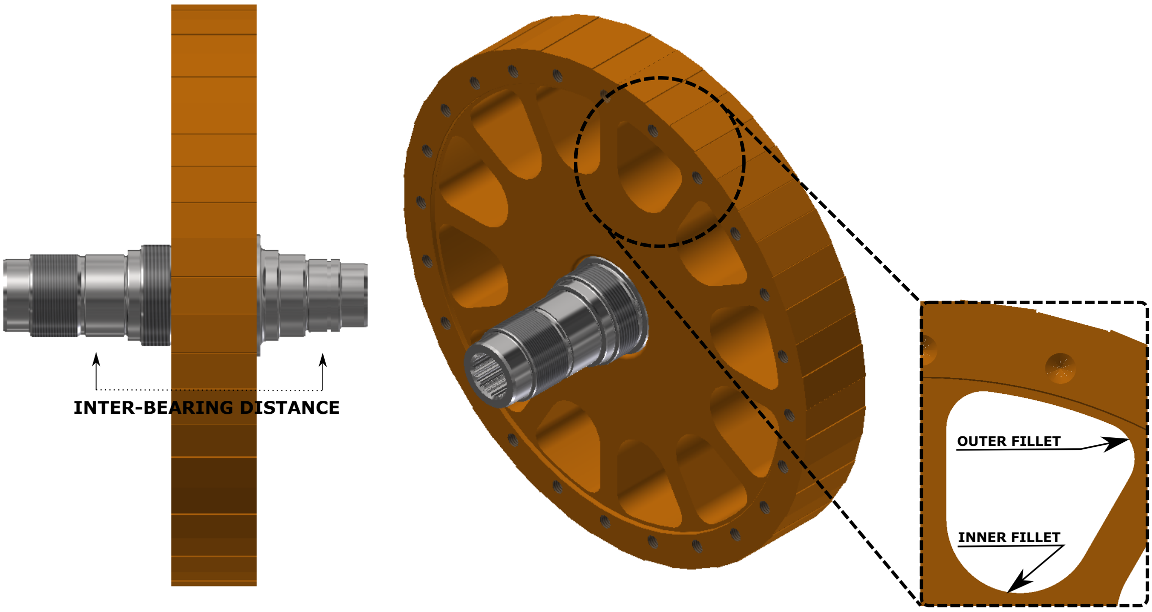

Fig. 5.27. Geometrical features varied for sensitivity and optimization against critical speeds.

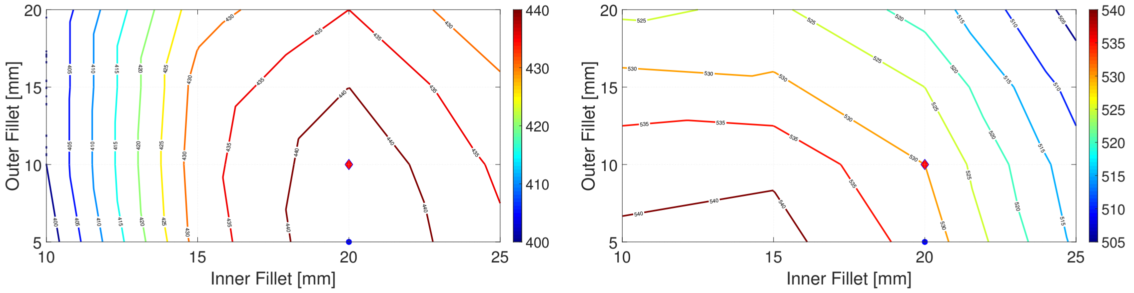

(a) *Torsional vibration mode*

(b) *First bending mode*

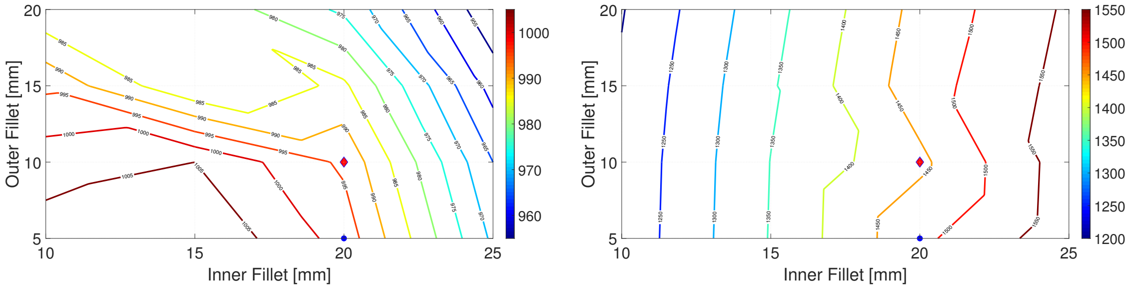

(c) *Second bending mode*

(d) *Membrane shaped vibration mode*

Fig. 5.28. Shaft sensitivity analysis.

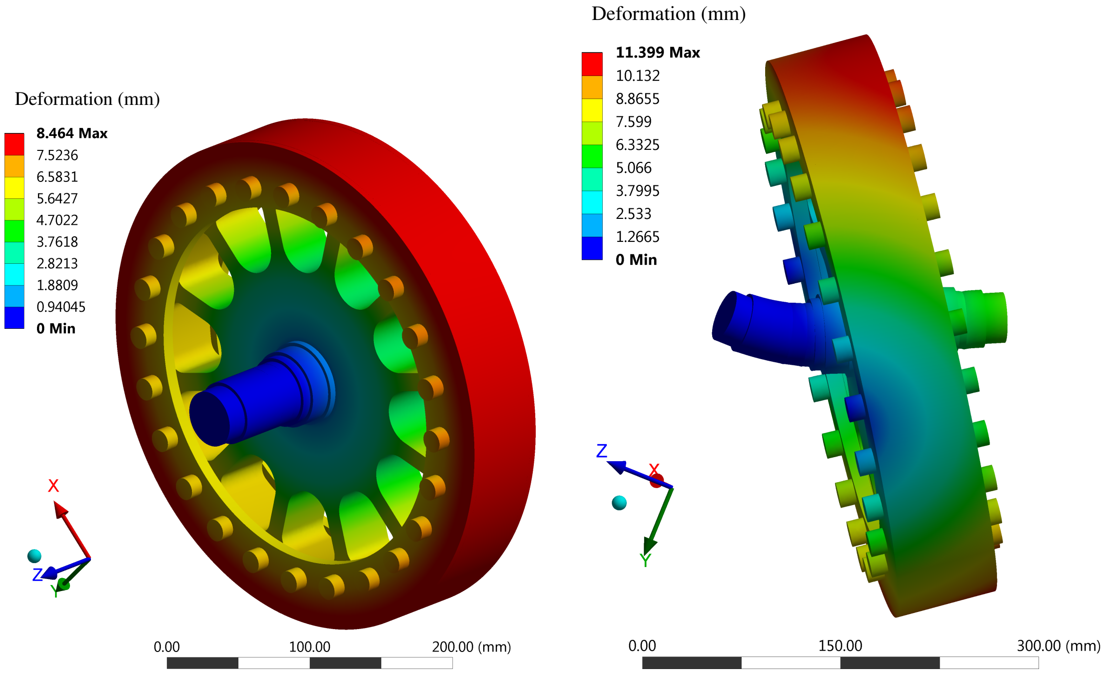

(a) *Torsional vibration mode* (b) *First bending mode (13X)*

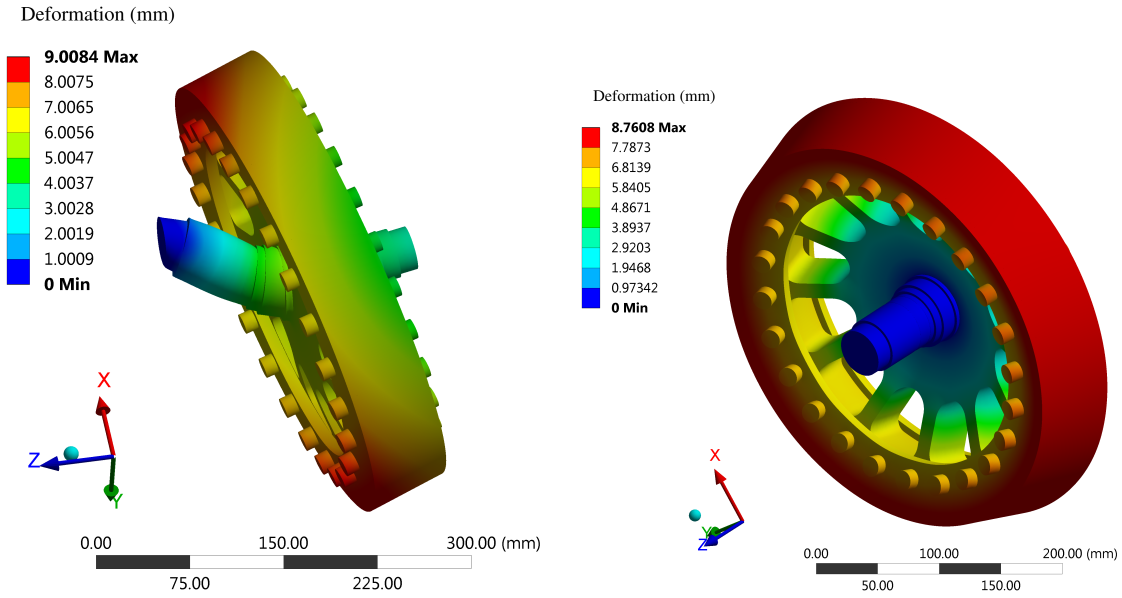

(c) *Second bending mode (9X)* (d) *Membrane shaped vibration mode (6X)*

Fig. 5.29. Vibration modes.

5.6 Thermal aspects

Thus far the thermal management demand of the motor has not been considered. Recalling the assumption for the final design choice made in the first paragraph of this chapter, the decision has fallen to limit the electric loading to 100000 [A/m], a limit recognized as a standard for air-cooled electrical machines. This has been supported by the fact that considering a hypothetical operational at altitude, the environment temperature is typically -50 °C. This will enhance heat extraction performance, within the limits of a reduced pressure at altitude. Nonetheless, considering that the targeted current density for continuous operation is 12 [A/mm^2] (a value associated usually with liquid cooled management systems) liquid cooling was chosen for validating the prototype in the laboratory conditions; at standard atmospheric pressure and 20°C temperature. To keep the design reasonably simple, yet representative, a channel solution similar to the one presented in [120] has been implemented. This is presented at design stage in sub-figure 5.30 (a), highlighting the flow direction and the intricacy needed to accommodate the locating bolts of the three stator components. At prototype stage a detail for the cooling channel on the stator housing plate is shown in sub-figure 5.30 (b).

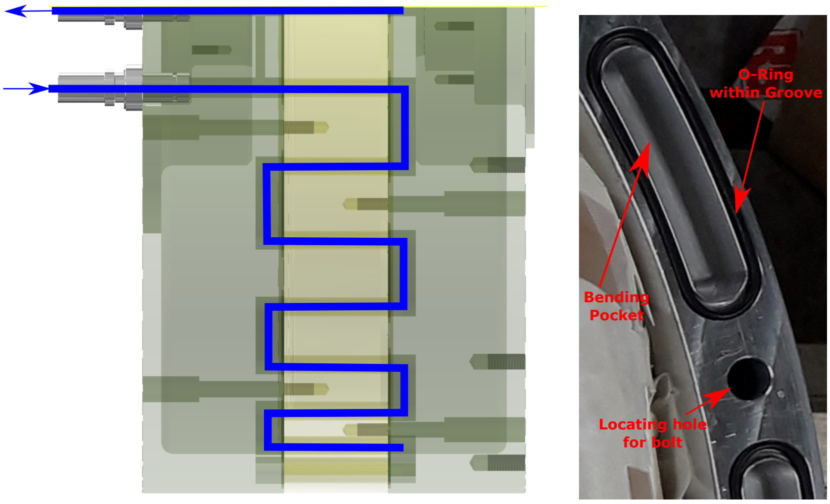

(a) *2D cooling channels view.*

(b) *Cooling channel picture detail*

Fig. 5.30. Cooling channels views.

5.7 Final design

After the initial topologies choices of Chapter. 3, geometrical optimisation of Chapter 4, and the tuning design performed in this chapter the final geometrical, electrical and mechanical design features are defined in Tab. 5.5. The geometrical values are drawn from the SmCo optimum chosen from the Pareto front represented in Fig. 4.28 at the horizontal limit of the electrical loading boundary defined. As seen in the more detailed electromagnetic rotor and drive modeling the shield thickness is established to be 1.00 [mm], made by Aluminium. The sleeve thickness of 7.1 [mm] delivered by the coupled electro-mechanical optimisation was considered to be safe from the manufacturer. Parallel paths equal 4 represent four bundles of rectangular Litz Wire utilized to make up a single coil in slot. This will be presented in details in the next chapter. As mentioned in Chapter 4 the integer slot winding arrangement has one single turn per phase. Being 2 slots per pole per phase the best short pitching to limit asynchronous harmonics is one single slot. The rated [rms] current is the minimum current able to provide the rated torque at rated 14000 [rpm] speed.

Item	Value	Units
Rotor ID	300	mm
Rotor OD	355	mm
Active Length	46	mm
Air-gap	2	mm
PM thickness	9.5	mm
Shield thickness	1	mm
Sleeve thickness	7.1	mm
Rot. Yoke thickness	9.5	mm
Sta. Yoke thickness	12	mm
Slot depth	23	mm
Slot width	9.5	mm
Slot number	72	
Parallel Paths	4	
Short Pitching	1	
Turns per phase	1	
Line-To-Line Voltage	380	V
Phase Current	509	A [rms]

Table 5.5. Final design features.

Chapter 6

Manufacture and testing

This chapter is split into two topics: the first part deals with the manufacturing process. The second part of the chapter addresses the testing of the prototype. An exploded view of all the components is given in Fig. 6.1. The main aim of the prototype, at this stage of work is to validate the essential electromagnetic behavior, i.e. torque delivery given a specific armature current as well as the back-emf characterization in time and frequency spectrum. The focus on the mechanical retaining forces could not be given in this body of work, due to test bench limitations at University premises. More details about this is given within the chapter and also in the final thesis conclusions.

6.1 Rotor assembly

The rotor assembly consists of a shaft, permanent magnet assembly, retaining magnet parts (sleeve and end-cheek plates), bolts for assembly, bearings and bearing shields. The rotor assembly constituted a combined effort between the University lab staff and industrial partners. The steel rotor parts, together with the two Titanium plates, have been machined by NTG Ltd High Precision Engineering. The PMs assembly has been performed by Arnold Magnetic Technologies, as well as the retainment sleeve wrapping. The University workshop delivered the wire eroded shield component and performed the shaft/hub shrink fitting.

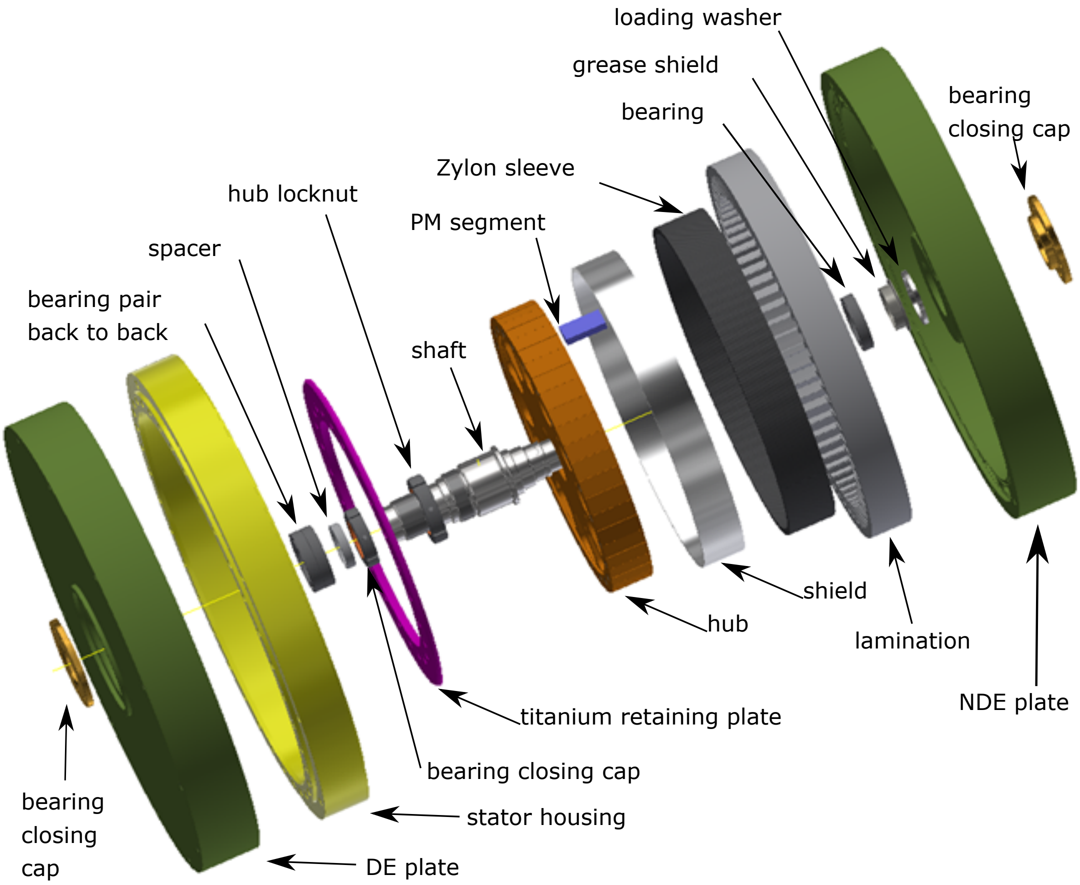

Fig. 6.1. Exploded view for full assembly without winding.

6.1.1 Shaft and Hub

The shaft was manufactured from 17-4PH (Precipitation hardened) stainless steel. This guarantees, apart from high yield strength properties, a certified material for aerospace applications. The stainless feature gives protection against atmospheric agents as well as providing the lowest possible electrical conductivity amongst magnetic materials. Fig 6.2 (a) shows the inner shaft manufactured piece. Two lock-nuts guides have been designed for pre-loading the drive end back-to-back bearing pair and to prevent any axial movement of the hub in case of detachment/slipping at high speed operation. Fig 6.2 (b) zooms in over the coupling spline detail.

The initial choice of a single piece shaft/hub was ruled out for cost and practicality reasons: it would be very expensive and also too big and difficult to handle. The chosen alternative was to shrink fit a shaft within the hub. Safe values of interference fit were needed.

Expansion was simulated for the real shaft and hub geometry due to both centrifugal forces (at over-speed condition) and temperature increments. The centrifugal expansion and the

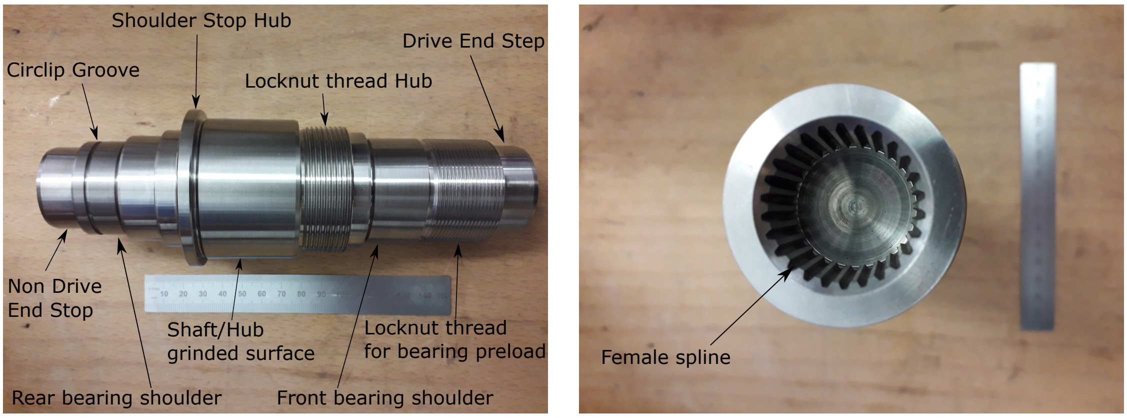

(a) *Shaft horizontal view* (b) *Shaft spline detail*

Fig. 6.2. Shaft details.

Hub ID [mm]	Centrifugal [mm]	Heat [mm]	Diff. [mm]	LN Shrink [mm]	D. gap [mm]
45	0.047	0.06	0.013	0.0405	0.107
50	0.05	0.067	0.017	0.045	0.124
60	0.064	0.08	0.016	0.054	0.14
60	0.06	0.08	0.02	0.054	0.148
75	0.083	0.1	0.017	0.0675	0.169

Table 6.1. Interference design

heat expansion at zero speed were compared and their difference was examined against the interference gap needed. Liquid Nitrogen cooling of the shaft to reduce the shaft diameter was considered, alongside the standard heat up procedure for typical of shrink fitting. Both a high temperature oven and Liquid Nitrogen flasks were readily available at University facilities: both have contributed to give reassurance onto the diameter and interference choice. The results are reported in Tab. 6.1. The different columns, given a certain hub inner diameter, report the expansion due to centrifugal forces and heat; and the reduction due to liquid nitrogen cooling. As a conclusion, a bore of 60 [mm] has been considered sufficient to provide enough clearance. By design tolerances, please refer to Appendix A, the shrink fit between shaft and disk is 0.11 [mm]. This grew to a gap of 0.14 [mm] as it can be seen from the third row of Tab. 6.1, during the shrink fit process, allowing for coupling. Are hereby reported the simple theoretical derivations for interference fits used for the same material shaft/hub, with modulus of elasticity E. The oven heated the rotor hub up to 300° C, whereas the liquid nitrogen temperature was the maximum needed to keep it from boiling: -196° C.

Supposing the torque to be transmitted is T, it's value depends on pressure p, interference diameter $D = 2R$, interference length L and friction coefficient μ. This yields:

$$\tau = \frac{p_r \pi D^2 L \mu}{2} \tag{6.1}$$

Defining the radial interference as δ the interface pressure is:

$$p_r = \frac{E\,\delta}{R} \frac{(r_o^2 - R^2)(R^2 - r_i^2)}{2R^2(r_o^2 - r_i^2)} \tag{6.2}$$

The associated hoop/tensile stress is given by:

$$\sigma_O = p\frac{(r_o^2 + R^2)}{(r_o^2 - R^2)} \tag{6.3}$$

for the hub inner diameter

$$\sigma_I = -p\frac{(R^2 + r_i^2)}{(R^2 - r_i^2)} \tag{6.4}$$

for the shaft outer diameter (compressive). The radial stresses have the same formulation given by (6.3) and (6.4), featuring a subtraction rather than addition at the numerator.

The Finite Element Analysis was used to validate the analytically derived acceptable values of interference. Fig. 6.3 depicts the stress variations at both shaft OD and hub ID. The compressive strength, both hub and shaft were designed for, needs to stay within the limits of the compressive yield strength for the 17-4PH allow. This is more than 1200 [MPa], three times higher than the maximum stress obtained and shown in sub-figure (a) and (c) Even though some spikes can be noticed at the interface border, where the shaft sticks out of the hub axially, they are most likely to be attributed to numerical approximation errors and singularity points due to mesh discretization. Also, although the hoop stress appears to be very close the tensile yield threshold (sub-figure (b) and (d)) the zone affected is very limited. Even if the material yields in that point, it will yield in compression, which is recognized as not excessively damaging. As highlighted by the probing point in the middle of the interface surface the stress is safely below the yield point, both in terms of radial and hoop stress.

Fig 6.4 (a) shows the outer-shaft/hub manufactured component. The castellated rotor outer

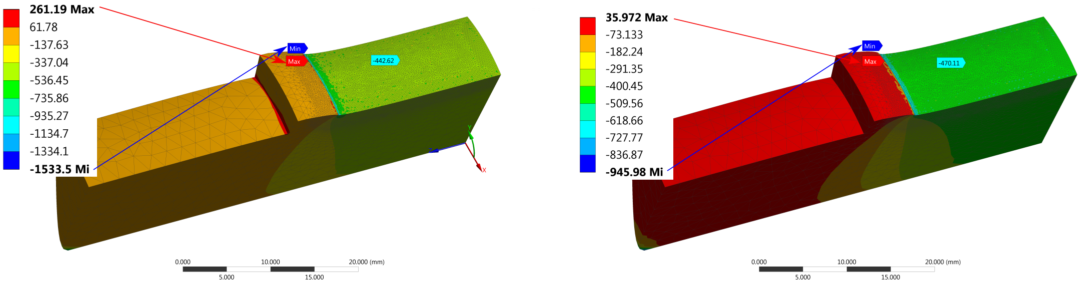

(a) *Radial stress shaft* (b) *Hoop stress shaft*

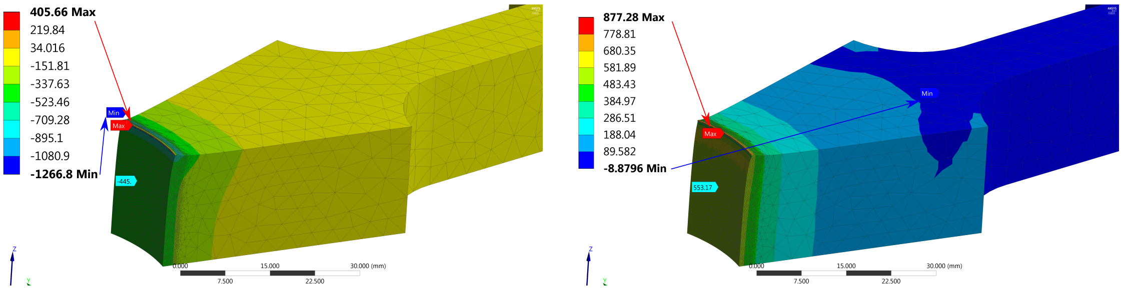

(c) *Radial stress hub* (d) *Hoop stress hub*

Fig. 6.3. Shaft/Hub shrink fitting.

boundary allows for an easy location of the PMs Halbach array segments. The magnets will nicely locate in place during the assembly process, avoiding undesirable jumps due to the interaction of differently magnetized segments. Fig 6.4 (b) shows the successful shrink fitting of the shaft within the hub. The shaft was frozen in a Liquid Nitrogen bath, whereas the hub was heated up to 300° C; hence allowing contraction of the former and expansion of the latter, necessary to perform the insertion. The overall assembly was held in place, under pressure, during the thermal transient following afterwards, in order to avoid any jump or displacement of the shaft from the hub.

6.1.2 Shield and End Plates

Fig 6.5 (a) shows the wire eroded Aluminium electromagnetic shield. The Aluminium alloy has been chosen to be Al - 6061 (61% IACS - $2.827 \times 10^{-8}\,\Omega/m$): a common alloy providing good machining with a quite high electrical conductivity. This will help the high order harmonic shielding. The shield has been machined to be larger than the actual design size: the outer diameter of the shield before final external grinding was left 4 [mm] thicker. This was done in order to guarantee enough thermal mass for shrink fitting on top of the PMs array as well as safe

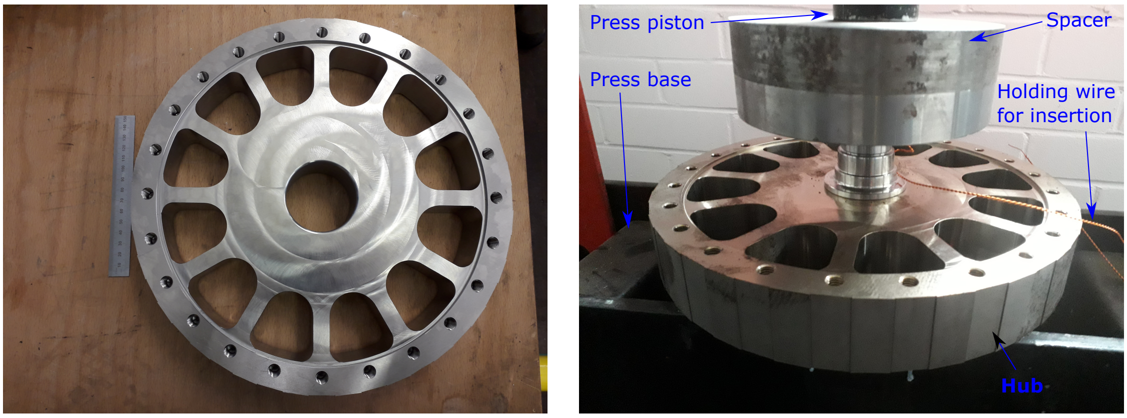

(a) *Hub view* (b) *Assembly shaft/hub, under press*

Fig. 6.4. Hub and fitting.

handling of the aluminium ring [1]. Fig 6.5 (b) presents one of the two machined Titanium 6Al-4V (grade 5) plates/ end cheeks for sleeve axial containment.

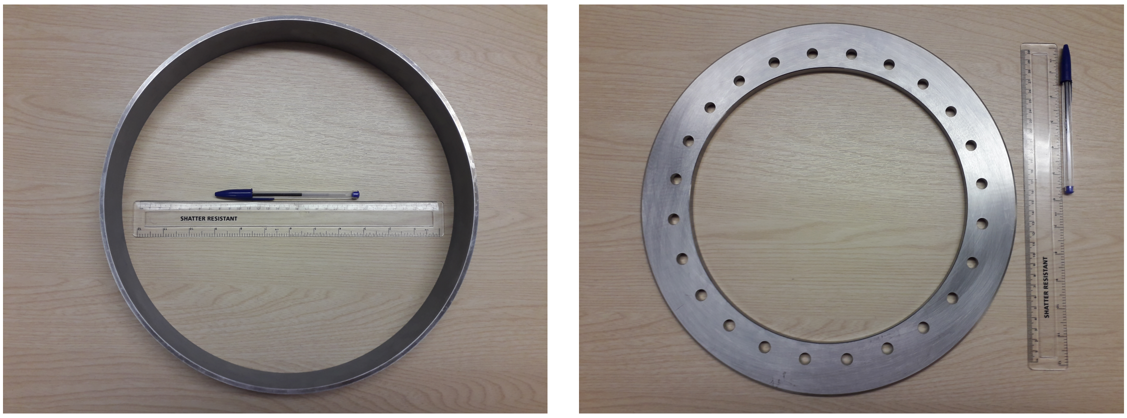

(a) *Electromagnetic shield* (b) *Titanium plate*

Fig. 6.5. Shield and titanium axial retainment plates.

6.1.3 PM array

The Halbach array manufacturing stage comprised the following steps: 1) Positioning of PMs on top of the rotor hub outer surface. 2) Fixing and mounting of one of the two Titanium end plates. 3) Extra axial machining of the aluminium shield, in order to keep back the PMs faces so that the assembly is perfectly flush. 4) Shield shrink fitting. 5) Fitting of the second Ti plate on the free end axial end. 6) Sleeve wrapping and final curing.

---

[1] A 1 mm thick shield with a diameter of more than 300 mm will be extremely fragile to shocks and buckling.

Fig. 6.6 (a) presents the Halbach array arrangement employing 7-stages per pole pair. Note the clear marking for the different magnetization directions. Fig. 6.6 (b) is a zoom in onto the retaining plate features. In order to avoid uneven stress relief during assembly twenty four retaining bolts, double the number of spokes, has been adopted.

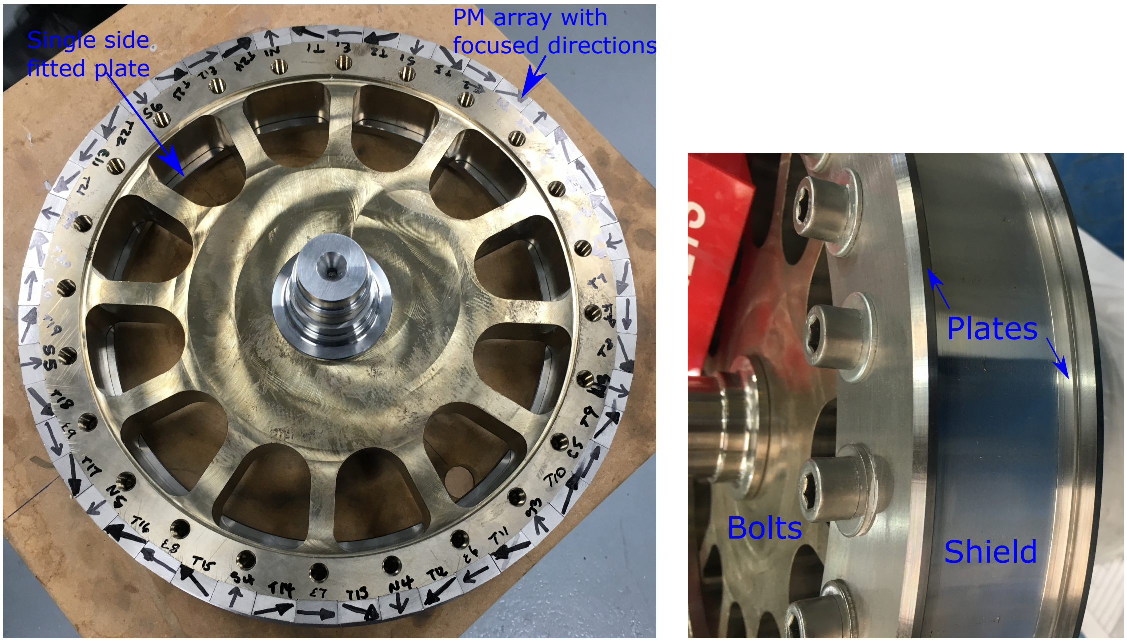

(a) *PM assembly prior to glue and plate enclosure*

(b) *PM array enclosed by shield and bolted Ti plates*

Fig. 6.6. Rotor assembly.

In Fig. 6.7 (a) the rotor assembly is shown before the shield grinding stage. Although innocuous-looking the carbon fibre in Fig. 6.7 (b) is responsible for considerable axial stresses to be transferred onto the end plates. In order to ameliorate the stress transfer between components in an even and distributed manner during the wrapping, extra tooling, in the form of clamping plates, has been positioned at the two sides of the rotor, effectively trapping the plates and preventing any bending while rotating. The figure highlights also the black carbon fibre depicting one of the final stages of the wrapping process. In fact the Zylon wrapping step has been performed in darkness to prevent any side effects, given the unknown behavior of this composite to visible radiation. The wrapping composite visible constitutes the layer of protection fiber placed at the very outer boundary of the rotor.

The completed rotor is shown in Fig. 6.8. The two figures capture the process assembly carried out in the University premises. The assembly needed to be performed in a single step: drive end

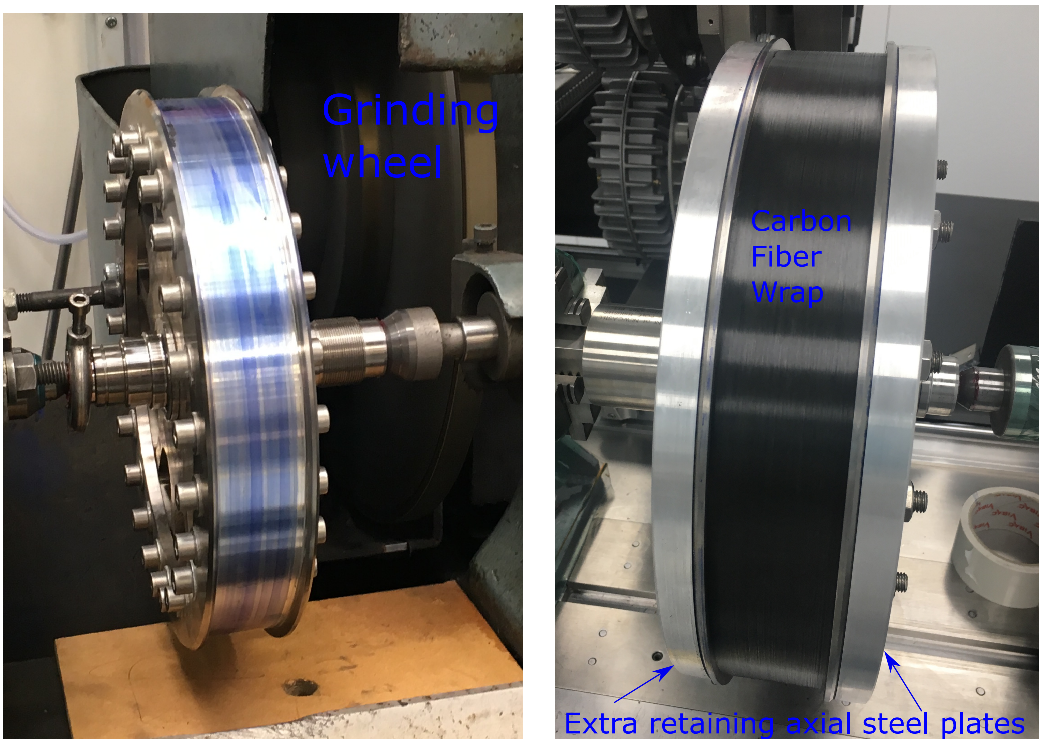

(a) *Rotor assembly before Shield grinding* (b) *First stage Rotor Wrapping*

Fig. 6.7. Grinding and Wrapping.

bearing and cap were held together with the rotor from above, sliding down and matching the rest of the stator.

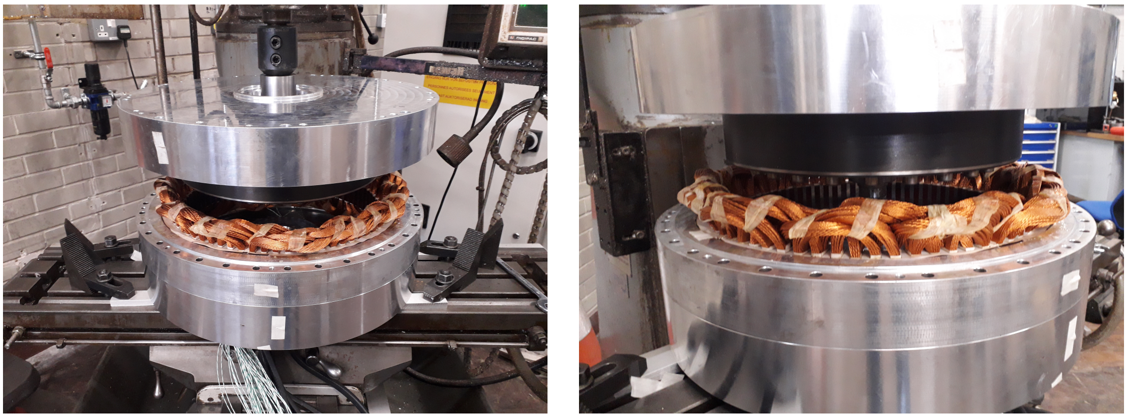

(a) *Assembly stand* (b) *Details of rotor suspended before assembly*

Fig. 6.8. Stator/Rotor assembly.

6.2 Winding

As specified multiple times throughout the previous chapters, the winding choice ruled out fractional slot configurations, in favour of a more traditional, although more lengthy and heavy, solution. Due to high fundamental frequency operation a fine stranded copper wire needs to be considered as the ultimate, unique solution to minimize proximity loss. The winding choice has fallen inevitably onto a pre-formed compact Litz-Wire. Specifically the wire is a Type 8 Litz. This solution has a pre-formed rectangular shape. The cable specification is 8 AWG 16x7/28 Heavy solderable Polyester (MW77-C). The cable features 7 transposed braids of 16 wires each of 28 AWG. The equivalent AWG obtained is 8. The transposition eliminates effectively the circulating currents that arise due to slot leakage inductance. The rectangular conductor shape permits a sound fitting within rectangular slots. MW77-C refers instead to the insulation nomenclature, in this case a heavy, solderable, polyester capable of continuous operation up to 180° C and transient operation up to 200° C.

6.2.1 Choice of the number of parallel paths

Although the manufacturer allowed some room for ad-hoc formed designs the easiest solution is to employ standard off-the-shelf wires. This constrained the winding to have four parallel paths for full utilization, without shifting too far away from the "theoretically" optimized slot dimensions. The four parallel paths are actually within a single phase in a slot. Being a short-pitched double layer each phase will occupy a layer; there will be four parallel Litz-wires per phase, thus totaling eight conductors within a slot as in Fig. 6.10. This is the best trade-off between optimal slot dimensions drawn from the optimization and the wire dimensions available, without modifying further the slot profile. The open stator slot topology suffers from issues related to fringing flux entering from the air-gap: the permanent magnet flux is not conveyed as efficiently to the teeth as in a semi-closed slot geometry. The open slot also increases the overall leakage inductance which is already strongly affected by the positioning of the conductors within a slot.

It is necessary then to estimate how could this generate current imbalance within a single phase, along the sub-parallel paths. A quick way to perform this is to simulate a three phase short circuit at the terminals. If there is an unbalance of inductance, circulating current can flow

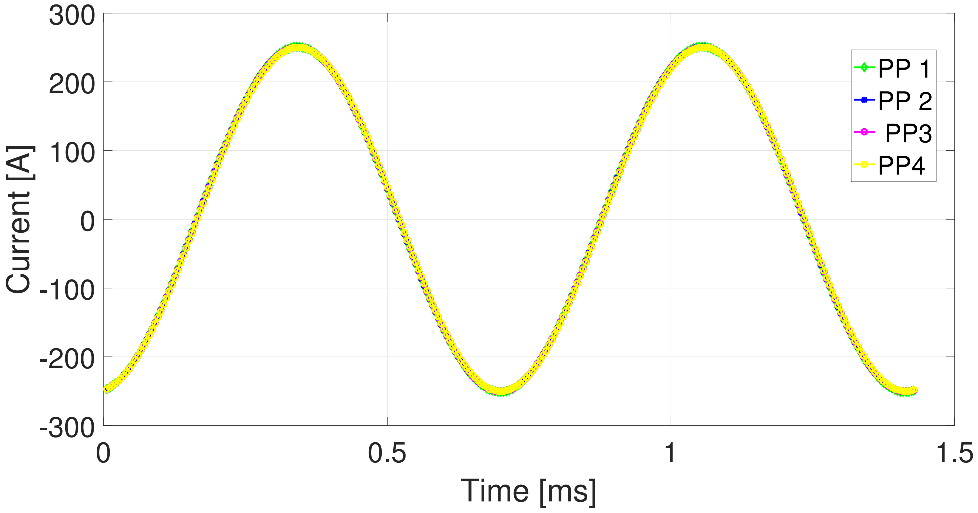

(a) *Phase A subparallel short circuit currents*

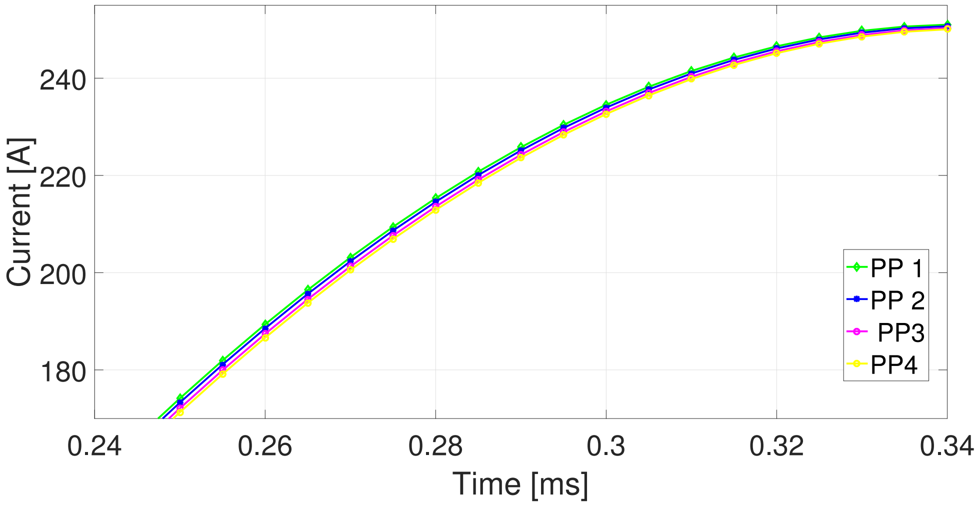

(b) *Zoomed currents*

Fig. 6.9. Current unbalance at rated speed (14k rpm).

from one parallel path to another. From FEA estimation (assuming 100° C rotor temperature operation) the results can be seen in Fig. 6.9. This estimation has assumed a 2D geometry for the simulation, accounting for the end-winding inductance as an additional added parameter in the circuit. Resistances and end-winding inductances have been assumed to be equally balanced along all the parallel paths. It is observed as there is almost no current unbalance between the sub-paths of a single phase in a single layer within slot.

Fig 6.12 (a) provides a detailed and accurate design of the full winding assembly within the stator lamination stack. It is clearly noticeable as a distributed winding design possesses very large and long end windings protrusions. The challenging task has been fitting the end winding within the

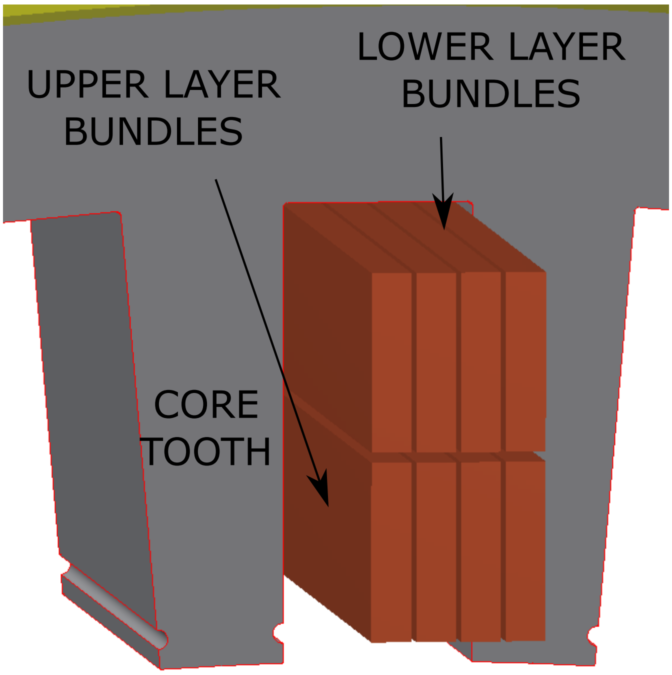

Fig. 6.10. Slot bundle sketch.

end-caps without excessively increasing the machine outer dimensions and excessively augment the motor non active mass. A detail of the end winding feature during the design synthesis stage is given in 6.12 (b).

6.3 Lamination and Housing

The stator assembly needs the same procedure for the shaft/hub: shrink fitting. In this case the interface hosts two different materials in contact, namely laminated Silicon Steel and Aluminium. A modification to the pressurized cylinder formula given by (6.2) is adopted as follows:

$$p_r = \frac{\delta}{\frac{R}{E_o}\left(\frac{r_o^2+R^2}{r_o^2-R^2}+\nu_o\right)+\frac{R}{E_i}\left(\frac{R^2+r_i^2}{R^2-r_i^2}-\nu_i\right)} \tag{6.5}$$

where the subscripts r_o and r_i stands for outer and internal component radius-es, R for the contact radius, δ for the shrink fitting interference E_o and E_i for the two components Young's modulus, and ν_o, ν_i for the Poisson's coefficients. The inner diameter in this case corresponds to the core outer diameter of 430 [mm]. The shrink fit chosen, accounting for different materials (steel and

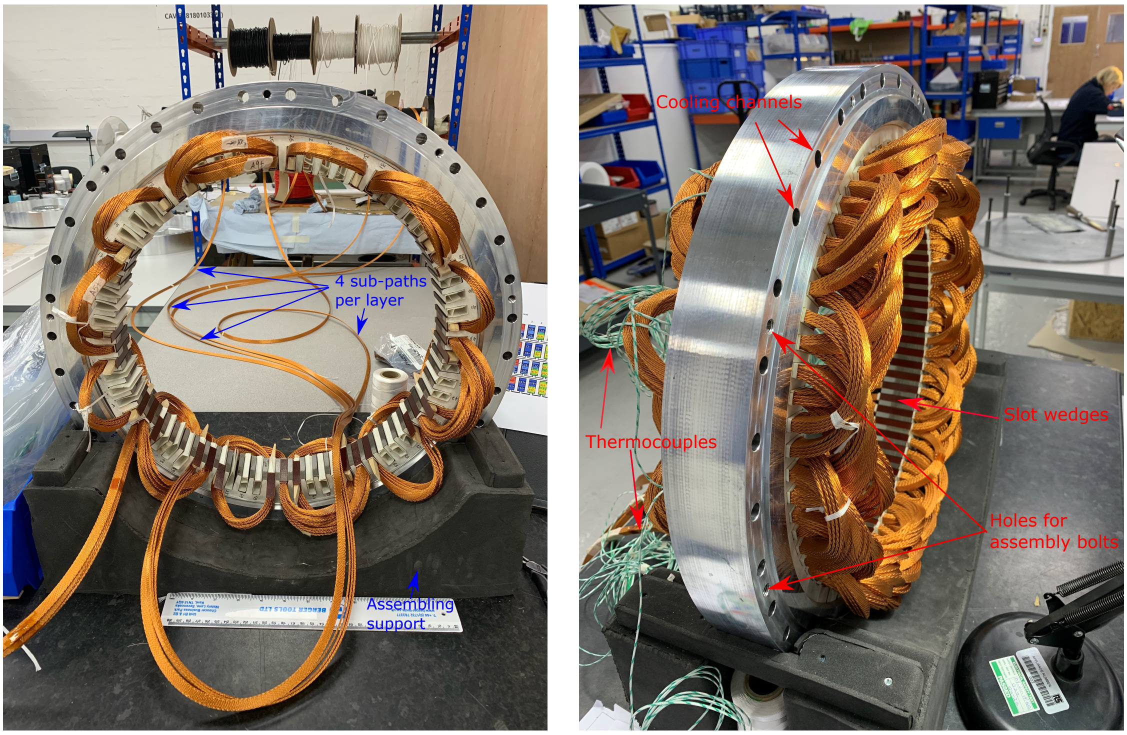

(a) *Single phase loaded*

(b) *Wound stator side view*

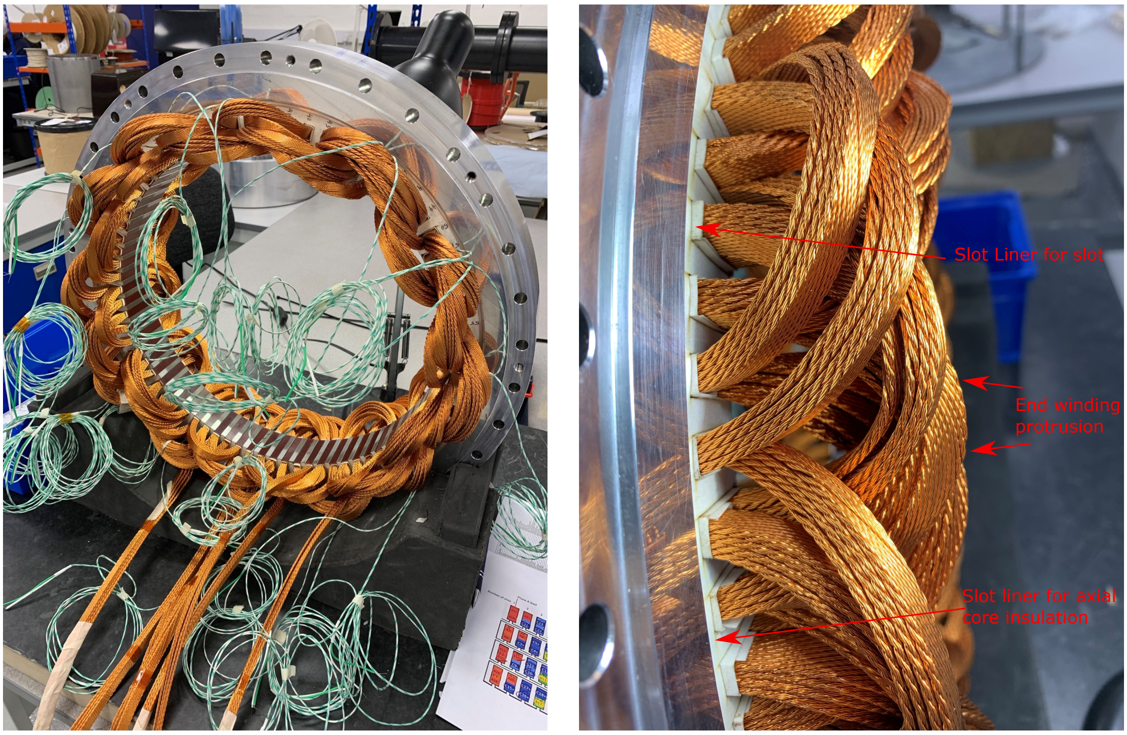

(c) *Wound stator front view*

(d) *Wound stator, End Winding zoom in*

Fig. 6.11. Stator assembly, before varnish impregnation.

aluminium) in contact, was chosen to be 0.2 [mm]. The stresses simulated are less than 50 [MPa] for the aluminium hub, and less than 80 [MPa] at the core outer boundary.

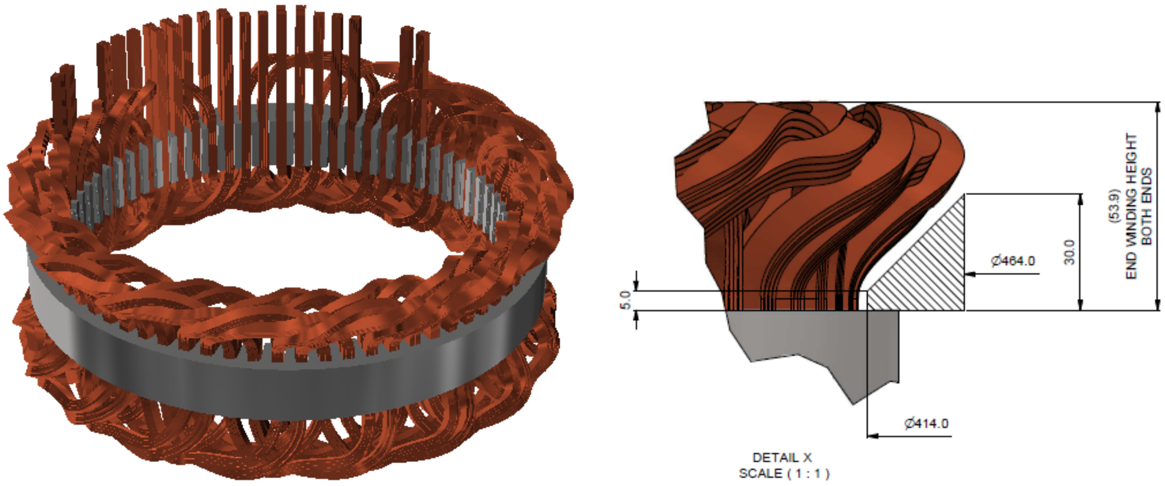

(a) *Wound stator side view* (b) *End winding detail*

Fig. 6.12. 3D modeling of full winding and end winding detail.

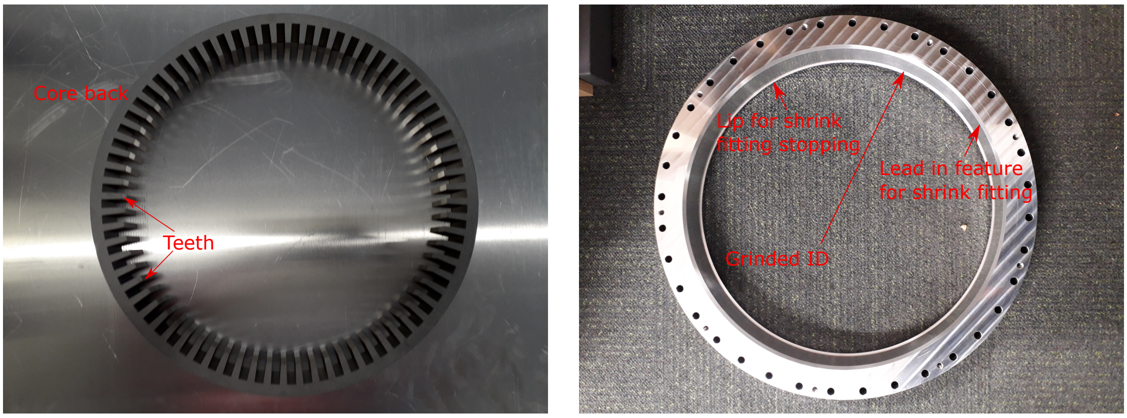

(a) *Laminations prior to assembly* (b) *Housing prior to assembly*

Fig. 6.13. Rotor assembly.

6.3.1 Symmetry of the magnetic circuit

Steel punching, cutting, and subsequent shrink fitting assembly in the motor casing can result in additional losses associated with the iron core [121]. This is physically related to the unintentional creation of short-circuits at the lamination ends as well as a residual stress accumulated within the core-pack that can result in additional losses due to magnetostriction effects. Because the motor has a high number of teeth the question of variation of iron magnetic properties between teeth was posed. This has led the author to investigate this before loading the coils into the stator assembly. Fig. 6.14 (a) shows the impedance analyzer employed for performing a Resistance-Inductance sweep test for the teeth. Fig. 6.14 (b) zooms in on the search coil manufactured for this purpose.

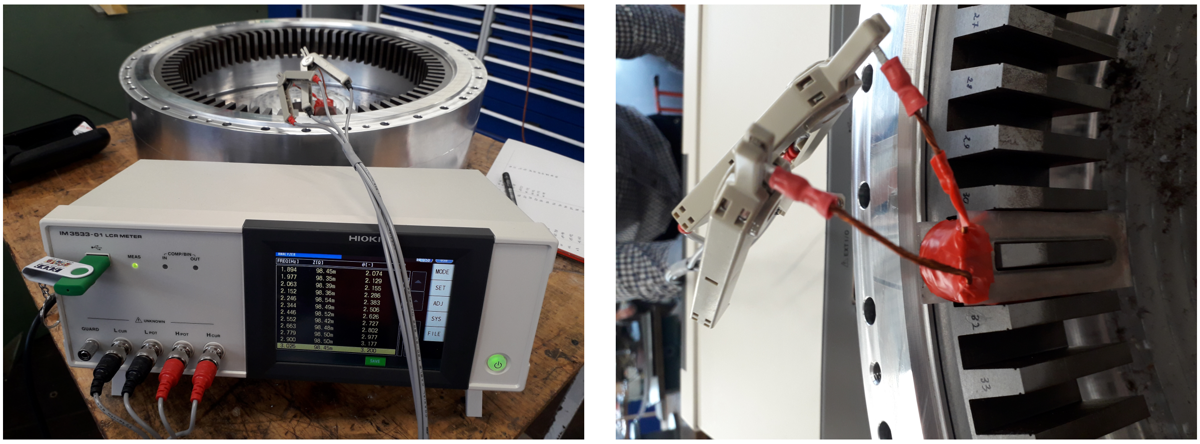

(a) *Impedance analyzer* (b) *Probing coil zoom in*

Fig. 6.14. Impedance over all the frequencies.

As it can be noticed from Fig. 6.15 both real and imaginary parts of the coil impedance rise quadratically along the frequency spectrum. The zoomed sub-figures highlights that there is not a substantial discrepancy between different teeth. This can be more clearly understood from Fig. 6.16 for the highest frequency probed. A significant difference in some specific tooth or in more than one would have signified a loss imbalance for the core. This could be due to a weak mechanical point that accumulated stress witnessing a higher loss component. The real part of the impedance represent an equivalent estimation of the AC losses behavior of the component under investigation. A uniform distribution of impedance across all the teeth, as in our case, should ensure a uniform loss distribution around the core.

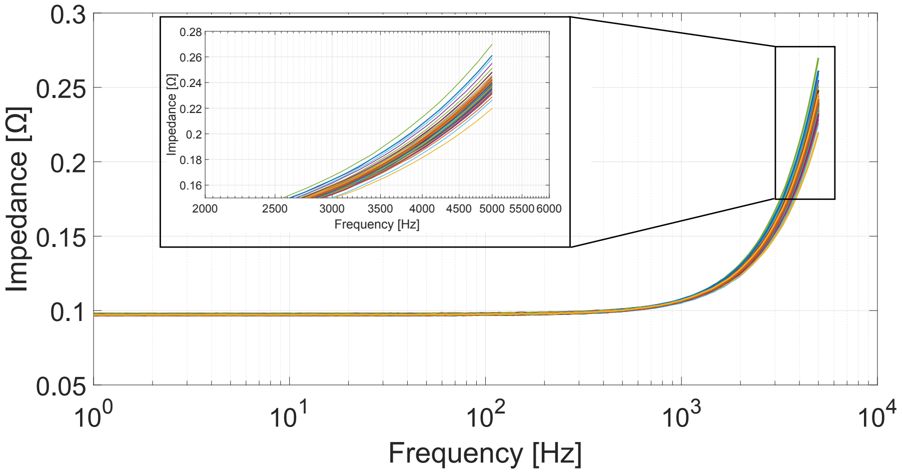

(a) *Impedance Real part*

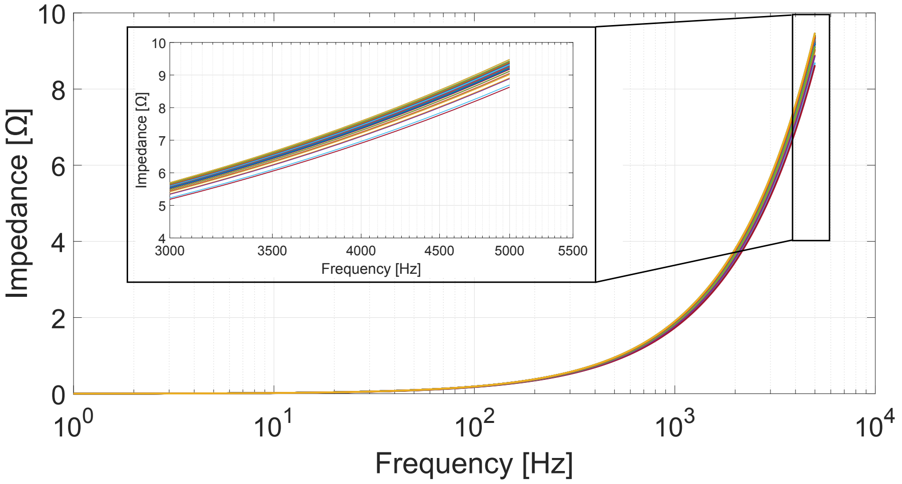

(b) *Impedance Imaginary part*

Fig. 6.15. Impedance over all the frequencies.

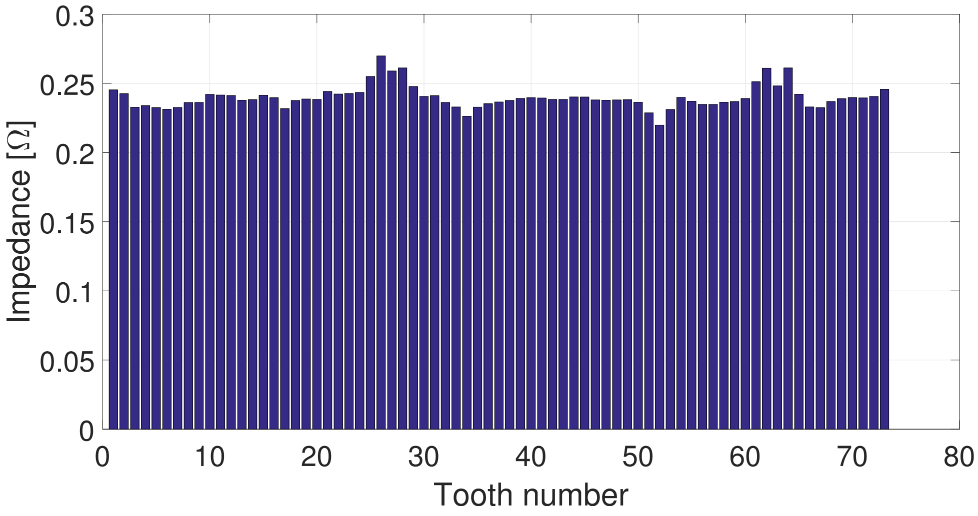

(a) *Real Part*

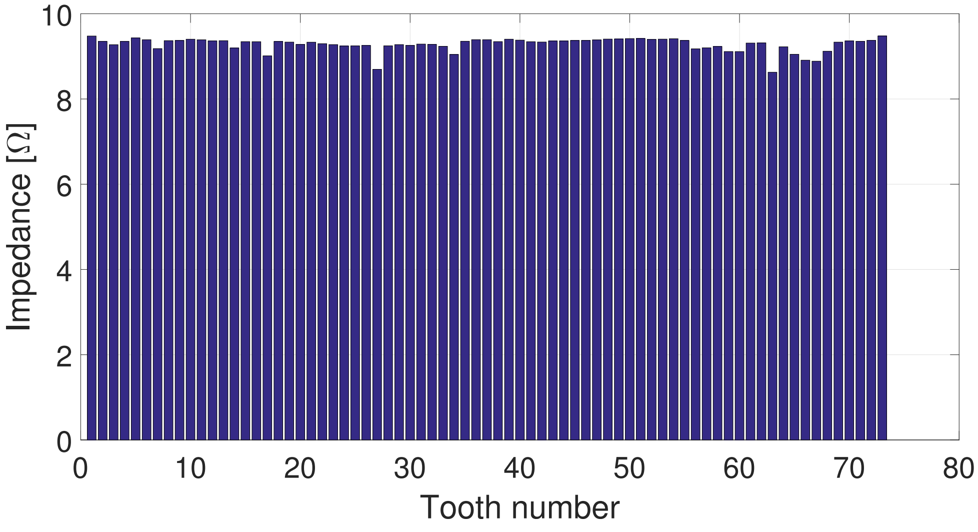

(b) *Impedance Imaginary part*

Fig. 6.16. Impedance over all the teeth at maximum frequency.

6.4 Motor Stator Static Tests

The complete stator winding construction process has been carried out externally by MTD Ltd. The three phases have been inserted by hand within the slots following the specified pattern by hand. Thermocouples have been placed in every pole at the bottom of the slot and between layers. As observed in Fig. 6.11, the slot liner has been placed both within the slot to prevent any winding core short, as well as alongside the axial periphery of the whole core to similarly prevent any short between end winding and stator yoke. Slots have been closed at their tips with a non-magnetic, non-conducting slot wedge. After slot liner, winding and slot wedge loading the whole stator package has undergone Vacuum Pressure Impregnation (VPI). Regarding the impregnation process and resin type, the varnish varnish employed was a CC-1105. The stator was cured at 120° C for 4 hours. The CC-1105 is a 1K resin based on polyester of thermal class H. It is styrene monomer and vinyl toluene free. It has excellent thermal resistance and can be used up to 212° C. This varnish is suitable for a wide range of impregnating applications for electrical rotating machinery, especially for hermetic motors.

The complete wound stator has been tested already electrically by the manufacturing company in charge of the winding process. The tests performed relate to the electrical insulation and phase balance. The following have been performed:

- Ground wall insulation test at 1000 V.
- Surge test at 1000 V
- HiPOT test
- DC resistance measurements

All the listed tests have been performed once again on the prototype in the University Lab with a Mega-Analyzer (Baker Mega Tester). All results between the manufacturing report and tests conducted afterwards matched and validated the electrical integrity of phases and corresponding insulation.

6.4.1 Resistance and inductance tests

Resistance and inductance tests have been conducted by using an impedance analyzer. The same device utilized for teeth analysis and their "sanity check" photographed in Fig. 6.14 (b) has been employed. All possible combinations of phases connections have been tested. Fig. 6.17 yields the resistance frequency spectrum for the single phases taken independently, one by one, from lead to neutral. Fig. 6.19 presents the values for all the different star connected cases. Fig. 6.20 for the delta connected cases. Fig. 6.21 for one single phase taken alone from lead to neutral and the other 2 phases connected via their leads. This forces a current share of 1,1/2 and 1/2, for an ideal symmetrical and balanced system. All the different circuit configurations are briefly presented in Fig. 6.18.

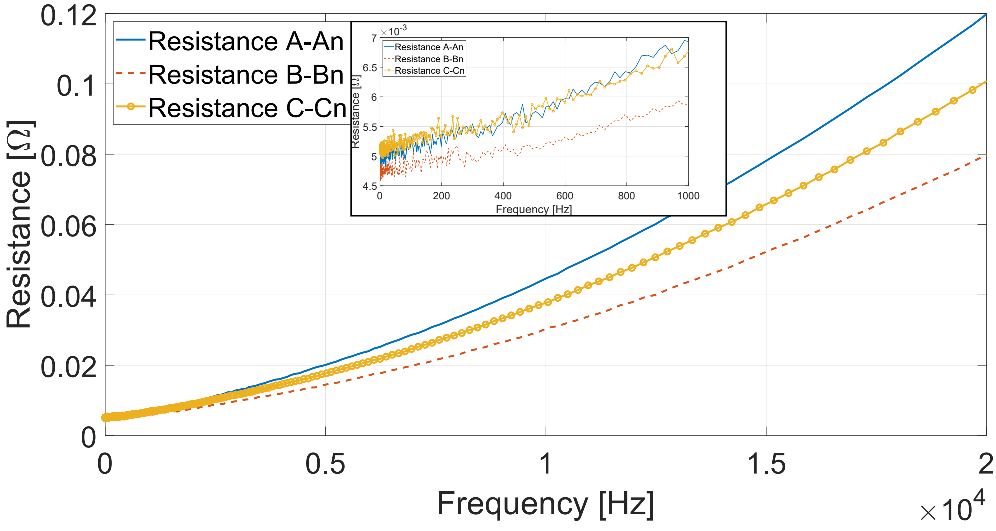

Fig. 6.17. Single phase resistances.

All the zero frequency resistance tests matched almost perfectly with both Mega-Tester checks performed by the manufacturer and on the prototype at the University.

Consider the variation of resistance with frequency. The ratio of AC to DC resistance value is approximately 1.4 at 1 [kHz]. Fig. 6.17 shows this in the zoom-in box. To better appreciate this Fig. 6.22 depicts the a-dimensional ratio of AC to DC resistance. This trend seems reasonable and not too discouraging for the actual performance and validity of the choice to employ Litz-Wire for this motor design. It is also encouraging that the estimation of single phase resistance during the design synthesis, as detailed in Tab. 5.1, is close to the measured value. For not including any AC-resistance effect at the time. The measured DC resistance is low (under 6 mΩ)

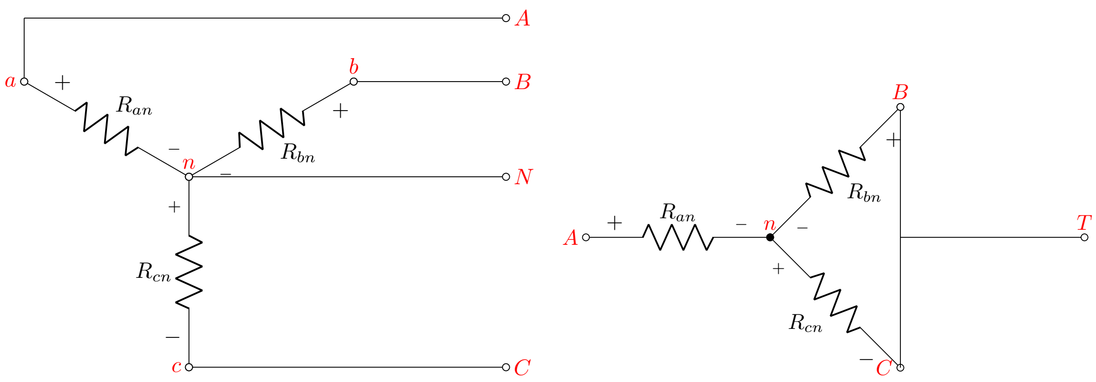

(a) *Star connection* (b) *Half phase connection*

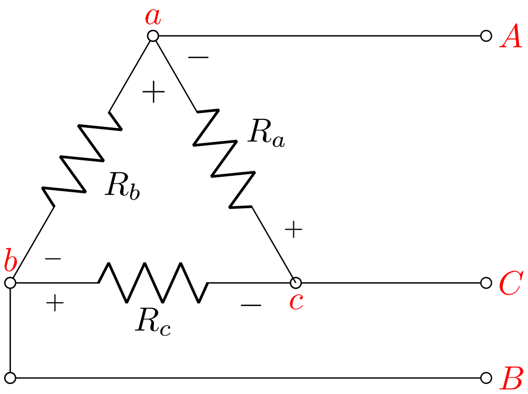

(c) *Delta connection*

Fig. 6.18. Leads connections measured.

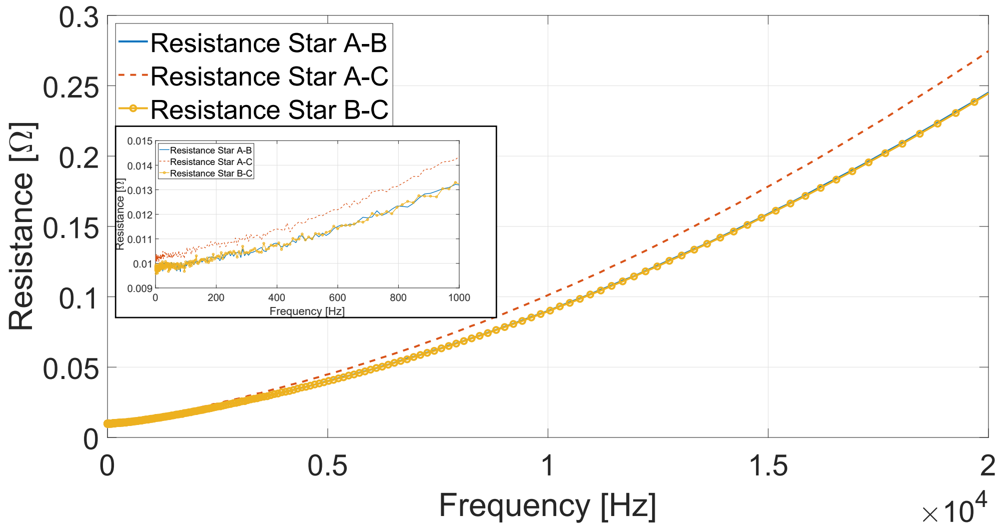

Fig. 6.19. Star resistances.

for zero frequency. However, the only phase which stays within the range of 6-7 [mΩ] at the rated operating frequency of 1400 [Hz] is only phase A. Phase B and C exceed this value.

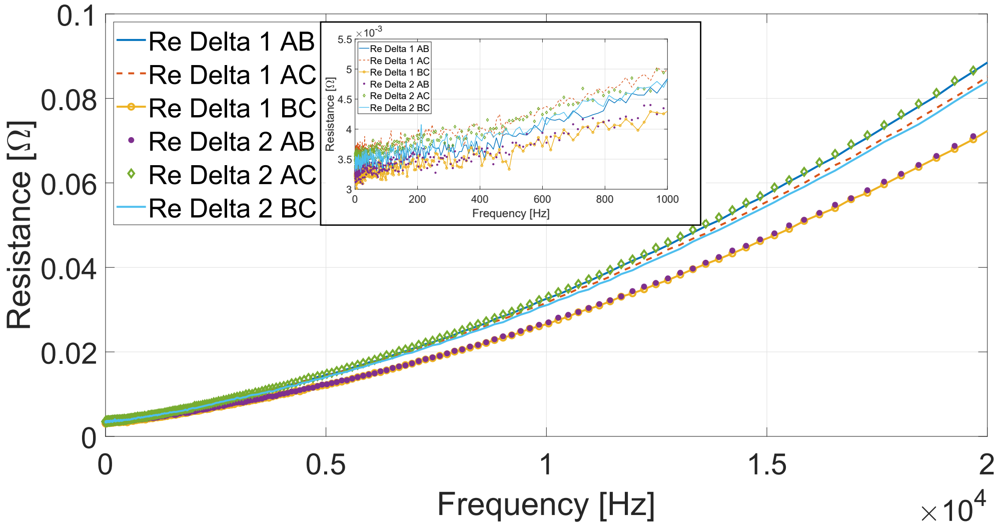

Fig. 6.20. Delta resistances.

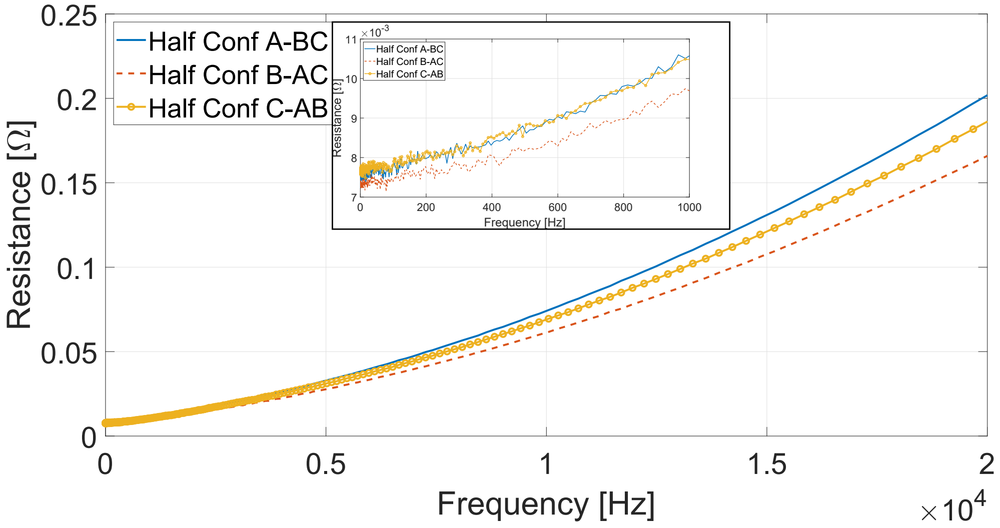

Fig. 6.21. Half connection resistances.

It is noticeable that there is a phase imbalance, both in terms of resistance and inductance. This is exacerbated when the frequency increases. All the connection combinations measured exhibit this behaviour. This might be attributed to the fact that the machine was delivered from the manufacturer with a lead shorter than the other two. Also, because the winding loading was performed by hand, the end windings are not guaranteed to have exactly the same length for all the phases, this is exacerbated by the several number of slots that the phase needs to traverse.

Consider the inductive term. The single phase inductance measured without the rotor inserted can be compared with the far frequency spectrum of Fig. 5.14, 5.15, 5.16, referring to the Non

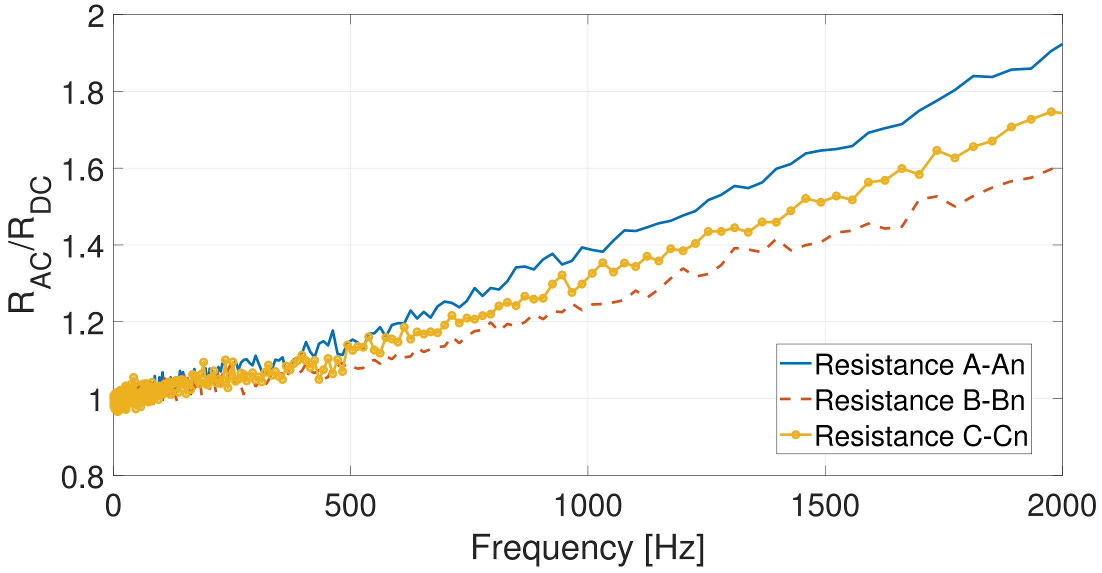

Fig. 6.22. Normalized AC resistance vs DC.

shielded solution. This is essentially the leakage inductance because no flux links the rotor magnetic side at very high frequency. It is important to notice, as shown in Fig. 6.23, the simulated inductance in case of full leakage (highest frequency) is a little lower than the actual one. Another aspect which was not really desirable is the slight inductance imbalance of the phases. The only cause that comes to mind to the author is again due to the different length of end windings that might have occurred during winding loading. This can make sense considering that the magnetizing inductance, due to the very short axial length of the iron stack, the leakage term contributes significantly to the overall inductive value.

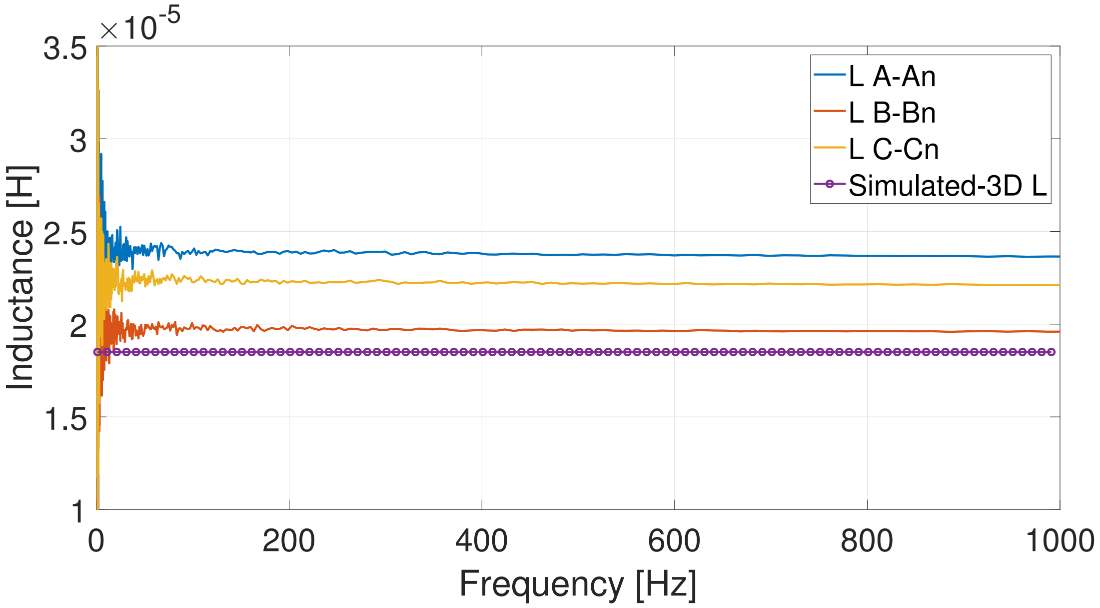

Fig. 6.23. Delta resistances.

6.5 Thermal tests on the Stator sub-assembly

Fig. 6.24 describes the thermal testing setup for the stator sub-assembly employed. It consists of a DC power supply, capable of a maximum of 600 [A] current as a source. The cooling system employs a temperature controlled chiller/heater. The temperature can be controlled within ±1C.

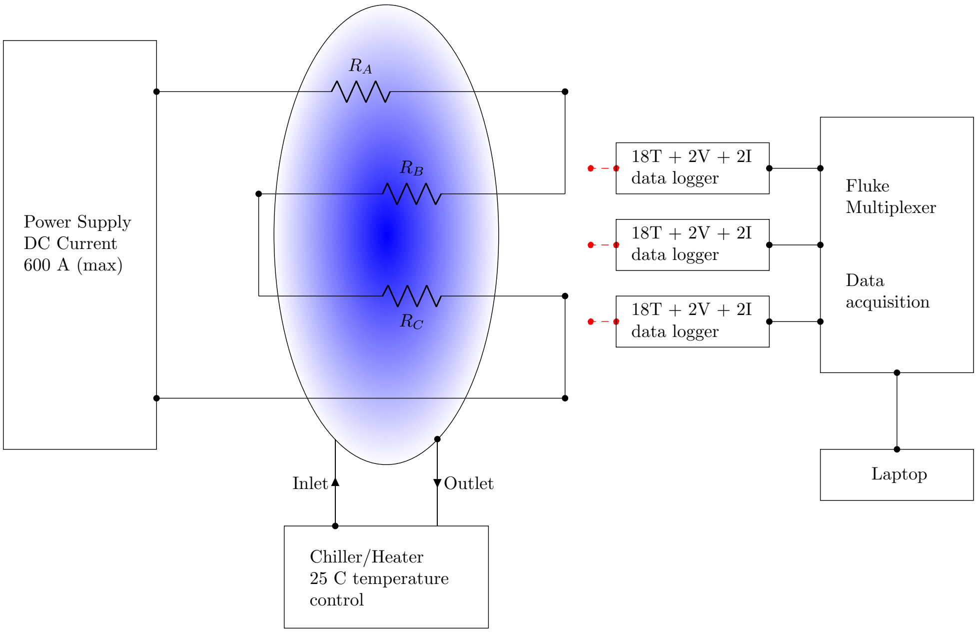

Fig. 6.24. Thermal test bench setup.

It has been set to a constant reference value of 25° C in all the experiments conducted. All the temperatures are sensed using type K thermocouples. The data acquisition consists of 3 cards/logging units, which gives in total 54 channels for temperature measurements in real time. This is because there are 18 temperature inputs, 2 voltage inputs and 2 current inputs per box. As can be seen from the circuit layout, all the three phases are connected in series. Apart from being the easiest connection possible to implement, this is a sensible way to emulate a uniform distribution of winding loss expected in a balanced 3-phases electrical machine. The rationale behind the test is to identify the thermal management capabilities of the machine. A further insight was thought to relate to the insulation of the end caps, to detect how much, the aluminum end caps are capable of heat flux extraction from the end winding protrusions which are likely to be the hot spots of the thermal circuit. For this reason the end caps were deliberately insulated on purpose for the first round of current loading. Subsequently they have been removed. In the results section this last test condition is referred to as the Non Insulated condition.

Fig. 6.25 shows the hardware setup for the stator thermal tests. Sub-figure (a) zooms over the slot liner insulation applied to the front (Drive-End) end cap. Sub-figure (b) displays the inner insulating cylinder. Making use of this component allows, as explained before, to self isolate the stator assembly, allowing no heat transfer through the rotor void. Sub-figure (c) presents the stator and housing assembly during instrumentation, while no end caps are in place. Finally sub-figure (d) is a shot of the complete assembly, sitting within a wooden 'stand', so the only heat transfer paths are via the liquid cooled motor housing and end-caps, i.e. no mounting features are transferring/sinking the generated heat.

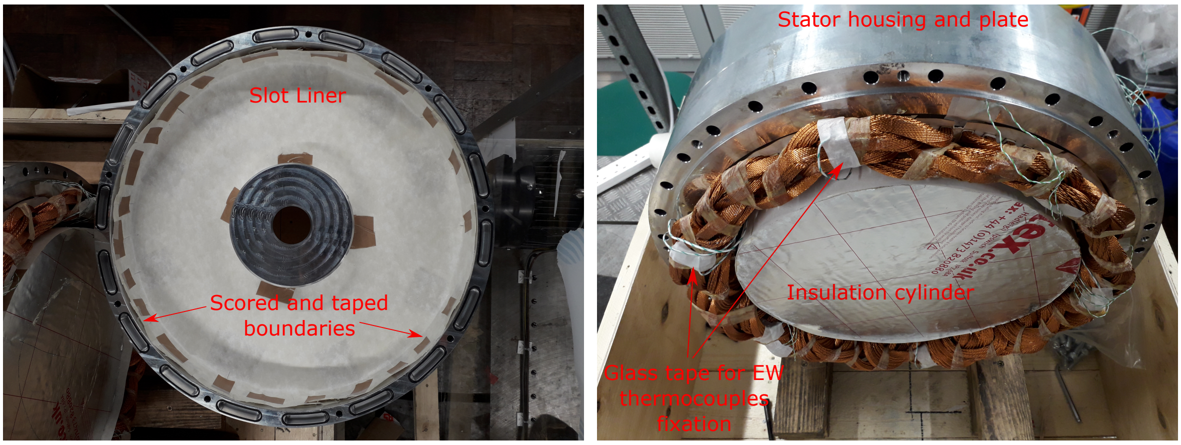

(a) *Insulated plate with Slot liner.*

(b) *Inner stator insulation.*

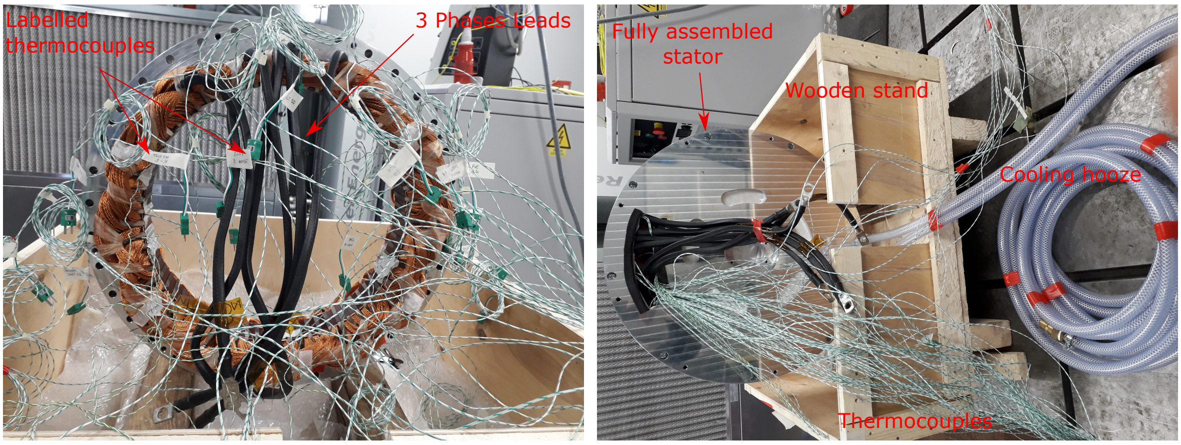

(c) *Stator instrumentation.*

(d) *Stator assembly on the bench.*

Fig. 6.25. Motor instrumentation for initial thermal testing.

6.5.1 Results from thermal testing

Fig. 6.27 portrays the temperature variation against the current in different locations of the stator assembly. The temperatures are plotted with the aid of an error bar, which accounts for the temperature variation from thermocouples placed onto the same feature (House, Tooth, etc) of the machine, but in different locations, accounting therefore for multiplicity (the motor has 72 slots/teeth). All results are presented as temperature rise above reference water cooled housing at 25° C. This allows removal of any effect associated with the 'behavior' of the cooling system during tests over different days. It is clear that the temperature increase follows the expected parabolic variation with current. To visualize the results it is worth mentioning the following nomenclature. The DE and NDE acronyms stand for Drive-End and Non-Drive-End. While EW stands for End Winding. Fig. 6.26 shows the location of the thermocouples with respect to the stator cross section.

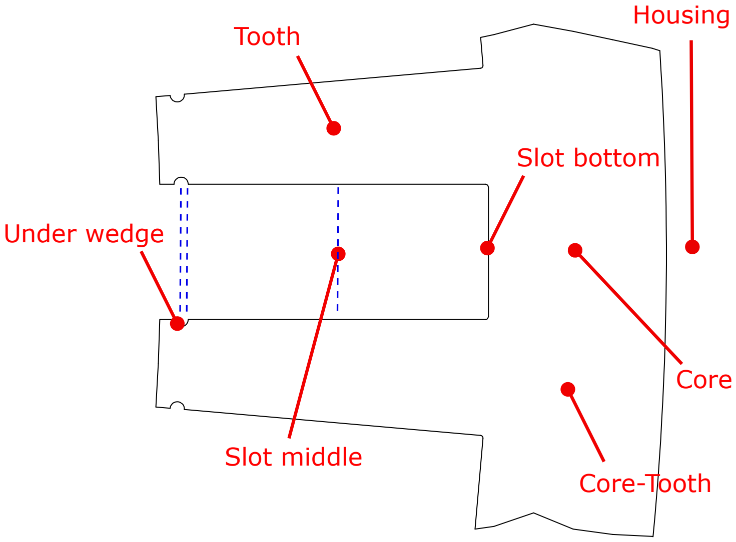

Fig. 6.26. Thermocouple positioning.

Fig. 6.28 illustrates the same results, but with respect to power variation. In here it is evident that the temperature rise is linear with the power.

Fig. 6.29 highlights the temperatures value in a histogram. The temperatures are all the maximum values gathered among the same feature thermocouples sets (for instance among all the teeth sensors the maximum value over all of them is plotted). Since the most thermally stressed components are undoubtedly the end windings, there is a bar chart representing the averaged values all over the end winding thermocouples, for the sake of comparison.

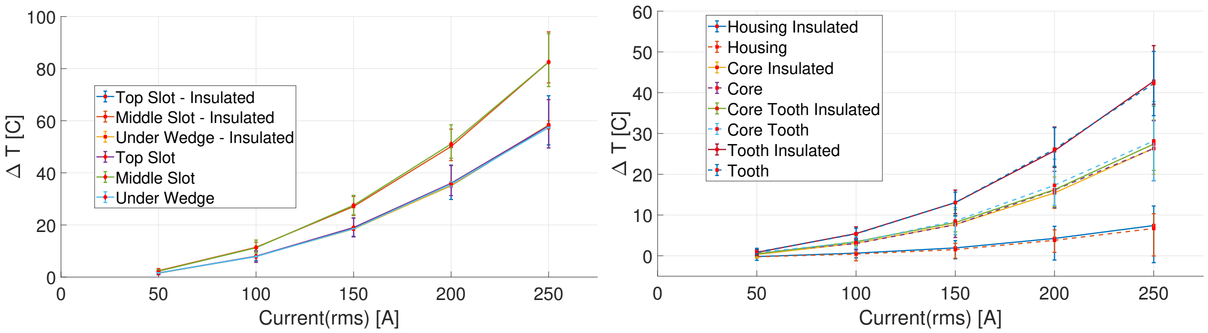

(a) *Middle Slot vs Bottom Slot temperature.* (b) *Housing,Core and Tooth temperature.*

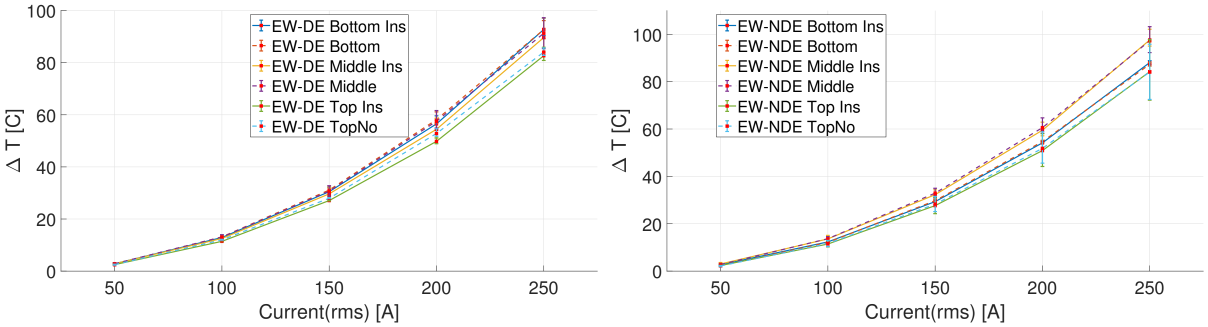

(c) *End winding.* (d) *Additional spots of interest.*

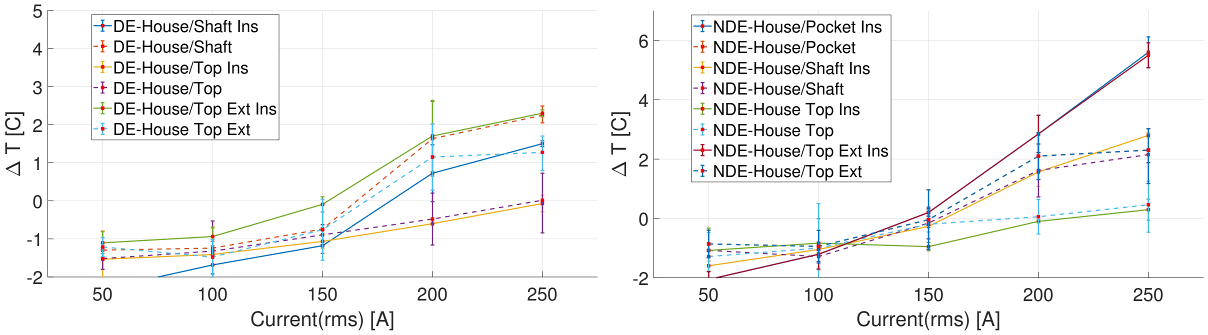

(e) *Middle Slot vs Bottom Slot temperature.* (f) *Housing,Core and Tooth temperature.*

Fig. 6.27. Temperature variation vs currents in stator assembly.

Fig. 6.30 (a) portrays the difference that is encountered among different slots for the highest current applied.

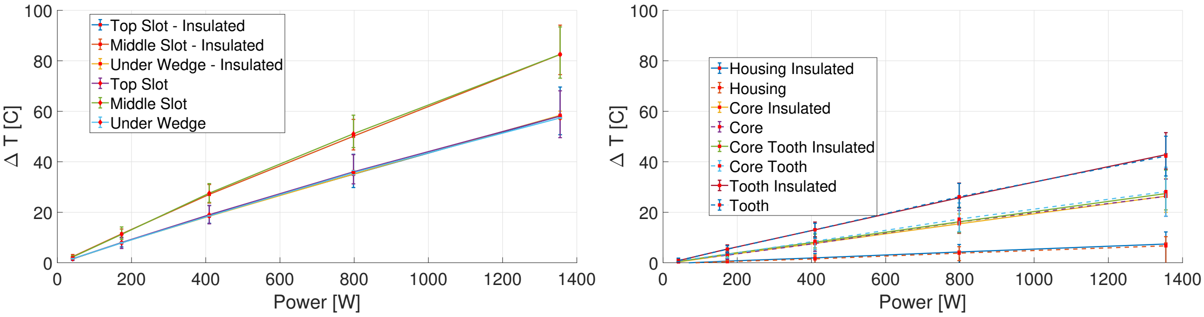

(a) *Middle Slot vs Bottom Slot temperature.* (b) *Housing,Core and Tooth temperature.*

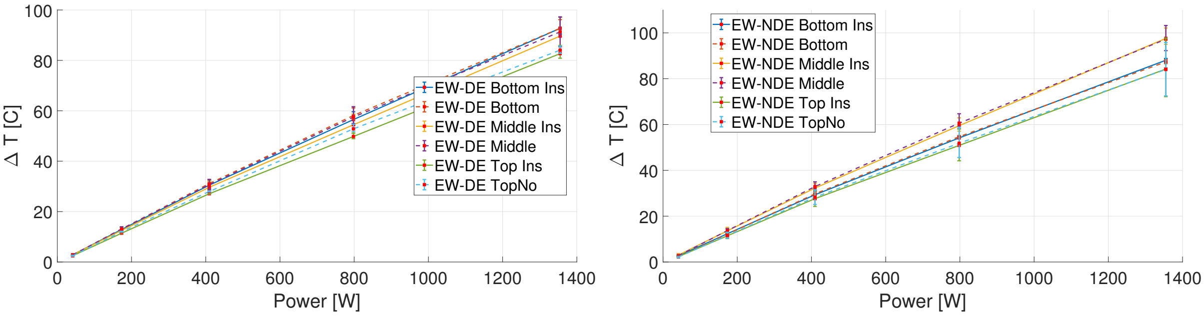

(c) *End winding.* (d) *Additional spots of interest.*

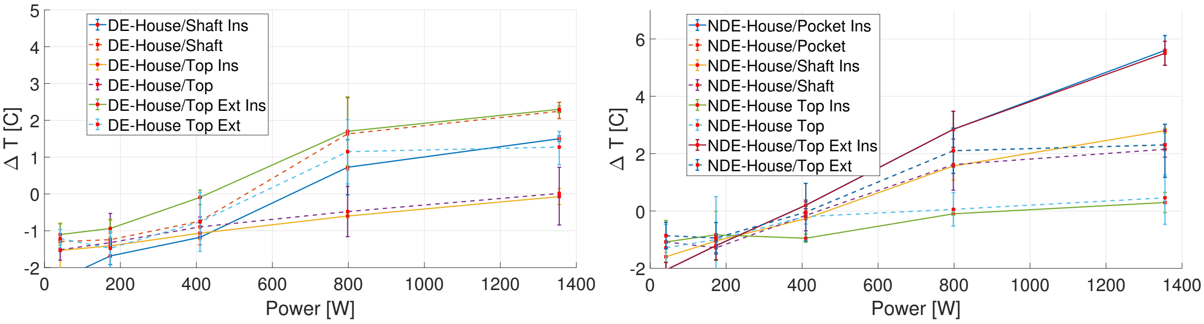

(e) *Middle Slot vs Bottom Slot temperature.* (f) *Housing,Core and Tooth temperature.*

Fig. 6.28. Temperature variation vs currents in stator assembly.

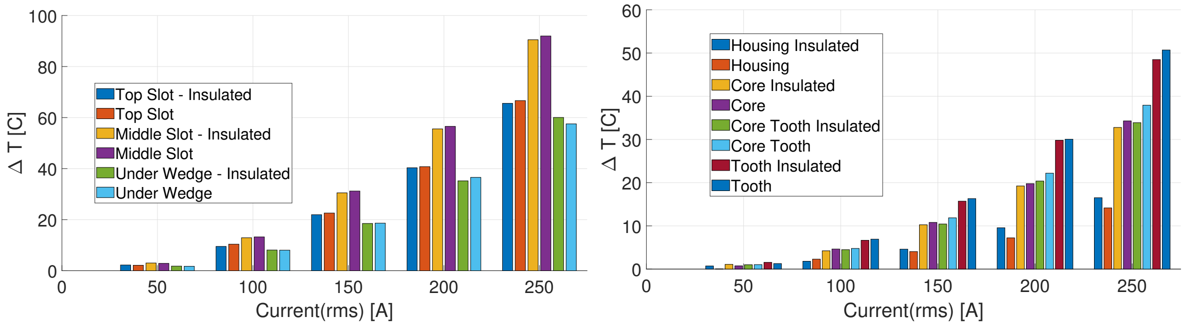

(a) *Max Temp in slots.* (b) *Max Temp in Housing,Core, Tooth.*

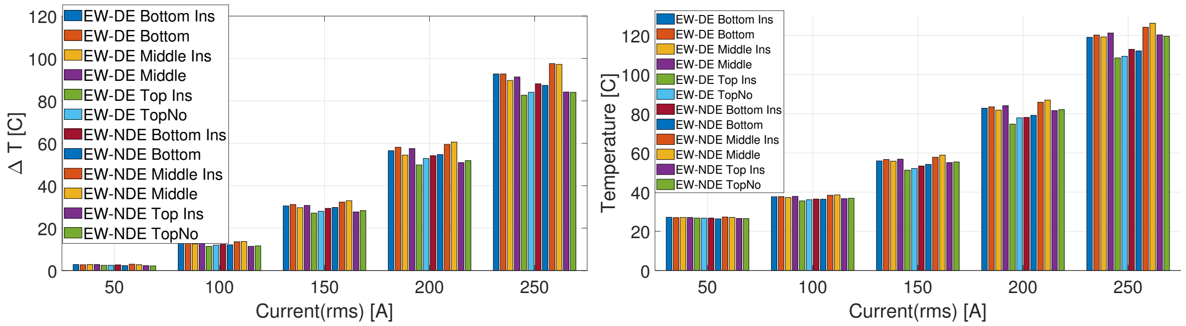

(c) *Avg Temp in End winding.* (d) *Max Temp in End Winding.*

Fig. 6.29. Temperature variation vs currents in stator assembly, Bar chart.

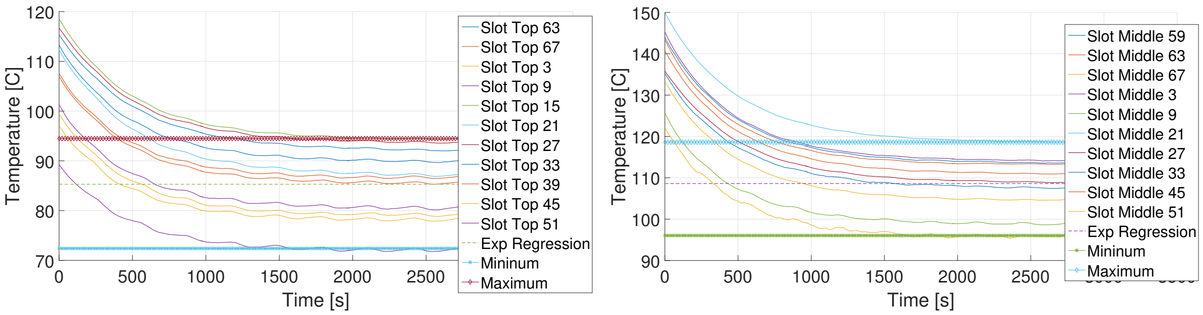

(a) *Top slot variations.* (b) *Middle slot variations.*

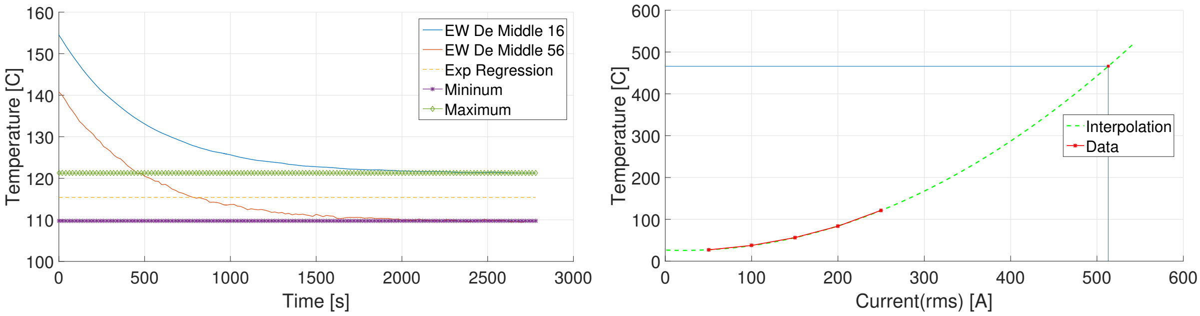

(c) *End windings temperature variations.* (d) *Interpolation of rated current.*

Fig. 6.30. Temperature variation in windings and theoretical regression for EW Hot-Spot. (250 [A] DC-current).

6.5.2 Considerations and partial conclusions

- Although the winding varnish insulation is capable to withstand up to 180° C for continuous operation, and up to 200° C for transient operation, and this would allow up to 300 [A] DC-current loading, the tests have been conducted up to only 250 [A] current level. This is because the leads' plastic covers started smoking. The hot-spots are the end-windings, as expected. This is mainly due to two reasons: former is the considerable length which is in air, the latter the mass winding share of the ends with respect to the whole winding length, as they are proportionally carrying a higher percentage of the total winding loss.

- The classic quadratic dependency over current and equivalent dependency over current is fulfilled, as described by Fig. 6.27 and 6.28.

- There is no substantial difference between the insulated and non insulated tests, as shown in Fig. 6.29. This applies to both average values over the different sensing point of the thermal circuit, as well as to the maximum values of temperature recorded. This might be attributed to the very high reflectivity of Aluminum. In other words, as there is no air moving during the tests, the only way the Aluminum caps could allow heat flux to enter them directly from the end windings is via radiation. As this is not the case the only heat transfer occurring outwards from the end windings relies on the winding itself, which in turn will transfer heat via conduction to the rest of the stator pack. If the inner side of the end-caps were painted black this will alleviate the thermal stress on the end winding as the emissivity will be higher. It is expected that the temperature will reduce, when the end-cap air is moved around during rated operation.

- It is evident that the stator assembly, at rated load is not capable of withstanding the thermal stress. This is candidly simple from Fig. 6.30 (d). The rated current is highlighted at 509 [A] (rms). In order to stay within the admissible thermal limits in a situation as the one replicated the current that can be sustained is 320 [A]. As a result the current density is limited to 7.6 [A/mm^2]. The power is therefore reduced to 157 [kW].

  There is also some unbalance around the stator circumferential periphery in terms of heat dissipation: there is not a complete uniformity in temperature steady state level, although the machine is electrically loaded with a series connection. This is clear for different parts of the stator windings as depicted in 6.30 (a), (b), (c).

- It is essential to have forced air to allow convection, especially convoying air streams against the end windings themselves. Even in this case, it is still not certain that the machine could withstand the full operational load at a standard 20° C ambient temperature. This is mainly because these preliminary tests have considered only the DC components (AC rms) of the injected current, whereas the machine in full torque operation, depending on the drive will have a significant AC loss component, due to iron losses, and AC resistance effects in the windings.

6.6 Full assembly experimental conditions and limits

Unfortunately the circumstances and the available equipment limited the variety of tests conducted on the designed machine. A major setback was due to the absence of a suitable inverter capable to bring the machine up to full rated power. Specifically, it is important to possess, as shown in details in Chapter 5, a very high switching frequency converter to prevent excessive rotor losses. Such equipment is not present at the University premises, preventing to perform loaded tests. Additionally, predominantly mechanical tests as run-downs cannot really be performed, as the whole testing facility couples the two bodies' inertia for master and slave electrical machines onto the test rig. The Torquemeter Dyno allows a gearbox shift among three different shafts: 4000, 10000, and 20000 [rpm]. Theoretically, it would be then possible to perform tests at rated speed (14000 [rpm]). For such a high inertial machine, an over-speed test would be required. This was not possible within time and scope of this work, due to lack of a proper and safe design for a dedicated high speed bench. Furthermore, difficulties due to the coronavirus pandemic prevented it being conducted elsewhere. In the laboratory environment, the speed limit is dictated by mechanical safety issues, as well as proper coupling available between different shafts. The lowest speed available (4000 [rpm] limit) has been the only choice for testing. All results related to speed needs then to be considered in light of the speed limitation, and proportional scaling/interpolation needs then to be considered when necessary. Undoubtedly all these aforementioned preconditions and limitations represent a major setback for this work as a whole. Tests therefore focused on the basic and general electromagnetic features that can be extrapolated.

6.7 No-Load Tests

The no load test aims to assess the magnetic circuit, i.e. the flux level is indirectly derived from the voltage collected at machine terminals. The relationship is purely linear with rotational speed. During testing a resonance in the test rig was identified at around 3400 [rpm]. This was associated with the rig gearbox vibration. For this reason the speed was not forced to be higher than 3200 [rpm]. Fig 6.31 (a) and (b) portray voltage measurement and related computed flux, respectively. Fig 6.32 (a) displays the experimental values for the peak sinusoidal first harmonic voltage over all speeds. Simple least squares linear interpolation is employed for extrapolating the values at higher speeds, up to rated speed. The red diamond marker locates the predicted voltage at rated conditions from simulation. Following the linear interpolation the results obtained are perfectly matching the expectation. Fig 6.32 (d) highlights the flux harmonic content. The flux level is on purpose presented using a logarithmic scale as in 5.4, to better appreciate the frequency spectrum, as opposed to the one presented at design stage in sub-figure 5.4 (b). The harmonic content is excellently satisfactory, as more than 99% of the spectrum is dominated by the first harmonic. This is expected from the Halbach array design, yet such a high value, despite the manufacture intrinsic tolerances, is quite remarkable.

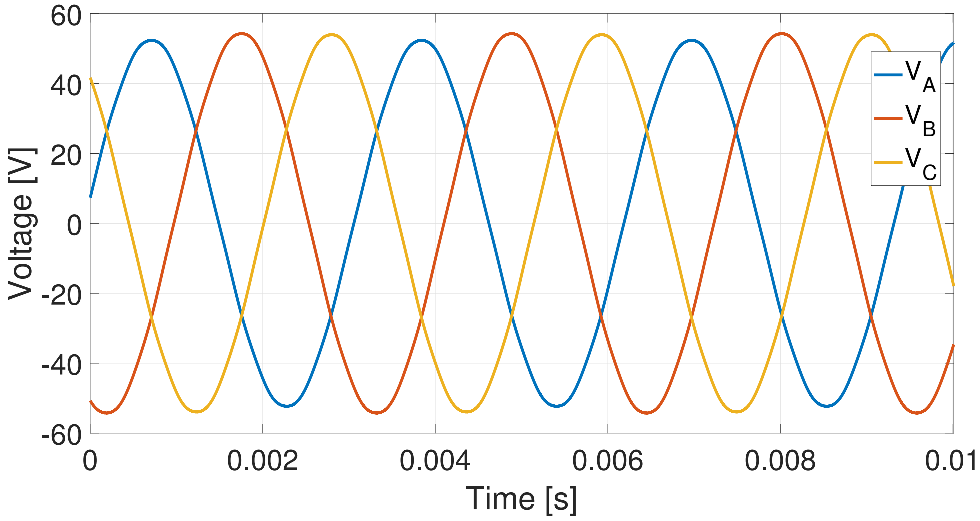

(a) *Voltage measurement (3200 rpm)*

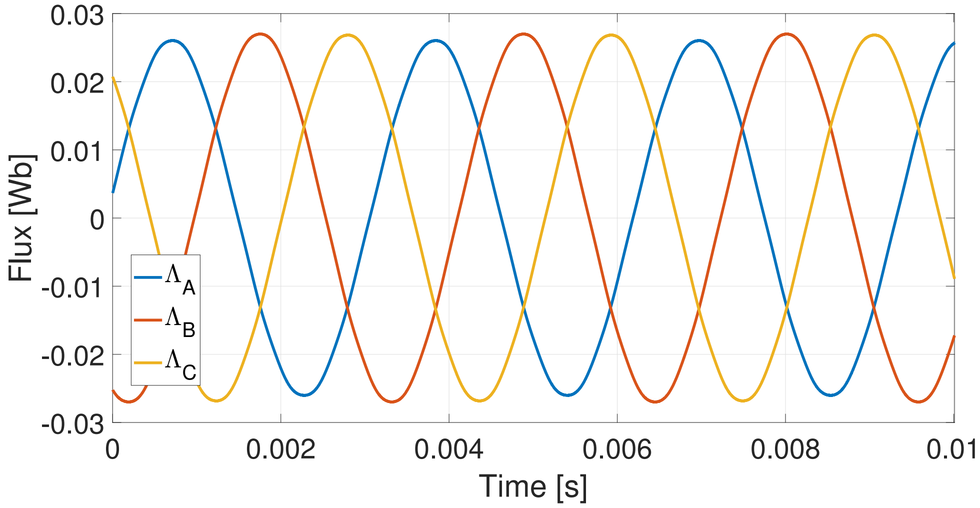

(b) *Derived flux (3200 rpm)*

Fig. 6.31. Experimental back-emf evaluation.

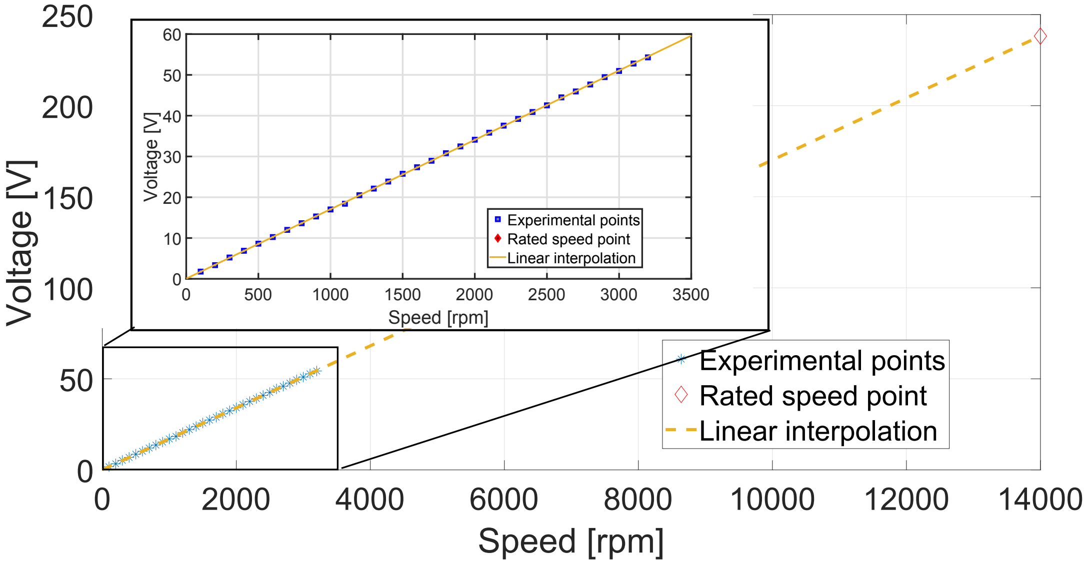

(a) *Linear interpolation*

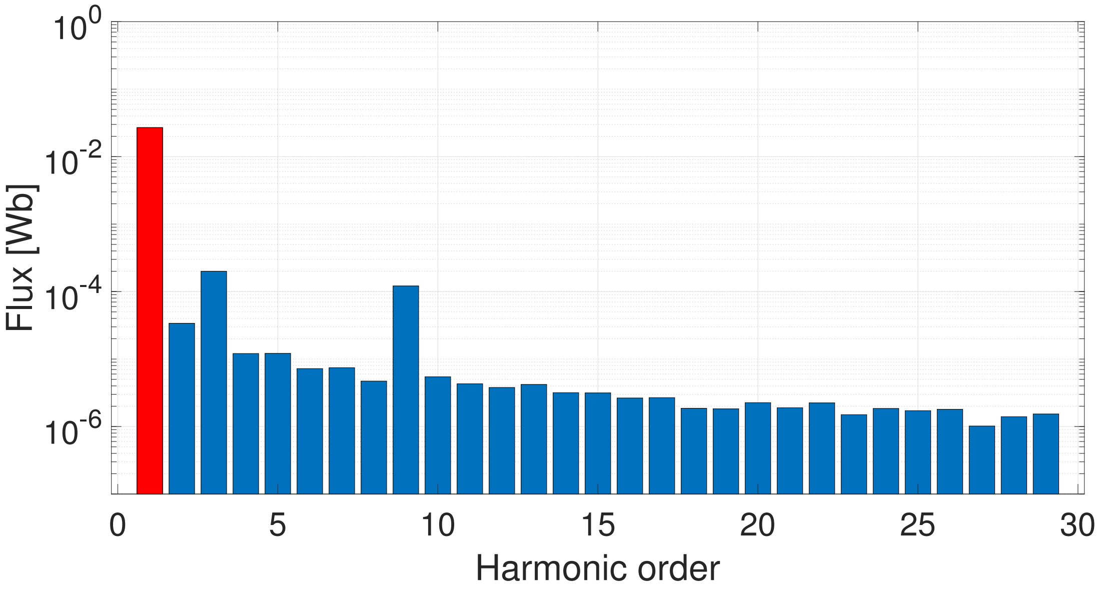

(b) *Harmonics spectrum (3200 rpm)*

Fig. 6.32. Experimental back-emf evaluation.

6.8 Short-circuit tests

There is no doubt that, with such a small magnetizing inductance, this machine is not really suitable for fault tolerance applications. This is visible by applying the standard linear synchronous reference frame theory for a permanent magnet machine and evaluating the short circuit current against the rotational speed, presented in Fig. 6.33 (a). Even at low speed, currents are high in magnitude, given the fact that the phase resistance is also remarkably low. Tests were conducted for speeds of 60, 80, 100 [rpm]. Lower than 55 [rpm] the rig could not be controlled in speed feedback properly, maintaining a constant steady state reference, due to significant ripple induced by the gearbox. Nevertheless, the values of current (first order sinusoidal harmonic) do not exhibit a too high discrepancy from the expected values: zoomed detail in Fig. 6.33 (b). The expected values are drawn from (6.6). The form is kept consistent with the standard theory of anisotropic machines, however in the calculation, as always done thorough this work direct and quadrature inductances are equivalent.

$$\begin{bmatrix} i_d^{ss} \\ i_q^{ss} \end{bmatrix} = -\frac{1}{\omega_e^2 L_d L_q + R_s^2} \begin{bmatrix} \omega_e^2 L_q \psi_{PM} \\ Rs\omega_e \psi_{PM} \end{bmatrix} \tag{6.6}$$

6.9 Generator tests

The generator test is simply an extension of the short circuit case. For simplicity and limited equipment that could sustain significantly high currents, the test has been conducted at limited speed with a simple resistive three-phase load. As before mentioned the speed was limited by the test rig gearbox behavior. Fig. 6.34 (a) provides a detail of the current waveform at 3000 [rpm], whereas (b) compares the theoretical current peak value trend with the experimental values.

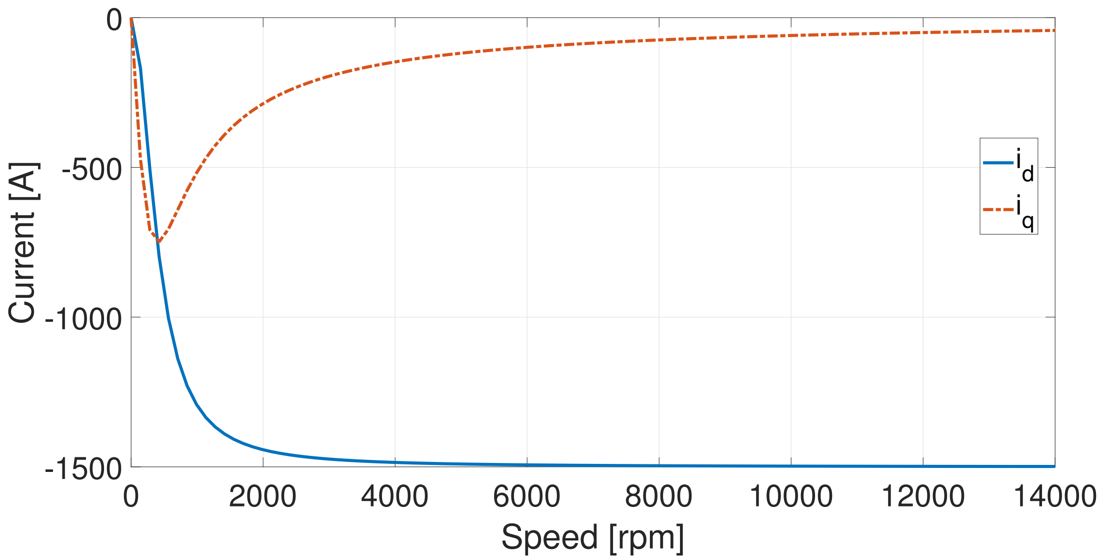

(a) *Theoretical dq currents.*

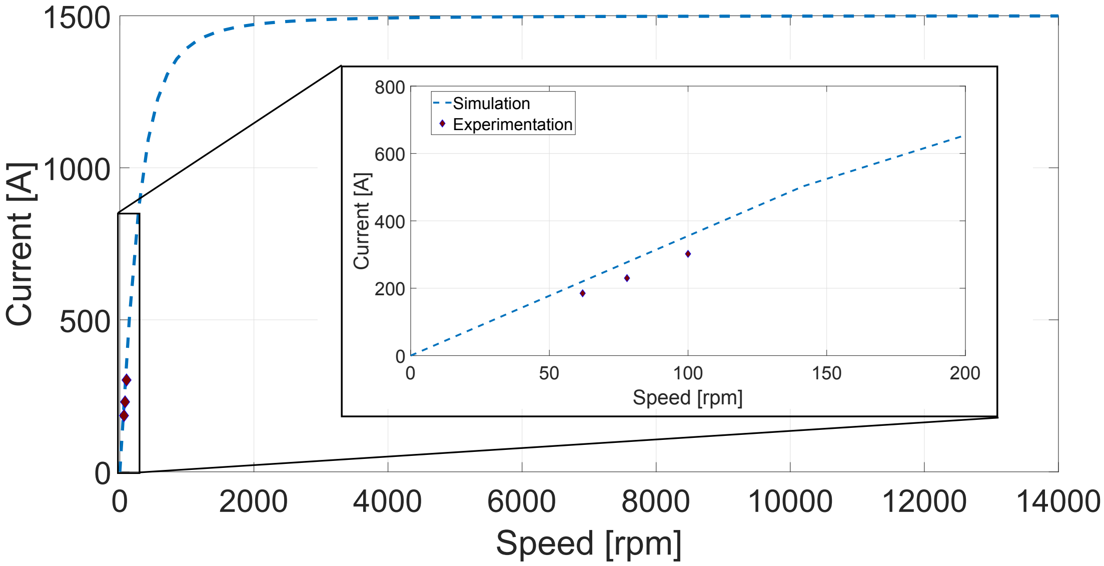

(b) *Simulation versus experimentation.*

Fig. 6.33. Short circuit test simulation vs experimentation.

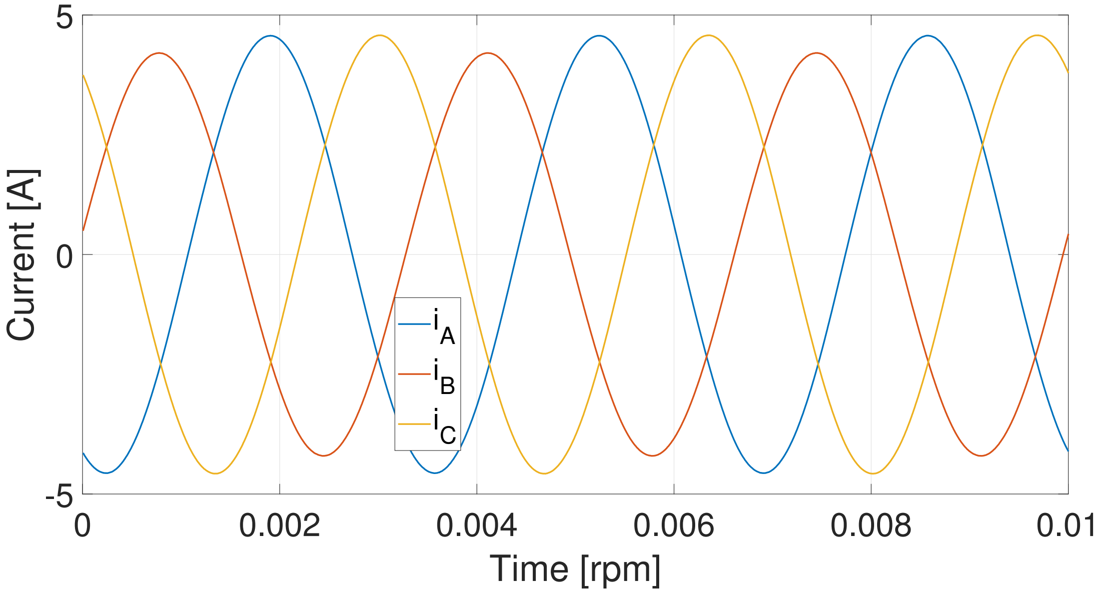

(a) *Current at 3000 rpm - Experimentation.*

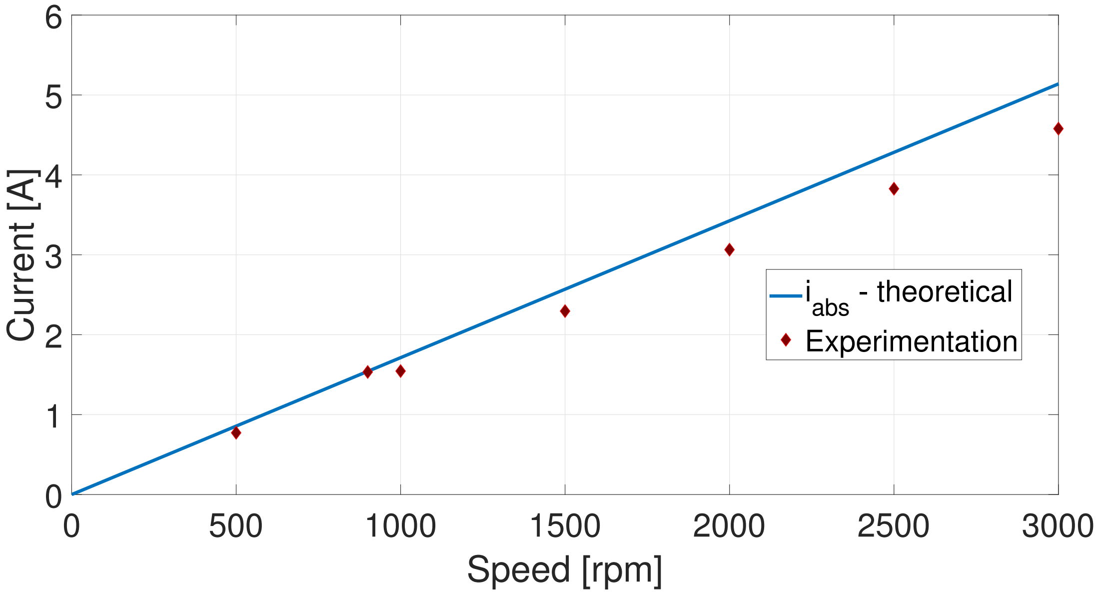

(b) *Simulation versus experimentation.*

Fig. 6.34. Generator test simulation vs experimentation.

6.10 Static Torque Tests

A static torque test detects the torque delivery the machine is capable of providing for a given current at a certain rotor position. The experiment conducted serves to validate the excitation side of the electromagnetic circuit. Fig. 6.35 (a) shows the equipment for this test, with a detail on the rotary table in (b).

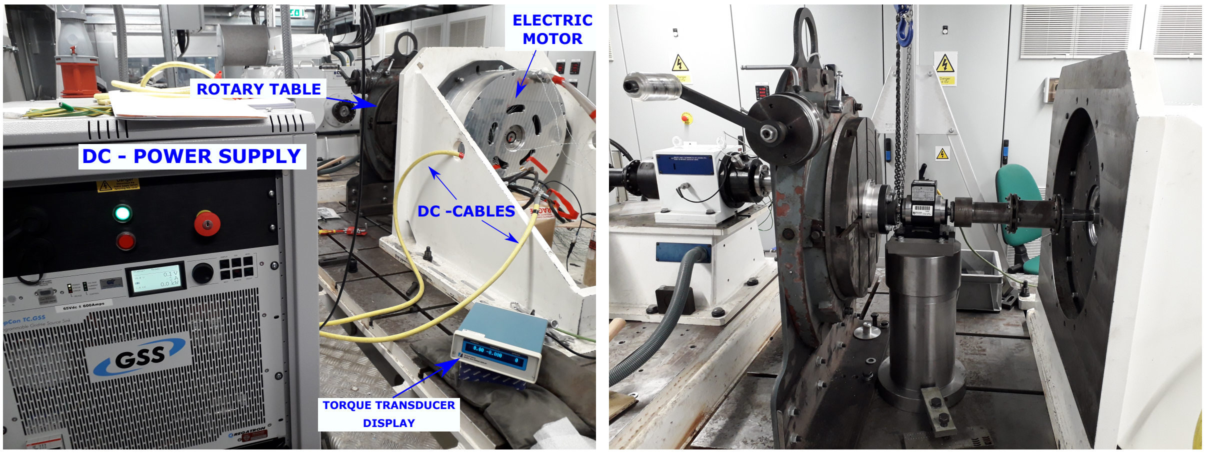

(a) *DC torque setup.* (b) *Rotary table, torque transducer and coupling.*

Fig. 6.35. Static torque measurement setup.

Injected currents were limited by the temperature rise and with associated losses. The torque transducer is rated up to 500 [Nm]. Current was raised up to 420 [A] - DC. The test was conducted with a fixed dc current, e.g. Phase A 1.0 , Phase B -0.5 and Phase C -0.5. A sinusoidally shaped torque waveform over an electric period is detected. For a full single mechanical revolution there are 6 periods, and 12 peaks. In Fig. 6.36 (b) a two PM pole sweep is presented (120 mechanical degrees) for two level of currents. . Any departure of the measured waveform from a smooth sinusoid is due to hysteresis from the torque transducer, backlash from rotating table which might allow for some very small, yet present slippage, and other additional factors which are at this point unknown. In Fig. 6.36 (a) the static torque against applied current is compared with the simulated value. Note that as the simulation shows clearly that the machine does not saturate, there is no significant torque derivative drop with respect to current at high current values. This is due to a very big electromagnetic airgap, so as observed in Chapter 4 the machine does not really operate in a non linear regime. From experimental results the torque constant is slightly lower than expected from simulations: 0.24 against 0.27 [Nm/A]. This is highlighted by the zoomed detail in Fig. 6.36 (a).

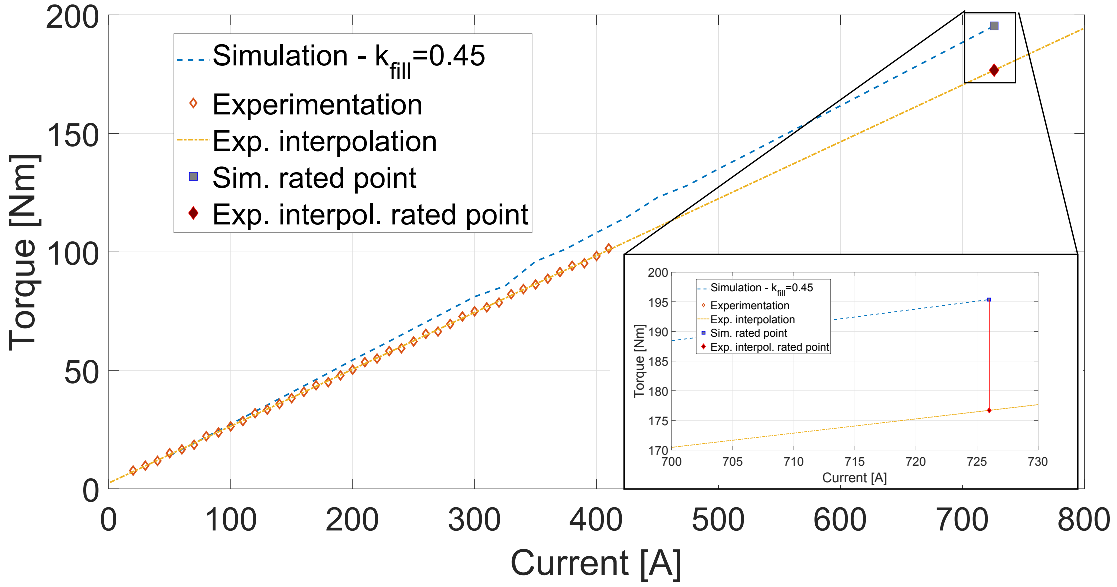

(a) *DC torque vs current.*

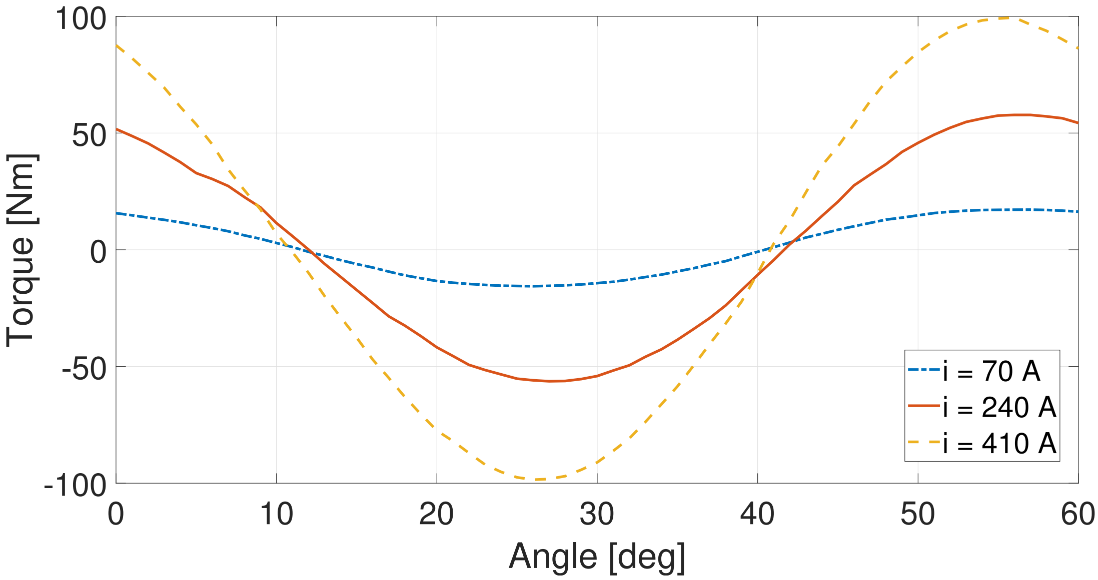

(b) *DC torque vs angular mechanical position, over one electrical period.*

Fig. 6.36. Static torque test results.

The interpolation results compare reasonably enough with the simulation to validate the machine electromagnetic circuit: at rated current a linear interpolation provides a discrepancy of 10% torque. About 19 [Nm] are missing at rated operational point. This is due to the winding choice providing a higher leakage and lower magnetizing component than the design stage. The motor during test was kept at constant temperature by liquid cooling setting water temperature at 20° C. In case of full rated speed and current operation the expectation is that the torque constant will further drop due to resistance increase on the stator side and magnetic field strength reduction from permanent magnet heating. To adjust for all these possible causes of discrepancy the motor stack length should have been amended adding some millimeters in excess, being more conservative, with respect to the optimal simulated solution extracted from Pareto fronts' (Refer back to Chapter 4). For completeness the torque against position is plotted in Fig. 6.36, for three different values of current over a single electrical period.

6.11 Impedance frequency response test

A frequency response test replicates the predictions presented in section 5.2. The same equipment used in Fig. 6.14 is needed. A frequency sweep from 2 to 200000 [Hz] has been conducted [2]. Fig. 6.37 defines the isotropy of the magnetic circuit against changes in frequency. It can be noticed for very low frequency a positive and negative spike. This is attributed to the known inaccuracy of the impedance analyzer at very low frequencies. Neglecting this most probably measurement inaccuracy the isotropy (invariance against rotor angular position) can be appreciated with a zoom provided by Fig. 6.38. This is not surprising and expected due to the almost perfect isotropy of a SPM first, exacerbated by the usage of a Halbach array which makes the recoil permeability constant all along the magnetic air-gap second. In Fig. 6.39; a specific position at 10° electrical angle is compared with simulations for an Aluminium shield presented in the previous chapter. The reduction in inductance with frequency rise is generally following predictions. Nonetheless there is a noticeable difference above 50 [Hz] throughout the whole spectrum. The measurement show a first flexural point at 400 [Hz]. Although the inductance value is higher than the simulation predicts, the convexity/concavity point occurs at the same frequency, which is approximately 1 [kHz]. A second flexural point is noticed at 10 [kHz], directing the inductance slope to a progressively decreasing value which does not follow the stabilizing trend of a flat inductance towards extremely high frequencies, given by the simulation. The fact that the actual inductance manifests an overall higher value than the expectation is to be considered a positive outcome: the THD due to lowered inductance at high frequency

---

[2] The impedance analyzer is limited to this value

value is reduced, therefore not aggravating the current ripple from a VSI, as much as previously evaluated. On the other hand, a clear motivation for a different trend after 10 [kHz] cannot be given. Only speculations can be drawn: possibly the interaction of more than just shield, PM and retaining plates and locating/clamping bolts, as well as the contact conductivity between all these materials play a role in shaping the frequency response.

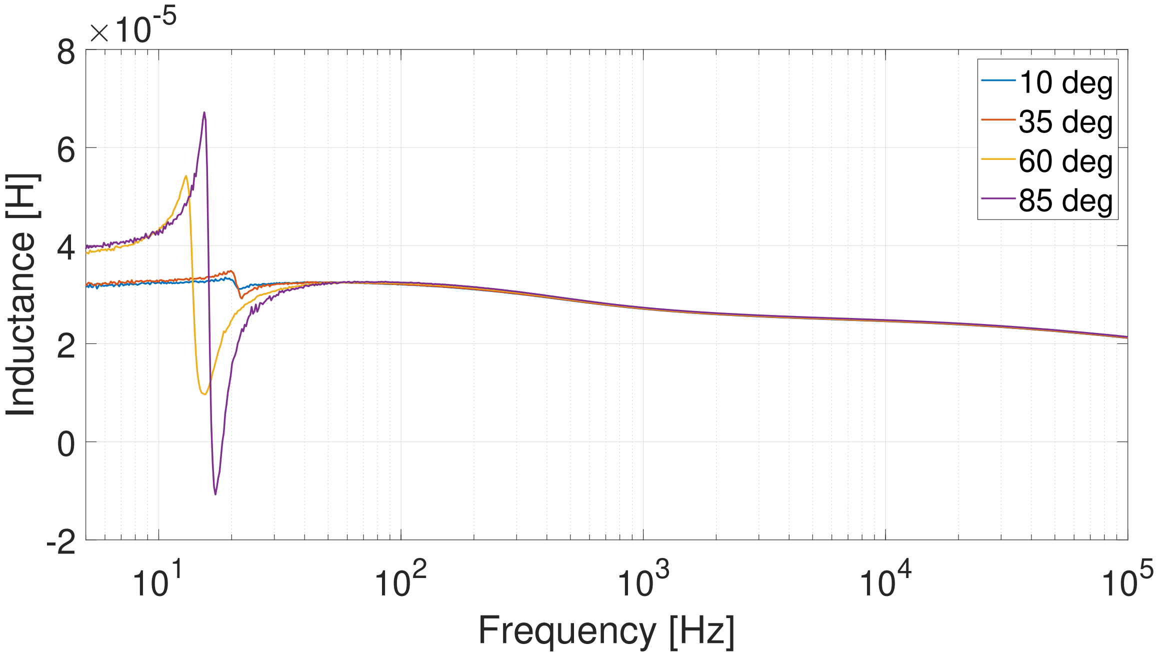

Fig. 6.37. Inductance vs frequency, experimentation at different rotor positions.

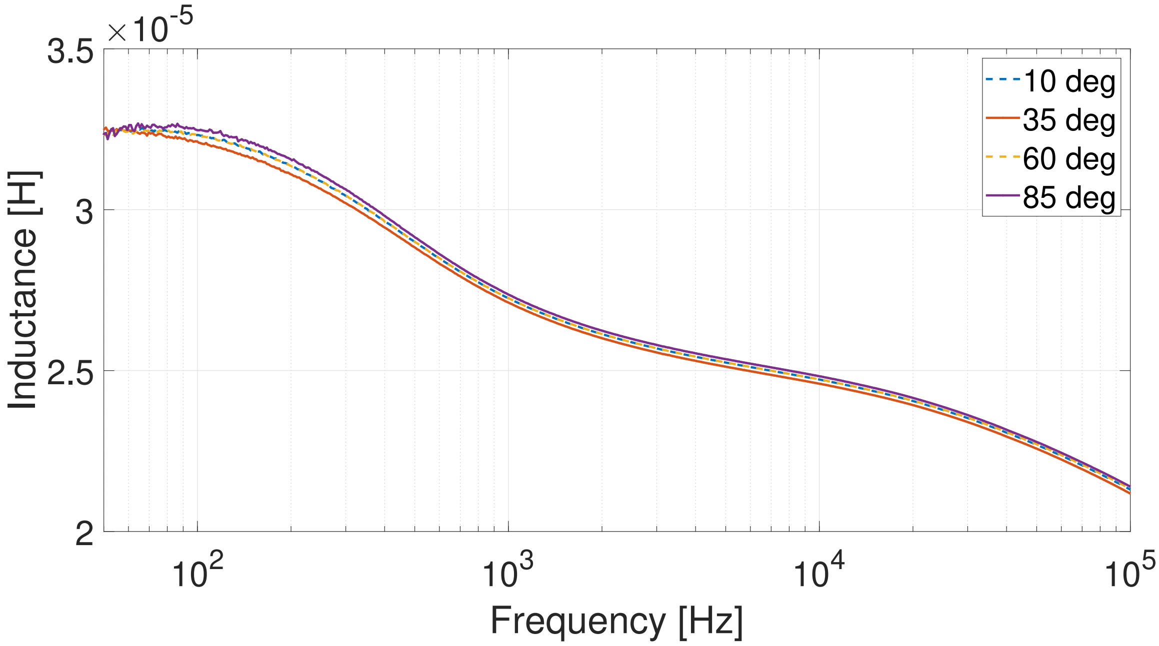

Fig. 6.38. Inductance vs frequency, experimentation at different rotor positions.

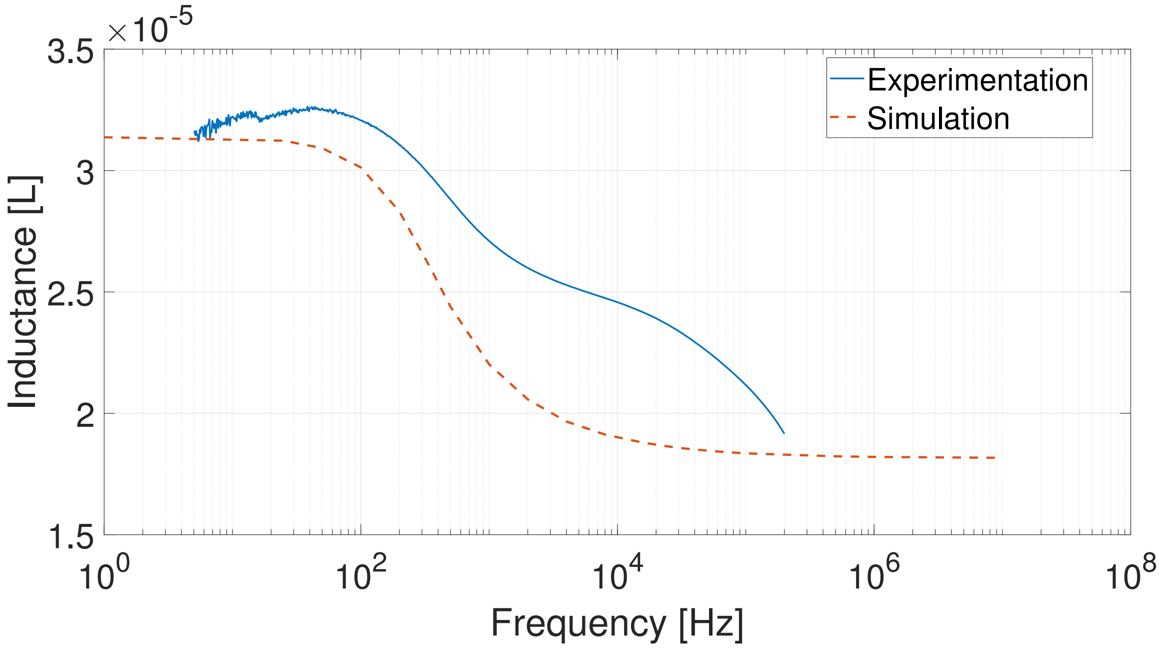

Fig. 6.39. Inductance vs frequency, experimental vs simulation.

Chapter 7

Conclusions

This research has dealt with the electro-mechanical design and optimisation of a high-speed-high-power (HSHP) electric motor. The machine under study is tailored for an aerospace propulsion known as Boundary-Layer-Ingestion (BLI). It can be concluded that:

- a suitable electric motor topology for this application resulted in a rim drive solution, opposed to a direct drive which would have been under-performing due to geometrical limitations and electric loading. Nonetheless, it must be recognized, that tailoring this specific design-for-application forced the electrical engineer to consider unconventional geometries, more appropriately aspect-ratios, in order to cope with the assumed propeller specifications. Summarizing the rationale behind the research conducted, it can be stated that, although the presence of propeller geometric constraints would have forced a topology leaning towards an axial flux machine, the extremely high tangential velocity ruled out in the very beginning such a choice.
- the winding arrangement for achieving the best performance fell onto integer windings, was identified. Although very appealing, a fractional slot winding arrangement, contemplated in the beginning to guarantee a lower total mass for a set torque, resulted in a failure to provide a sufficiently bigger increment in power density, compared to a standard distributed winding. Moreover, the optimization conducted supported a distributed arrangement, delivering a relatively low rotor loss figure, due to almost inexistent asynchronous harmonics caused by the discrete spatial arrangement of the armature winding.

- the best choice for rotor magnetization was identified. Although, as mentioned previously, and heavily investigated in [21], a permanent magnet outer rotor topology might have been of interest, an out-runner design would have been probably too adventurous to undertake, given technical and manufacturing difficulties. Confined then to the realm of interior rotor radial flux machines, excluding the induction motor, the Surface Permanent Magnet topology won the test, providing a superior robustness against the Interior Permanent Magnet. Solutions such as Switched Reluctance, or Synchronous Reluctance have not been even considered for their inherently low power density. Moreover, as the research was focused on continuous operation, the IPM would have not been exploited properly (its main attribute is the versatility to fit well within flux weakening and high operational point variability in the motor utilization), leaving room for the SPM alone. Although relying on a standard surface permanent magnet common topology, the design presented challenges which affected significantly the optimisation procedure which has been conducted considering mechanical, electrical and geometrical constraints. The best solution for maximizing the power density was also identified to be a Halbach array permanent magnet arrangement.

- the rotor solution employed needs an electromagnetic screen to take into counteract additional rotor loss due to power electronic interaction. Interesting aspects as the implication of time harmonics on the overall machine performance have arisen, giving room for an investigation that might be interesting for all those applications which encompass a very high operational frequency in which the inductance is dependent on frequency. This can ameliorate the system dynamic modeling in state space, and provide a better performing feedback control for high frequency operation.

- such a design needed to be finally tuned considering additional aspects and details. In the final stages this was twofold: both mechanical and electromagnetic aspects were of interest. The former regards holding forces in order to sustain the retaining sleeve, components stresses, bearings choice, and rotordynamic behaviour of the rotor assembly. The latter addresses eddy current losses arising in different rotor parts. Usually different physics involving rotor losses, mechanical and thermal stresses are treated separately or superficially analysed with rules of thumbs approaches. This work addressed the lack of a more detailed comprehensive design, treating mechanics and electromagnetic challenges together.

The optimised final design yields a very large outer diameter at the expense of a reduced stack length. At first glance an electric motor design featuring a very short axial length, compared to a predominant copper share in favour of end-windings, does not seem sensible. This is reasonably associated to the abundant presence of bulky end windings, which are not responsible of any torque production, contributing, if not detrimentally, to a reduction in power density. Therefore, even if stated as one of the main goals at the beginning of the thesis an increase in power density is still very questionable, in light of the limited cooling capacity that the machine exhibits, and the amount of non active winding the prototype possesses. Other concepts drifting from conventional electric motors are needed for this application and the most natural one seems to be represented by superconducting solutions or heavily cooled motors, such as machines where the stator is cooled by liquid nitrogen. These solutions are under study at the moment, but a significant breakthrough has not been achieved yet.
Finally, some elements to consider for further research are hereby listed:

1. First and foremost, it is the belief of the author that a dynamic test for the machine is necessary to evaluate the full rated operational capabilities. A mapping of torque vs speed would be of interest, although the device has been designed for a fixed speed operation (no flux weakening capabilities taken into account during the design process). At the moment, University facilities do not comprise a powerful enough electronic converter with a sufficiently high switching frequency. It is for this reason, that the motor could not be run at fundamental frequency.

2. The thermal modelling could be further expanded considering a full device dynamics. Although most of thermal management performances referred to the stator could be deduced from thermal tests conducted, there is no full comprehension of the cooling extraction and heating dynamics of the rotor. This is mainly due to the unknown or very scarce knowledge of flows, mechanical friction losses and heat extraction from the rotor assembly. The rotor is in fact spoked and vortexes are expected to arise, modifying possibly both frictional behaviour on one hand and heat extraction capability on the other. The nature of heat generation in the rotor has been analyzed assuming the electromagnetically

shielded operation, for a supposed worst-case-scenario situation (the shield with maximum resistance due to an assumed 200° C temperature). However, it is reiterated that only a full load test could yield the whole discernment with reference to the rotor loss dynamic.

3. Further on thermal performance, it is righteous to stress how, even though the motor was equipped with a cooling jacket, the hot spots were represented by the end windings. As presented in Chapter 6, a DC current test highlighted very high temperatures, close to the allowable insulation limits, for the end windings, already at 300 [A] (In steady state conditions). Considering that the rated design features a current of 509 [A] (rms), concerns on a forced air cooling strategy might be raised. The assumption of 100000 [A/m] as electric loading limit was most probably too generous. This however, does not exclude that such a heavy thermal stress on the end windings, might be dealt with in a situation where extremely cold air (-40° C), with extremely high velocity (200 [m/s]), is impinging on the motor ends. In this case, particular care should be given though to the possible temperature gradient between Drive-End and Non-Drive-End side of the winding.

4. A mechanical strength over-speed test for assessing whether the rotor is mechanically sound would be a necessity for an industrial case. Considering this research result a proof of concept prototype in order to perform such a test, the motor would need to be disassembled (extract the rotor from the stator), extract and substitute the angular contact bearings. The bearings are extremely delicate being angular contact and pre-loaded already, they would be damaged by extraction, being them manufactured for high-precision. An over-speed test was not possible during this work, because the University does not own facilities possessing a safe and anti-explosion chamber, capable to withstand the sort of impact that might arise from a mechanical failure during operation at rated speed. Reiterating some concepts presented in Chapter 3, even though the rated [rpm] specification does not seem high, the issue relates to the energy. It is wise to remember that kinetic energy is directly proportional to the mass, linearly; but most importantly to the speed (tangential [m/s]) quadratically.

5. The prototype constructed employed a spoked geometry, in order to very roughly emulate the propeller. A CFD modeling for understanding how much is the impact of such a rotor

geometry, as well as how much is the impact of other retaining parts (as the axially located plates and bolts) is needed. This could be modeled and tested against rundown tests, encapsulating the rotor axial ends with plastic or other low density materials to prevent flow through the rotor pockets. Once more, this test will imply stator/rotor disassembly, bearing extraction and substitution, provided there is an ad-hoc high speed bench and a safe testing environment.

6. Towards a more final end application oriented perspective, it is a must assessing the mechanical axial load provided by employing a real propeller fan. This will have strong implications towards the bearing choice and arrangements, as well as towards the torsional vibration behaviour.
7. The research conducted did not include the analysis, detection and/or mitigation of high order electromagnetic interaction, like the ones arising from unbalanced magnetic pulls due to eccentricity, or simply magnetic attraction. This could cause additional noise, vibrations and losses. Given the winding choice it is fairly safe to rule out any magnetic pull due to space harmonics interaction. In terms of eccentricity the same cannot be stated.

References

[1] Committe on Climate Change. The 2050 target - achieving an 80international aviation and shipping. 2012.

[2] Eric S. Hendricks. A review of boundary layer ingestion modeling approaches for use in conceptual design. Technical report, NASA, Glenn Research Center, Cleveland, Ohio, 2018.

[3] C. D. Manolopoulos, M. F. Iacchetti, A. C. Smith, P. M. Tuohy, X. Pei, M. Husband, and P. Miller. Design of superconducting ac propulsion motors for hybrid electric aerospace. In *2018 AIAA/IEEE Electric Aircraft Technologies Symposium (EATS)*, pages 1–9, July 2018.

[4] F. Berg, J. Palmer, P. Miller, M. Husband, and G. Dodds. Hts electrical system for a distributed propulsion aircraft. *IEEE Transactions on Applied Superconductivity*, 25(3): 1–5, June 2015. ISSN 1051-8223. doi: 10.1109/TASC.2014.2384731.

[5] NASA. *NASA Technology Roadmaps TA 15: Aeronautics*. NASA, May 2015.

[6] A. K. Yoon, J. Xiao, D. Lohan, F. Arastu, and K. S. Haran. High frequency electric machines for boundary layer ingestion fan propulsor. *IEEE Transactions on Energy Conversion*, pages 1–1, 2019. doi: 10.1109/TEC.2019.2942775.

[7] W. Cao, B. C. Mecrow, G. J. Atkinson, J. W. Bennett, and D. J. Atkinson. Overview of electric motor technologies used for more electric aircraft (mea). *IEEE Transactions on Industrial Electronics*, 59(9):3523–3531, Sept 2012. ISSN 0278-0046. doi: 10.1109/TIE.2011.2165453.

[8] A. Tuysuz, A. Schaubhut, C. Zwyssig, and J. W. Kolar. Model-based loss minimization in high-speed motors. In *Electric Machines Drives Conference (IEMDC), 2013 IEEE International*, pages 332–339, May 2013. doi: 10.1109/IEMDC.2013.6556272.

[9] Cao Wenping, B. C. Mecrow, G. J. Atkinson, J. W. Bennett, and D. J. Atkinson. Overview of electric motor technologies used for more electric aircraft (mea). *IEEE Transactions on Industrial Electronics*, 59(9):3523–3531, 2012. ISSN 0278-0046 1557-9948. doi: 10.1109/tie.2011.2165453.

[10] Daniel Smith. *High speed high power electrical machines*. PhD thesis, Electrical Engineering, Newcastle University, 2014.

[11] M. Degano, P. Arumugam, W. Fernando, T. Yang, H. Zhang, J. B. Bartolo, S. Bozhko, P. Wheeler, and C. Gerada. An optimized bi-directional, wide speed range electric starter-generator for aerospace application. In *7th IET International Conference on Power Electronics, Machines and Drives (PEMD 2014)*, pages 1–6, April 2014. doi: 10.1049/cp.2014.0483.

[12] F. Marignetti. On liquid-nitrogen-cooled copper-wound machines with soft magnetic composite core. *IEEE Transactions on Industry Applications*, 46(3):984–992, May 2010. ISSN 0093-9994. doi: 10.1109/TIA.2010.2045328.

[13] F. Marignetti, S. Carbone, V. Delli Colli, and C. Attaianese. Cryogenic characterization of copper-wound linear tubular actuators. *IEEE Transactions on Industrial Electronics*, 59 (5):2167–2177, May 2012. ISSN 0278-0046. doi: 10.1109/TIE.2011.2164749.

[14] A. El-Refaie and M. Osama. High specific power electrical machines: A system perspective. *CES Transactions on Electrical Machines and Systems*, 3(1):88–93, March 2019. ISSN 2096-3564. doi: 10.30941/CESTEMS.2019.00012.

[15] X. Yi, A. Yoon, and K. S. Haran. Multi-physics optimization for high-frequency air-core permanent-magnet motor of aircraft application. In *2017 IEEE International Electric Machines and Drives Conference (IEMDC)*, pages 1–8, May 2017. doi: 10.1109/IEMDC.2017.8002293.

[16] A. Yoon and K. Haran. Scaling study of high frequency machine for electric aircraft propulsion. In *2018 IEEE Energy Conversion Congress and Exposition (ECCE)*, pages 4439–4444, Sep. 2018. doi: 10.1109/ECCE.2018.8557886.

[17] L. Li, J. Zhang, C. Zhang, and J. Yu. Research on electromagnetic and thermal issue of high-efficiency and high-power-density outer-rotor motor. *IEEE Transactions on Applied Superconductivity*, 26(4):1–5, June 2016. ISSN 1051-8223. doi: 10.1109/TASC.2016.2542192.

[18] K. Kim, B. Lee, H. Kim, J. Hong, and J. Jun. Thermal analysis of outer rotor type ipmsm using thermal equivalent circuit. In *2012 15th International Conference on Electrical Machines and Systems (ICEMS)*, pages 1–4, Oct 2012.

[19] X. Yi, R. Sanchez, K. Haran, J. Veres, A. T. Perry, and P. J. Ansell. Self-pumped air-cooling design for a high-speed high-specific-power motor. In *2018 IEEE Transportation Electrification Conference and Expo (ITEC)*, pages 274–279, June 2018. doi: 10.1109/ITEC.2018.8450114.

[20] Y. Chen, R. Sanchez, A. Yoon, and K. S. Haran. Mechanical design considerations of an ironless, high-specific-power electric machine. *IEEE Transactions on Transportation Electrification*, 3(4):855–863, Dec 2017. ISSN 2332-7782. doi: 10.1109/TTE.2017.2733763.

[21] R. Sanchez, A. Yoon, X. Yi, L. Zheng, Y. Chen, K. S. Haran, A. Provenza, and J. Veres. Mechanical validation of a high power density external cantilevered rotor. *IEEE Transactions on Industry Applications*, 54(4):3208–3216, July 2018. ISSN 0093-9994. doi: 10.1109/TIA.2018.2813336.

[22] A. D. Anderson, Y. Wang, Y. Yu, and K. S. Haran. Experimental validation of a high-power slotless stator. In *2019 IEEE International Electric Machines Drives Conference (IEMDC)*, pages 1564–1569, May 2019. doi: 10.1109/IEMDC.2019.8785264.

[23] D. Lee, A. Yoon, S. Sirimanna, S. Salon, and K. Haran. Impact of manufacturing tolerances on a low-reactance slotless pm synchronous machine. *IEEE Transactions on Energy Conversion*, pages 1–1, 2019. ISSN 0885-8969. doi: 10.1109/TEC.2019.2938144.

[24] R. R. Moghaddam. High speed operation of electrical machines, a review on technology, benefits and challenges. In *2014 IEEE Energy Conversion Congress and Exposition (ECCE)*, pages 5539–5546, 2014. doi: 10.1109/ECCE.2014.6954160.

[25] M. van der Geest, H. Polinder, J. A. Ferreira, and M. Christmann. Power density limits and design trends of high-speed permanent magnet synchronous machines. *IEEE Transactions on Transportation Electrification*, 1(3):266–276, Oct 2015. doi: 10.1109/TTE.2015.2475751.

[26] Z. Kolondzovski, A. Arkkio, J. Larjola, and P. Sallinen. Power limits of high-speed permanent-magnet electrical machines for compressor applications. *IEEE Transactions on Energy Conversion*, 26(1):73–82, March 2011. ISSN 0885-8969. doi: 10.1109/TEC.2010.2089459.

[27] A. Borisavljevic, H. Polinder, and J. A. Ferreira. On the speed limits of permanent-magnet machines. *IEEE Transactions on Industrial Electronics*, 57(1):220–227, Jan 2010. ISSN 0278-0046. doi: 10.1109/TIE.2009.2030762.

[28] D. Gerada, A. Mebarki, N. L. Brown, C. Gerada, A. Cavagnino, and A. Boglietti. High-speed electrical machines: Technologies, trends, and developments. *IEEE Transactions on Industrial Electronics*, 61(6):2946–2959, June 2014. ISSN 0278-0046. doi: 10.1109/TIE.2013.2286777.

[29] J. A. Ferreira. Improved analytical modeling of conductive losses in magnetic components. *IEEE Transactions on Power Electronics*, 9(1):127–131, Jan 1994. ISSN 1941-0107. doi: 10.1109/63.285503.

[30] C. R. Sullivan. Computationally efficient winding loss calculation with multiple windings, arbitrary waveforms, and two-dimensional or three-dimensional field geometry. *IEEE Transactions on Power Electronics*, 16(1):142–150, Jan 2001. ISSN 0885-8993. doi: 10.1109/63.903999.

[31] A. Fatemi, D. M. Ionel, N. A. O. Demerdash, D. A. Staton, R. Wrobel, and Y. C. Chong. Computationally efficient strand eddy current loss calculation in electric machines. *IEEE Transactions on Industry Applications*, 55(4):3479–3489, 2019. doi: 10.1109/TIA.2019.2903406.

[32] A. Lehikoinen and A. Arkkio. Efficient finite-element computation of circulating currents in thin parallel strands. *IEEE Transactions on Magnetics*, 52(3):1–4, March 2016. ISSN 0018-9464. doi: 10.1109/TMAG.2015.2481934.

[33] A. Lehikoinen, N. Chiodetto, E. Lantto, A. Arkkio, and A. Belahcen. Monte carlo analysis of circulating currents in random-wound electrical machines. *IEEE Transactions on Magnetics*, 52(8):1–12, Aug 2016. ISSN 0018-9464. doi: 10.1109/TMAG.2016.2535332.

[34] A. Lehikoinen, A. Arkkio, and A. Belahcen. Reduced basis finite element modeling of electrical machines with multiconductor windings. *IEEE Transactions on Industry Applications*, 53(5):4252–4259, Sep. 2017. doi: 10.1109/TIA.2017.2696509.

[35] A. Lehikoinen, J. Ikaheimo, A. Arkkio, and A. Belahcen. Domain decomposition approach for efficient time-domain finite-element computation of winding losses in electrical machines. *IEEE Transactions on Magnetics*, 53(5):1–9, May 2017. doi: 10.1109/TMAG.2017.2681045.

[36] R. Wrobel, D. E. Salt, A. Griffo, N. Simpson, and P. H. Mellor. Derivation and scaling of ac copper loss in thermal modeling of electrical machines. *IEEE Transactions on Industrial Electronics*, 61(8):4412–4420, 2014. doi: 10.1109/TIE.2013.2266088.

[37] R. Wrobel, P. H. Mellor, M. Popescu, and D. A. Staton. Power loss analysis in thermal design of electrical machines. In *2015 IEEE Workshop on Electrical Machines Design, Control and Diagnosis (WEMDCD)*, pages 118–126, 2015. doi: 10.1109/WEMDCD.2015.7194519.

[38] P. Mellor, R. Wrobel, and N. Simpson. Ac losses in high frequency electrical machine windings formed from large section conductors. In *2014 IEEE Energy Conversion Congress and Exposition (ECCE)*, pages 5563–5570, 2014. doi: 10.1109/ECCE.2014.6954163.

[39] G. Bertotti. General properties of power losses in soft ferromagnetic materials. *IEEE Transactions on Magnetics*, 24(1):621–630, Jan 1988. ISSN 0018-9464. doi: 10.1109/20.43994.

[40] G. Bertotti. Physical interpretation of eddy current losses in ferromagnetic materials. i. theoretical considerations. *Journal of Applied Physics*, 57(6):2110–2117, 1985.

[41] C. P. Steinmetz. On the law of hysteresis. *Transactions of the American Institute of Electrical Engineers*, IX(1):1–64, Jan 1892. ISSN 0096-3860. doi: 10.1109/T-AIEE.1892.5570437.

[42] J.D. Jackson. *Classical Electrodynamics*. John Wiley & Sons, 1998.

[43] Sheppard J. Salon. *Finite Element Analysis of Electrical Machines*. Springer, 1995.

[44] J. Yim, S. Sul, B. Bae, N. R. Patel, and S. Hiti. Modified current control schemes for high-performance permanent-magnet ac drives with low sampling to operating frequency ratio. *IEEE Transactions on Industry Applications*, 45(2):763–771, 2009. doi: 10.1109/TIA.2009.2013600.

[45] K. Huh and R. D. Lorenz. Discrete-time domain modeling and design for ac machine current regulation. In *2007 IEEE Industry Applications Annual Meeting*, pages 2066–2073, 2007. doi: 10.1109/07IAS.2007.312.

[46] T.J.E. Miller J.R. Hendershot. *Design of Brushless Permanent-Magnet Machines*. Motor Design Books LLC, 2010.

[47] M. Schoning. Automated electrical machine design with differential evolution techniques. In *2011 1st International Electric Drives Production Conference*, pages 221–224, Sep. 2011. doi: 10.1109/EDPC.2011.6085574.

[48] P. E. Kakosimos, A. G. Sarigiannidis, M. E. Beniakar, A. G. Kladas, and C. Gerada. Induction motors versus permanent-magnet actuators for aerospace applications. *IEEE Transactions on Industrial Electronics*, 61(8):4315–4325, 2014. doi: 10.1109/TIE.2013.2274425.

[49] Z. P. Xia, Z. Q. Zhu, and D. Howe. Analytical magnetic field analysis of halbach magnetized permanent-magnet machines. *IEEE Transactions on Magnetics*, 40(4):1864–1872, July 2004. ISSN 0018-9464. doi: 10.1109/TMAG.2004.828933.

[50] M. Marinescu and N. Marinescu. New concept of permanent magnet excitation for electrical machines: analytical and numerical computation. *IEEE Transactions on Magnetics*, 28(2):1390–1393, 1992. doi: 10.1109/20.123952.

[51] H. Jun, J. Lee, H. Lee, and W. Kim. Study on the optimal rotor retaining sleeve structure for the reduction of eddy-current loss in high-speed spmsm. *IEEE Transactions on Magnetics*, 51(3):1–4, 2015. doi: 10.1109/TMAG.2014.2361861.

[52] F. Zhang, G. Du, T. Wang, G. Liu, and W. Cao. Rotor retaining sleeve design for a 1.12-mw high-speed pm machine. *IEEE Transactions on Industry Applications*, 51(5): 3675–3685, 2015. doi: 10.1109/TIA.2015.2423659.

[53] Y. Lv, D. Xia, Q. Wang, and L. Li. Post-assembly magnetization of high speed pm rotor with metallic sleeve. In *2017 20th International Conference on Electrical Machines and Systems (ICEMS)*, pages 1–5, 2017. doi: 10.1109/ICEMS.2017.8056482.

[54] M. Galea, L. Papini, H. Zhang, C. Gerada, and T. Hamiti. Demagnetization analysis for halbach array configurations in electrical machines. *IEEE Transactions on Magnetics*, 51 (9):1–9, Sept 2015. ISSN 0018-9464. doi: 10.1109/TMAG.2015.2429645.

[55] S. Ruoho, E. Dlala, and A. Arkkio. Comparison of demagnetization models for finite-element analysis of permanent-magnet synchronous machines. *IEEE Transactions on Magnetics*, 43(11):3964–3968, 2007. doi: 10.1109/TMAG.2007.906749.

[56] D. Woo and B. H. Jeong. Irreversible demagnetization of permanent magnet in a surface-mounted permanent magnet motor with overhang structure. *IEEE Transactions on Magnetics*, 52(4):1–6, 2016. doi: 10.1109/TMAG.2015.2476782.

[57] B. Guo, Y. Huang, F. Peng, and J. Dong. General analytical modeling for magnet demagnetization in surface mounted permanent magnet machines. *IEEE Transactions on Industrial Electronics*, 66(8):5830–5838, 2019. doi: 10.1109/TIE.2018.2873099.

[58] B. M. Ebrahimi and J. Faiz. Demagnetization fault diagnosis in surface mounted permanent magnet synchronous motors. *IEEE Transactions on Magnetics*, 49(3):1185–1192, 2013. doi: 10.1109/TMAG.2012.2217978.

[59] K. Halbach. Permanent multipole magnets with adjustable strength. *IEEE Transactions on Nuclear Science*, 30(4):3323–3325, Aug 1983. doi: 10.1109/TNS.1983.4336645.

[60] R. Bjork. The ideal dimentions of a halbach cylinder of finite length. *Journal of Applied Physics*, 109(1), Nov 2011. doi: https://doi.org/10.1063/1.3525646.

[61] Zhuoran Zhang, Chen Wang, and Weiwei Geng. Design and optimization of halbach-array pm rotor for high-speed axial-flux permanent magnet machine with ironless stator. *IEEE Transactions on Industrial Electronics*, 67(9):7269–7279, 2020. doi: 10.1109/TIE.2019.2944033.

[62] Kai Liu, Ming Yin, Wei Hua, Ziqi Ma, Mingyao Lin, and Yong Kong. Design and analysis of halbach ironless flywheel bldc motor/generators. *IEEE Transactions on Magnetics*, 54 (11):1–5, 2018. doi: 10.1109/TMAG.2018.2833958.

[63] Tobias Tymosch, Manuel Fischer, Vasken Ketchedjian, Yutaka Terao, and Hiroyuki Ohsaki. Analysis of superconducting synchronous motors with halbach array field excitation. *IEEE Transactions on Applied Superconductivity*, 31(2):1–5, 2021. doi: 10.1109/TASC.2020.3041314.

[64] P. M. Tuohy, A. C. Smith, M. Husband, and P. Hopewell. Rim-drive marine thruster using a multiple-can induction motor. *IET Electric Power Applications*, 7(7):557–565, Aug 2013. ISSN 1751-8660. doi: 10.1049/iet-epa.2012.0247.

[65] A. Borisavljevic, H. Polinder, and J. A. Ferreira. Enclosure design for a high-speed permanent magnet rotor. In *5th IET International Conference on Power Electronics, Machines and Drives (PEMD 2010)*, pages 1–6, April 2010. doi: 10.1049/cp.2010.0141.

[66] Z. Huang and Y. Le. Rotordynamics modelling and analysis of high-speed permanent magnet electrical machine rotors. *IET Electric Power Applications*, 12(8):1104–1109, 2018. doi: 10.1049/iet-epa.2017.0739.

[67] W. Dai, H. Zhang, D. Halim, J. Yang, Z. Xu, and J. Li. Rotordynamic analysis of a permanent magnet synchronous motor considering nonlinear unbalanced magnetic pull. In *2019 22nd International Conference on Electrical Machines and Systems (ICEMS)*, pages 1–6, 2019. doi: 10.1109/ICEMS.2019.8921924.

[68] Z. Kolondzovski, P. Sallinen, A. Belahcen, and A. Arkkio. Rotordynamic analysis of different rotor structures for high-speed permanent-magnet electrical machines. *IET Electric Power Applications*, 4(7):516–524, 2010. doi: 10.1049/iet-epa.2008.0272.

[69] Annabel Shahaj. *Mitigation of vibration in large electrical machines*. PhD thesis, University of Nottingham, 2010.

[70] Wiart A. New high-speed high-power machines with converter power supply. *Motorcon Proceedings, September 1982*, pages 641–6, 1982.

[71] J.P. Den Hartog. *Mechanical Vibrations*. Dover Publications, 2013.

[72] N. Bianchi, S. Bolognani, and P. Frare. Design criteria for high-efficiency spm synchronous motors. *IEEE Transactions on Energy Conversion*, 21(2):396–404, 2006. doi: 10.1109/TEC.2005.853720.

[73] B. C. Mecrow, A. G. Jack, J. A. Haylock, and J. Coles. Fault tolerant permanent magnet machine drives. In *1995 Seventh International Conference on Electrical Machines and Drives (Conf. Publ. No. 412)*, pages 433–437, 1995. doi: 10.1049/cp:19950909.

[74] N. Bianchi and S. Bolognani. Design techniques for reducing the cogging torque in surface-mounted pm motors. *IEEE Transactions on Industry Applications*, 38(5):1259–1265, 2002. doi: 10.1109/TIA.2002.802989.

[75] B. C. Mecrow, A. G. Jack, D. J. Atkinson, S. R. Green, G. J. Atkinson, A. King, and B. Green. Design and testing of a four-phase fault-tolerant permanent-magnet machine for an engine fuel pump. *IEEE Transactions on Energy Conversion*, 19(4):671–678, 2004. doi: 10.1109/TEC.2004.832074.

[76] F. Magnussen, P. Thelin, and C. Sadarangani. Performance evaluation of permanent magnet synchronous machines with concentrated and distributed windings including the effect of field-weakening. In *Second International Conference on Power Electronics, Machines and Drives (PEMD 2004).*, volume 2, pages 679–685 Vol.2, 2004. doi: 10.1049/cp:20040370.

[77] N. Bianchi and E. Fornasiero. Impact of mmf space harmonic on rotor losses in fractional-slot permanent-magnet machines. *IEEE Transactions on Energy Conversion*, 24(2):323–328, June 2009. ISSN 0885-8969. doi: 10.1109/TEC.2008.2006557.

[78] E. Fornasiero, N. Bianchi, and S. Bolognani. Slot harmonic impact on rotor losses in fractional-slot permanent-magnet machines. *IEEE Transactions on Industrial Electronics*, 59(6):2557–2564, June 2012. ISSN 0278-0046. doi: 10.1109/TIE.2011.2168794.

[79] Z. Q. Zhu, D. Ishak, D. Howe, and J. Chen. Unbalanced magnetic forces in permanent-magnet brushless machines with diametrically asymmetric phase windings. *IEEE Transactions on Industry Applications*, 43(6):1544–1553, 2007. doi: 10.1109/TIA.2007.908158.

[80] C. A. M. Weber and F. W. Lee. Harmonics due to slot openings. *Journal of the A.I.E.E.*, 43(12):1129–1132, Dec 1924. ISSN 2376-5976. doi: 10.1109/JAIEE.1924.6534464.

[81] Bianchi N. *Electrical Machine Analysis Using Finite Elements*. CRC Press, 2005.

[82] Bianchi N. Bolognani S. *Metodologia di progettazione delle macchine elettriche*. CLEUP, 2001.

[83] Hamata V. Heller B. *Harmonic Field Effects in Induction Machines*. Elsevier Scientific Publishing Company, 1977.

[84] Fornasiero E. Bianchi N., Dai Pre' M. Alberti L. *Theory and Design of Fractional-Slot PM Machines*. CLEUP, 2007.

[85] K. Yamazaki, Y. Kanou, Y. Fukushima, S. Ohki, A. Nezu, T. Ikemi, and R. Mizokami. Reduction of magnet eddy-current loss in interior permanent-magnet motors with concentrated windings. *IEEE Transactions on Industry Applications*, 46(6):2434–2441, Nov 2010. ISSN 0093-9994. doi: 10.1109/TIA.2010.2073672.

[86] M. Popescu and D. G. Dorrell. Proximity losses in the windings of high speed brushless permanent magnet ac motors with single tooth windings and parallel paths. *IEEE Transactions on Magnetics*, 49(7):3913–3916, 2013. doi: 10.1109/TMAG.2013.2247382.

[87] N. Taran and D. M. Ionel. A hybrid analytical and fe-based method for calculating ac eddy current winding losses taking 3d effects into account. In *2019 IEEE Energy Conversion Congress and Exposition (ECCE)*, pages 4867–4872, 2019. doi: 10.1109/ECCE.2019.8912784.

[88] J. W. Polkowski. Turbulent flow between coaxial cylinders with the inner cylinder rotating. *Journal of Engineering for Gas Turbines and Power*, 1984.

[89] L. A Dorfman. *Hydrodynamic Resistance and the Heat Loss of Rotating Solids*. Oliver and Boyd, 1963.

[90] Juha Saari. *Thermal Analysis of High Speed Induction Machines*. PhD thesis, Helsinki University of Technology, 1998.

[91] K. Deb and H. Jain. An evolutionary many-objective optimization algorithm using reference-point-based nondominated sorting approach, part i: Solving problems with box constraints. *IEEE Transactions on Evolutionary Computation*, 18(4):577–601, Aug 2014. ISSN 1089-778X. doi: 10.1109/TEVC.2013.2281535.

[92] H. Jain and K. Deb. An evolutionary many-objective optimization algorithm using reference-point based nondominated sorting approach, part ii: Handling constraints and extending to an adaptive approach. *IEEE Transactions on Evolutionary Computation*, 18 (4):602–622, Aug 2014. ISSN 1089-778X. doi: 10.1109/TEVC.2013.2281534.

[93] M. Elarbi, S. Bechikh, A. Gupta, L. Ben Said, and Y. Ong. A new decomposition-based nsga-ii for many-objective optimization. *IEEE Transactions on Systems, Man, and Cybernetics: Systems*, 48(7):1191–1210, July 2018. ISSN 2168-2216. doi: 10.1109/TSMC.2017.2654301.

[94] Song Li. Ngpm – a nsga-ii program in matlab v1.4, 2020. URL https://uk.mathworks.com/matlabcentral/fileexchange/31166-ngpm-a-nsga-ii-program-in-matlab-v1-4.

[95] Mentor, a siemens business. https://www.mentor.com/products/mechanical/magnet/magnet/. Accessed: 2016-09-26.

[96] K. Yamazaki. Modification of 2d nonlinear time-stepping analysis by limited 3d analysis for induction machines. *IEEE Transactions on Magnetics*, 33(2):1694–1697, March 1997. ISSN 1941-0069. doi: 10.1109/20.582598.

[97] K. Yamazaki and Y. Fukushima. Effect of eddy-current loss reduction by magnet segmentation in synchronous motors with concentrated windings. *IEEE Transactions on Industry Applications*, 47(2):779–788, March 2011. ISSN 1939-9367. doi: 10.1109/TIA.2010.2103915.

[98] K. Yamazaki, Y. Fukushima, and M. Sato. Loss analysis of permanent-magnet motors with concentrated windings variation of magnet eddy-current loss due to stator and rotor shapes. *IEEE Transactions on Industry Applications*, 45(4):1334–1342, July 2009. ISSN 1939-9367. doi: 10.1109/TIA.2009.2023393.

[99] K. Yamazaki, M. Shina, Y. Kanou, M. Miwa, and J. Hagiwara. Effect of eddy current loss reduction by segmentation of magnets in synchronous motors: Difference between interior and surface types. *IEEE Transactions on Magnetics*, 45(10):4756–4759, Oct 2009. ISSN 1941-0069. doi: 10.1109/TMAG.2009.2024159.

[100] K. Yamazaki and A. Abe. Loss investigation of interior permanent-magnet motors considering carrier harmonics and magnet eddy currents. *IEEE Transactions on Industry Applications*, 45(2):659–665, March 2009. ISSN 1939-9367. doi: 10.1109/TIA.2009.2013550.

[101] Hiperco 50 and hiperco 50a soft magnetic alloys. https://edfagan.com/litPDF/Hiperco4-29-09F.pdf. Accessed Oct. 2, 2018.

[102] Jfe n-core jfe steel corporation. https://www.jfe-steel.co.jp. Accessed Nov. 30, 2018.

[103] W. Q. Chu and Z. Q. Zhu. Average torque separation in permanent magnet synchronous machines using frozen permeability. *IEEE Transactions on Magnetics*, 49(3):1202–1210, March 2013. ISSN 0018-9464. doi: 10.1109/TMAG.2012.2225068.

[104] W. Q. Chu and Z. Q. Zhu. On-load cogging torque calculation in permanent magnet machines. *IEEE Transactions on Magnetics*, 49(6):2982–2989, June 2013. ISSN 0018-9464. doi: 10.1109/TMAG.2012.2236348.

[105] Pbo fiber zylon toyobo. https://www.toyobo-global.com/seihin/kc/pbo/. Accessed: 2018-11-30.

[106] H. Polinder and M. J. Hoeijmakers. Effect of a shielding cylinder an the rotor losses in a rectifier-loaded pm machine. In *Conference Record of the 2000 IEEE Industry Applications Conference. Thirty-Fifth IAS Annual Meeting and World Conference on*

Industrial Applications of Electrical Energy (Cat. No.00CH37129), volume 1, pages 163–170 vol.1, Oct 2000. doi: 10.1109/IAS.2000.881056.

[107] K. W. Klontz, T. J. E. Miller, M. I. McGilp, H. Karmaker, and P. Zhong. Short-circuit analysis of permanent-magnet generators. *IEEE Transactions on Industry Applications*, 47(4):1670–1680, July 2011. ISSN 0093-9994. doi: 10.1109/TIA.2011.2154370.

[108] D. J. B. Smith, S. M. Lambert, B. C. Mecrow, and G. J. Atkinson. Interaction between pm rotor design and voltage fed inverter output. In *6th IET International Conference on Power Electronics, Machines and Drives (PEMD 2012)*, pages 1–6, 2012. doi: 10.1049/cp.2012.0274.

[109] Qiang Yu, Sai Chu, Wentao Li, Lisi Tian, Xuesong Wang, and Yuhu Cheng. Electromagnetic shielding analysis of a canned permanent magnet motor. *IEEE Transactions on Industrial Electronics*, 67(10):8123–8130, 2020. doi: 10.1109/TIE.2019.2950870.

[110] J. D. Ede, K. Atallah, G. W. Jewell, J. B. Wang, and D. Howe. Effect of axial segmentation of permanent magnets on rotor loss in modular permanent-magnet brushless machines. *IEEE Transactions on Industry Applications*, 43(5):1207–1213, Sep. 2007. ISSN 0093-9994. doi: 10.1109/TIA.2007.904397.

[111] G. Berardi and N. Bianchi. High-speed pm generators for organic rankine cycle systems: Reduction of eddy current rotor losses. *IEEE Transactions on Industry Applications*, 55 (6):5800–5808, Nov 2019. ISSN 1939-9367. doi: 10.1109/TIA.2019.2935413.

[112] G. Berardi, N. Bianchi, and D. Gasperini. A high speed pm generator for an organic rankine cycle system. *IEEE Transactions on Industry Applications*, 55(5):4633–4642, Sep. 2019. ISSN 1939-9367. doi: 10.1109/TIA.2019.2922623.

[113] C. Babetto, G. Bacco, G. Berardi, and N. Bianchi. High speed motors: A comparison between synchronous pm and reluctance machines. In *2017 IEEE Energy Conversion Congress and Exposition (ECCE)*, pages 3927–3934, Oct 2017. doi: 10.1109/ECCE.2017.8096689.

[114] I. M. Canay. Causes of discrepancies on calculation of rotor quantities and exact equivalent diagrams of the synchronous machine. *IEEE Transactions on Power Apparatus and Systems*, PAS-88(7):1114–1120, 1969. doi: 10.1109/TPAS.1969.292512.

[115] D. Mingardi and N. Bianchi. Fe-aided analytical method to predict the capabilities of line-start synchronous motors. In *2014 IEEE Energy Conversion Congress and Exposition (ECCE)*, pages 5123–5130, 2014. doi: 10.1109/ECCE.2014.6954104.

[116] M. Hinkkanen, H. Asad Ali Awan, Z. Qu, T. Tuovinen, and F. Briz. Current control for synchronous motor drives: Direct discrete-time pole-placement design. *IEEE Transactions on Industry Applications*, 52(2):1530–1541, March 2016. ISSN 1939-9367. doi: 10.1109/TIA.2015.2495288.

[117] E. P. Wiechmann, P. Aqueveque, R. Burgos, and J. Rodriguez. On the efficiency of voltage source and current source inverters for high-power drives. *IEEE Transactions on Industrial Electronics*, 55(4):1771–1782, 2008. doi: 10.1109/TIE.2008.918625.

[118] Schaeffler bearings high precision spindle product catalogue. https://medias.schaeffler.co.uk/plp/SpindleBearings. Accessed: 2017-12-15.

[119] Genta G. *Dynamics of Rotating Systems*. Springer, 2005.

[120] A. Acquaviva, O. Wallmark, E. A. Grunditz, S. T. Lundmark, and T. Thiringer. Computationally efficient modeling of electrical machines with cooling jacket. *IEEE Transactions on Transportation Electrification*, 5(3):618–629, Sep. 2019. ISSN 2372-2088. doi: 10.1109/TTE.2019.2936122.

[121] R. Sundaria, D. G. Nair, A. Lehikoinen, A. Arkkio, and A. Belahcen. Effect of laser cutting on core losses in electrical machines - measurements and modeling. *IEEE Transactions on Industrial Electronics*, pages 1–1, 2019. doi: 10.1109/TIE.2019.2942564.

Appendix A

Technical drawings

Hereafter, for completeness are included the mechanical technical drawings for the prototype. The drawing list consists of:

- Shaft (with related female-spline) and Rotor Hub
- Titanium axial retainment rings/end cheek
- Single permanent magnet segment (45 degrees DOM case)
- Stator Stack
- Housing ring
- Front and rear housing caps
- Coupling male-spline for rig torque transmission
- Bearing Front and Rear Housing Stops (for pre-load and bearing-washer locking)
- Grease shield for NDE bearing
- Inlet and Outlet Push fitting for cooling channels

UNLESS OTHERWISE STATED	
All dimensions to be within	0.1
All faces to be parallel or square within	0.1
All diameters to be concentric within	0.05
Sharp edges to be broken to	0.1 to 0.3
Surface texture (Ra) not to exceed	1.6µm

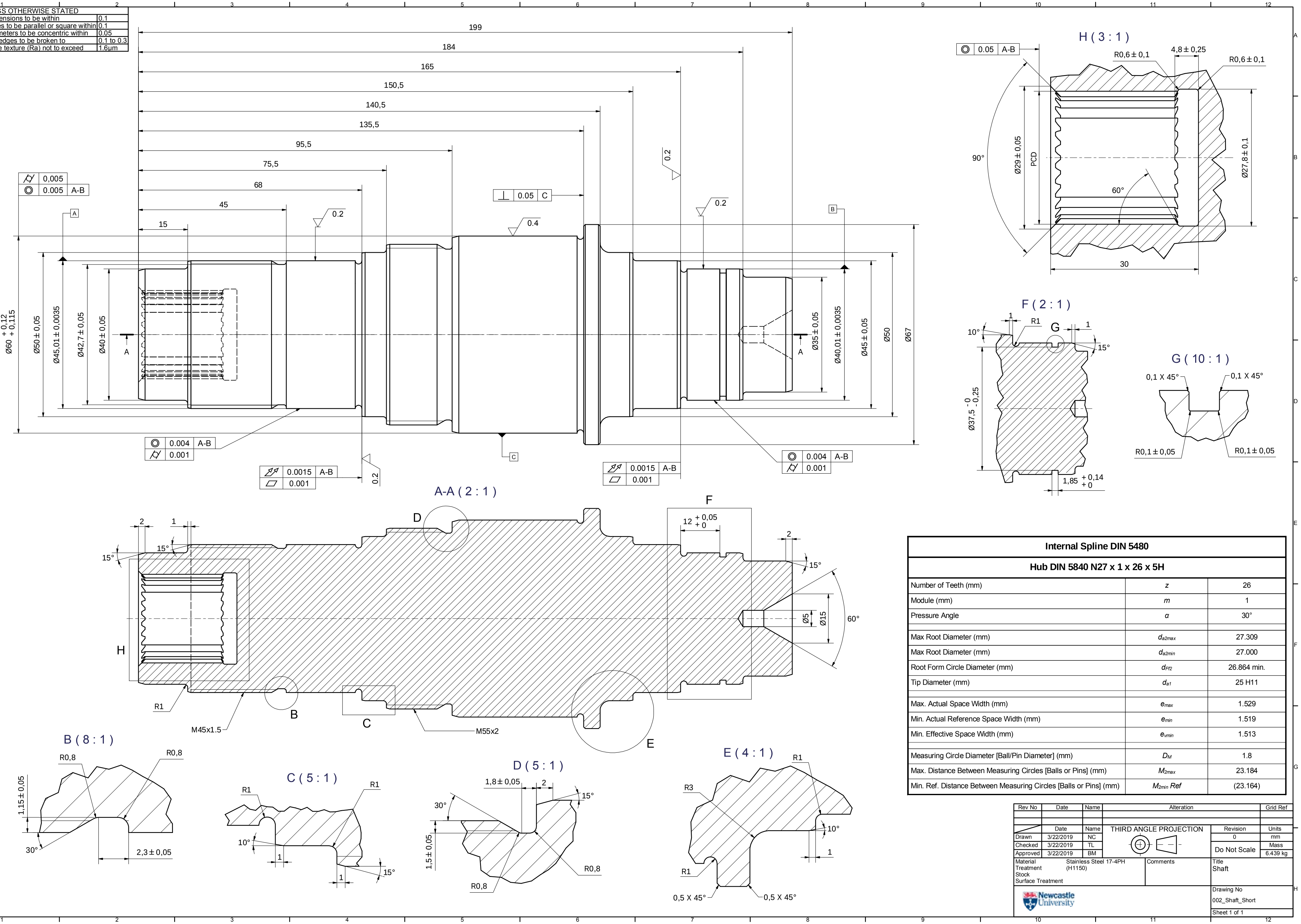

Internal Spline DIN 5480		
Hub DIN 5840 N27 x 1 x 26 x 5H		
Number of Teeth (mm)	z	26
Module (mm)	m	1
Pressure Angle	α	30°
Max Root Diameter (mm)	d_{a2max}	27.309
Max Root Diameter (mm)	d_{a2min}	27.000
Root Form Circle Diameter (mm)	d_{Ff2}	26.864 min.
Tip Diameter (mm)	d_{a1}	25 H11
Max. Actual Space Width (mm)	e_{max}	1.529
Min. Actual Reference Space Width (mm)	e_{min}	1.519
Min. Effective Space Width (mm)	e_{vmin}	1.513
Measuring Circle Diameter [Ball/Pin Diameter] (mm)	D_M	1.8
Max. Distance Between Measuring Circles [Balls or Pins] (mm)	M_{2max}	23.184
Min. Ref. Distance Between Measuring Circles [Balls or Pins] (mm)	M_{2min} *Ref*	(23.164)

Rev No	Date	Name	Alteration	Grid Ref

	Date	Name
Drawn	3/22/2019	NC
Checked	3/22/2019	TL
Approved	3/22/2019	BM

THIRD ANGLE PROJECTION

Revision	Units
0	mm
Do Not Scale	Mass 6.439 kg

Material Stainless Steel 17-4PH
Treatment (H1150)
Stock
Surface Treatment

Comments

Title
Shaft

Newcastle University

Drawing No
002_Shaft_Short

Sheet 1 of 1

UNLESS OTHERWISE STATED	
All dimensions to be within	0.1
All faces to be parallel or square within	0.1
All diameters to be concentric within	0.05
Sharp edges to be broken to	0.1 to 0.3
Surface texture (Ra) not to exceed	1.6μm

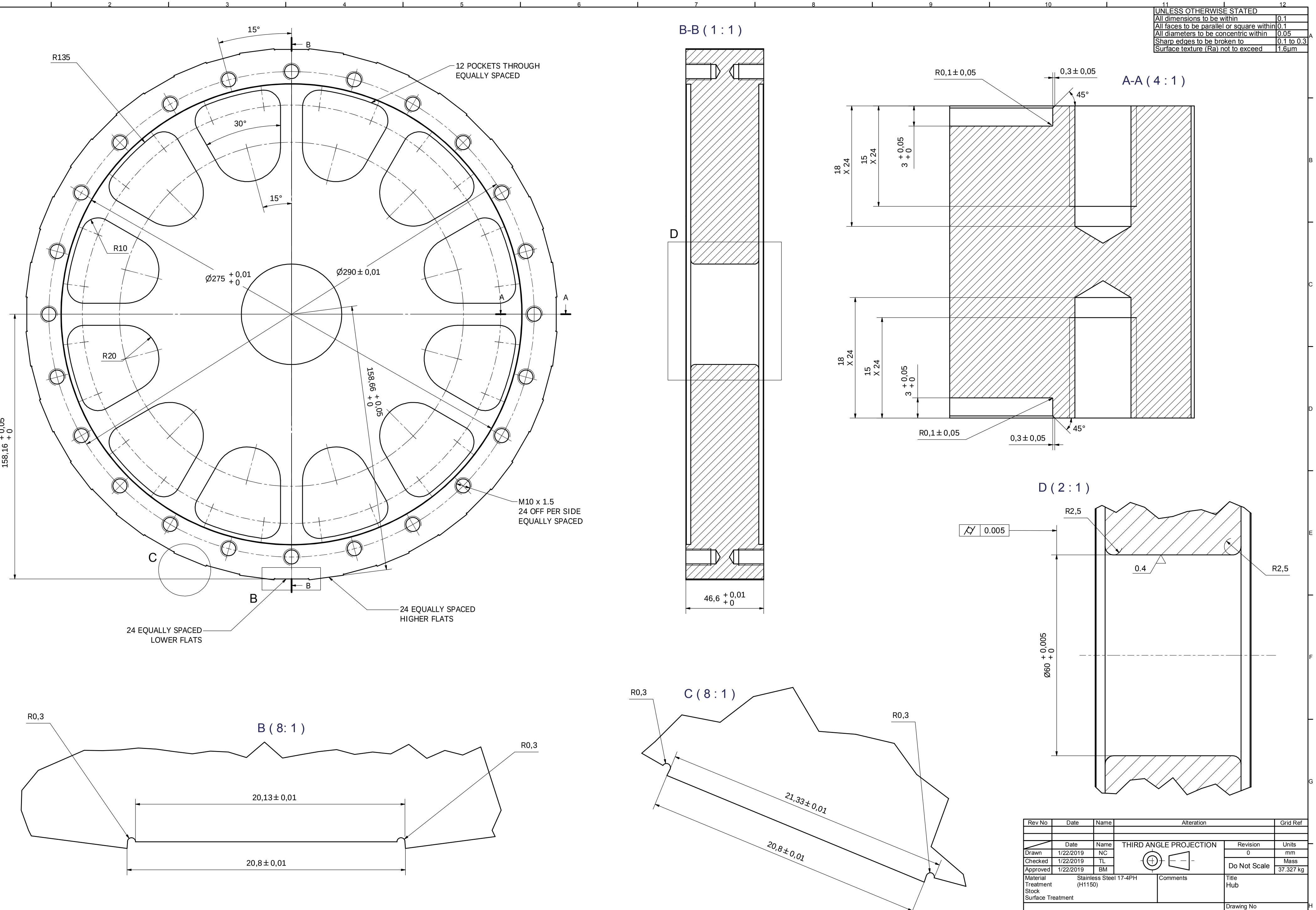

Rev No	Date	Name	Alteration	Grid Ref

	Date	Name	THIRD ANGLE PROJECTION	Revision	Units
Drawn	1/22/2019	NC		0	mm
Checked	1/22/2019	TL		Do Not Scale	Mass
Approved	1/22/2019	BM			37.327 kg

Material Treatment Stock Surface Treatment	Stainless Steel 17-4PH (H1150)	Comments	Title Hub
			Drawing No 002_Hub Sheet 1 of 1

Newcastle University

UNLESS OTHERWISE STATED	
All dimensions to be within	0.1
All faces to be parallel or square within	0.1
All diameters to be concentric within	0.05
Sharp edges to be broken to	0.1 to 0.3
Surface texture (Ra) not to exceed	1.6µm

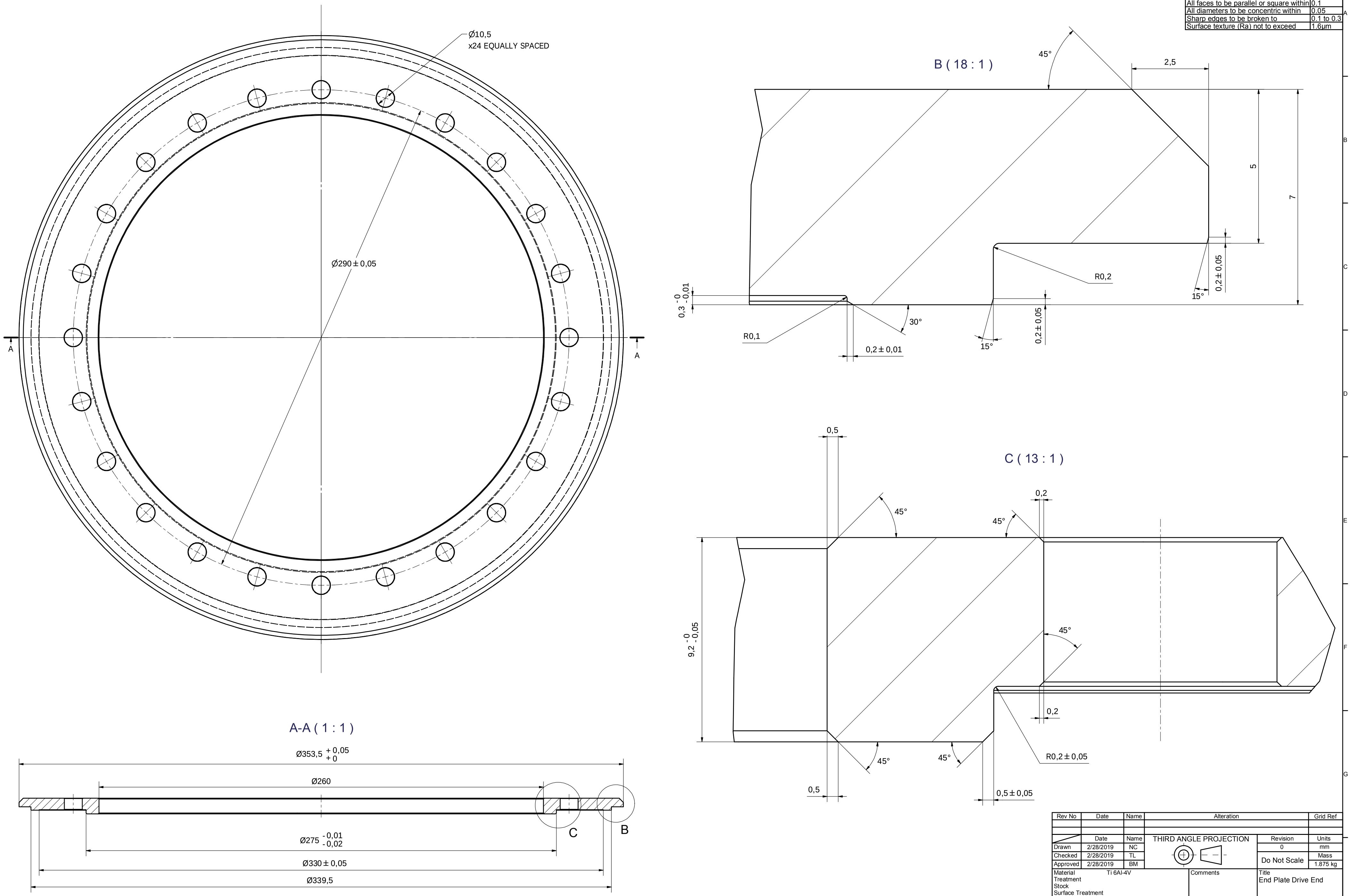

Rev No	Date	Name	Alteration		Grid Ref
	Date	Name	THIRD ANGLE PROJECTION	Revision	Units
Drawn	2/28/2019	NC		0	mm
Checked	2/28/2019	TL		Do Not Scale	Mass
Approved	2/28/2019	BM			1.875 kg
Material	Ti 6Al-4V		Comments	Title End Plate Drive End	
Treatment					
Stock					
Surface Treatment					
Newcastle University				Drawing No 011	
				Sheet 1 of 1	

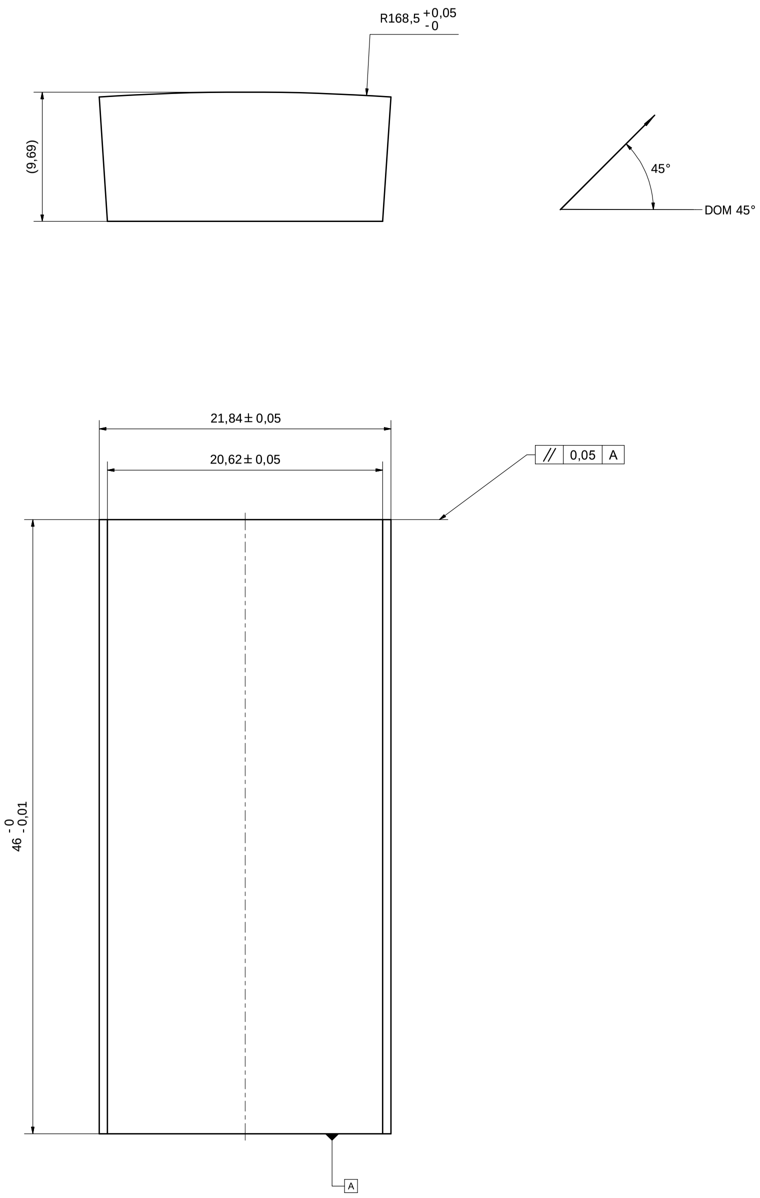

UNLESS OTHERWISE STATED	
All dimensions to be within	0.1
All faces to be parallel or square within	0.1
All diameters to be concentric within	0.05
Sharp edges to be broken to	0.1 to 0.3
Surface texture (Ra) not to exceed	1.6µm

NOTE

1. INSERT A COMMENT FOR THE GLUE
2. 45 DEGREES OF MAGNETIZATION - SKEWED PIECE
3. INSERT MORE..
4. INSERT MORE

Rev No	Date	Name	Alteration	Grid Ref

	Date	Name	THIRD ANGLE PROJECTION	Revision	Units
Drawn	11/30/2018	NC		0	mm
Checked	12/4/2018	TL		Do Not Scale	Mass
Approved	12/5/2018	BM			N/A

Material Recoma 30 Samarium Cobalt
Treatment
Stock
Surface Treatment

Comments

Title
PM#2

Drawing No
004

Sheet 1 of 1

UNLESS OTHERWISE STATED	
All dimensions to be within	0.1
All faces to be parallel or square within	0.1
All diameters to be concentric within	0.05
Sharp edges to be broken to	0.1 to 0.3
Surface texture (Ra) not to exceed	1.6µm

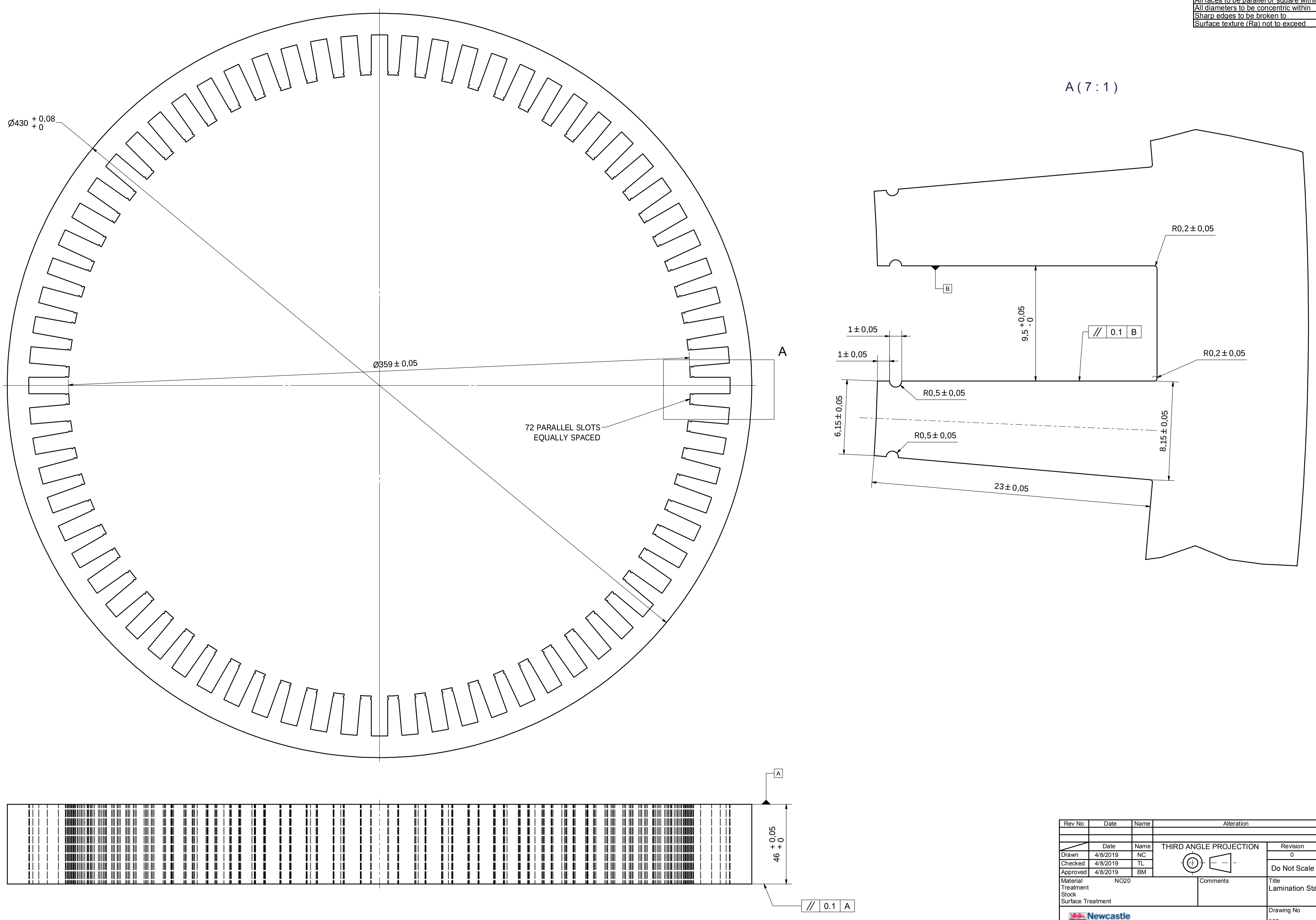

Rev No	Date	Name	Alteration		Grid Ref
	Date	Name	THIRD ANGLE PROJECTION	Revision	Units
Drawn	4/8/2019	NC		0	mm
Checked	4/8/2019	TL		Do Not Scale	Mass
Approved	4/8/2019	BM			1.800 kg

Material NO20 Treatment Stock Surface Treatment	Comments	Title Lamination Stack
		Drawing No 025
		Sheet 1 of 1

UNLESS OTHERWISE STATED	
All dimensions to be within	0.1
All faces to be parallel or square within	0.1
All diameters to be concentric within	0.05
Sharp edges to be broken to	0.1 to 0.3
Surface texture (Ra) not to exceed	1.6µm

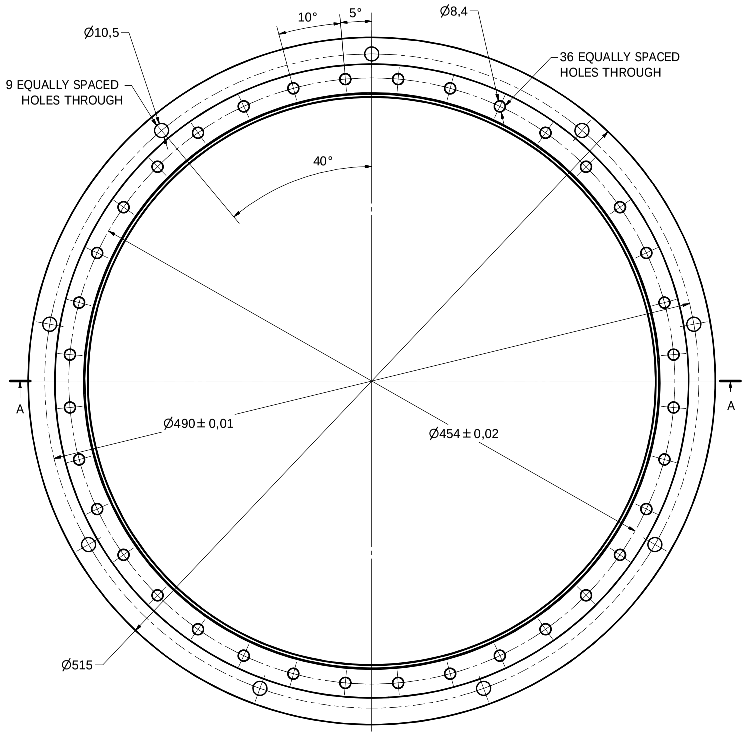

A (8 : 1)

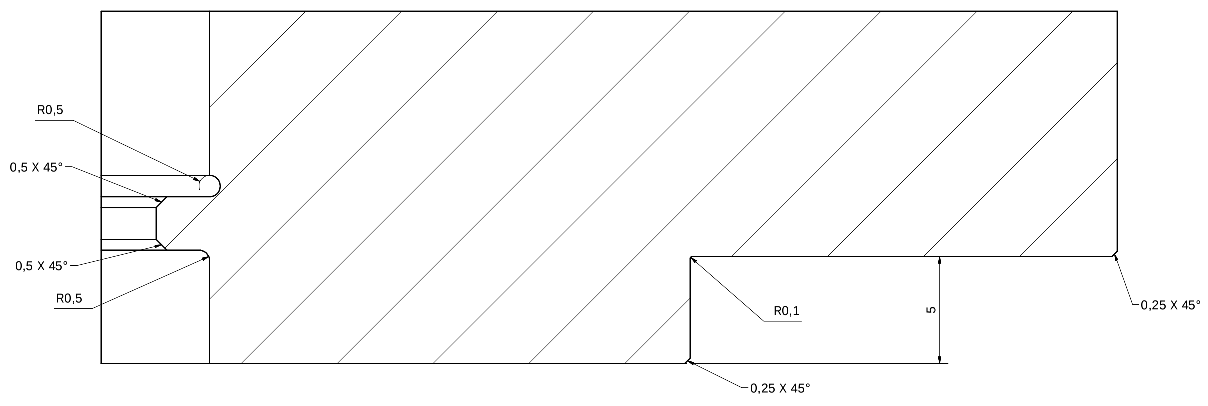

B (3 : 1)

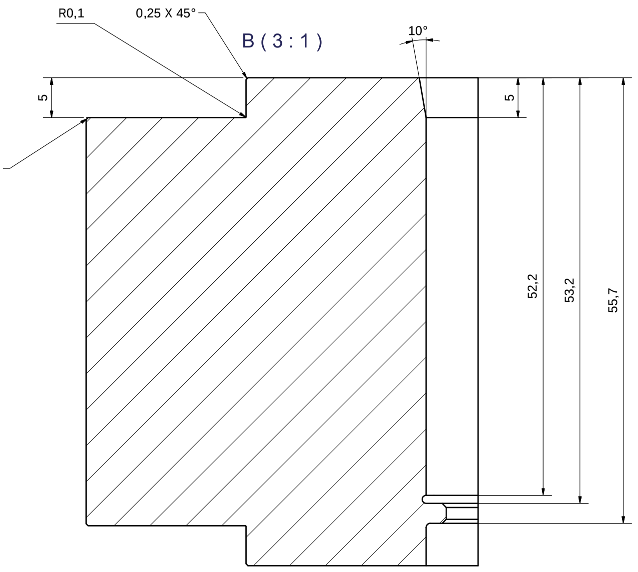

A-A (1 : 1)

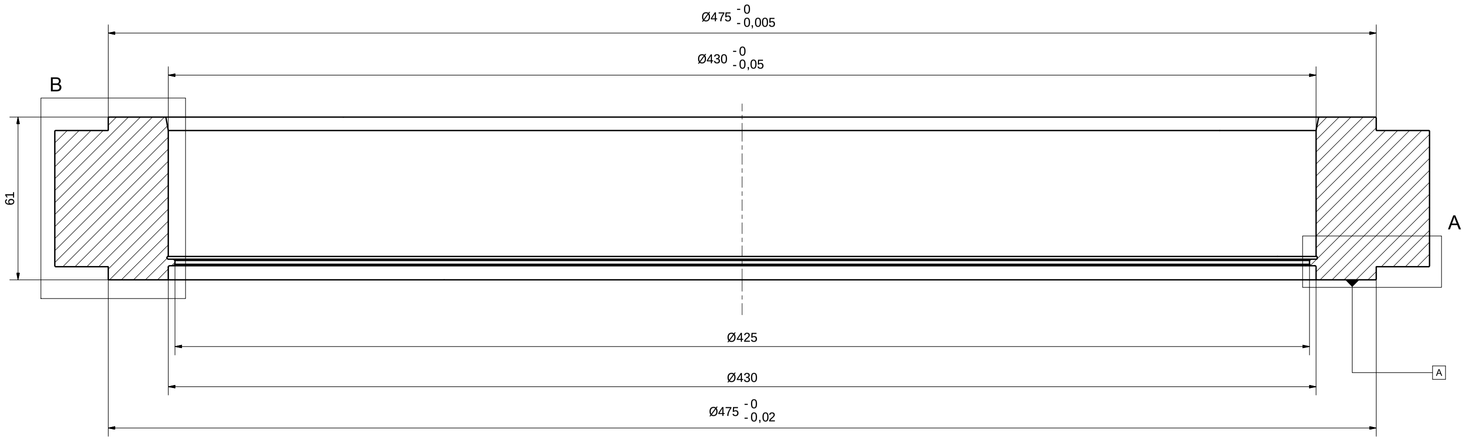

Rev No	Date	Name	Alteration		Grid Ref
	Date	Name	THIRD ANGLE PROJECTION	Revision	Units
Drawn	4/8/2019	NC		0	mm
Checked	4/8/2019	TL		Do Not Scale	Mass
Approved	4/8/2019	BM			N/A
Material Treatment Stock Surface Treatment	Aluminium 6082-T6		Comments	Title Stator Housing	
Newcastle University				Drawing No 020	
				Sheet 1 of 1	

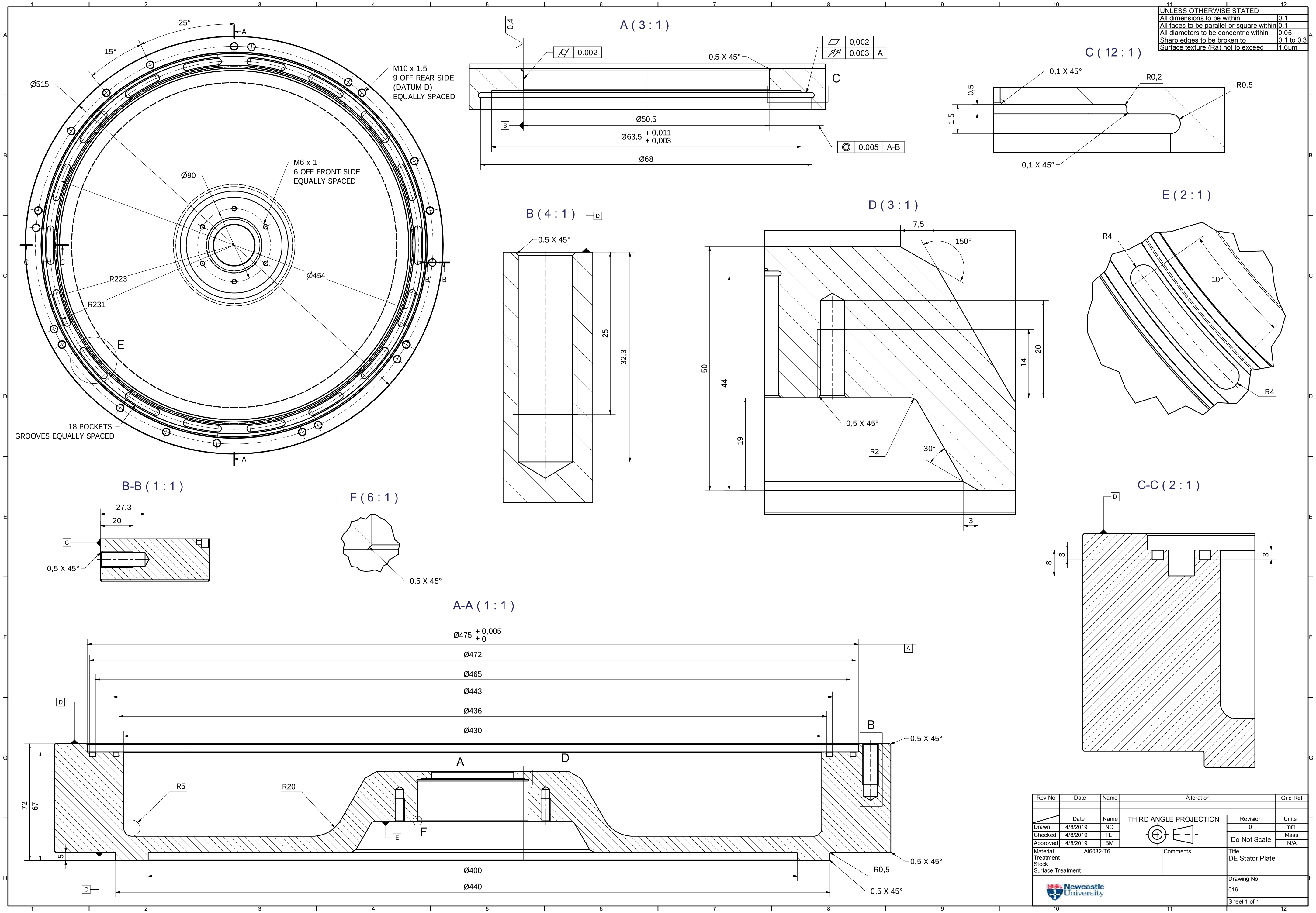

UNLESS OTHERWISE STATED	
All dimensions to be within	0.1
All faces to be parallel or square within	0.1
All diameters to be concentric within	0.05
Sharp edges to be broken to	0.1 to 0.3
Surface texture (Ra) not to exceed	1.6µm

Rev No	Date	Name	Alteration	Grid Ref

	Date	Name
Drawn	4/8/2019	NC
Checked	4/8/2019	TL
Approved	4/8/2019	BM

THIRD ANGLE PROJECTION

Revision	Units
0	mm
Do Not Scale	Mass N/A

Material Al6082-T6
Treatment
Stock
Surface Treatment

Comments

Title
DE Stator Plate

Drawing No
016

Sheet 1 of 1

UNLESS OTHERWISE STATED	
All dimensions to be within	0.1
All faces to be parallel or square within	0.1
All diameters to be concentric within	0.05
Sharp edges to be broken to	0.1 to 0.3
Surface texture (Ra) not to exceed	1.6µm

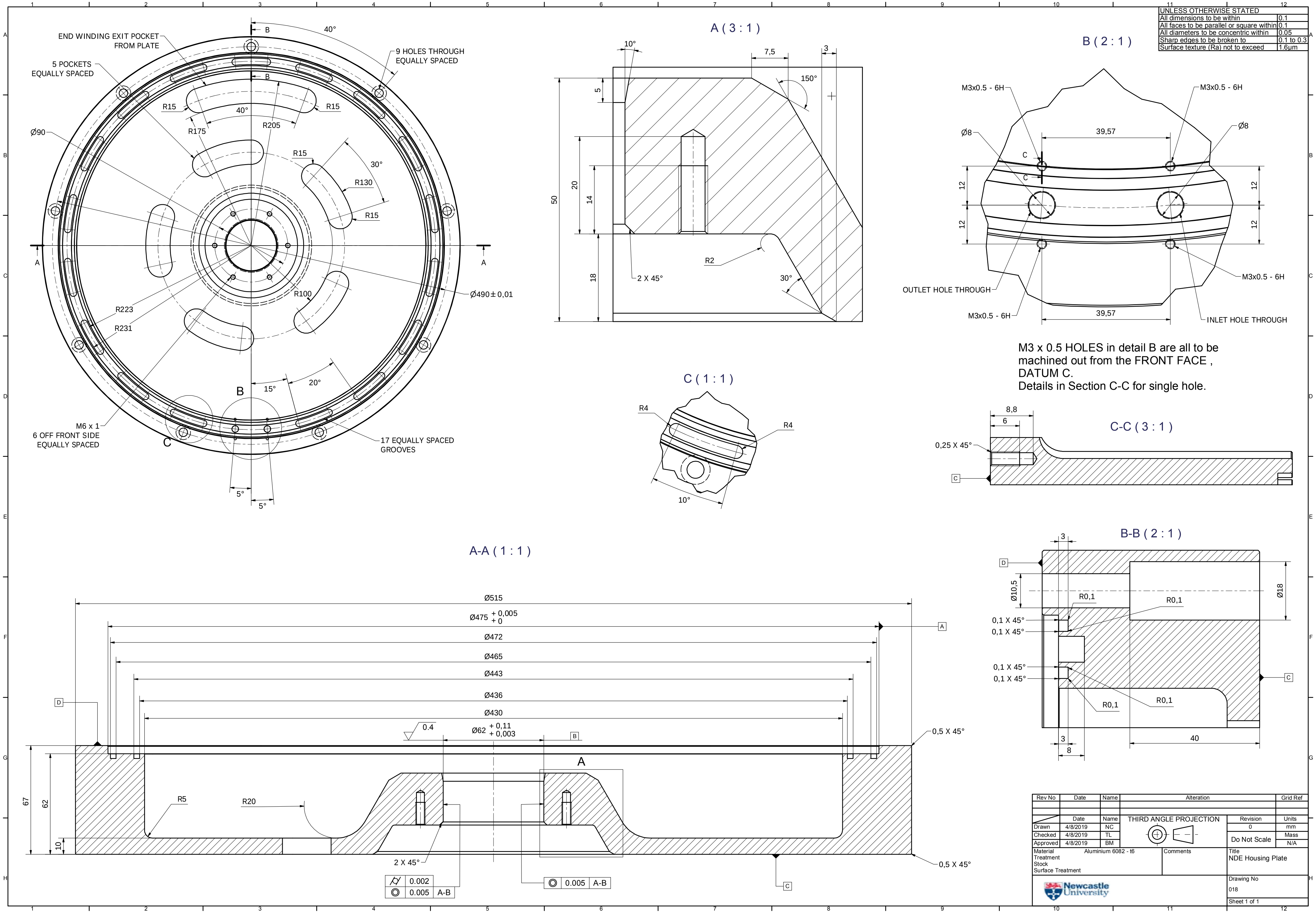

M3 x 0.5 HOLES in detail B are all to be machined out from the FRONT FACE , DATUM C.
Details in Section C-C for single hole.

Rev No	Date	Name	Alteration	Grid Ref

	Date	Name
Drawn	4/8/2019	NC
Checked	4/8/2019	TL
Approved	4/8/2019	BM

THIRD ANGLE PROJECTION

Revision	Units
0	mm
Do Not Scale	Mass
	N/A

Material Aluminium 6082 - t6
Treatment
Stock
Surface Treatment

Comments

Title
NDE Housing Plate

Newcastle University

Drawing No
018

Sheet 1 of 1

UNLESS OTHERWISE STATED	
All dimensions to be within	0.1
All faces to be parallel or square within	0.1
All diameters to be concentric within	0.05
Sharp edges to be broken to	0.1 to 0.3
Surface texture (Ra) not to exceed	1.6µm

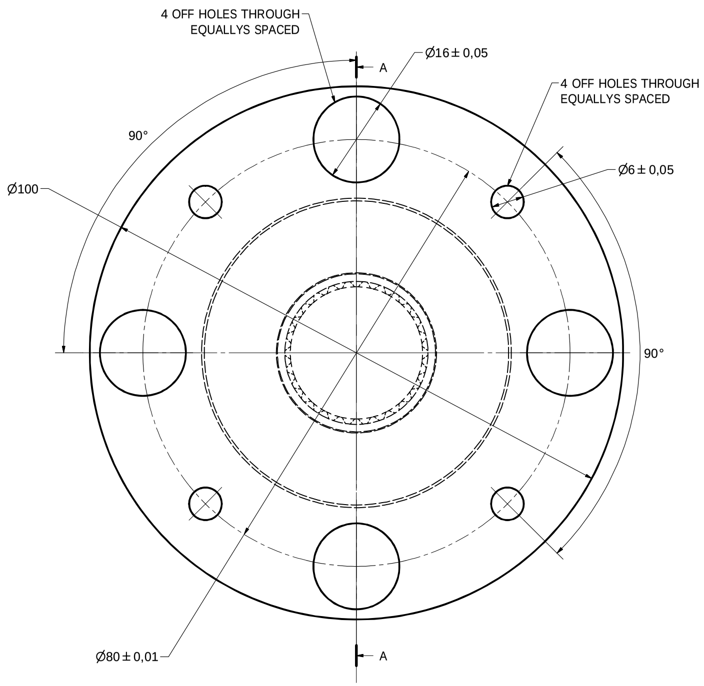

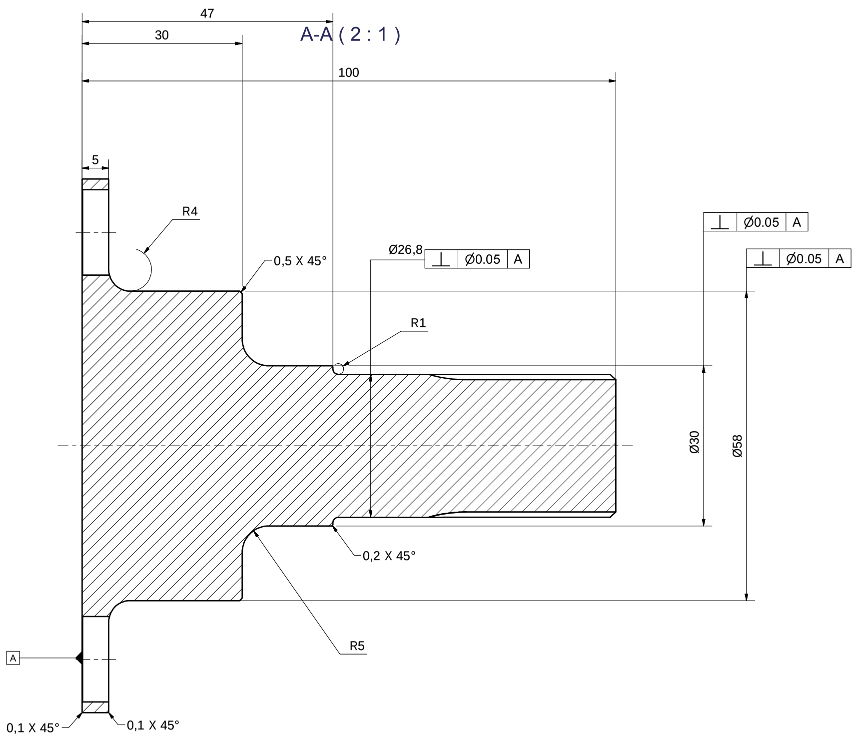

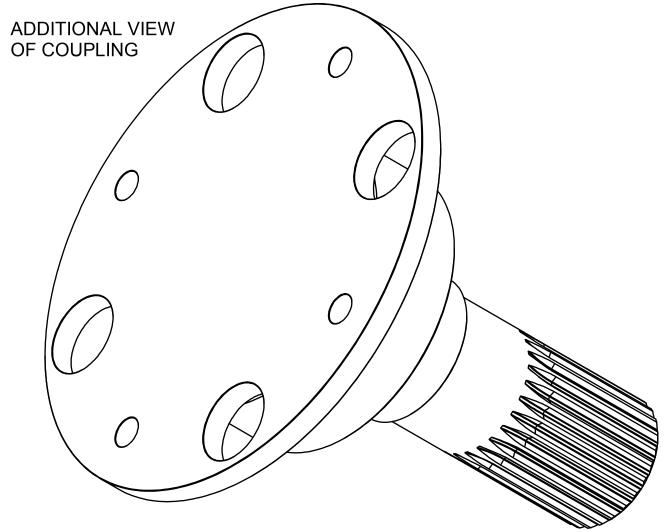

1) ALL HOLES EDGES CHAMFERED
AT 0.1mm x 45°

External Spline DIN 5480		
Shaft DIN 5840 W27 x 1 x 26 x 5f		
Number of Teeth (mm)	z	26
Module (mm)	m	1
Pressure Angle	α	30°
Tip Diameter (mm)	d_{a1}	26.800 h11
Root Form Circle Diameter (mm)	d_{Ff1}	24.936 max.
Max Root Diameter (mm)	d_{f1max}	24.700
Min Root Diameter (mm)	d_{f1min}	24.111
Max. Effective Tooth Thickness (mm)	s_{vmax}	1.493
Max. Actual Reference Tooth Thickness (mm)	s_{max}	1.487
Min. Actual Tooth Thickness (mm)	s_{min}	1.477
Measuring Circle Diameter [Ball/Pin Diameter] (mm)	D_M	1.8
Max. Ref Dimension Over Measuring Circles [Balls or Pins] (mm)	M_{1max} Ref.	(28.507)
Min. Dimension Over Measuring Circles [Balls or Pins] (mm)	M_{1min}	28.491

Rev No	Date	Name	Alteration	Grid Ref

	Date	Name
Drawn	4/29/2019	NC
Checked	4/29/2019	TL
Approved	9/3/2019	BM

THIRD ANGLE PROJECTION

Revision	Units
0	mm
Do Not Scale	Mass N/A

Material EN24T
Treatment
Stock
Surface Treatment

Comments

Title
Male Spline Coupling

Newcastle University

Drawing No
030

Sheet 1 of 1

UNLESS OTHERWISE STATED	
All dimensions to be within	0.1
All faces to be parallel or square within	0.1
All diameters to be concentric within	0.05
Sharp edges to be broken to	0.1 to 0.3
Surface texture (Ra) not to exceed	1.6µm

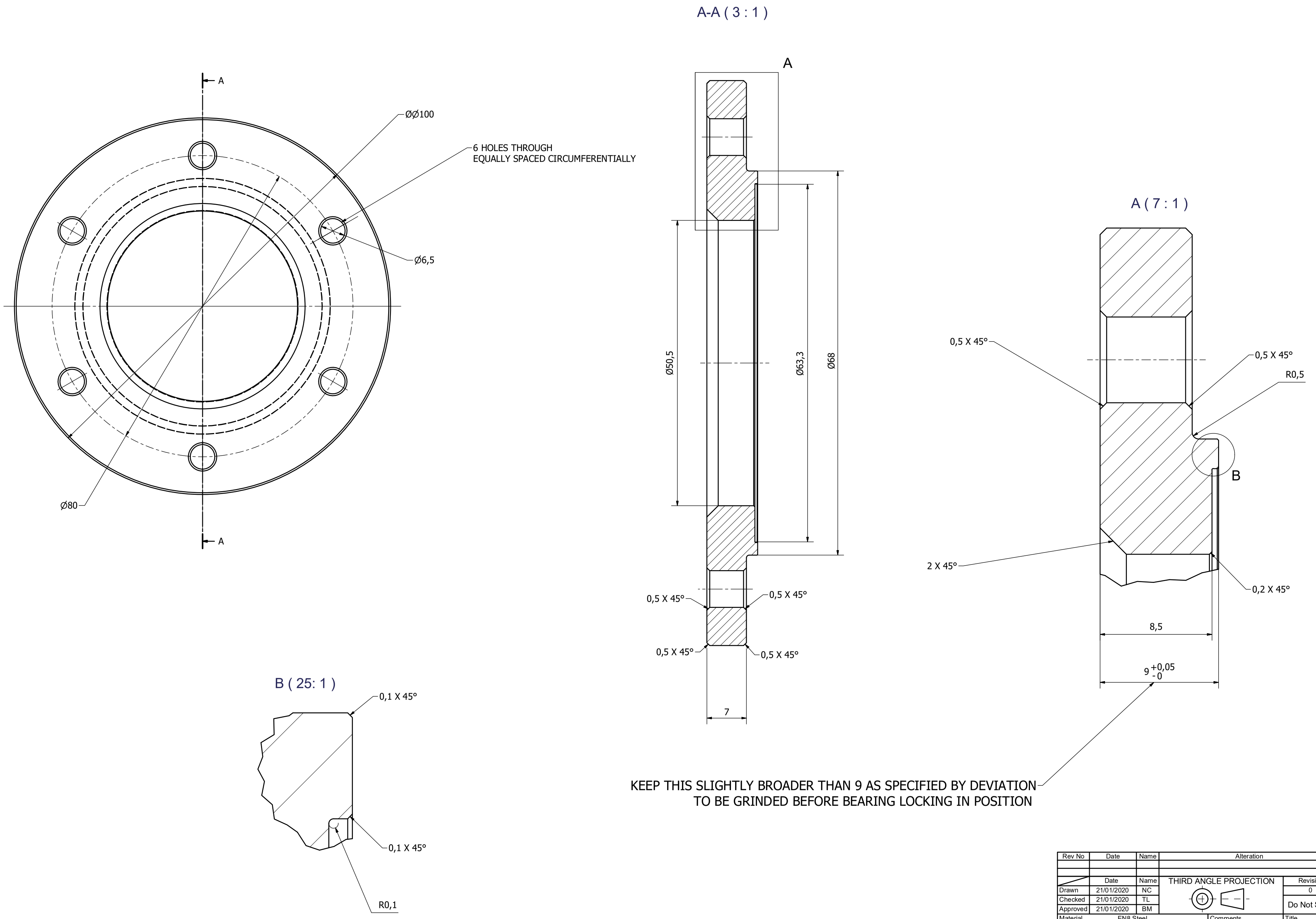

KEEP THIS SLIGHTLY BROADER THAN 9 AS SPECIFIED BY DEVIATION
TO BE GRINDED BEFORE BEARING LOCKING IN POSITION

Rev No	Date	Name	Alteration	Grid Ref

	Date	Name
Drawn	21/01/2020	NC
Checked	21/01/2020	TL
Approved	21/01/2020	BM

THIRD ANGLE PROJECTION

Revision	Units
0	mm
Do Not Scale	Mass N/A

Material EN8 Steel
Treatment
Stock
Surface Treatment

Comments

Title
DE Bearing Cup

Newcastle University

Drawing No
017

Sheet 1 of 1

UNLESS OTHERWISE STATED	
All dimensions to be within	0.1
All faces to be parallel or square within	0.1
All diameters to be concentric within	0.05
Sharp edges to be broken to	0.1 to 0.3
Surface texture (Ra) not to exceed	1.6μm

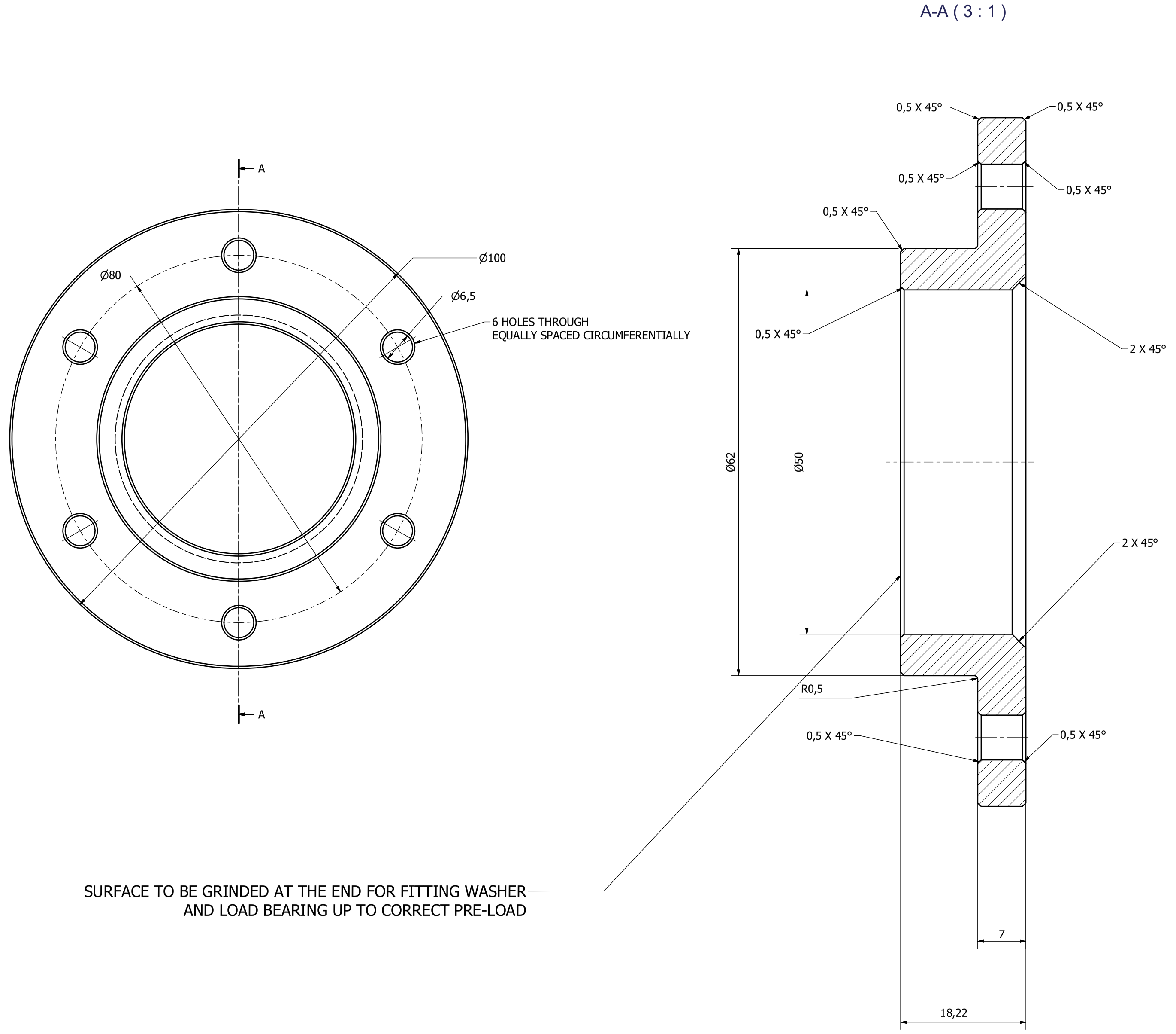

SURFACE TO BE GRINDED AT THE END FOR FITTING WASHER
AND LOAD BEARING UP TO CORRECT PRE-LOAD

Rev No	Date	Name	Alteration		Grid Ref
	Date	Name	THIRD ANGLE PROJECTION	Revision	Units
Drawn	21/01/2020	NC		0	mm
Checked	21/01/2020	TL		Do Not Scale	Mass
Approved	21/01/2020	BM			N/A
Material Treatment Stock Surface Treatment	EN8 Steel		Comments	Title NDE Bearing Cup	
Newcastle University				Drawing No 019	
				Sheet 1 of 1	

UNLESS OTHERWISE STATED	
All dimensions to be within	0.1
All faces to be parallel or square within	0.1
All diameters to be concentric within	0.05
Sharp edges to be broken to	0.1 to 0.3
Surface texture (Ra) not to exceed	1.6µm

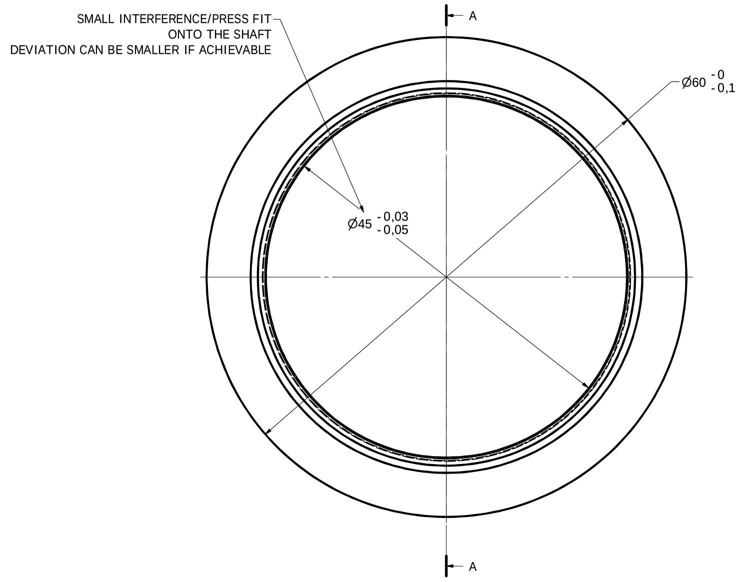

A-A (6 : 1)

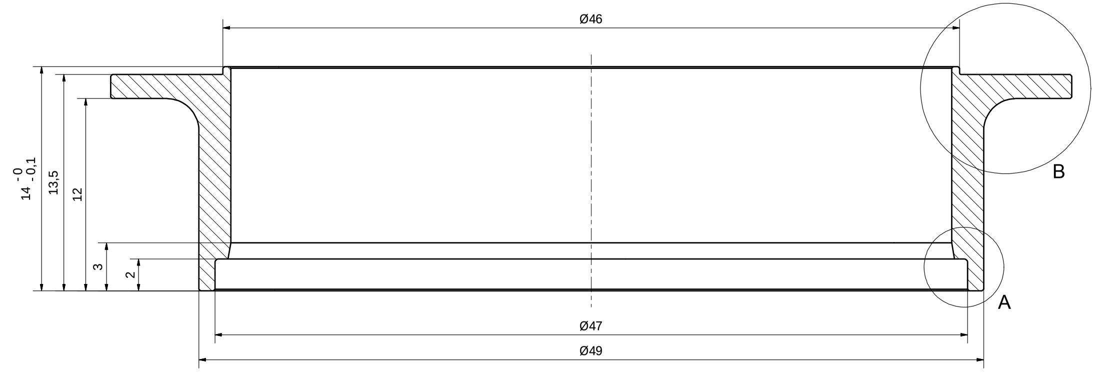

A (20: 1)

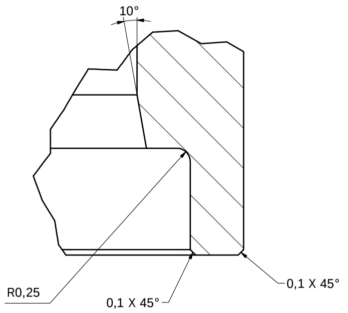

ADDITIONAL VIEW

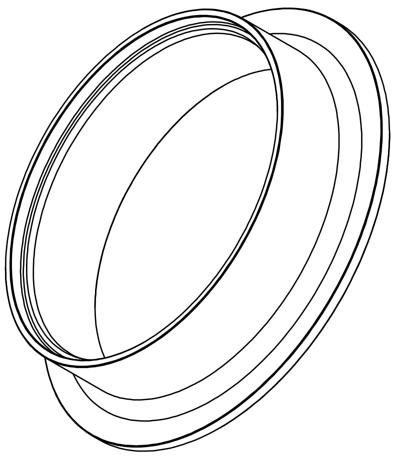

B (20 : 1)

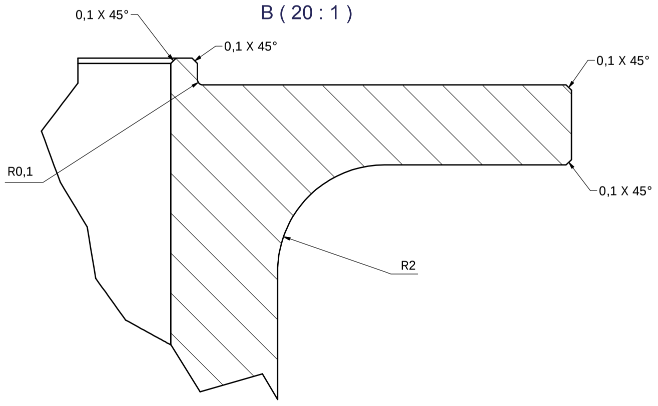

Rev No	Date	Name	Alteration	Grid Ref

	Date	Name
Drawn	4/11/2019	NC
Checked	4/11/2019	TL
Approved	4/11/2019	BM

THIRD ANGLE PROJECTION

Revision	Units
0	mm
Do Not Scale	Mass
	N/A

Material EN24T
Treatment
Stock
Surface Treatment

Comments

Title
Grease Shield NDE

Drawing No
027

Sheet 1 of 1

UNLESS OTHERWISE STATED	
All dimensions to be within	0.1
All faces to be parallel or square within	0.1
All diameters to be concentric within	0.05
Sharp edges to be broken to	0.1 to 0.3
Surface texture (Ra) not to exceed	1.6µm

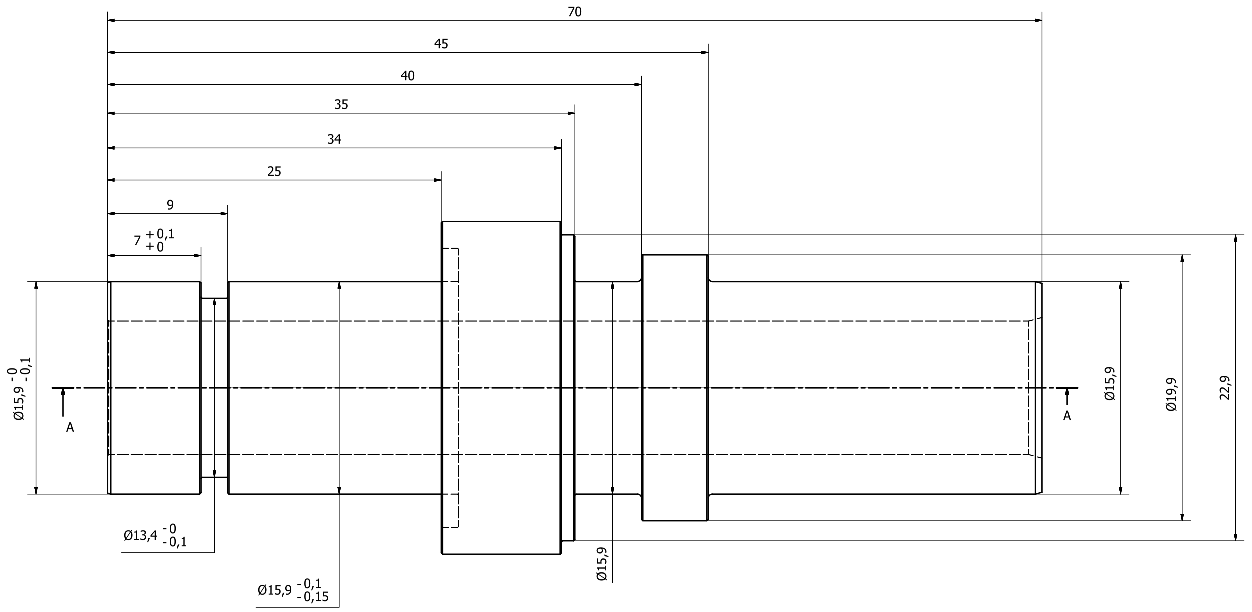

A (20 : 1)

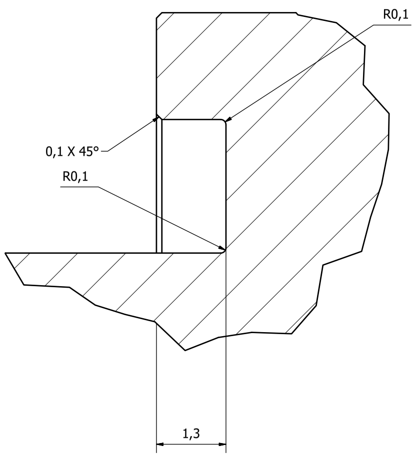

B (25: 1)

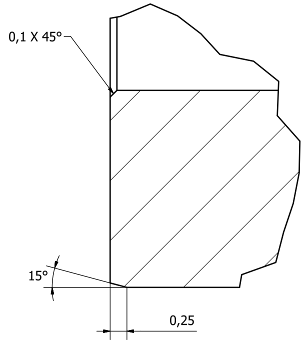

A-A (5 : 1)

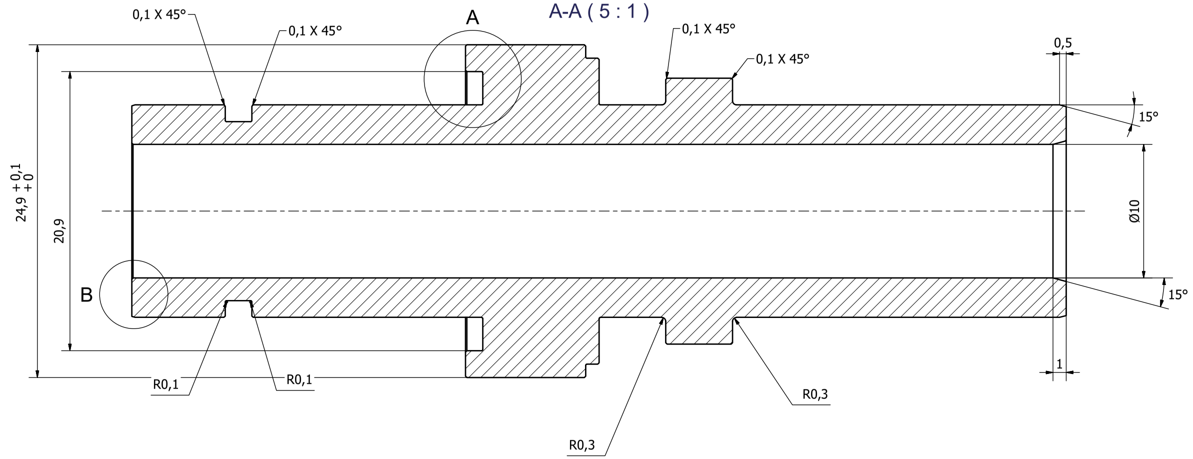

Rev No	Date	Name	Alteration	Grid Ref

	Date	Name	THIRD ANGLE PROJECTION	Revision	Units
Drawn	02/12/2019	NC		Do Not Scale	mm
Checked	02/12/2019	TL			Mass
Approved	02/12/2019	NC			N/A

Material	EN8 Steel	Comments	Title Push Fitting
Treatment			
Stock			
Surface Treatment			
Newcastle University			Drawing No 035
			Sheet 1 of 1

UNLESS OTHERWISE STATED	
All dimensions to be within	0.1
All faces to be parallel or square within	0.1
All diameters to be concentric within	0.05
Sharp edges to be broken to	0.1 to 0.3
Surface texture (Ra) not to exceed	1.6µm

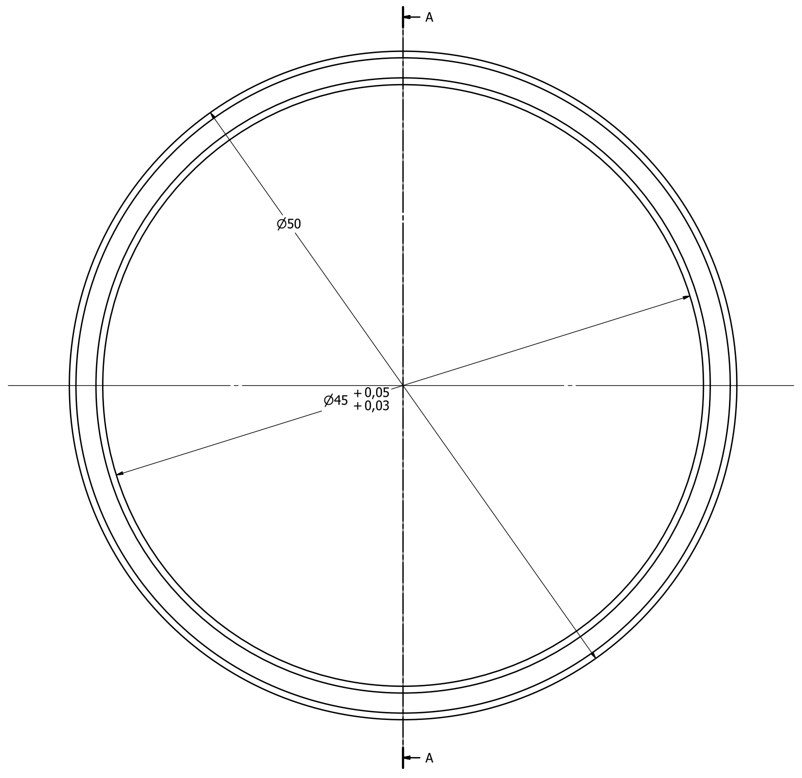

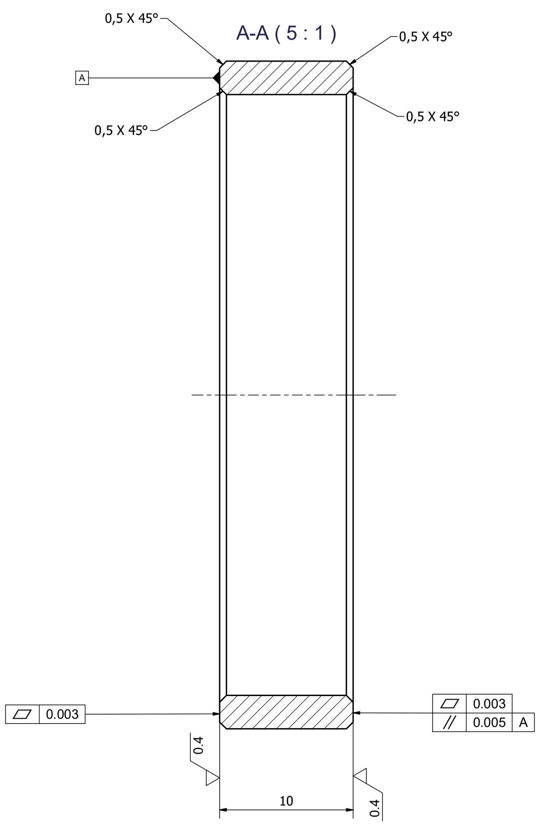

1) THE SPACER MUST BE GRINDED WITH THE SAME ROUGHNESS OF THE HIGH PRECISION BEARING.
TRY TO ACHIEVE 0.4 microns AT THE FLAT SIDES

2) TRY TO BE AS TIGHT AS POSSIBLE FOR THE FLATNESS AND PARALLEL TOLERANCES AT THE FACES.
THEY SHOULD BE AS PARALLEL AS POSSIBLE.

Rev No	Date	Name	Alteration	Grid Ref

	Date	Name	THIRD ANGLE PROJECTION	Revision	Units
Drawn	02/12/2019	NC		0	mm
Checked	02/12/2019	TL		Do Not Scale	Mass
Approved	02/12/2019	BM			3.656 g

Material
Treatment
Stock
Surface Treatment

Comments

Title
Spacer

Newcastle University

Drawing No
024

Sheet 1 of 1